

Language of Foreign Document: German

Translated Title of Document: Accident Simulations and Post-Irradiation Investigations on Spherical Fuel Elements for High Temperature Reactors

Untranslated Title: Störfallsimulationen und Nachbestrahlungsuntersuchungen an kugelförmigen Brennelementen für Hochtemperaturreaktoren

Author(s): Grad. Eng. Daniel Freis

Translated Name and Address of Corporate Author: Dissertation Approved by the Department of Mechanical Engineering of the Rhineland-Westphalian Engineering College for Attainment of the Academic Degree of Doctor of Engineering Sciences

Untranslated Name and Address of Corporate Author: Von der Fakultät für Maschinenwesen der Rheinisch-Westfälischen Technischen Hochschule Aachen zur Erlangung des akademischen Grades eines Doktors der Ingenieurwissenschaften genehmigte Dissertation

Date of Original Foreign Document(s): March 1, 2010

Foreign Document ID Number(s):

Number of Pages in Translation: 1

Date Translated for NRC: August 16, 2011

NRC Requester/Office: Jonathan Barr/CSB-C5 C26

**Translated by:
Name and
Address** U.S. Translation Company
www.ustranslation.com
1893 East Skyline Drive, Ste. 203
South Ogden, UT 84403

**Accident simulations and post-irradiation investigations on spherical fuel
elements for high temperature reactors**

Dissertation approved by the Department of Mechanical Engineering of the Rhineland-
Westphalian Engineering College for attainment of the academic degree of Doctor of
Engineering Sciences

submitted by

Grad. Eng. Daniel Freis

Advisers: University Professor Hans-Josef Allelein, Dr. rer. Nat.
University Professor Thomas Fanghänel, Dr. rer. nat. habil.

Date of oral examination 01. March 2010

“This dissertation is available on the internet pages of the Hochschulbibliothek online.”

Foreword

My particular thanks to

Professor Kurt Kugeler and Professor Hans-Josef Allelein for personal academic encouragement during my doctoral work from Aachen.

My thanks to Professor Hans-Josef Allelein and Professor Thomas Fanghänel for accepting the advisor function and providing the certification as well as to Professor Lorenz Singheiser and Proferssor Detlev Stöver for accepting the chairmanship and assistantship positions during the doctoral examination.

My sincere thanks to Dr. Enrique Toscano and Dr. David Bottomley for outstanding mentoring while the work was being conducted at the Institute for Transuranium Elements and for their support, the good advice and their assistance in all of my questions and for feedback on my work.

I would also like to thank in particular all my colleagues at the Institute for Transuranium Elements and especially the Department of Hot Cells, who cooperated directly with me and always supported me and accepted me in their community. My special thanks to Mr. John Ejton, Mr. Herbert Kostecka, Mr. Wim de Weerd and Dr. habil. Alban Kellerbauer. I would also like to thank my own department directors Dr. Jean-Paul Glatz and Dr. Vincenzo Rondinella for their benevolent support on all occasions.

Dr. Werner Schenk, Dr. Heinz Nabielek, Dr. Karl Verfondern and Dr. Heinz Werner† are thanked for their advice and involved support from Jülich. Based on their decade long experience with post-irradiation investigations on HTR fuel element they always provided me with valuable assistance.

My thanks to Dr. Anton Schmidt and Mr. Markus Esch of Westinghouse and also to my parents for the proofreading (a small line for a lot of work).

I would also like to express my gratitude to many other colleagues with whom I collaborated in the course of my three years at the Institute for Transuranium Elements or otherwise had

contact with and who also helped me whenever they could. Specifically I would like to thank Mme.Dr. Laura Aldave de las Heras, Mr. Jean-Luc Arnoult, Mr. Denis Baudot, Mr. Antonio Busto, Dr. Paul Carbol, Mme. Dr. Birgit Christiansen, Mr. Jean-Yves Colle, Mr. Dragan Coric, Mr. Markus Ernstberger, Mr. Ernesto Fontana, Mr. Markus Gammelín, Mr. Ralf Gretter, Mrs. Irmgard Henzel, Dr. Jean-Pol Hiernaut, Mr. Francois Kinnart, Mr. Joachim Küst, Dr. Joseph Magill, Dr. Rikard Malmbeck, Mr. Gerard Montagnier, Mrs. Sophie Mühlberger, Mr. Paulo Nascimento, Mr. Ramil Nasyrow, Dr. Michel Ougier, Dr. Dimtri Papaioannou, Mr. Didier Pellotiero, Mr. Thierry Romero, Dr. Joseph Somers, Mr. Michael Spreizenbarth, Mr. Hartmut Thiele, Mr. Matthias Uhlig, Mr. Jacques van de Laar, Dr. Stefaan van Winckel, Dr. Clive Walker, Mr. Arndt Walschburger, Mr. Werner Weber and Dr. Detlef Wegen.

My special thanks to my dear parents who always gave me unconditional moral and material support both during my studies and also during the doctoral work.

I thank my wife for her love, her support and her understanding during the last phase of the work.

I thank the citizens of Europe for supporting this work with their taxes at such a well equipped and excellent research institute. I hope that this work will bring them some benefit.

Summary

An important aspect of the safety of high-temperature reactors is the quality of the fuel and its ability to remain intact even at high temperatures and to safely incorporate the fission products. In conjunction with a suitable reactor design, in this way a system-inherent safety against major releases of fission products can be achieved.

Within the scope of this work, experimental accident simulations were conducted on highly burnt-down spherical fuel elements for high temperature reactors with TRISO-coated particles from different irradiation experiments and fission product releases measured. For this purpose, the cold finger apparatus was used, an experimental device whose precursor had already been used in the Jülich Nuclear Research installation, the present Jülich Research Center.

The new Cold Finger apparatus has been installed in the hot cells of the European Institute for Transuranium elements since 2005. The Cold Finger apparatus at the Transuranium Institute permitted accident simulations on irradiated high temperature reactor fuel elements in a helium atmosphere, at ambient pressure, at temperatures up to 1800°C and for time periods of several hundred hours. At that time both the release of fission gases and the release of solid fission products was registered.

In addition, within the scope of the study presented here, the mechanical behavior of the particles and the transporting mechanisms of the most important fission products were analyzed and the releases recalculated.

For a better understanding of the processes, in addition, various post-irradiation studies were conducted on the fuel elements that were accessible. Finally, an evaluation was made of the test results and compared with the results in the available literature. An important goal of this work was to expand the database for modern HTR fuel to include higher burn-ups, higher fluences of fast neutrons, higher operating temperatures and higher accident temperatures.

Abstract

An important aspect of the safety of high temperature reactors is the quality of the nuclear fuel and its ability to remain intact even at high temperatures and to safely contain the radioactive fission products. In combination with a suitable reactor an inherent safety against large release of fission products can be achieved.

In this work experimental simulations of severe accidents were conducted on spherical fuel elements for high temperature reactors with TRISO-coated particles and fission product release was measured. The fuel elements originated from various irradiation experiments conducted at high temperatures with high burn-up. The experiments were performed using the cold finger apparatus, a test apparatus which was already used in the past in a former version at the Research Center Jülich.

The new cold finger apparatus is installed since 2005 in the Hot Cells of the European Institute for Transuranium Elements. The cold finger apparatus at the Institute for Transuranium Elements enabled incident simulations on irradiated high temperature reactor fuel elements in a helium atmosphere at ambient pressure, at temperatures up to 1800 °C and for periods of several hundred hours. Here, both the release of fission gases and the release of solid fission products were measured.

In addition, in the context of the present study, the mechanical behavior of the fuel particles and the transport mechanisms of the main fission products were analyzed and the expected release was computed.

For a better understanding of the processes post irradiation examinations were conducted on the available fuel elements. It was finally made an assessment of the test results which were compared with results in the existing literature. A key objective of the work was the extension of the existing data base for modern HTR-fuel towards higher burn-up and higher fluences of fast neutrons, higher operating temperatures and extended accident temperatures.

Contents

Foreword	1
Summary	3
Abstract	4
Contents	5
Abbreviations	9
Symbols	12
List of illustrations	15
List of tables	19
1. Introduction	22
2. Background	
2.1 High temperature reactor	24
2.2 Development and structural types	27
2.3 Reactor physics and safety behavior	31
2.4 State of the art for HTR fuel elements	33
2.5 Relevant fission products	40
3. Earlier works	44
4. Statement of the problem for the present study	51
5. Execution of the tasks described here	54
5.1 Cold finger apparatus	54
5.2 Course of the bakeout tests	57
5.3 Fission gas measurement	59
5.4 Measurement of solid fission product release	63
5.5 Calibration of the cold finger efficiency	65
5.6 Unusual incidents	67
5.6.1 Irruption of cell atmosphere	68
5.6.2 Temperature rise on the condensate plate due to graphite deposition	69
5.6.3 Cooling cycle regulation problems	69
5.6.4 Spark jumps	69
5.7 Gamma spectrometric fission product inventory measurement and burn-up determination	70
6. Results of the experimental work	78

6.1	AVR 73/21	78
6.2	AVR 74/18	80
6.2.1	Dates of the experiment	80
6.2.2	Measured fission product releases	81
6.2.3	Summary	82
6.3	HFR K6/2	83
6.3.1	Dates of the experiment	83
6.3.2	Measured fission product releases	85
6.3.3	Special events - observations	85
6.3.4	Summary	86
6.3.5	Additional studies on HFR K6/2	87
6.4	HFR K6/3	87
6.4.1	Dates of the experiment	87
6.4.2	Measured fission product releases	88
6.4.3	Ceramographic studies and microhardness measurement	89
6.4.4	Electron microscopy and EDX studies	94
6.4.5	Determination of the SiC layer thickness	97
6.4.6	Summary	100
6.5	HFR Eu1bis	102
6.5.1	Dates of the experiment	102
6.5.2	Measured fission product releases	104
6.5.3	Summary	105
6.6	HFR Eu1bis 3	107
6.6.1	Dates of the experiment	107
6.6.2	Measured fission product releases	108
6.6.3	Summary	109
6.7	HFR Eu1bis 4	110
6.7.1	Dates of the experiment	110
6.7.2	Measured fission product releases	112
6.7.3	Summary	114
7.	Interpretation and modeling	115
7.1	Damage mechanisms	115
7.1.1	Pressure vessel failure	115
7.1.2	Fabrication defects	117

7.1.3	Ameba effect	117
7.1.4	Decay of the SiC coating by fission product corrosion	118
7.1.5	Oxidic and thermal decomposition of the SiC coating	118
7.2	Gas release	119
7.3	Release of solid fission products	121
7.4	Diffusion model	124
7.5	Mechanical particle failure	131
7.5.1	Internal gas pressure	132
7.5.2	Material data for the FEM simulation	134
7.5.3	Simulation of the voltage curve and failure statistics	138
7.6	AVR 74/18	140
7.6.1	Mechanical particle failure	140
7.6.2	Fission product release (Cs-137) by diffusion	142
7.7	HFR K6/2	143
7.7.1	Mechanical particle failure	143
7.7.2	Fission product release by diffusion	146
7.8	HFR K6/3	149
7.8.1	Mechanical particle failure	149
7.8.2	Fission product release by diffusion	151
7.9	HFR Eu1bis irradiation	154
7.10	HFR Eu1bis1	156
7.10.1	Mechanical particle failure	156
7.10.2	Fission product release by diffusion	159
7.11	HFR Eu1bis3	162
7.11.1	Mechanical particle failure	162
7.11.2	Fission product release by diffusion	163
7.12	HFR Eu1bis 4	165
7.12.1	Mechanical particle failure	165
7.12.2	Fission product release by diffusion	167
8.	Significance of the results	170
9.	Prospects	178
	References	180
I.	Appendix – Results in tabular form	189
Ia.	AVR 74/18	189

Ib.	HFR K6/2	191
Ic.	HFR K6/3	193
Id.	HFR Eu1bis 1	196
Ie.	HFR Eu1bis 3	201
If.	HFR Eu1bis 4	204
II.	Appendix – voltage analysis	207
III.	Appendix – temperature calculations	213
IIIa.	Temperature distribution in the fuel elements	213
IIIb.	Temperature distribution in the CoFA-II	217
IIIc.	AVR 74/18	220
IV.	Appendix – determination of the uncertainty	222
V.	Appendix – diffusion parameters	227
VI.	Appendix – correction factors for gamma spectrometry	230
VII.	Appendix – Determination of ball diameter	235

Abbreviations

Abbreviation	Meaning
AVR	Test reactor operating association
BAF	Bacon Anisotropy Factor
BISO	Fuel particles with two mechanically stable jacket layers (Bi-ISOTrop)
BNFL	British Nuclear Fuel
Buffer	Buffer layer/film of pyrolytic carbon
CP	<i>Coated Particle</i>
CVD	<i>Chemical Vapor Deposition</i>
EDN	Unit for the fluence of fast neutrons (Equivalent Dido Nickel)
efpd	Irradiation time in full power days (Effective Full Power Days)
FEM	Finite Element Method
FIMA	Burn-up – fissions per initially present heavy metal atoms (<i>Fissions per Initial Metal Atoms</i>)
FR	<i>Fractional Release</i>
FZJ	Jülich Research Center
GT-MHR	American HTR (<i>Gas Turbine – Modular Helium Reactor</i>)
HEU	<i>Highly Enriched Uranium</i>
HFR	Material test reactor in Petten / Netherlands (<i>High Flux Reactor</i>)
HTR	High temperature reactor

HTTR	Japanese high temperature reactor (<i>High Temperature Engineering Test Reactor</i>)
HV	Vickers hardness
IE	Joint Research Station of the European Commission – Institute für Energie (Petten, Netherlands)
IPyC-Schicht	<i>Inner Pyrocarbon coating/layer</i>
ITU	Joint Research Station of the European Commission – Institute for Transuranium Elements (Karlsruhe)
KLAK	Small absorber balls
CoFA	Cold finger apparatus
LEU	<i>Low Enriched Uranium</i>
LWR	Light water reactor
NRG	Netherlands Nuclear Research Institution " <i>Nuclear Research and Consultancy Group</i> "
OPF	Number of oxygen atoms released per fission (<i>Oxygen per Fission</i>)
OPyC-Schicht	Outer pyrocarbon coating
ORNL	US research laboratories in Oak Ridge (<i>Oak Ridge National Laboratory</i>)
PBMR	South African Modular pebble bed high temperature reactor (<i>Pebble Bed Modular Reactor</i>)
PIE	<i>Post Irradiation Examination</i>
PyC	Pyrocarbon
R/B	<i>Release to Birth Rate</i>
SiC	Silicon carbide jacket layer
THTR	Thorium high temperature reactor

TRISO	Fuel particles with three mechanically stable jacket layers (TRi-ISOtrop)
UC	Uranium carbide
UCO	<i>Uranium Oxycarbide</i>
UO ₂	Uranium dioxide
V-HTR	Future HTR concept (Very High Temperature Reactor)

Symbols

Symbol	Meaning
A	Activity (Bq)
b	Transport coefficient (1 / s)
BU	<i>Burn-up</i> (% FIMA)
C	Concentration (1 / mm ³)
d	diameter (m)
D	Diffusion coefficient (m ² / s)
D'	reduced diffusion coefficient (1 / s)
D ₀	Frequency factor (m ² / s)
E	Neutron or gamma energy (MeV)
E _{KF}	Cold finger efficiency
f _k	Calibration factor
<i>i</i>	Impulse rate (1/s)
K	Correction factor
K	Creep constant (MPa 10 ²⁵ m ⁻²) ⁻¹
K _U	Free uranium contamination in the graphite matrix
m	material concentration (1 / mm ³)
m	Weibull parameter
n	Material quantity (moles)

N	Number of atoms
P	Probability of failure
Q	Activation energy (J)
r	Radius (m)
R	general gas constant (8.3144 J/mol K)
R	Released activity (Bq)
s	Layer thickness (m)
t	Time (s)
$t_{1/2}$	Half-life (a)
T	Temperature (K)
V	Volume (m ³)
\dot{V}	Volume flow (m ³ / s)
α	Dimensionless temperature-dependent mass transport coefficient
γ	Fission output
$\varepsilon / \dot{\varepsilon}$	Elongation / Elongation rate (1/s)
λ	Decomposition constant (1/s)
λ	Thermal conductivity (W / mK)
ρ	Density (kg / m ³)
σ_b	Cross section of effect (barn)
σ	Tension or tensile strength (MPa)
v	Cross contraction number

μ	Transport coefficient (1 / s)
Φ	Neutron flux (1/m ² s)
Φ_s	Fast neutron fluence (E > 0,1 MeV) (1025 / m ²)
θ	Temperature (°C)

List of illustrations

Figure 1: Basic representation of a pebble heap HTR (PBMR-400) with annual reactor core [Venter & Mitchell 2007]	26
Figure 2: Anticipated temperature curve for pressure loss accident in the HTR module reactor and typical CoFA bakeout test	33
Figure 3: Prismatic HTR fuel element for the Japanese HTTR [Shiozawa, et al. 2004	34
Figure 4: Spherical HTR fuel element	35
Figure 5: Polished section micrograph of a TRISO coated particle under the scanning electron microscope	37
Figure 6: Kr-85 releases during bakeout test in the FZJ on LEU TRISO fuel elements up to 2100°C (CoFA and A test) [Schenk et al. 1988]	49
Figure 7: Cs-137 releases during FZJ bakeout test on LEU TRISO fuel elements up to 2000°C (CoFA and A test) [Schenk et al. 1988]	50
Figure 8: Irradiation and accident parameter range for HTR model in comparison with this work.....	53
Figure 9: Schematic representation of the CoFA II	55
Figure 10: CoFA standard test [Schenk et al. 1988]	58
Figure 11: Schematic representation of the cold trap	60
Figure 12: Time activity curve in the cold trap after calibration with 135 kBq Kr-85	62
Figure 13: Graphite ball with Cs-137 standard for cold finger efficiency determination.....	65
Figure 14: Corrosion on the heating element.....	70
Figure 14: Heating element destroyed by short circuit	70
Figure 16: Gamma spectrometry measurement setup	71
Figure 17: HTR fuel element gamma spectrum (HFR Eu1bis3)	72
Figure 18: Temperature curve of AVR 73/21 bakeout experiment	79
Figure 19: Temperature curve and fission product release of AVR 74/18 bakeout experiment	82
Figure 20: Temperature curve and fission product release of AVR K6/2 bakeout experiment... ..	86
Figure 21: Temperature curve and fission product release of AVR K6/3 bakeout experiment... ..	89
Figure 22: Section plan for the cylinder from HFR K6/3	90
Figure 23: Micrograph of HFR K6/3, Particle A (after 400 h at 1800°C)	90
Figure 24: Micrographs of HFR K6/3, Particle B (after 400h h at 1800°C)	92

Figure 25: Micro-hardness test after Vickers, sample with test markings	93
Figure 26: Scanning electron-microphotograph of HFR K6/3, particle C.....	95
Figure 27: Scanning electron-microphotograph of HFR K6/3, particle D	96
Figure 28: Determination of section height of a studied particle	97
Figure 29: ECX spectrum in the buffer layer of HFR K6/3 particle E (measurement time=1457 s).....	99
Figure 30: Particle E from HFR K6/3 with EDX measurement positions (magnification 100x)	100
Figure 31: Bakeout experiment HFR Eu1 to 1 – temperature curve and fission product release	105
Figure 32: Bakeout experiment HFR Eu1 to 3 – temperature curve and fission product release	109
Figure 33: Bakeout experiment HFR Eu1 to 4 – temperature curve and fission product release	113
Figure 34: Equilibrium release and release jumps for HFR Eu1 to 4.....	120
Figure 35: Excerpt from Excel calculation page	126
Figure 36: Cs-137 diffusion through an A3 graphite bead at 1300°C	130
Figure 37: Benchmark of the diffusion model employed at 1600°C test temperature (HFR K3/3).....	131
Figure 38: FEM model of the three layer system IPyC, SiC and OPyC layer	132
Figure 39: Elasticity modulus of PyC acc. to FZJ and BNFL [Pelletier 2003]	135
Figure 40: Elasticity modulus of PyC acc. CEGA [Pelletier 2003]	135
Figure 41: HFR K6/3 – tangential stress curve during irradiation	138
Figure 42: AVR 74/18 – calculated probability for failure of a PyC layer during irradiation	141
Figure 43: AVR 74/18 – Particle failure probability and measured Kr-85 release.....	142
Figure 44: AVR 74/18 bakeout experiment – calculated and measured Cs-137 release	143
Figure 45: HFR K6/2 – calculated probability for failure of a PyC layer during irradiation	144
Figure 46: HFR K6/3 – calculated tangential stress curve during bakeout test	145
Figure 47: HFR K6/2 – Particle failure probability and measured Kr-85 release	146
Figure 48: HFR K6/2 – calculated Cs-137 distribution in the graphite matrix at end of irradiation	147
Figure 49: HFR K6/2 – calculated Cs-137 distribution in a coated particle [at end of irradiation	148
Figure 50: HFR K6/2 bakeout experiment – calculated and measured Cs-137 release	148
Figure 51: HFR K6/3 – calculated probability for failure of a PyC layer during irradiation	149

Figure 52: K6/3 – calculated particle failure probability and measured Kr-85 release	150
Figure 53: HFR K6/3 bakeout experiment – calculated and measured Cs-137 release	152
Figure 54: K6/3 – calculated and measured Cs-137 distribution in the coated particle at end of test	153
Figure 55: HFR Eu1bis – calculated Ag-110 release during irradiation	154
Figure 56: HFR Eu1bis – calculated cesium release during irradiation	155
Figure 57: HFR Eu1bis – calculated Cs-137 distribution in the graphite matrix at end of irradiation	156
Figure 58: HFR Eu1bis1 – calculated probability of particle fracture during irradiation	157
Figure 59: HFR Eu1bis 1 – calculated tangential stress curve during the irradiation of already failed IPyC layer	158
Figure 60: HFR Eu1bis1 – Particle failure probability and measured Kr-85 release.....	159
Figure 61: HFR Eu1bis1 bakeout experiment – calculated and measured cesium release	160
Figure 62: HFR Eu1bis1 bakeout experiment – calculated and measured silver release	161
Figure 63: HFR Eu1bis3 – calculated probability of particle fracture during irradiation	162
Figure 64: HFR Eu1bis3 – Particle failure probability and measured Kr-85 release	163
Figure 65: HFR Eu1bis3 bakeout experiment – calculated and measured cesium release	164
Figure 66: HFR Eu1bis3 bakeout experiment – calculated and measured silver release	165
Figure 67: HFR Eu1bis 4 – calculated tangential stress curve during irradiation	166
Figure 68: HFR Eu1bis 4 – calculated probability of particle fracture during irradiation	166
Figure 69: HFR Eu1bis4 – Particle failure probability and measured Kr-85 release.....	167
Figure 70: HFR Eu1bis4 bakeout experiment – calculated and measured cesium release	168
Figure 71: HFR Eu1bis bakeout experiment – calculated and measured silver release	169
Figure 72: Summary of the Cs-137 releases at 1600°C	172
Figure 73: Summary of the Cs-137 releases at 1800°C	176
Figure 74: Release of Cs-137 at 1600°C as a function of the irradiation temperature	177
Figure 75: Summary of the Kr-85 releases as a function of the heating temperature	177
Figure 76: Tangential stress distribution for a linear-elastic, spherically symmetrical three layer system at an internal pressure of 33 MPa	210
Figure 77: Radial stress distribution for a linear-elastic, spherically symmetrical three layer system at an internal pressure of 33 MPa	211
Figure 78: Irradiation-induced dimensional change of PyC in the radial and tangential direction as a function of the fast neutron fluence ($E>0.1$ MeV).....	212

Figure 79: Relative thermal conductivity of matrix graphite as a function of the fast neutron fluence and temperature [Kugeler & Schulten 1989]	215
Figure 80: Thermal conductivity of particle layer materials as a function of the temperature [Nabielek et al. 1992]	216
Figure 81: Calculated and measured CoFA temperature as a function of the thermal output..	218
Figure 82: Temperature distribution (in K) in the CoFA II at 1650°C temperature on the thermal element	219
Figure 83: Temperature distribution (in K) in the fuel element at 1650°C temperature on the thermal element	219
Figure 84: Assumed temperature curve during the irradiation of AVR 74/18 [Nabielek 2008]	221
Figure 85: Representation of the measurement geometry for the activity measurement of the condensate plates.....	225
Figure 86: Summary of the temperature-dependent diffusion coefficient of cesium in silicon carbide ($\Phi = 4.6 \cdot 10^{25} \text{ m}^{-2}$)	229
Figure 87: Laminar structure of a bead of cylinder elements.....	230
Figure 88: Composition of a bead of cylinder elements.....	231
Figure 89: Standard cylinder for dimension measurement	235
Figure 90: Measurement positions for measuring the dimensional variation of the fuel elements	236

List of Tables

Table 1: High temperature reactors already in operation.....	28
Table 2: Selected HTR designs	30
Table 3: Properties of A3-3 graphite [Hrovat et al. 1988], [Petti et al. 2002]	36
Table 4: Fuel element types with LEU TRISO coated particle after 1981 [Nabielek et al. 2005]	38
Table 5: Properties of relevant fission products.....	43
Table 6: Irradiation data of four HTR fuel elements with high burn-ups studied at the FZJ [Schenk & Nabielek 1989].....	47
Table 7: Earlier CoFA experiments with LEU TRISO fuel elements [Nabielek et al. 2009]	47
Table 8: Properties of fission gases.....	59
Table 9: Melting and boiling points of metallic fission products and cold finger efficiencies	64
Table 10: Cs-137 activity of the calibration plates	67
Table 11: Measured Cs-137 inventories (related to end of irradiation) and calculated burn-ups	75
Table 12: Nd-148 and Cs-137 burn-up determination	77
Table 13: Irradiation data of the AVR 73/21 fuel element	78
Table 14: Summary of results of the AVR 73/21 CoFA experiment	80
Table 15: Irradiation data of the AVR 74/18 fuel element.....	80
Table 16: Fission product inventory of AVR 74/18 at beginning of experiment (17 Jan 2006) ...	81
Table 17: Summary of results of the AVR 74/18 CoFA experiment	83
Table 18: Irradiation data for HFR K6/2 fuel element	84
Table 19: Fission product inventory of HFR K6/2 at beginning of experiment (06 Jul 2006).....	84
Table 20: Summary of results of the HFR K6/2 CoFA experiment	87
Table 21: Irradiation data for HFR K6/3 fuel element	88
Table 22: Fission product inventory of HFR K6/3 at beginning of experiment (15 Feb 2006) ...	88
Table 23: Microhardness testing on HFR K6/3	93
Table 24: Average layer thickness of the SiC layer	98
Table 25: Cesium concentration profile	100
Table 26: Summary of results of the HFR K6/3 CoFA experiment	102
Table 27: Irradiation data for HFR Eu1bis 1 fuel element	103

Table 28: Fission product inventory of HFR Eu1bis1 at beginning of experiment (28 Mar 2006)	104
Table 29: Summary of results of the HFR Eu1bis1 CoFA experiment.....	106
Table 30: Irradiation data for HFR Eu1bis 3 fuel element	107
Table 31: Fission product inventory of HFR Eu1bis3 at beginning of experiment (23 Jul 2008)	107
Table 32: Summary of results of the HFR Eu1bis 3 CoFA experiment.....	110
Table 33: Irradiation data for HFR Eu1bis 4 fuel element	111
Table 34: Fission product inventory of HFR Eu1bis 4 at beginning of experiment (23 Jul 2008)	111
Table 35: Summary of results of the HFR Eu1bis4 CoFA experiment.....	114
Table 36: Irradiation data for HFR K3/3 fuel element	130
Table 37: Irradiation data for AVR 74/18	140
Table 38: Input data for HFR K6/2	143
Table 39: Input data for HFR K6/3	149
Table 40: Input data for HFR Eu1bis 1	156
Table 41: Input data for HFR Eu1bis 3	162
Table 42: Input data for HFR Eu1bis 4	165
Table 43: Summary of experimental/test data	172
Table 44: Summary of experimental/test results.....	174
Table 45: Heating program and plate exchange of AVR 74/18	189
Table 46: Cs-137 activity of the condensate plates of AVR 74/18	190
Table 47: Cs-137 activity of the condensate plates of HFR K6/2	191
Table 48: Heating program and plate exchange of HFR K6/2	192
Table 49: Heating program and plate exchange of HFR K6/3	193
Table 50: Cs-137 activity of the condensate plates of HFR K6/3	195
Table 51: Heating program and plate exchange of HFR Eu1bis1	196
Table 52: Cs-137 and Cs-134 activities of the condensate plates of HFR Eu1bis 1	198
Table 53: Ag-110m and Ru-106 activities of the condensate plates of HFR Eu1bis 1	199
Table 54: Cumulative release amounts for HFR Eu1bis1	199
Table 55: Heating program and plate exchange of HFR Eu1bis3	201
Table 56: Cs-137 and Cs-134 activities of the condensate plates of HFR Eu1bis 3	202
Table 57: Ag-110m and Ru-106 activities of the condensate plates of HFR Eu1bis 3	202
Table 58: Cumulative release amounts for HFR Eu1bis3	203

Table 59: Heating program and plate exchange of HFR Eu1bis4	204
Table 60: Cs-137 and Cs-134 activities of the condensate plates of HFR Eu1bis 4	205
Table 61: Ag-110m and Ru-106 activities of the condensate plates of HFR Eu1bis 4	205
Table 62: Cumulative release amounts for HFR Eu1bis4	206
Table 63: Irradiation temperatures of the fuel elements studied	216
Table 64: Required CoFA heating capacities for different temperatures	217
Table 65: Diffusion parameters for cesium in jacketing layers and A3 graphite [Verfondern et al. 1997]	227
Table 66: Diffusion parameters for strontium in jacketing layers and A3 graphite [Verfondern et al. 1997]	227
Table 67: Diffusion parameters for silver in jacketing layers and A3 graphite [Verfondern et al. 1997]	228
Table 68: Diffusion parameters for krypton, xenon and iodine in jacketing layers and A3 graphite [Verfondern et al. 1997]	228
Table 69: Correction factors for different fuel element types at 661.66 keV.	234

1. Introduction

An important aspect of the safety of high temperature reactors (HTR) is the quality of the fuel and its ability to remain intact even at high temperatures and to incorporate the fission products safely. In the interplay with a suitable reactor design layout, in this way a system-inherent safety against major fission product release can be achieved. Modern HTR fuel with multiply-coated uranium dioxide particles, the so-called TRISO coated particles, of low enrichment is designed for maximal fuel temperatures during irradiation of about 1100°C and burn-ups of 10% FIMA.

During the operation, practically all fission products are retained in the fuel element so that the contamination of the primary circuit components and therefore the annual doses received by the operating personnel during repair work, maintenance and repeated tests are significantly reduced. In the event of an accident, especially with a pressure loss in the primary circuit and the outage of the active secondary heat removal, distinctly elevated temperatures may occur. Small modular HTR designs are laid out in such a way today that only passive heat removal mechanisms suffice to keep the maximal temperature below 1600°C under all operating and accident conditions, with allowance for the uncertainties [Reutler & Lohnert 1984].

In comprehensive testing programs it could be shown that the release of fission products from HTR fuel elements up to a burn-up of 11% FIMA and at a simulated accident temperature of 1600°C for more than 100 hours is negligibly small [Schenk et al, 1997]. Therefore, the effects of a pressure loss accident with failure of all active heat removal mechanisms is confined to the plant. Under some conditions, as a result a gas-tight safety container could be dispensed with, thereby increasing the competitiveness of HTR.

Future HTR designs such as the V-HTR envision higher gas exit temperatures, larger buildings, higher power densities and higher target burn-ups. From the higher burn-up a greater fission product inventory as well as a higher burden/stress on the fuel result. Higher fuel temperatures under operating and accident conditions follow from the higher power density, the higher coolant temperature and the larger building size. Statements regarding the fuel behavior in high burn-up stages and at elevated temperature are possible only with sufficient knowledge of the active mechanisms and material properties. These facts can only be obtained in costly irradiation and heating experiments.

As part of this project, experimental accident simulations were conducted on highly burnt off HTR spherical fuel elements from different irradiation experiments and the fission product releases measured. For this purpose the cold finger apparatus (CoFA II) was used, a testing device that had already been used in the nuclear research facility in Jülich, the present Jülich Research Center (FZJ) (CoFA I) and has been installed since 2005 in the Hot Cells of the European Institute for Transuranium Elements (ITU) [Schenk et al. 1988, Toscano et al. 2004]. The CoFA II permitted simulations of accidents on irradiated HTR fuel elements in a helium atmosphere at ambient pressure at temperatures up to 1800°C and for time intervals of several hundred hours. In this case both the fission gas release and the release of solid fission products were registered. In addition, the mechanical behavior of the particles and the transporting mechanisms of the most important fission products were analyzed and the releases recalculated.

For a better understanding of the processes, in addition, various post-irradiation studies (PIE) were performed on the available fuel elements. Finally, an evaluation of the results of the tests was performed and compared with the results in the available literature.

2. Background

2.1 High temperature reactor

A high temperature reactor (HTR) is a graphite-moderated and helium-cooled nuclear reactor. All components in the reactor core of an HTR are ceramic and therefore permit high fuel and coolant temperatures. Due to the high outlet temperature of the coolant, between 700 and 1000°C, HTR are widely used. Direct circulations with helium turbines or combined gas and steam turbine processes permit current generation with high efficiency. Other high temperature processes also, e.g., coal gasification or hydrogen generation are also conceivable with an HTR as the heat source.

Side, floor and ceiling reflectors of an HTR as well as other firm/solid core structures are usually made of graphite. The fuel elements consists of a graphite matrix with embedded coated fuel particles. The fuel exists in the form of uranium dioxide (UO_2), uranium carbide (UC_2) or uranium oxide carbide (UCO) with a low U-235 enrichment (LEU) of 9 to 20%. In the past, particles with highly enriched uranium (HEU) with enrichment factors of up to 95% were used. These were combined with breeder particles of thorium oxide or natural uranium oxide in order to generate additional fuel during the burn-up cycle and save on resources (e.g., THTR).

HTR fuel elements can be of block shape, cylindrical or spherical. HTR with block shaped or cylindrical fuel elements have a static core that is newly charged and recoated during a revision phase. In the case of the spherical fuel elements, the reactor core consists of a loose heap of fuel elements that migrate slowly through the core by gravitation from top to bottom during a burn-up cycle. The fuel elements are fed in here continuously from above, removed at the bottom and their burn-up is then determined. Corresponding to their burn-up stage, the fuel elements are then returned to the reactor or disposed of. Depending on the design, during this a fuel element passes through the reactor up to six times until the target burn-up is achieved.

The coolant helium flows through the reactor core, is heated up in the process and leaves the reactor. The heat generated is then taken from the helium cycle and fed to a user process. A gas blower finally sends the cooled helium back to the reactor and compensates for pressure losses.

To control the reactivity of an HTR, as a rule, neutron-absorbing control rods are used that are either driven directly into the pebble bed or into borings in the side reflectors. For reasons of diversity and to assure the long-term subcriticality in the cold state, HTR usually have other switch-off systems, therefore, e.g., bead of boron carbide (KLAK) which when necessary can be allowed to drop into borings in the side reflector [Kugeler & Schulten 1989].

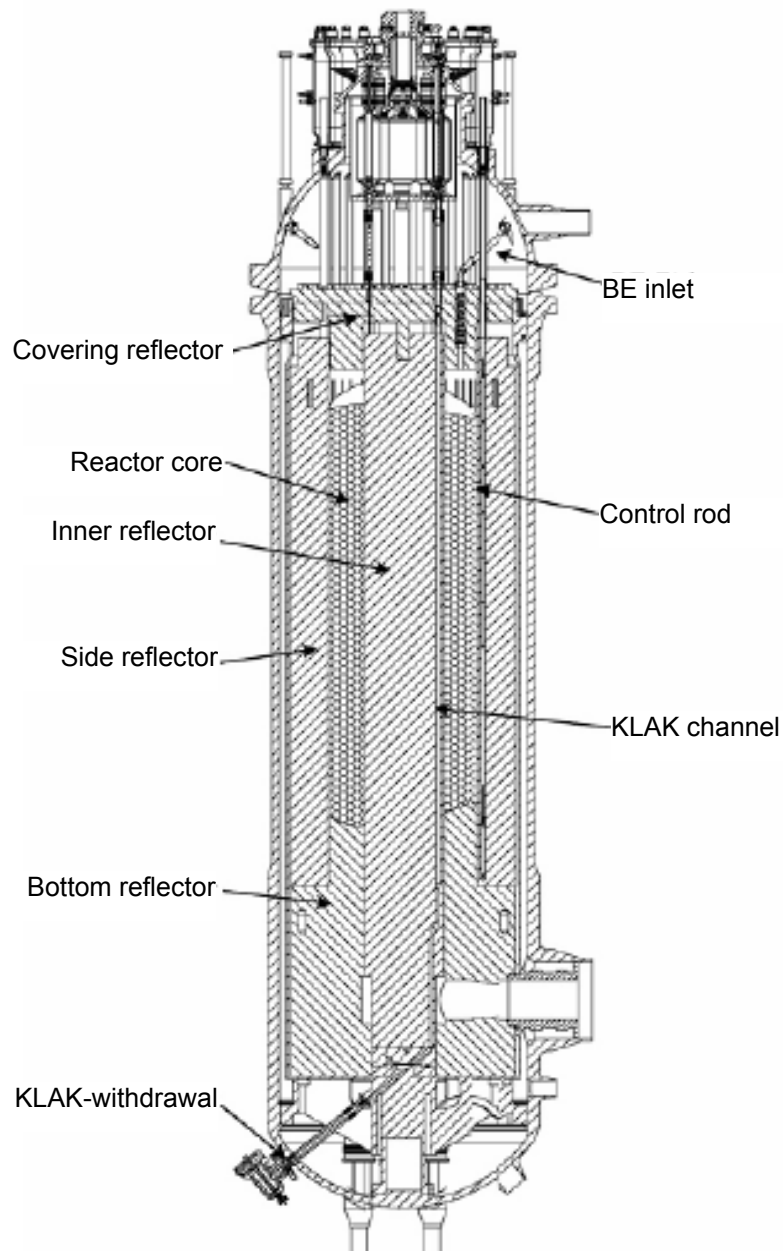


Figure 1: Principle representation of a pebble bed HTR (PBMR-400) with annular reactor core [Venter & Mitchell 2007]

A modular pebble bed reactor of the smaller type such as the HTR module reactor contains about 250,000 fuel elements for a thermal power of 200 MWth. More recent designs such as the PBMR-400 envision filling with about 450,000 fuel elements for a thermal power of 400 MWth. Since every fuel element contains about 10,000 coated particles, the radioactive

inventory of an HTR is enclosed behind several billion parallel barriers. Figure 1 shows the basic structure of a pebble bed reactor (PBMR-400) with annular reactors.

2.2 Development and structural types

Gas-cooled and graphite-moderated reactors have been built since the very beginning of reactor development. The first continuously operating reactor, the X-10 graphite reactor for plutonium production at the Oak Ridge National Laboratory (ORNL) was air-cooled and graphite moderated. The development of helium-cooled high temperature reactors began in the fifties of the twentieth century in the US, Great Britain and Germany. Later HTR were developed in Japan and Russia also and more recently in France, China and South Africa.

The first helium-cooled high temperature reactor was the Dragon reactor that was built from 1959 on as an OECD project in Great Britain. It was supposed to demonstrate the feasibility of HTRs and during its service life provided a lot of information on fuel and material behavior [Dragon Project Report 1000, 1978]. At roughly the same time, in the US and Germany, respectively, the Peach Bottom and AVR reactors were constructed. While the efforts in the US and Great Britain were concentrated on reactors with block-shaped fuel elements, in Germany HTR with spherical [beadlike] fuel elements were developed. The present projects under way in France (Antares), the US (GTMHR), Russia (VGM) and Japan (HTTR) are based on the block-shaped design, while the projects of China (HTR-PM) and South Africa (PBMR) use spherical fuel elements and are based largely on the German experience.

In the past the development was chiefly in the direction of HTR with high power output for economic reasons. Both the Fort St. Vrain reactor in the US and the THTR-300 in Germany were designed accordingly with a multiple of the power output of their predecessor plants. Both the Block HTRs and the pebble heap reactors contained the fuel in the form of particles with a double pyrolytic carbon coating (PyC), the so-called BISO coated particles. With the introduction of the TRISO coated particles with an additional silicon carbide coating (SiC), it became possible, because of their outstanding fission product retention capacity, to conceive excellent safety properties for small units with relatively low operating temperature and inherent temperature limitation in the event of an accident. Most of these modular HTR designs envision bringing several reactors together as modules to form a plant so that the conventional part and

a part of the safety and control systems can be used jointly. HTR module and HTR-100, neither of which was actually built, are early examples of this philosophy [Brandes & Kohl 1988].

Current development that are usually associated with the concept of Very High Temperature Reactor (V-HTR) and the new fourth generation of nuclear reactors [Sterbentz 2007] envision higher gas exit temperatures of up to 1000°C in order to be able to make the process heat available at a high temperature level. Higher operating temperatures of the fuel of up to 1250°C would be associated with this, which can lead in the long term to increased release of fission products by diffusion or to particle failures due to increased internal pressure or jacket corrosion. Table 1 and Table 2 list the parameters of decisive importance for fuel element behavior for already operating and future reactor types.

Table 1: High temperature reactors already in operation

Reactor	AVR¹	THTR¹	Dragon¹	Peach Bottom^{1,8}	Fort St. Vrain^{1,5}	HTTR^{2,7}	HTR10³
Country	G	G	GB	US	US	Japan	China
Type	Bead	Bead	Cylind.	Cylind.	Block	Block	Bead
Structure	Cylind.	Cylind.	Cylind.	Cylind.	Cylind.	Cylind.	Cylind.
Initial startup	1967	1985	1964	1967	1976	1998	2000
Shutdown	1988	1989	1976	1974	1989	in operation	in operation
Power (MW _{th})	46	750	20	115,5	842	30	10
Power density (MW _{th} /m ³)	2,2	6	14	8,3	6,3	2,5	2
Helium pressure primary circuit (MPa)	1,1	4	2	2,4	4,92	4	3
Gas inlet temperature	270 °C	250 °C	350 °C	344 °C	400 °C	395 °C	250 °C
Gas exit	950 °C	750 °C	750 °C	770 °C	770 °C	950 °C	700 °C

temperature							
max. BE-operating temperature	>1260 °C ⁶	1150 °C	1580 °C	1330 °C	1260 °C	1463 °C	1000 °C ⁴
max. BE-accident temperature		2500 °C	kA	kA	kA	1555 °C	1600 °C
Fuel	div.	(U,Th)O ₂ (HEU),	(U,Th)C (HEU)	(U,Th)C	(U,Th)C	UO ₂ (LEU)	UO ₂ (LEU)
Particle type	BISO / TRISO	BISO	BISO	BISO	TRISO	TRISO	TRISO
Packing density (vol.%)	div.	11,4	kA	kA	kA	kA	5,9
Target burnout (% FIMA)	div.	10,6	31,9	6,6	10,6	2,1	8,5
Neutron fluence (E >0.1 MeV)	div.	< 6,3 · 10 ²⁵ m ⁻²	kA	kA	kA	kA	< 2,6 · 10 ²⁵ m ⁻²

1: [Kugeler & Schulten 1989], 2: [Shiozawa et al. 2004], 3: [Wu et. Al. 2002], 4: [Tang et al. 2002],

5: [Habush and Harris 1968], 6: [Nabielek 2008], 7: [Takada et al. 2004], 8: [Birely 1973]

Table 2: Selected HTR designs

Reactor	HTR - Module ^{1,8}	HTR - 100 ^{1,7}	Antares ²	GTM- HR ³	HTR- PM ⁴	GT- HTR 300 ⁵	PBMR ⁶
Country	G	G	F	US	China	Japan	SA
Type	Bead	Bead	Block	Block	Bead	Block	Bead
Reactor core	Cylind.	Cylind.	Annular	Annular	Cylind.	Cylind.	Annular
Power output (MW _{th})	200	250	600	600	500**	600	400
Power density (MW _{th} /m ³)	3	4,2	6,5	6,5	3,2	5,4	3
Helium pressure primary circuit (MPa)	6	7	7	7,07	7	7	9
Gas inlet temperature	250 °C	255 °C	400 °C	490 °C	250 °C	587°C °C	500 °C
Gas exit temperature	700 °C	740 °C	850 °C - 1000 °C	850 °C	750 °C	850 °C	900 °C
max. BE- operating temperature	~1100 °C	~1100 °C	1300 °C	1060 °C	889 °C	1398°C	1080 °C
max. BE- accident temperature	1620 °C*	1680 °C	1600 °C	1560 °C	1537 °C	<1600 °C	1517 °C
Fuel	UO ₂ (LEU)	UO ₂ (LEU)	UCO, UO ₂ (LEU)	UCO, UO ₂ , PuO ₂	UO ₂ (LEU)	UO ₂ (LEU)	UO ₂ (LEU)
Particle type	TRISO	TRISO	TRISO	TRISO	TRISO	TRISO	TRISO
Packing density (vol.%)	5,9	5,9	kA	13	5,9	29	5,9

Target burn-up (% FIMA)	9 (< 9,8)	10,6	18	69	8,5	12,8	9 (< 9,8)
Neutron fluence (E >0.1 MeV)	2,4 · 10 ²⁵ m ⁻²	kA	kA	4 · 10 ²⁵ m ⁻²	kA	kA	2,4 · 10 ²⁵ m ⁻²

1: [Kugeler und Schulten 1989], 2: [Gauthier et al. 2006], 3: [Haque et al. 2006], [Kiryushin et al. 1997] and [Lee et al. 2008], 4: [Zhang et al. 2009], 5: [Kunitomi et al. 2004], 6: [Ball 2006], 7: [Brandes and Kohl 1988], 8: [Reutler & Lohnert 1984], * considering about 100 °C uncertainty add-on, ** in two cores

A more extensive and detailed overview of the different structural forms and aspects of high temperature reactors and also of reactors already operating is given, e.g., in "Hochtemperaturreaktortechnik" [Kugeler and Schulten 1989].

2.3 Reactor physics and safety behavior

The neutron spectrum of an HTR is in the thermal range. The coolant helium is chemically and neutron-physically inert. The moderator graphite is a solid at operational and accident temperature and undergoes no phase change in the reactor. Therefore, neither a rise nor a lowering of the moderator or coolant temperature results in a gain in reactivity (no positive steam bubble effect). Since the fuel is present in the form of finely dispersed particles, it has a relatively high specific surface and therefore a strong neutron absorption by U-238 and Th-232 in the resonance range. Due to this, HTR have a strongly negative reactivity coefficient with rising fuel temperature (nuclear doppler effect). Properly engineered HTR therefore display a system-inherent safety against nuclear power excursions due to a sudden gain in reactivity, such as would occur, e.g., in the case of a thrown out control rod. Besides this, the chain reaction is interrupted even in the case of outage of the active heat removal system within a brief time span by the strong temperature feedback. In the case of a pebble bed reactor, in addition, due to the continuous charging, a great reserve of reactivity is unnecessary. HTR with block-shaped fuel elements are usually equipped with consumable neutron poisons to compensate for the required excessive reactivity.

Modern HTR have a relatively low power density (3 –6 MW/m³), a relatively low power output, a high heat capacity and a favorable surface to volume ratio. In deviation from the neutron-physical optimum, HTR are designed with a large height to diameter ratio of about 3 to 1 or

even with an annular reactor core (see Fig. 1). In the case of outage of the active heat removal system, with or without a fast reactor shutdown and with or without pressure relief of the primary circuit, the system is therefore heated up only very slowly by the post-decomposition heat. As a rule, the peak temperatures in the case of a pressure release accident with failure of the active secondary heat removal systems, which represents the accident with the highest temperatures, are reached after about 30 hours (Fig. 2). After this, the heat transfer to the environment exceeds the heat production due to purely passive mechanisms, such as heat conduction and radiation, and the system cools down. Only a small percentage of the reactor core reaches the maximal temperature of about 1520°C. Ordinarily, a 100°C uncertainly margin is included in the calculations so that one can generally speak of 1620°C. With a suitable structural designed, therefore it can be guaranteed that the peak temperatures reached in the case of failure of all active secondary heat removal systems will remain below the permissible limits for fuel elements and structural parts and will not destroy the reactor core [Reutler & Lohnert 1984], [Haque et al. 2006], [Ball 2006].

Figure 2 shows the anticipated temperature curve of the fuel at the hottest place in the reactor core during a pressure loss accident with failure of the active secondary heat removal system. The reactor discussed here is the HTR module reactor of Interatom, which was designed with a thermal power output of 200 MWth but was never constructed. For comparison, the temperature curve during a typical CoFA bakeout test is shown. To be certain, the heating curve does not completely cover the accident transients shown, but it already contains an uncertainty margin of 100°C (see above).

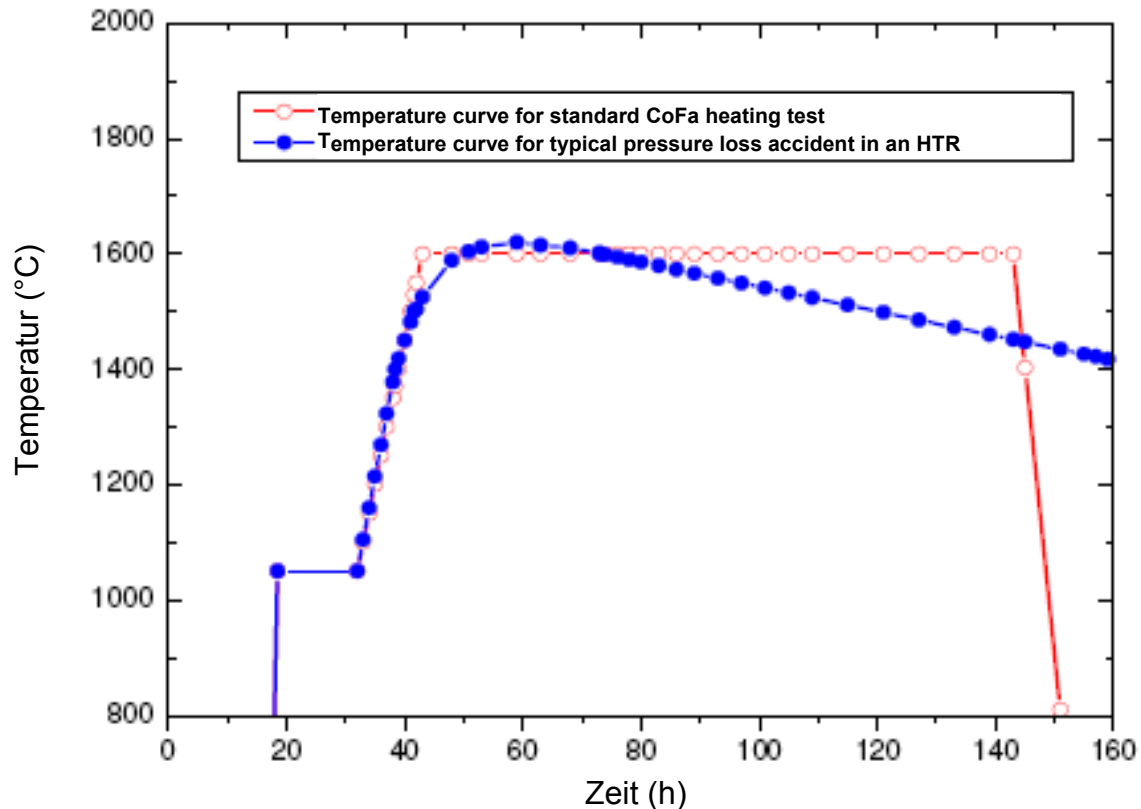


Figure 2. Anticipated temperature curve for a pressure loss accident in the HTR module reactor and a typical CoFA bakeout test.

2.4 State of the art for HTR fuel elements

HTR fuel elements consist of a graphite matrix with embedded multiply-coated fuel particles, the so-called coated particles (CP). The fuel elements serve to receive/hold the fuel as well as to release/transfer power to the coolant. They are also supposed to retain fission products in a reliable manner and to withstand the mechanical and thermal stresses in the reactor. In addition, they have to display good thermal conductivity so that the particle temperatures do not get too high in operation. In an accident, the fuel elements should also serve as heat storage units until the heat loss to the outside exceeds the source term by passive heat removal mechanisms.

HTR fuel elements may be spherical, prismatic (block shaped) or cylindrical. Cylindrical or rod-shaped fuel elements were used in the Dragon reactor and in the Peach Bottom reactor (see Table 1), but have not been accepted in further development. Prismatic fuel elements were first used in the Fort St. Vrain reactor and today represent the reference design for all reactor

concepts with static core. They consist of a hexagonal block with borings to receive cylindrical fuel rods. In the US design, the fuel rods are inserted directly into the borings as pressed cylindrical compacts. In the Japanese design, the fuel rods consist of a shell/jacket as well as pellet-like compacts. The compacts contain the coated particles in a high packing density (see Figure 3).

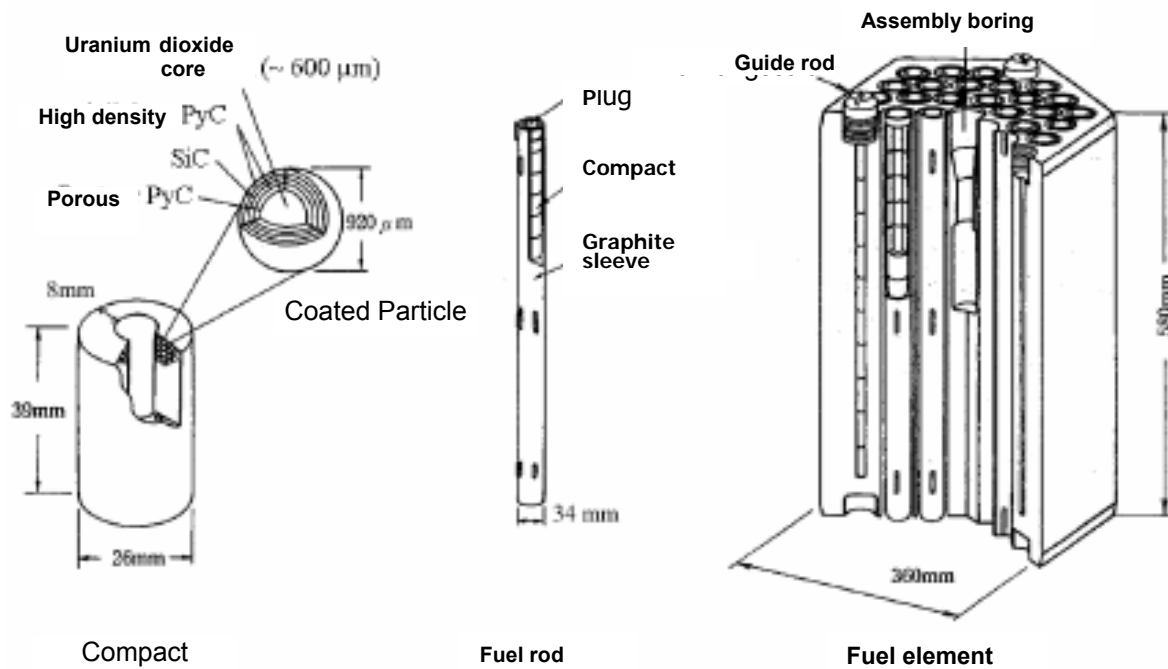


Figure 3: Prismatic HTR fuel element for the Japanese HTTR [Shiozawa et al. 2004]

Since the studies in this work were performed exclusively on spherical fuel elements of German production, the block-shaped fuel elements will not be discussed further here.

Spherical HTR fuel elements have an outer diameter of 60 mm and consist of an internal fuel material zone with a nominal diameter of 50 mm and an outer shell that is void of fuel. In the fuel zone, several thousand coated particles are uniformly distributed (see Fig. 4).

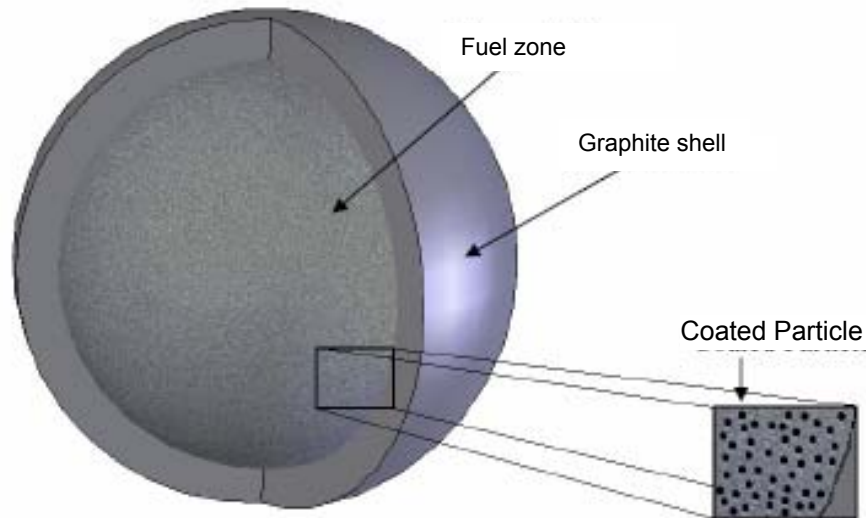


Figure 4: Spherical HTR fuel element

The actual average thickness of the nominally 5 mm thick shells is about 6.2 mm [Nabielek et al. 2005]. A fuel element weighs about 200 g. In Table 4, an overview is given of the fuel element types with TRISO particles after 1981.

The matrix of modern spherical fuel elements consists of so-called A3-3 and A3-27 graphite. Graphite of the A3-27 types was a refinement of the A3-3 that was used in the first charges of the LEU TRISO fuel program, but it contained health-hazardous materials and its production had to be stopped for occupational safety reasons [Nabielek et al. 2005]. The matrix functions essentially as structural material, heat conductor, heat storage and moderator. In addition, fission products released from the particles are partly absorbed in the matrix graphite.

The A3-3 fuel element is manufactured by hot blending of a powder of natural graphite with petroleum coke and binding resin. The coated particles are first given an approximately 2 μm thick coating with this powder (overcoating) and are then mixed with more powder and, at room temperature, pressed quasi-isostatically in a rubber mold at 30 MPa into the internal fuel zone [Heit et al. 1985]. The overcoating assures that all particles have a minimal distance from each other and cannot mechanically influence each other later. In addition, in this way, temperature peaks presumably caused by locally elevated packing densities are avoided. After the pressing operation, the shells now free of fuel are pressed at about 300 MPa, the binding resin carbonized at about 900°C, and impurities and gas residues are driven out in a final heat treatment at 1950°C.

A3-3 graphite has a density of about 1.75 g/cm³ and an adequate mechanical stability for withstanding the forces acting inside the reactor (see Table 3). The thermal conductivity in the unirradiated state is about 35 W/mK (at 1000°C) but drops off strongly during fast neutron irradiation (see Appendix III). The porosity of the matrix graphite is relatively high so that gaseous fission products released from the particles diffuse to the outside through the matrix practically without delay.

Table 3: Properties of A3-3 graphite [Hrovat et al. 1988], [Petti et al. 2002]

Density	1.,75 ± 0.,004 g / cm ³
Crush resistance	23.7 ± 0.3 kN – 26.3 ± 0.4 kN
Elasticity modulus	1.2 · 10 ⁴ MPa
Heat conductance at 20°C (1000°C)	~ 66 (35) W / m K
Standard corrosion rate	0.62 ± 0.08 mg / cm ² h
Standard abrasion rate	2.9 ± 0.7 mg / cm ² h

TRISO coated particles have an outer diameter of about 1 mm. They consist of a fuel core of UO₂ and several shell layers surrounding the core. First a buffer layer (buffer) of pyrolytic carbon of high porosity and low density surrounds the core. This is followed by an inner pyrolytic carbon layer (IPyC) with high density. This layer is followed by a silicon carbide layer (SiC) and finally an outer layer of pyrolytic carbon (OPyC) of high density surrounds the entire particle (see Fig. 5).

The UO₂ core of a coated particle has a diameter of about 500 µm, about 98%-99% theoretical density and good roundness. They are produced by an external precipitation process [Hrovat et al. 1988]. Then the unround, too large or too small cores are sorted out.

There are four shell/jacket layers surrounding the core that are supposed to securely enclose the fuel and radioactive fission products under all operating and accident conditions. They are produced in a continuous process in batches by chemical gas phase deposition (CVD) in a fluidized bed furnace. Due to the continuous transition between the process steps a strong connection/bond between the individual layers is assured [Petti et al. 2002], which is important later for mechanical integrity of the particle.

The buffer layer with its thickness of about 90 μm and a high porosity of about 50% serves to absorb CO and fission gases released during the burn-up. In addition it provides room for the fuel core for swell caused by burn-up without transmitting mechanical forces to the other layers/coatings. Furthermore, the fission fragments emerging from the fuel core with high kinetic energy are braked down in the buffer layer and therefore cannot damage the dense, inner pyrolytic carbon layer.

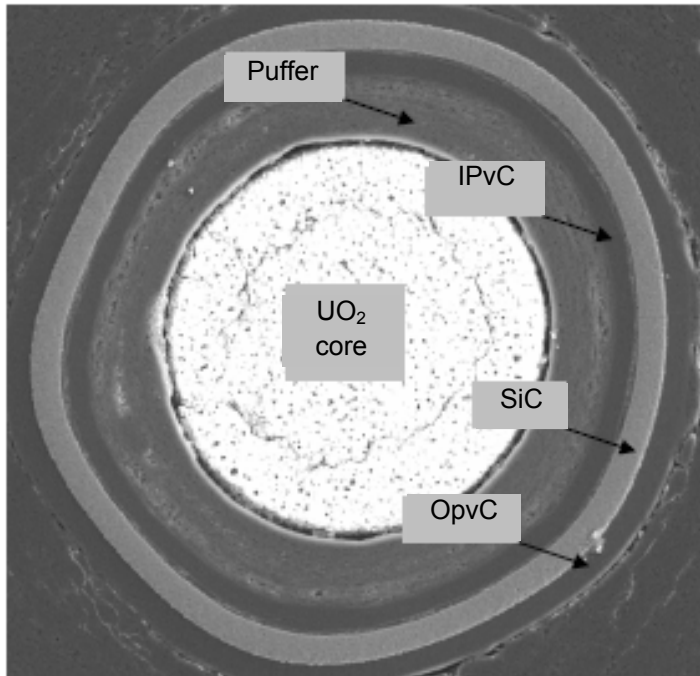


Figure 5: Polished section [micrograph] of a TRISO coated particle under the scanning electron microscope

The IPyC layer is essentially impermeable for gaseous fission products and represents a first diffusion barrier for the metallic fission products. In collaboration with the OPyC layer and the SiC layer, it acts as a pressurized boiler for the gas pressure building up in the particle during burn-up. In addition, the IPyC layer serves to reduce the chemical decomposition of the SiC layer by corrosive fission products [Lohnert et al. 1988]. During the production of the particles, the IPyC layer also shields the core against leaching out by the hydrochloric acid that is released from methyl trichlorosilane during the addition of the SiC [Petti et al. 2002].

Table 4: Fuel element types with LEU TRISO coated particles after 1981 [Nabielek et al. 2005]

Type	GLE-3	LEU-Phase 1	GLE-4.1	GLE-4.2	Proof
Matrix	A3-27	A3-27	A3-27	A3-3	A3-3
Heavy metal burden	10 g	10 g	6 g	6 g	9.4 g
U-235 Enrichment	9,82 %	9,82 %	16,67 %	16,67 %	10,6 %
Free uranium content	$50.7 \cdot 10^{-6}$	$35 \cdot 10^{-6}$	$43.2 \cdot 10^{-6}$	$7.8 \cdot 10^{-6}$	$13.5 \cdot 10^{-6}$
CPs for BE	16.400	16.400	9.560	9.560	14.600
Packing density	9.9 vol. %	10.2 vol. %	5.7 vol. %	5.9 vol. %	9.6 vol. %
Particle variety	HT 232-245	EUO 2308	HT 354-383	HT 384-393 HT 395-404 HT 406-423	EUO 2358-2365
Core diameter	500 μm	497 μm	501 μm	502.2 μm	508 μm
Core density	10.8 g/cm ³	10.81 g/cm ³	10.85 g/cm ³	10.86 g/cm ³	10.72 g/cm ³
Buffer thickness	93 μm	94 μm	92 μm	92,3 μm	102 μm
Buffer density	1.01 g/cm ³	1 g/cm ³	1.013 g/cm ³	1.012 g/cm ³	1.02 g/cm ³
IPyC thickness	38 μm	41 μm	38 μm	40.6 μm	39 μm
IPyC density	1.86 g/cm ³	~ 1.9 g/cm ³	~ 1.9 g/cm ³	1.87 g/cm ³	1.92 g/cm ³
IPyC BAF	kA	1,053	1,029	1,02	1,042
SiC thickness	35 μm	36 μm	33 μm	35.9 μm	36 μm

SiC density	3.19 g/cm ³	3.2 g/cm ³	3.2 g/cm ³	3.2 g/cm ³	3.2 g/cm ³
OPyC thickness	40 μm	40 μm	41 μm	39.6 μm	38 μm
OPyC density	1.89 g/cm ³	1.88 g/cm ³	1.88 g/cm ³	1.87 g/cm ³	1.92 g/cm ³
OPyC BAF	kA	1.019	1.02	1.02	1.023

The SiC layer represents the actual fission product barrier and mechanically stable layer. It is composed of beta SiC and is about 35 μm thick. The density of the SiC layer almost reaches the theoretical value of 3.21 g/cm³ at a very high hardness (~2600 HV) and a high strength (reference value: $\sigma_m \sim 834$ MPa). In addition, the effective diffusion coefficients for metallic fission products in SiC are extremely low. Depending on the production process and radiation load, the mechanical strength as well as the diffusion coefficients for different fission products may, however, differ considerably from particle type to particle type. Low diffusion coefficients can be achieved by the finest-grained possible isotropic microstructure. A high density and the fewest defective sites possible are necessary for mechanical stability.

The OPyC layer is the layer sealing from the outside. It protects the SiC layer against outer corrosion and mechanical effects from the outside and is part of the pressure vessel assembly.

During production, cores, particles and fuel elements are constantly subjected to random quality inspections. At this time, both the geometric (roundness, diameter, coating thickness, defects etc.) as well as the mechanical and thermal properties are checked.

During operation, the jacket/shell coatings of intact particles retain fission products to the greatest possible degree. Therefore, the decisive parameters for the operational fission product release of modern HTR fuel elements are the free uranium contamination of the graphite matrix and the number of particles that are defective due to production factors. It is possible with today's production methods to achieve an initial defective particle content of less than one particle per fuel element and an effective free uranium contamination in the range of 10⁻⁵. The free-uranium contamination is usually determined by random sampling with the burn-leach test. For this purpose the graphite matrix of some fuel elements of a production series is burnt in the laboratory and the remaining ashes as well as the particles leached out. The free uranium

content in the graphite and the uranium from defective particles pass into the acid at this time and can be quantified by chemical means.

During an accident, fission products are released intensively by diffusion from intact particles. In this case, the decisive parameters are the retention capacity of the SiC coating and the absorption capacity of the graphite matrix. At high temperatures, finally entire particles may fail and release their inventory into the graphite matrix. From there the fission products are released with a delay into the primary cycle.

The safety concept of an HTR is based on the quality of the fuel used. Only if it is assured that the radioactive inventory in the particles is securely enclosed/contained in operation and in the case of an accident the entire system can be approved without costly, multiple active secondary heat removal systems and without a safety container. As opposed to fuel rods for light water reactors, it is impossible to check each individual particle for production defects. While every LWR fuel rod is tested by nondestructive methods for defects before delivery, one can only resort to random investigations for a production batch of coated particles. In addition, to date it has not been sufficiently explained which parameters are decisive for a high fission product retention capacity. Only a strict observance of the production parameters for a fuel once it is qualified can therefore guarantee that all fuel elements have the required quality. For this reason, not only the process itself but also the installations used for production of fuel elements, especially the fluidized bed furnaces for particle coating, are approved for the insertion of the fuel elements.

Within the scope of the qualification process, some of the fuel elements produced are irradiated under operating conditions and then subjected to accident tests that cover the assumed scenarios. The cold finger apparatus used in this work is an important tool for conducting these tests.

2.5 Relevant fission products

During the burn-up, in the fuel as a result of fission, radioactive fission products are formed and transuranium elements as well as radioactive activation products by broader processes. This radioactive inventory represents the real source of danger of a nuclear reactor. As opposed to the heavy transuranium elements, the fission products are, in part, highly volatile and are therefore already under operating conditions released from the fuel elements to a small extent.

Activation products are present only in small quantities since, besides graphite, no structural materials are used in the reactor core. Due to impurities on naturally occurring uranium and thorium in the graphite and impurities of the outer pyrolytic carbon layer by the production process, there is an effective free uranium contamination in the fuel element that leads to the buildup of fission products in the graphite matrix during irradiation. Therefore small quantities of fission gases are already liberated during operation. At elevated temperatures, the releases can increase strongly due to diffusion or in the case of particle failure.

One of the radiologically most important fission products is Cs-137. Because of its high fission yield (about 6.5%) and its long half-life of 30.07 years, it is, besides Sr-90, the isotope chiefly responsible for the long-term radioactivity load in the case of release. Cs-137 is a beta emitter and decomposes with high probability into the short-lived daughter isotope Ba-137m, with which it is in secular equilibrium. Ba-137m itself emits a gamma quantum when transitioning to the ground state with an energy of 661.66 keV. Generally speaking, therefore, the Cs-137 activity of a sample can be determined quite simply by gamma spectrometry.

Cs-134 is also a beta emitter and decays with a half-life of 2.0648 year. At the same time gamma rays of variable energy are emitted with high probability. As opposed to Cs-137, Cs-134 is not a direct fission product but is formed in the reactor by an (n,g) capture reaction from Cs-133, which in turn is formed by the beta decay of Xe-133. The Cs-134 inventory of a steady state HTR has roughly the same order of magnitude as the Cs-137 inventory and is important for the intermediate-term pollution of the environment after its release.

Cesium under operating conditions is almost completely retained in the TRISO particles and fuel elements. However, studies have shown that cesium is released for the most part from the core and accumulates in the buffer coating [de Groot 2008]. Part of it also diffuses into the internal pyrolytic carbon coating layer but no longer through the SiC layer since high-density SiC represents an effective diffusion barrier for cesium [Verfondern et al. 1997]. Graphite has a good adsorption capacity for cesium so that the minimal releases from the particles are retained for the most part in the fuel element matrix. At accident temperatures, the diffusion processes are indeed clearly accelerated, but cesium is still substantially retained by the SiC layer at 1600°C. Even higher temperatures then lead to distinct releases, in which case the retention capacity of the graphite matrix retards the process [Schenk et al. 1988].

With a half-life of 28.79 years, Sr-90 in addition to Cs-137 is the isotope that is chiefly responsible for the long term contamination of the environment if it is released from the reactor. The long biological half-life of 18 years is problematic. During the irradiation, strontium is largely retained in the UO₂ core. Since Sr-90 is a pure beta emitter, it cannot be detected by gamma spectrometry. Alternative methods are perhaps beta or mass spectrometry. During operation, strontium, because of its good solubility in UO₂ is retained for the most part in the core. At accident temperatures, strontium is partly released from the core and diffuses through the shell/jacket coatings. The graphite matrix has a high storage capacity for strontium. Therefore, the amount released is generally about one power of ten smaller than the cesium release. At 1600 °C practically no strontium is released from intact particles [Schenk & Nabielek 1989].

Ag-110m represents a relatively small inventory in the reactor and therefore has only subordinate importance for the accident analysis. Due to its high volatility, however, it is already released at operating temperatures and therefore represents one of the main sources of contamination for the primary cycle components. In particular, in the case of the direct cycle with helium turbines, Ag-110m can lead to a high radiation field in the pipelines and turbines and therefore to problems during repair and maintenance work. The reasons for the increased release of silver from intact particles have not been fully explained at present. However, it has been suggested that the microstructure and the smallest cracks in the SiC may play a part [MacLean 2004]. Ag-110m has a short half-life of 249.79 days so that it can no longer be detected in older fuel elements. However, on freshly irradiated fuel elements it is readily measured by gamma spectrometry.

I-131 is the most important fission product for the short-term radiological burden after a release due to an accident. Because of its high fission yield and its high specific activity, it represents a large inventory. It is easily released from defective particles because of its high volatility. Generally it can no longer be detected in the laboratory since it decays within a short time. However, studies have shown that gaseous fission products such as xenon and krypton display a release behavior similar to that of iodine and can therefore be used as a reference [Verfondern et al. 1997].

Xe-135 and Kr-85 are fission gases that have no radiological significance in the case of an accident. Since they, as noble gases, are chemically inert, they do not diffuse through intact, dense jacket coatings. However, they are rapidly released from failed particles. Therefore, Xe-

135 and Kr-85 can serve as indicators of particle failure. Xe-135 has a brief half-life and is usually no longer present in quantities sufficient to be detected in the fuel elements. On the other hand, Kr-85 is sufficiently present and can therefore be detected by gas spectrometry. A low emission probability of the gamma quantum most frequently emitted during decay with an energy of 514 keV of 0.434%, however, leads to very high detection limits.

In this report we shall distinguish between gaseous fission products and solid fission products. The term “gaseous” in this case refers to the isotopes of the noble gases krypton and xenon. The term “solid” refers to fission products existing as solids at room temperature. In this report, these are mainly the isotopes of cesium, strontium, iodine, silver and ruthenium.

Table 5: Properties of relevant fission products

Fission product	Half-life	Fission yield (U-235, thermal)	Aggregate state (20 °C)	Meaning
Cs-137	30.07 a	0,0627	solid	Long term environmental contamination
Cs-134	2.0648 a	Shielded nuclide	solid	Long term environmental contamination
Sr-90	28.79 a	0,059	solid	Long term environmental contamination
I-131	8.02 d	0,0288	solid	Short-term environmental contamination, very volatile
Ag-110m	249.79 d	Shielded nuclide	solid	Contamination of primary cycle in reactor operation, very volatile
Ru-106	373.59 d	0,004	solid	Little importance for accident analysis
Kr-85	10.77 a	0,0027	gaseous	Indicator of particle failure
Xe-133	5.24 d	0,067	gaseous	Indicator of particle failure

3. Earlier works

As part of the development of HTR fuel elements, in the past numerous irradiation experiments and post-irradiation investigations were performed. In addition, the accident behavior due to bakeout was studied in different sets of equipment. At that time tests on individual coated particles and also on complete fuel elements and especially prepared compacts were conducted. The studies of individual particles had the advantage that they could be implemented relatively simply with small testing devices. In addition, very detailed information could be obtained regarding the time curve of the fission product release and on the mechanisms of damage and transporting. However, it was not possible in this way to generate an adequate database for damage statistics of coated particles that would be needed for reliable modeling. In addition, the effect of the graphite matrix was not allowed for. For this reason, various devices were developed in which experiments could be performed on entire fuel elements with several thousand coated particles.

In „Apparatur zur Messung der Freisetzung von Spaltgasen und anderer Spaltprodukte durch Ausheizen“ [Stradal 1970], an apparatus is described that was already developed in the mid-sixties at the FZJ. In this apparatus, spherical HTR fuel elements could be selectively baked out and the fission gas release measured. The experiments that were performed with this apparatus were limited in time and required the constant presence of an operator. Accordingly, only relatively fast temperature rises and short bakeout times could be realized. However, the main interest was not to simulate hypothetical accidents with transients of several hundred hours but rather the measurement of the equilibrium release in the reactor under laboratory conditions. In addition, fundamental mechanisms were still unknown and had to be investigated first. By determining the inventory of fuel elements before and after the bakeout and by measuring out the parts of the furnace, besides the fission gas release, the integral release of solid fission products could also be measured. This process was employed since the fuel elements available at that time from the first production series with particles of the BISO type already significantly release fission products at relatively low temperatures. Therefore, the inventory differences before and after an experiment were large enough to be detected by gamma spectrometry.

With progressing development of helium-cooled high temperature reactors, there was increased interest in the long term behavior of the fuel elements in the event of an accident with failure of the active secondary heat removal. In „*Untersuchungen zum Verhalten von beschichteten*

Brennstoffteilchen und Kugelbrennelementen bei Störfalltemperaturen“ [Studies of the behavior of coated fuel particles and spherical fuel elements at accident temperatures] [Schenk 1978] an apparatus is described that was installed as part of the Thorium High Temperature Reactor (THTR) Project in the hot cells of the FZJ. With this apparatus which was called the A test (bakeout test) (see below), accidents of several hundred hours could be simulated without supervision. Due to the relatively high thermal power of the THTR of 750 MWth and in general in the case of HTR of large and intermediate size, in the event of outage of the active secondary heat removal temperatures significantly higher than 1600°C are to be expected. For interventions from the outside, however, a relatively long cooling period was available during which the core remained capable of being cooled. For a pressure loss accident with outage of the active secondary heat removal in medium-sized HTR it was expected that the maximal core temperature of 2500°C would not be exceeded. Accordingly, the apparatus was designed with two graphite furnaces installed in parallel with maximal temperature of 2500°C. Like the predecessor apparatus, the A test also had a fission gas measuring device. The fuel elements studied at that time of the THTR type with mixed oxide BISO particles retained fission products relatively poorly compared with the later fuel elements with TRISO particles. Therefore, here also by inventory measurement of the fuel elements before and after the trials, the integral release of solid fission products could also be determined. However, no transient release curves could be plotted. The apparatus was also used later for tests on TRISO fuel elements at high temperatures from 1900 to 2500°C [Schenk & Nabielek 1989].

With the introduction of the TRISO coated particles with an extra SiC coating representing a highly efficient diffusion barrier, we now had a fuel element that in operation only released very tiny quantities of fission products stemming chiefly from the uranium contamination of the matrix. In *“Spaltproduktverhalten – Speziell Cs-137 in HTRTRISO-Brennstoffteilchen”* [Fission product behavior – especially Cs-137 in HTR TRISO fuel particles] [Allelein 1980] a test apparatus is described with which individual particles could be baked out. The apparatus had an opening at the top and a water-cooled surface installed above it on which solid fission products could condense. By using this experimental apparatus, for the first time, temperature-dependent diffusion coefficients for cesium in the SiC coating of TRISO particles were determined.

At the beginning of the 1980s the construction of the CoFA-I in the hot cells of the FZJ was begun since the measurement of individual coated particles was not sufficient for making statistically weighted statements due to the high point spread of the results and because of the

small number of particles studied. The apparatus was supposed to be used for bakeout experiments on whole fuel elements and for the measurement of small releases and release curves of gaseous and, for the first time, also time-dependent releases of solid metallic fission products. Besides the study of the basic release mechanisms, the CoFA-I was intended to provide evidence that fuel elements with TRISO particles of high quality would withstand the accident conditions of an inherently safe reactor with heat removal devices based on purely passive mechanisms and the releases would lie far below the acceptable values.

In [Schenk et al. 1984], [Schenk et al. 1988], [Schenk & Nabielek 1989] and [Schenk et al. 1997] one can find voluminous results from CoFA bakeout tests and other post-irradiation studies on HTR fuel elements with TRISO coated particles that were conducted in the years 1984 to 1994 (see Figs. 6 & 7). Table 7 lists the parameters and results of 20 heating tests on HTR fuel elements with UO_2 fuel of low enrichment and modern TRISO coated particles up to 1800°C. The table was taken from [Nabielek 2009] (see also [Verfondern et al. 1997]). One can see that no particle failure occurred in any case during the first 100 hours of bakeout at a constant 1600°C. In some cases, in the experiment, the curve of the maximal temperature computed for the HTR module during a core heat up accident was accurately simulated up to 1620°C. At that time about three particles in five tested fuel elements with a total of 82,000 particles failed in one test. During the bakeout tests at 1700°C and 1800°C the numbers of defective particles clearly increased and with them the releases of fission products. Four of the fuel elements tested during this time came from controlled irradiation experiments in the material testing reactors of FRJ2 in Jülich and HFR in Petten (see Table 6). In particular, the fuel elements HFR K3/1 and HFR K3/3 displayed high burn-ups and high fast neutron fluence that extended close to the range of the work presented here.

Table 6: Irradiation data of four HTR fuel elements with high burn-ups studied at the FZJ [Schenk & Nabelek 1989]

Fuel element	Target burn-up (% FIMA)	Fast neutron fluence (>0.1 MeV)	Full load days	Average irradiation temperature
FRJ2-K13/2	8,1	$0.1 \cdot 10^{25} \text{m}^{-2}$	396	1000 °C - 1200 °C
FRJ2-K13/4	7,8	$0.1 \cdot 10^{25} \text{m}^{-2}$	396	1000 °C - 1200 °C
HFR K3/1	7,7	$3.9 \cdot 10^{25} \text{m}^{-2}$	359	1000 °C - 1200 °C
HFR K3/3	10,2	$6 \cdot 10^{25} \text{m}^{-2}$	359	800 °C - 1000 °C

Table 7: Earlier CoFA experiments with LEU TRISO fuel elements [Nabelek et al. 2009]

Fuel element	Burn-up %FIMA	Fast neutron fluence (10^{25}m^{-2})	Bakeout test	Number of defective particles **		Amounts released				
				Temperature (time)	Production	Heating test	Kr-85	Sr-90	Ag-110m	Cs-134
AVR 71/22	3,5	0,9	1600 °C (500 h)	0	0	$4,0 \cdot 10^{-7}$	$5,3 \cdot 10^{-6}$	$9,0 \cdot 10^{-4}$	$6,9 \cdot 10^{-5}$	$2,0 \cdot 10^{-5}$
HFR-K3/1	7,7	3,9	1600 °C (500 h)	0	0	$1,8 \cdot 10^{-6}$	$1,8 \cdot 10^{-7}$	$2,7 \cdot 10^{-2}$	$1,3 \cdot 10^{-4}$	$1,1 \cdot 10^{-4}$
FRJ2-K13/2	8,0	0,1	1600 °C (138 h)	0	0	$6,4 \cdot 10^{-7}$	$3,3 \cdot 10^{-7}$	$2,8 \cdot 10^{-3}$	$1,0 \cdot 10^{-4}$	$3,9 \cdot 10^{-5}$
AVR 82/20	8,6	2,4	1600 °C (100 h)	0	0	$1,5 \cdot 10^{-7}$	$3,8 \cdot 10^{-6}$	$4,4 \cdot 10^{-3}$	$1,2 \cdot 10^{-4}$	$6,2 \cdot 10^{-5}$
AVR 82/9	8,9	2,5	1600 °C (500 h)	0	0	$5,3 \cdot 10^{-7}$	$8,3 \cdot 10^{-5}$	$1,9 \cdot 10^{-2}$	$5,9 \cdot 10^{-4}$	$7,6 \cdot 10^{-4}$
AVR 89/13	9,1	2,6	1620 °C (~10 h)	0	0	$2,0 \cdot 10^{-7}$	***	$8,3 \cdot 10^{-4}$	$1,3 \cdot 10^{-5}$	$1,1 \cdot 10^{-5}$
			1620 °C (~10 h)	0	0	$1,3 \cdot 10^{-9}$	***	$1,5 \cdot 10^{-2}$	$1,6 \cdot 10^{-6}$	$1,4 \cdot 10^{-6}$
AVR 85/18	9,2	2,6	1620 °C (~10 h)	0	0	$1,4 \cdot 10^{-7}$	***	$6,5 \cdot 10^{-3}$	$1,0 \cdot 10^{-5}$	$1,3 \cdot 10^{-5}$
AVR 90/5	9,2	2,7	1620 °C (~10 h)	0	0	$1,9 \cdot 10^{-7}$	***	$1,1 \cdot 10^{-3}$	$7,7 \cdot 10^{-6}$	$9,0 \cdot 10^{-6}$

			1620 °C (~10 h)		0	6,6• 10 ⁻⁹	***	9,0• 10 ⁻⁴	3,5• 10 ⁻⁶	3,3• 10 ⁻⁶
AVR 90/2	9,3	2,7	1620 °C * (~10)	1	2	1,0• 10 ⁻⁴	***	3,7• 10 ⁻²	5,0• 10 ⁻⁵	4,6• 10 ⁻⁵
AVR 90/20	9,8	2,9	1620 °C * (~10)	2	3	2,4• 10 ⁻⁴	***	7,6• 10 ⁻²	5,6• 10 ⁻⁶	6,5• 10 ⁻⁶
AVR 91/31	9,0	2,6	1700 °C * (~10)	2	18	1,2• 10 ⁻³	***	6,2• 10 ⁻¹	3,7• 10 ⁻³	2,4• 10 ⁻³
AVR 74/11	6,2	1,6	1700 °C (185 h)	1	0	3,0• 10 ⁻⁵	7,2• 10 ⁻⁶	4,8• 10 ⁻²	8,4• 10 ⁻⁵	7,6• 10 ⁻⁵
FRJ2-K13/4	7,6	0,1	1600 °C (138 h)	0	0	3,0• 10 ⁻⁷	2,0• 10 ⁻⁸	4,5• 10 ⁻⁴	5,7• 10 ⁻⁶	2,5• 10 ⁻⁶
			1800 °C (100 h)		2	7,2• 10 ⁻⁵	1,4• 10 ⁻³	5,3• 10 ⁻¹	9,7• 10 ⁻³	9,9• 10 ⁻³
AVR 88/33	8,5	2,3	1600 °C (50 h)	0	0	1,0• 10 ⁻⁷	8,4• 10 ⁻⁶	1,2• 10 ⁻³	1,1• 10 ⁻⁴	1,2• 10 ⁻⁴
			1800 °C (20 h)		~4	1,8• 10 ⁻⁴	2,3• 10 ⁻⁴	2,1• 10 ⁻¹	4,4• 10 ⁻⁴	4,6• 10 ⁻⁴
AVR 88/15	8,7	2,4	1600 °C (50 h)		0	6,3• 10 ⁻⁸	***	9,1• 10 ⁻³	8,8• 10 ⁻⁶	1,2• 10 ⁻⁵
			1800 °C (50 h)	1	~6	2,9• 10 ⁻⁴	1,1• 10 ⁻²	8,1• 10 ⁻¹	1,3• 10 ⁻²	1,4• 10 ⁻²
AVR 70/33	1,6	0,4	1800 °C (175 h)	0	28	1,7• 10 ⁻³	***	***	***	2,2• 10 ⁻²
AVR 74/10	5,5	1,4	1800 °C (90 h)	0	30	8,1• 10 ⁻⁴	***	***	8,5• 10 ⁻²	7,9• 10 ⁻²
AVR 76/18	7,1	1,9	1800 °C (200 h)	0	~3	1,2• 10 ⁻⁴	6,6• 10 ⁻²	6,2• 10 ⁻¹	5,3• 10 ⁻²	4,5• 10 ⁻²
AVR 88/41	7,6	2,0	1800 °C (24 h)	0	0	2,4• 10 ⁻⁷	1,2• 10 ⁻⁴	7,7• 10 ⁻²	1,4• 10 ⁻⁴	1,5• 10 ⁻⁴
HFR-K3/3	10,2	6,0	1800 °C (100 h)	0	~12	6,5• 10 ⁻⁴	1,5• 10 ⁻³	6,7• 10 ⁻¹	6,4• 10 ⁻²	5,9• 10 ⁻²

* calculated heating curve for pressure loss accident
 ** of 16,400 particles in each case
 *** not measured

Besides the dependence on the heating temperature, a tendential dependence of the amounts released on the burn-up, the fast neutron fluence and the irradiation temperature was noted. Due to the still too small database, however, no unambiguous correlations could be formed. In [Schenk u. Nabelek 1989] it is recommended that the maximal burn-up height be limited to 11% FIMA and the maximally acceptable accident temperature to 1600 °C and that further studies be performed on highly burnt up fuel elements at high accident temperatures.

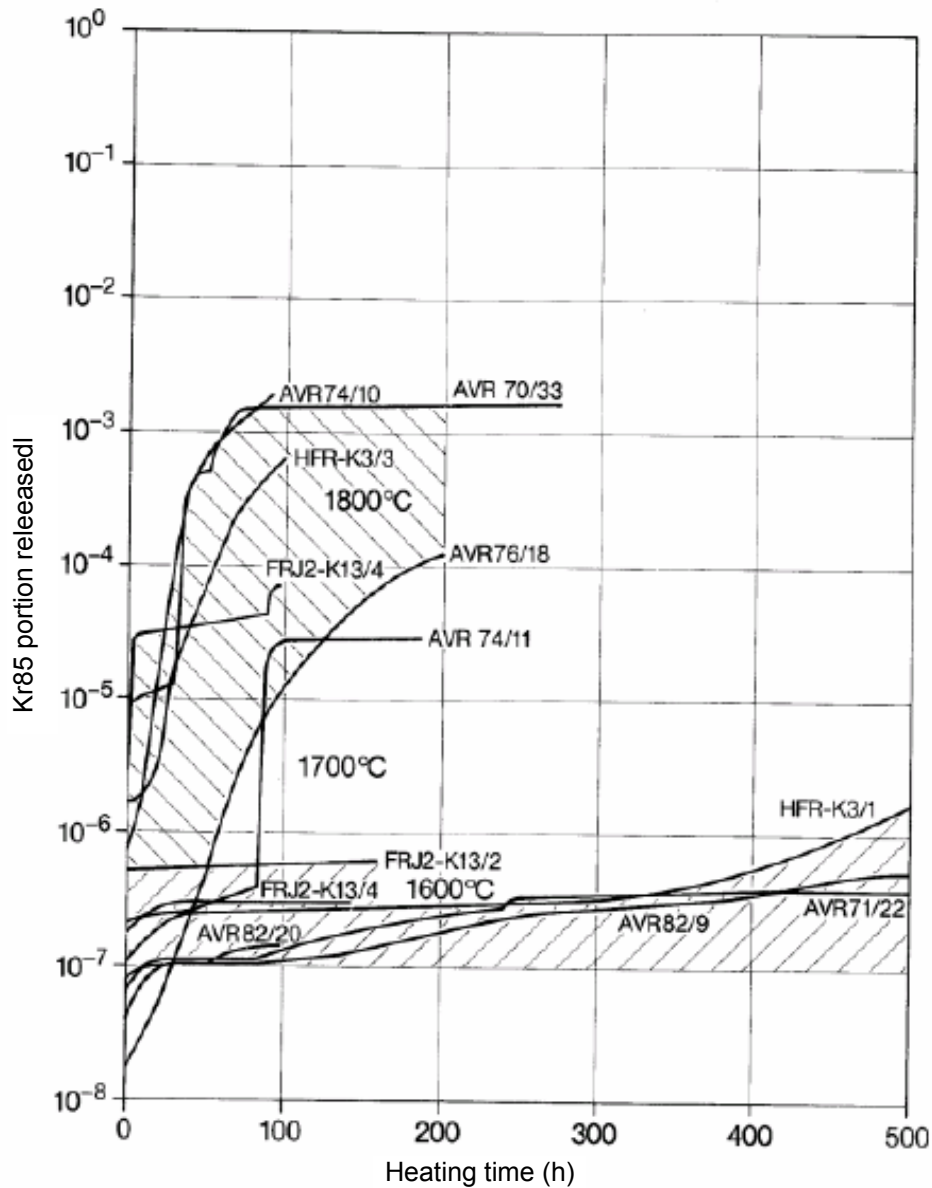


Figure 6: Kr-85 releases during bakeout test in the FZJ on LEU TRISO fuel elements up to 2100°C (CoFA and A test) [Schenk et al. 1988]

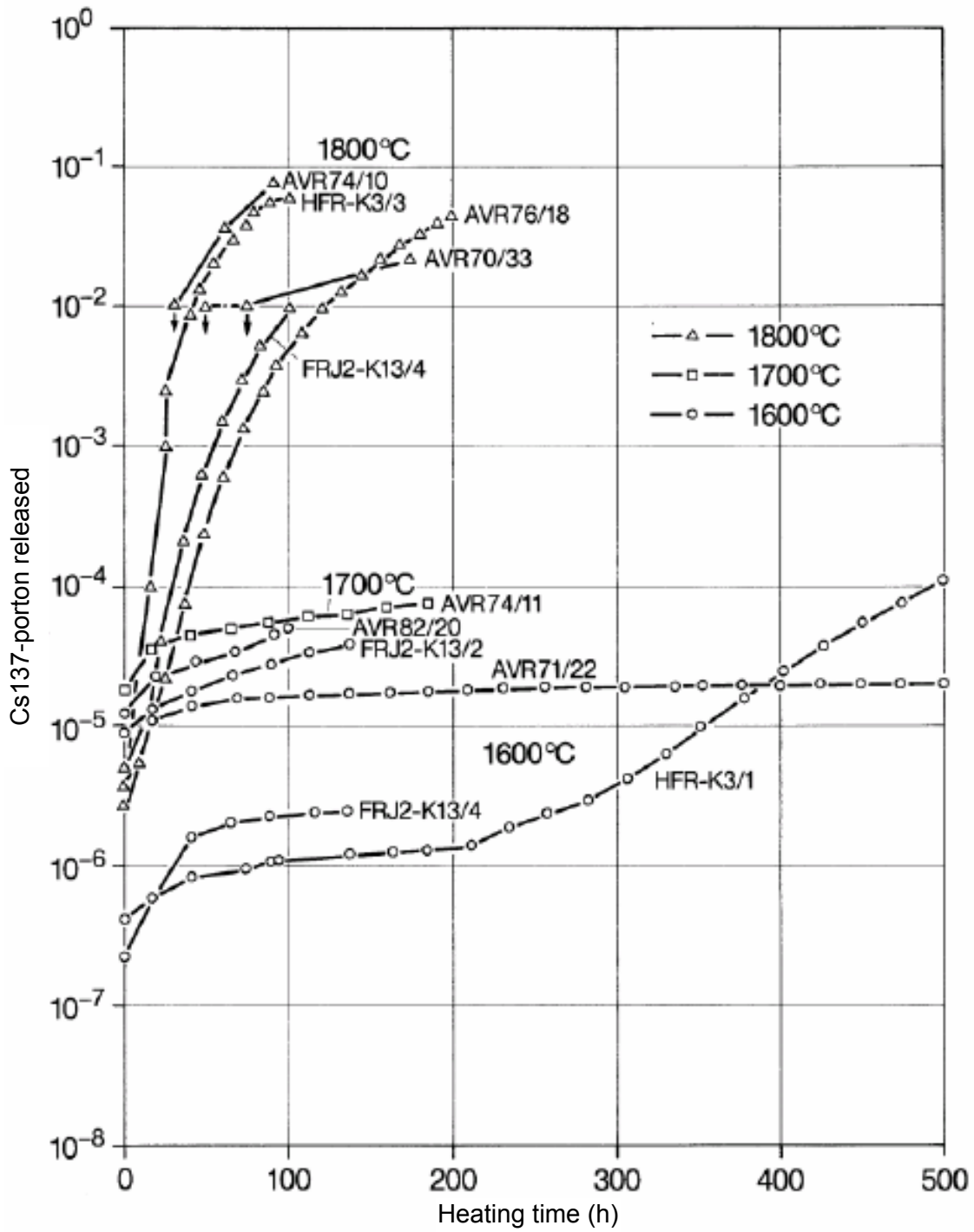


Figure 7: Cs-137 releases during FZJ bakeout tests on LEU TRISO fuel elements up to 2000°C (CoFA and A test) [Schenk et al. 1988]

4. Statement of the problem for the present study

As part of this research project, the behavior of modern HTR fuel element under extreme accident conditions was to be investigated and the existing database expanded as a result. For this purpose, experimental accident simulations were systematically conducted, evaluated and analyzed on burnt-off, spherical fuel elements for high temperature reactors with modern TRISO coated particles. The accident simulations were to be accomplished by selective heating of the fuel element in a helium atmosphere and at standard pressure. As a result the conditions were to be created that would be expected in the event of a pressure loss accident in the primary cooling cycle with outage of the active secondary heat removal system. The fuel elements to be studied were obtained from irradiation experiments in material testing reactors. Compared with earlier studies, these displayed a higher burn-up and were irradiated at a clearly more elevated temperature. In addition, an accelerated burn-up and enhanced fast neutron fluence led to clearly higher fuel burdens [alternative translation: stresses on the fuel].

Another goal of this study was to be the resumption of earlier activities in the FZJ and the assurance and recovery respectively of the previous competence in the field of post-irradiation studies on HTR fuel elements with improved methods. Besides conducting the experiment described within the scope of this project on old fuel of German origin, the activities with them served for preparation for future bakeout experiments on newly produced fuel from present and future irradiation experiments.

It is generally assumed that modern TRISO particles remain intact up to about 1600°C and securely contain the fission products. This could be proven in the past by extensive research programs [Schenk et al. 1988]. In this paper, we shall investigate whether the results obtained at that time can be confirmed. Following the accident simulation at 1600°C, in addition experiments were to be conducted at higher temperatures, i.e. up to 1800°C. This was intended to demonstrate, on the one hand, that the fuel elements heavily stressed/loaded during the irradiation can go beyond the previously accepted limit value undamaged and, on the other hand, the database was to be expanded to cover higher accident temperatures. During the tests, the release of the gaseous and solid fission products was to be measured and put in relation to the total inventory.

Besides the accident simulations, other characterization methods were to be applied. Thus the fuel elements were to be measured by gamma spectrometry before and after the heating tests and the burn-up determined. In addition, other post-radiation studies such as ceramography, electron microscopy and microprobe measurements were to be performed in order to obtain information on particle failure mechanisms and fission product distributions in fuel elements and particles.

The bakeout experiments were also to be recalculated and the calculations compared with the experimental results. Calculations and results were then to be compared with the results of experimental accident studies in the past and the results incorporated qualitatively into the literature. The facts obtained were finally intended to aid in expanding the database for the fission product retention capacity and the mechanical integrity of modern HTR fuel in the direction of higher irradiation and accident temperatures and also in the direction of higher burn-ups and higher fast neutron fluences and in the better understanding of the active mechanisms.

For the experimental work fuel elements were available from the proof trials for the HTR module reactor (HFR K5 and K6k)K from the early nineties as well as different AVR fuel elements with medium burn-up and four highly burnt-off fuel elements from the recently ended HFR Eu1bis irradiation experiment that was conducted under VHTR conditions. The fuel elements from the proof trials were irradiated at approximately 1000°C. The burn-ups of the proof elements amounted to up to 10% FIMA and the fast neutron fluence up to $4.8 \cdot 10^{25} \text{m}^{-2}$. With the execution of the accident simulations on these fuel elements a presently still open building block in the chain of evidence on the inherent safety of the HTR module design was to be closed.

The fuel elements from the HFR Eu1bis experiments were irradiated at 1250°C and had burn-ups up to 11% FIMA. The maximal fast neutron fluence here amounted to $3.98 \cdot 10^{25} \text{m}^{-2}$. The tests performed on these fuel elements were supposed to provide critical information on the fission product retention behavior of TRISO fuel that had previously not been irradiated at such temperatures. In Figure 8, the parameter range of this work is presented in comparison with the design/layout data for the HTR module reactor.

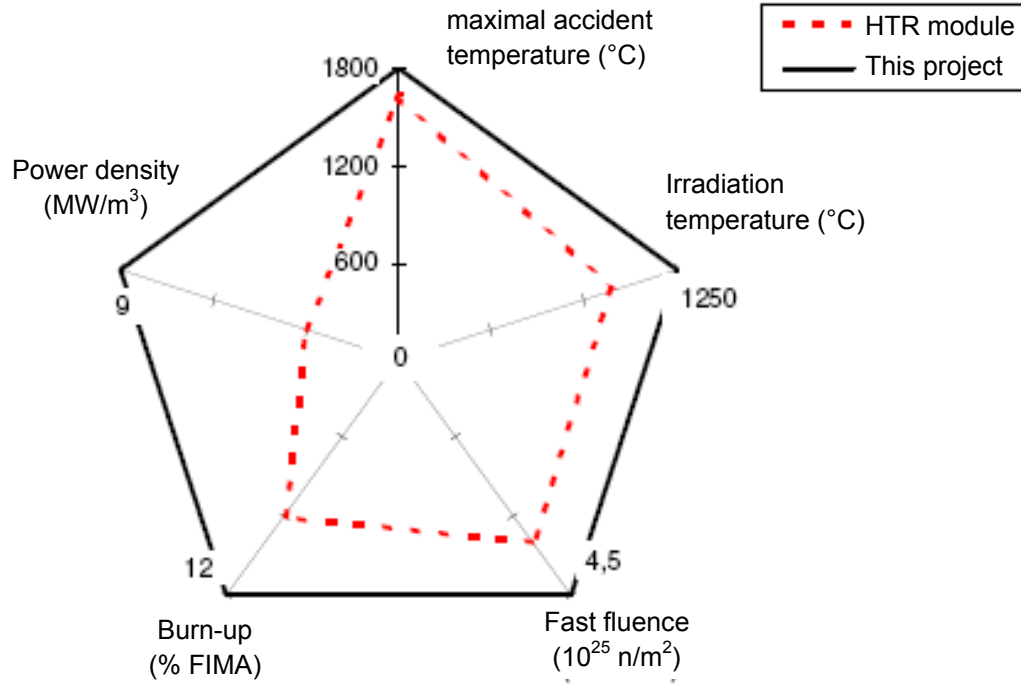


Figure 8: Irradiation and accident parameter range for HTR model in comparison with this work

5. Execution of the tasks described here

5.1 Cold finger apparatus

The cold finger apparatus (CoFA II) is a test installation in which spherical HTR fuel elements can be baked out at ambient pressure in a helium atmosphere at temperatures up to 2000°C and small releases of fission gases as well as of solid fission products can be measured. The first cold finger apparatus (CoFA I) was put into operation in 1984 as a supplement to an existing testing installation in the hot cells of the FZJ [Schenk et al. 1988]. The old installation, the so-called A test served primarily for accident simulation at temperatures from 1900 to 2500°C, such as are assumed for accidents in medium to large HTR. With the ending of the German HTR research program, the CoFA I in Jülich was taken out of operation. As part of the European HTR-F project, in the year 2001, parts of the CoFA I as well as spare parts, drawings and engineering documents were transferred to the European Institute for Transuranium Elements (ITU). In 2005, the CoFA II was put into operation in the Hot Cells of the ITU [Freis et al. 2008].

The A test consisted of two resistance furnaces of graphite that were integrated in a helium cycle. A cold trap also integrated in the helium cycle with a gamma detector connected to it permitted the measurement of the curves of the released fission gases, chiefly Kr-85, which is still present in sufficient quantities even in the case of older fuel elements because of its long half-life of 10.77 years. The release of solid fission products was determined in each case by a gamma spectrometric inventory measurement of the fuel element before and after the heating tests. Accordingly, here only integral release values and even this only for large releases of a few percent could be determined [Schenk 1978]. With the introduction of the TRISO coated particles with low releases under accident conditions up to 1600°C it was therefore necessary to develop a system with which even low activities of solid fission products and their time curve of release could be registered. With the new CoFA II it is possible to simulate calculated accident curves up to 2000°C and to measure Cs-137 releases in the range up to a release proportion of 10^{-7} .

The Cold Finger apparatus is positioned in a so-called Hot Cell, i.e. a space that is shielded against the outside by thick concrete walls. This is necessary since the fuel elements being studied are strong radiation emitters and cause high dose powers in their surroundings. Inside the Hot Cell is a gas-tight box of stainless steel, the so-called caisson, which securely encloses

the radioactive contamination. Remote-controlled manipulators permit the manipulation of samples and testing devices. If tasks cannot be accomplished with the manipulators, highly radioactive objects must be removed from the caisson. Then it is possible to intervene in the caisson from the rear wearing well fitting gloves. Tools, consumable materials, samples and spare parts can be brought in with the aid of a transporting system under the cells using the manipulators.

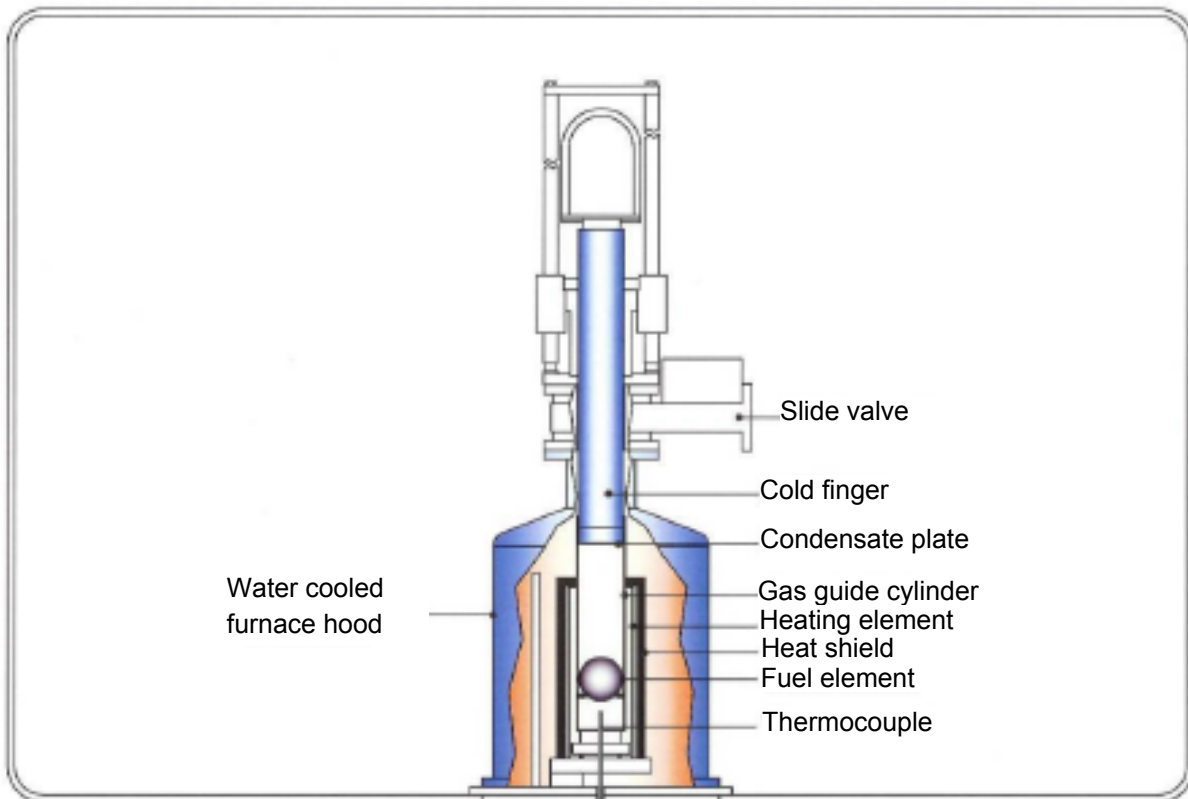


Figure 9: Schematic representation of the CoFA II

The furnace itself consists of an internal gas guide cylinder, a surrounding heating element that is affixed in a water-cooled copper block and of surrounding heat shields. To minimize the absorption of fission products in the furnace, the CoFA was designed as a metallic resistance furnace. Due to the strongly ionizing effect of the radioactive radiation of the fuel element, high voltages are prohibited so that it is necessary to work with high current intensities. A high current transformer installed behind the caisson provides the necessary amperage. The water-cooled copper block is connected by thick copper bolts to the transformer and conducts the current into the heating element.

All high temperature parts of the CoFA II consist of tantalum. Experience in Jülich has shown that tantalum has the lowest tendency toward carbidization at the site of contact with the fuel element. The fuel element is centered in a three-point support in the gas line cylinder. A tungsten/tungsten-rhenium (W/WRh) thermocouple measures the temperature about 3 mm below the fuel element and sends the control value for regulating the furnace power. In the first CoFA I, which was installed in the hot cells of the FZJ, in addition a side hole was provided through which the fuel element temperature could be measured with a pyrometer. It had already been demonstrated that the thermocouple registers the temperature reliably with an error of roughly 10°C so that this device was omitted in the new CoFA II (see Appendix IIIg) [Schenk et al. 1988].

The apparatus has a moveable cold finger at the lower end of which an exchangeable condensate plate of stainless steel is positioned (see Figure 9). An efficient water cooling assures that the surface temperature of the plate remains below 100°C even at high furnace temperatures so that solid fission products such as Cs-137, Cs-134, Sr-90, I-131 and Ag-110m condense there with high efficiency. The cold finger temperature is measured with an integrated Pt-100 resistance thermometer inserted in a boring extending to the bottom side of the plate. An active cooling system that is separate from the other cooling cycles and exclusively supplies the cold finger regulates the cooling water temperature so that the same conditions always prevail. During operation, the cold finger can be pulled through a sluice system with water-cooled slide valve and the condensate plate exchanged semi-automatically with the cell manipulators. During the exchange process, the slide valve is closed so that no cell atmosphere can penetrate into the furnace. After this, the cold finger is driven back into the furnace with the new plate. The replaced condensate plates are then transported to a laboratory with a low radiation background. There the plates can be measured with a highly pure germanium detector, and the isotopes that emit gamma radiation can be quantified [Freis et al. 2008]. Ordinarily the condensate plate is changed about once daily. It takes about five to ten minutes to change a plate.

The furnace is enclosed in a water-cooled and gas-tight hood. During a test the apparatus is flushed with helium. The helium enters the gas line cylinder under the fuel element, flows around the fuel element, flows past the condensate plate and spreads out in the hood. From there it is drawn off by a diaphragm pump and passes into a cold trap of active carbon cooled with liquid nitrogen. The fission gases released from the fuel element are transported with the

stream of helium, condense on the active carbon and can be measured by an NaI gamma detector installed under the cold trap. The method was already developed in the sixties of the last century at the FZJ and used both in the A test and in the CoFA I installed in Jülich [Stradal 1970].

To load the fuel element or to replace contaminated or defective parts of the furnace, the hood may be raised with a crane. During operation, an O ring seals the hood at the bottom. The cold finger is sealed by two O rings in the installed/inserted position. In the withdrawn position, the slide valve provides sealing. All other passages and connections are sealed with O rings. The furnace temperature is regulated and the operating processes and parameters are controlled centrally by a programmed memory controller (SPS) and a computer program connected to it with an input surface. All operating parameters such as furnace temperature, cold finger temperature, cooling water temperature, cooling water flow, internal pressure, helium flow, amperage and voltage are registered and recorded centrally.

5.2 Course of the bakeout tests

Before each test a new gas line cylinder is installed in order to minimize any possible falsification of the results by contamination from the previous experiment. After this, the fuel element is placed on the three point holder in the gas line cylinder using the cell vacuum cleaner. Then the furnace hood is closed and the testing program loaded. The time-temperature curves of the bakeout trials are patterned after the calculated accident curves or go beyond them. During the entire test, helium is flowing through the CoFA II at 30 standard liters per hour. The helium used has a purity of at least 99.996%. If a sealing flaw occurs at a place on the helium line, a combi filter integrated directly into the helium line before the installation will filter out moisture or oxygen.

Before the actual accident simulation is started, the cell atmosphere in the hood is drawn off with a connected vacuum pump and tested for tightness. This is done with the slide valve closed. Then the hood volume is refilled with helium and the program started. Following this, the cold finger is driven in and the rinse/flush cycle operated cold for a few hours to flush out contaminants. In this phase the seal of the cold finger bushing is also tested. Then the fuel elements heated for a short time of about 6 h at 300°C in order to drive water and contaminants out of the fuel element. Following this, there is a phase of about ten hours in which the operating temperature in the reactor of 1050 or 1250°C is adjusted. This is supposed to create the same

status as in operation so that equilibrium releases can be measured. Finally the actual accident simulation begins. In the standard test, at this time one heats to the maximal temperature at 47°C/h [Schenk et al. 1988]. Figure 10 shows the heating up phase of an ideal simulation curve covering a pressure loss accident with outage of the active post-decomposition heat removal in the HTR module reactor (see above). The programmable regulation, however, permits the setting of any temperature curves for different accident scenarios or reactor types.

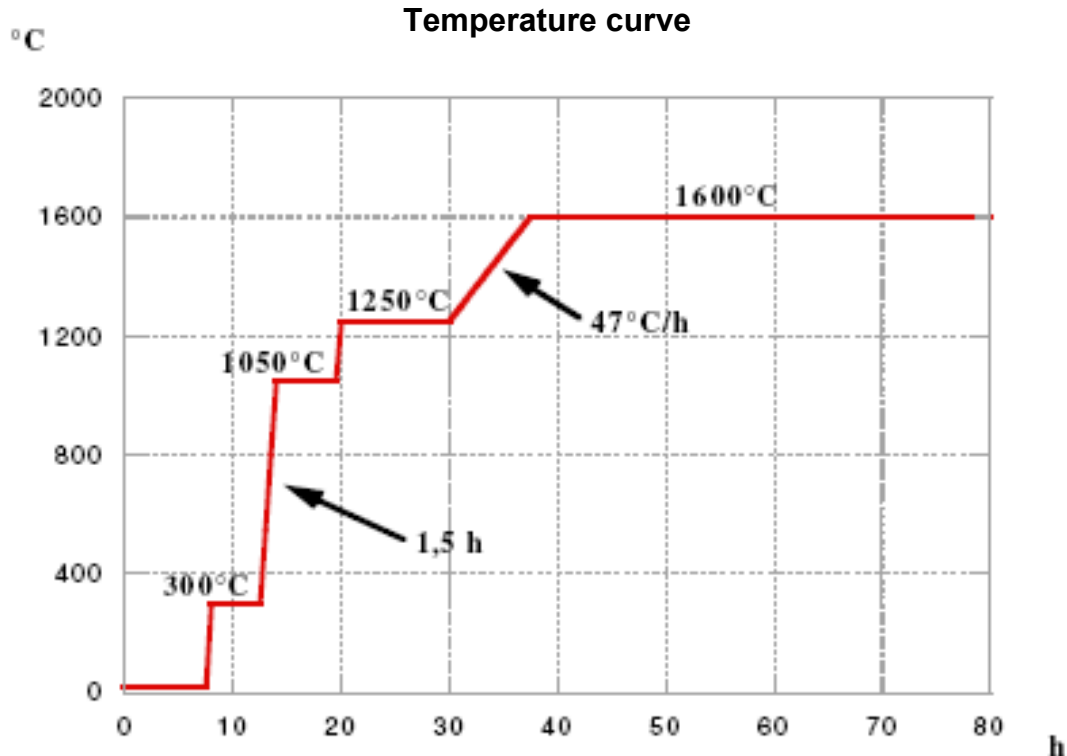


Figure 10: CoFA standard test [Schenk et al. 1988]

A volume flow regulator regulates the incoming helium stream and a diaphragm pump integrated behind the furnace hood into the helium line draws the helium out of the hood and sends it to the cold trap. An accurately adjustable throttle valve in front of the diaphragm pump permits the adjustment of an equilibrium pressure in the furnace interior. During a heating test, the furnace pressure is set at roughly 980 mbar. Therefore, in the furnace interior a slight underpressure prevails compared with the cell atmosphere. This assures that the furnace hood is pressed firmly against the bottom and is sealed by the O ring. However, in this case there is the risk that in the event of a sealing flaw, say on the sluice system of the cold finger, the cell atmosphere may penetrate into the furnace and corrode the tantalum parts. In the FZJ the apparatus is operated with a slight overpressure. This minimizes the risk of an air penetration,

but then it is difficult to determine whether furnace atmosphere is escaping through sealing flaws and part of the released fission gas possibly lost.

5.3 Fission gas measurement

If a radioactive noble gas is released from the fuel element during a CoFA test, it is first spread out in the hood volume (VH ~ 28.6 liters) and is transported from there, together with the flushing gas, to a cold trap under the Hot Cell. The cold trap consists of a small volume of activated carbon in a steel container. It is cooled in an insulated container with liquid nitrogen to -195.9°C . As a result, the fission gas freezes upon entering into the activated carbon while the carrier gas helium remains gaseous and passes through the cold trap.

Table 8: Properties of fission gases

Fission gas	Half-life	Boiling point	Melting point	γ-Energy	Emission probability
Kr-85	10.77 a	$-153.,22^{\circ}\text{C}$	$-157.,36^{\circ}\text{C}$	514 keV	0,434 %
Xe-133	5.243 d	-108.1°C	-111.8°C	81 keV	38 %
He	-	-269°C	-272.2°C	-	-

Under the cold trap is a 3x3 sodium iodide gamma detector (NaI detector) with high detection efficiency, which is connected to a measuring computer and detects the fission gas activity in the cold trap. To assure the highest possible measuring efficiency, the detector is positioned as close as possible to the cold trap. The bottoms/floors of the cold trap and of the nitrogen container are also selected as thin-walled in order to achieve the lowest possible gamma absorption.

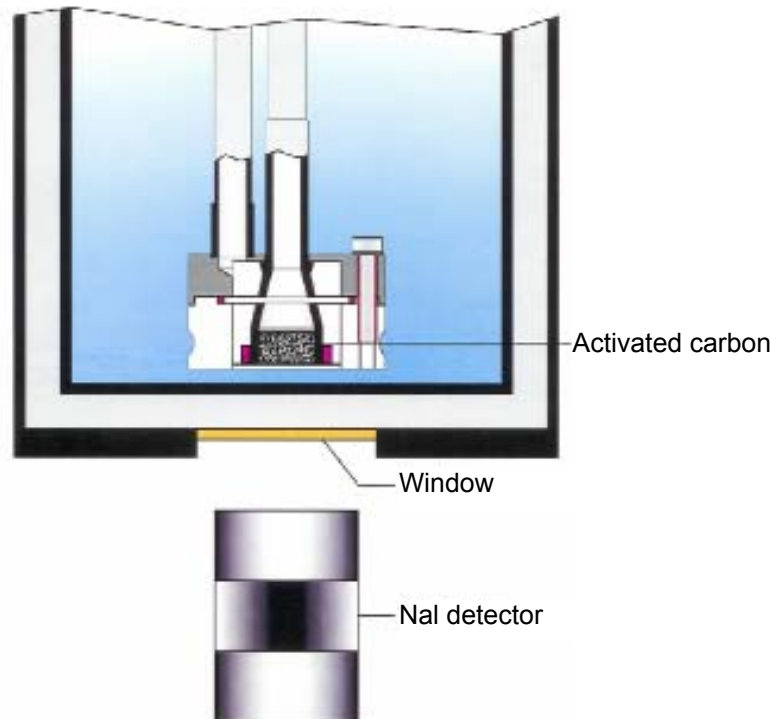


Figure 11: Schematic representation of the cold trap

Typical fission gases are krypton and xenon. As a rule, in an older fuel element only the krypton isotope Kr-85 with a half-life of 10.77 years is still present as a measurable fission gas in a quantity sufficient to be detectable. In the case of fuel elements that were irradiated only very recently, it is possible that enough Xe-133 is still present. All other radioactive fission gases have a too-short half-life to still be present in a sufficient quantity. Due to the low emission probability for a gamma quantum in the case of decay of Kr-85, the detection limit for the activity is relatively high, despite the short measuring distances and the efficient detector. Another disturbing factor is the rather high underground activity below the Hot Cells. Therefore, the entire measurement system is installed in a Bleiburg for shielding purposes. The present system can detect Kr-85 activities above some 700 Bq.

During one experiment, a series of successive measurements is constantly performed with the NaI detector. Each measurement lasts three minutes. A program controls the measurements, evaluates the gamma spectra and continuously records the measured values in a data file. In this way, a time curve of the activity of Kr-85 in the cold trap is obtained.

If fission gas is suddenly released in the furnace, then with a short time delay one can measure the rise of the activity in the cold trap. The time-activity curve in the cold trap is a function of the released activity, of the hood volume and of the helium flow and furnace temperature. The function can easily be derived with the material balances for furnace hood and cold trap (see equation 1). The typical exponential curve is clearly recognizable in the measurement curve and permits the accurate determination of the time of sudden Kr-85 releases due to particle failure during a heating test.

$$\frac{dA_G}{dt} = \left(-\frac{\dot{V}_{He} T_G}{V_G T_U} \right) \cdot A_G$$

$$\frac{dA_T}{dt} = -\frac{dA_G}{dt}$$

$$A_T(t) = A_{G,0} \cdot \left(1 - e^{\left(-\frac{\dot{V}_{He} T_G}{V_G T_U} \cdot t \right)} \right)$$

Equation 1

$A_T(t)$: Activity in the cold trap (Bq)

$A_G(t)$: Activity in the hood (Bq)

$A_{G,0}$: Released activity in the case of a sudden particle break (Bq)

\dot{V}_{He} : Helium flux (l/h)

V_G : Hood volume (liters)

T_G : Furnace temperature (K)

T_U : Ambient temperature (K)

The calibration of the cold trap measurement geometry is accomplished with a known quantity of Kr-85 that can be brought into the helium cycle. Optionally, the calibration gas can be introduced before entering into the furnace or directly before the cold trap. In this way it is assured that no sealing defects are present and no measuring gas is lost. Ordinarily, for each heating test, in each case, at least one calibration is performed since the measurement

geometry can change when the cold trap is replaced. The calibration factor (f_k) is the obtained from the ratio of the counted pulse rate (I) and the activity (A).

$$f_k = \frac{I}{A_{Kr-85}}$$

Equation 2

If the calibration is performed by introducing a known quantity of Kr-85 before the furnace, one will get a time-activity curve in the cold traps as described in equation 1.

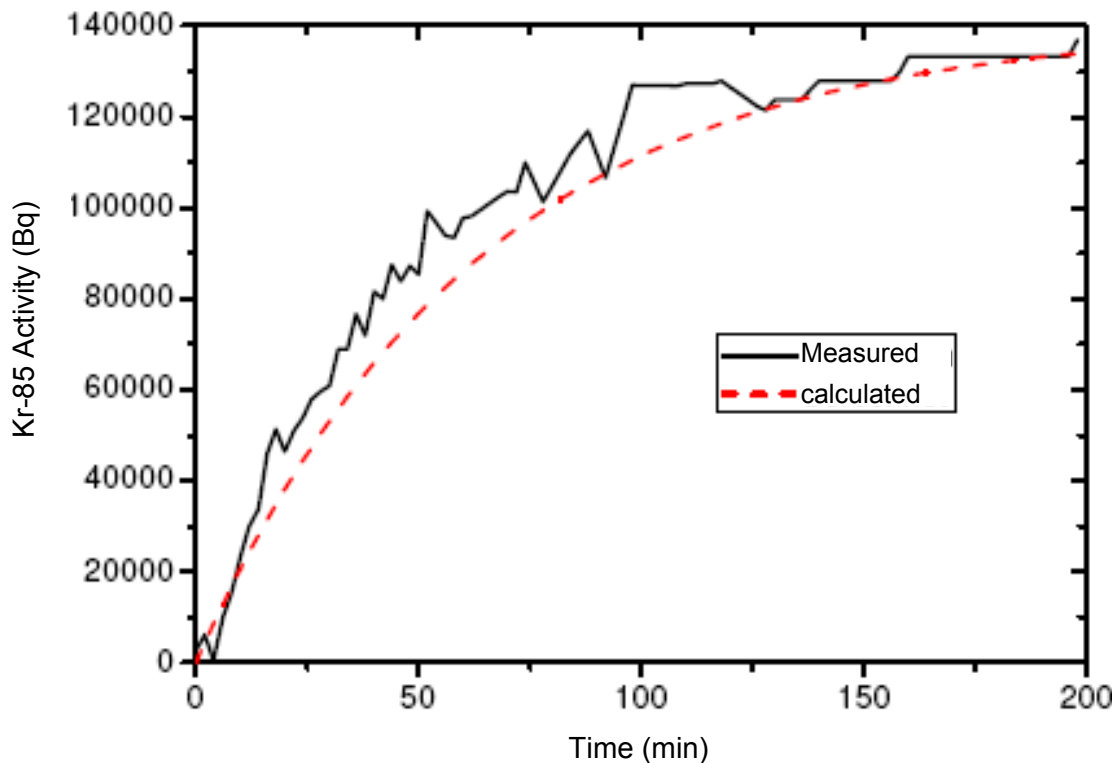


Figure 12: Time-activity curve in the cold trap after calibration with 135 kBq Kr-85

If a coated particle breaks in the heating test, fission gas is released and rapidly diffuses through the graphite matrix. The diffusion coefficient is about $10^{-5} \text{m}^2/\text{s}$ along the grain boundaries [Verfondern et al. 1997]. According to the diffusion theory, from this one calculates by equation 3 [Kugeler & Schulten 1989] a breakthrough time (t_D) of about 15 seconds for a particle failing in the center of the fuel element. The helium line from furnace to cold trap has a length of about 5 m. At a volume flow rate of 30 l/h and an inner diameter of about 6 mm, the

carrier gas therefore needs about 17 seconds to reach the cold trap. From this estimation it is apparent that a gas release can be detected almost immediately. In the release diagram that is plotted over several hundred hours a particle break can be seen as a sudden jump in activity.

$$t_D \approx \frac{r^2}{6D}$$

Equation 3

r = Fuel element radius (coating thickness)

D = Diffusion coefficient m/s

5.4 Measurement of solid fission product release

Solid fission products such as cesium, strontium or silver diffuse at elevated temperatures through the particle coatings and the graphite matrix and are subsequently released into the environment with low partial pressures. In the CoFA II, they are transported away by the constant flow of helium from the fuel element and condense on the condensate plate of the cold finger or on other cold places inside or outside the furnace. The condensate plates are then removed and transported in an aluminum container from the Hot Cell to a laboratory with low radiation background. To avoid incorrect measurements caused by contamination of the aluminum container, each plate is removed and placed in a new clean container. The container is placed in a fixed measurement position and measured with a germanium detector by gamma spectrometry. A standard point emitter of Cs-137 is used for quantifying the measurements. The actual distribution of the activity on the condensate plate is unknown but is assumed to be essentially homogeneous. The maximal systematic error would occur if the total activity were concentrated on the edge of the plate. The error is small even then due to the large measurement distance compared with the plate radius but is allowed for in the inaccuracy determination. The total error is obtained from the statistical error plus all systematic errors. The inaccuracy determination is made by using the GUM Workbench® program (see Appendix).

Thanks to the efficient and regulated water cooling of the cold finger, the great majority of the fission products condenses on the condensate plates. This is important for the accuracy of the measurement in the case of small releases. However, every unnecessary condensation of fission products on the furnace hood or on the slide valve leads to a constantly rising radiation

background in the Hot Cell. Manual maintenance work is made extremely difficult as a result and becomes totally impossible beyond a certain point. The cold finger efficiency (E_{KF}) is different for different chemical elements. The temperature of the plate surface, depending on position of the plate and furnace temperature, amounts to between 60 and 80°C. The released activity (R) is computed by equation 4.

$$R = \frac{A}{E_{KF}}$$

Equation 4

R: Release, A: activity on the condensate plate, E_{KF} : cold finger efficiency

For cesium, silver, ruthenium and iodine, a cold finger efficiency of about 70% is assumed, for strontium an efficiency of about 20%. These values were already determined in Jülich by repeated calibrations with known quantities of the corresponding radionuclides [Schenk et al. 1988] and in Karlsruhe for cesium. Since the two plants are of identical construction, it is assumed that the cold finger efficiencies for the remaining fission products are also in agreement.

Table 9: Melting and boiling points of metallic fission products and cold finger efficiencies

Fission product	Melting point	Boiling point	Cold finger efficiency
Cs-137, Cs-134	28.45 °C	671 °C	~ 70 % ± 16 %
Sr-90	777 °C	1382 °C	~ 20 %
Ru-106	2334 °C	4150 °C	~ 70 %
I-131	113.7 °C	184.2 °C	~ 70 %
Ag-110m	961.78 °C	2162 °C	~ 70 %

5.5 Calibration of the cold finger efficiency

For calibrating the cold finger efficiency, holes were drilled in two graphite balls and one glass ampoule each containing a solution with certified Cs-137 activity (100 kBq and 400 kBq) was introduced into each. The ampoules were opened and allowed to stand open in gloveboxes for several days to allow the liquid to evaporate. Before and after, in each case a gamma spectrometric test was made as to whether part of the Cs-137 activity had also volatilized or not. This was not the case. Finally, the boring was closed with a small aluminum plate and affixed with a graphite screw with an internal boring (see Figure 13).

The standards thus prepared were transported to the Hot Cell, successively placed in the CoFA II and baked out at 1600°C. The graphite balls were placed in the CoFA II with the opening on top for this purpose. Then the hood was closed, a helium flush performed, and a heating program was started. The balls were heated with the cold finger inserted within 50 minutes from room temperature to 500°C and subsequently heated to 1600°C within 60 minutes. Since the melting point of aluminum is 660.32°C, the aluminum cap fused during the second heating step so that the cesium could evaporate freely and condense on the cold finger.

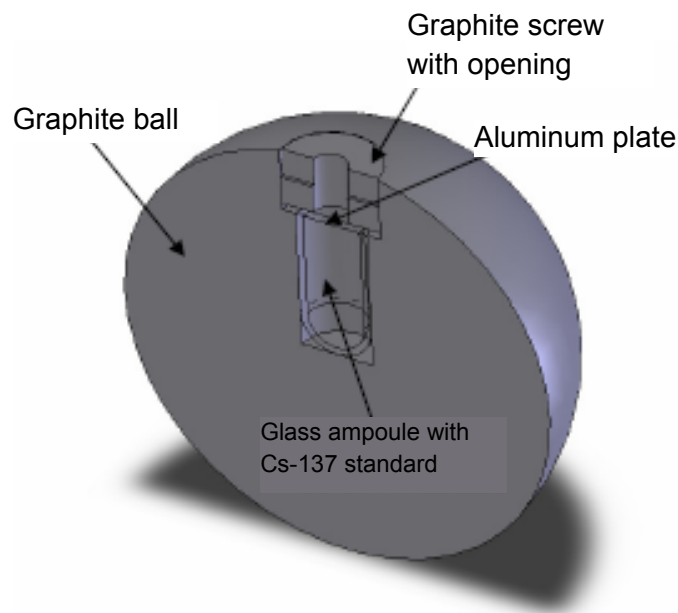


Figure 13: Graphite ball with Cs-137 standard for cold finger efficiency determination

After roughly 2 hours the calibration test was ended and the condensate plate replaced. A total of five heating processes were performed for the calibration using the above-described program. Two of the heating processes were conducted with prepared graphite balls and three without balls. The three blank heating processes were carried out before and between the calibration tests and served for determining the background contamination. This was also intended to avoid having activity from the previous calibration precipitate on the condensate plate in the second calibration test.

The condensate plates were then transferred to a laboratory with low radiation background and there measured by gamma spectrometry. Before this, the containers holding the condensate plates were replaced by new containers according to the standard procedure (see above).

Besides the balls with Cs-137, a graphite ball with 390 kBq of Sr-90 was prepared and baked out. Unfortunately, the required measurement process for the later quantification of the plate activity was not available at the time when the present study was carried out.

During the calibrations, a sealing defect appeared on the sluice system of the cold finger. This resulted in a steady input of cell atmosphere into the furnace hood, leading to slow corrosion of the tantalum parts. This was not noticed at first, but later upon visual inspection of the plates after the tests, a white film was discovered on the plate bottoms. When the condensate plates were measured, ultimately even on the plates that were used without active calibration balls, a relatively high Cs-137 activity was detected. In addition, low Cs-134 activities could also be detected (see Table 10). A sample of the white powder was scraped off after the activity measurement, analyzed by using energy dispersive x-ray spectroscopy (EDX) in an electron microscope and identified as tantalum oxide (Ta_2O_5).

Table 10: Cs-137 activity of the calibration plates

Plate number	Input Cs-137 activity ($\pm 3.5\%$)	Cs-137 activity	Cs-134 activity	Cs-134 / Cs-137
80	blank	118 kBq ± 6.6 kBq	2.5 kBq ± 1.1 kBq	0,021
81	390 kBq Cs-137	312 kBq ± 12.7 kBq	3.72 kBq ± 1.42 kBq	0,012
82	blank	74.7 kBq ± 6.6 kBq	2.86 kBq ± 1.92 kBq	0,038
83	390 kBq Sr-90	-	-	-
84	blank	124.1 kBq ± 5 kBq	1.67 kBq ± 0.74 kBq	0,013
85	98 kBq Cs-137	194.6 kBq ± 12 kBq	3 kBq ± 1.69 kBq	0,015

The ratio of the two cesium isotopes permitted the conclusion that the additional plate activity involved contamination from previous bakeout tests of old fuel elements. These were presumably released together with the tantalum oxide from the heat shields and the heating element and precipitated on the cold bottom sides of the plates.

Despite unexpectedly high background activity, an evaluation of the calibration tests and determination of a cold finger efficiency for cesium could be carried out. For this purpose, first, the background was computed by forming the arithmetic mean of the activities of the plates from the blank heating processes (C). After this, the average efficiency (E_{KF}) could be determined by equation 5.

$$E_{KF} = \frac{E_{KF,81} + E_{KF,85}}{2} = \frac{1}{2} \cdot \left(\frac{A_{81} - C}{A_{81,n}} + \frac{A_{85} - C}{A_{85,n}} \right) \quad \text{Equation 5}$$

The cold finger efficiency for cesium was ultimately found to be 72% with an inaccuracy of $\pm 16\%$.

5.6 Unusual incidents

During the operation of the CoFA II various unforeseen events occurred that led to outages and necessitated repair work. This became especially problematic in the later course of this work since the radiation background, due to the continuously rising contamination inside the gas-tight steel container made manual repair work difficult.

5.6.1 Irruption of cell atmosphere

During the calibration of the cold finger efficiency, first sealing flaws appeared on the sealing rings/gaskets of the furnace hood, leading to the entry of cell atmosphere and corrosion on the high-temperature parts. Later on, the corrosion intensified until there was a massive irruption of cell atmosphere and strong corrosion inside the furnace (see Figure 14). In particular, the two O rings for sealing the cold finger bushing, apparently due to radiation and wear due to the constant movement of the cold finger, became porous and had to be replaced. There was also a slight leak/sealing defect on the bushing of the thermocouple so that it also had to be replaced. Error search, repair preparations and repair work caused relative major delays and expenses.

Based on this experience, an additional testing step was made in the course of the tests. To be certain, the programming of the furnace control had already previously compelled the performance of a tightness test of the furnace hood before a heating program could be started. However, this tightness test [test for sealing defects] was performed with the cold finger withdrawn and the slide valve closed so that the sealing defect on the cold finger bushing was not discovered. The new procedure now envisioned a short phase of operation at room temperature. During this phase, now with the cold finger inserted, the gas feed could be shut off manually. With the cold finger bushing tight, at this time a negative pressure was created.

5.6.2 Temperature rise on the condensate plate due to graphite deposition

At high furnace temperatures, the polished surface of the condensate plate reflects a great part of the radiation heat back into the furnace. In collaboration with the efficient water cooling, therefore, a rather low plate temperature is established of roughly 60 to 80°C. During the first CoFA test, it was noted that the fuel elements in the first hours of the heating-up phase emitted dust that settled on the condensate plate as a black coating. As a result the emission coefficient of the plate surface was changed and the plate temperature rose, which could have an effect on the cold finger efficiency. In some cases, the plate temperature reached unacceptably high values of roughly 120°C so that the safety system reacted and the plant shut down automatically. For this reasons, the heating program had to be planned in such a way that at least during the critical phase, i.e. at the start of the accident simulation until 1600°C was reached, the plate temperature could be observed in order to intervene manually if necessary.

5.6.3 Cooling cycle regulation problems

Initially not only the cold finger cycle but also all cooling cycles were regulated. Due to problems with the adjustment of the control circuits, temperature fluctuations occurred and as a result sometimes high surface temperatures. In one case, the outside temperature of the furnace hood increased so strongly that the insulation of a control cable in contact with it partially melted. After this, later on regulation of the water cooling was abandoned with the exception of the cold finger (see above).

5.6.4 Spark jumps

During the CoFA operation, in one case there was a spark jump from one side of the heating element to the other (see Figure 15). As a result, at the site of the short circuit a hole about 2 cm in size was formed in the heating element. The apparatus shut itself down immediately afterward. The cause of the spark jump could not be fully clarified. However, it is conjectured that the heating element was inaccurately finished and had also lagged behind during the bakeout. As a result, the gap between the left and right halves probably became too small. Since the helium atmosphere was also ionized by the charged fuel element, the current could finally jump across with rising voltage. Following this incident, the heating element was replaced. As a consequence, for all tantalum parts in the future, greater emphasis is placed on the accuracy of the final machining.



Figure 14: Corrosion on the heating element

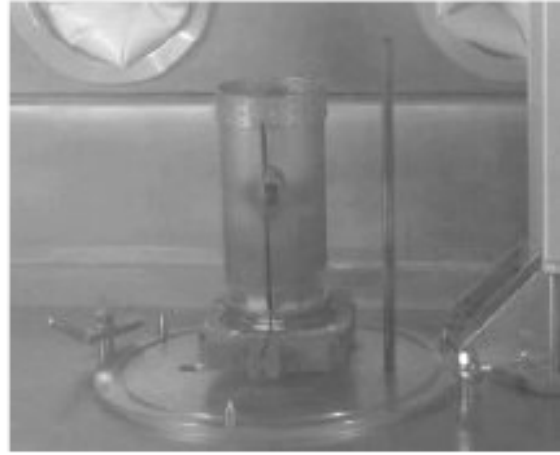


Figure 15: Heating element destroyed by short circuit

5.7 Gamma spectrometric fission product inventory measurement and burn-up determination

The fission product inventory of the fuel elements is determined by gamma spectrometry. For this purpose, the element to be measured is placed inside the Hot Cell in front of a conical collimator installed in an opening in the cell wall. On the other side of the opening, in the operation area, a high-purity germanium detector is positioned with high energy resolution. The fuel element is rotated at about 30 revolutions per minute during the measurement. In this way the most uniform measurement possible of the emitted gamma radiation is supposed to be assured.

The collimator is supposed to reduce the incident radiation on the detector and also the cell background and simultaneously assure that the fuel zone of the fuel element is completely detected. It was therefore designed as a hollow cylinder from a tungsten alloy whose inner diameter tapers toward the center to 0.8 mm. It therefore acts as a diaphragm and covers, according to the pinhole camera principle, the entire fuel zone [Duwe et al. 1977, Freis et al. 2006].

The measurement system consists of the germanium detector, which is cooled with liquid nitrogen, a pre-amplifier and a multichannel analyzer by the Canberra Co. (DSA 1000). The control of the measurement and the evaluation of the gamma spectra on the computer are accomplished by the gamma spectrometry software InterWinner.

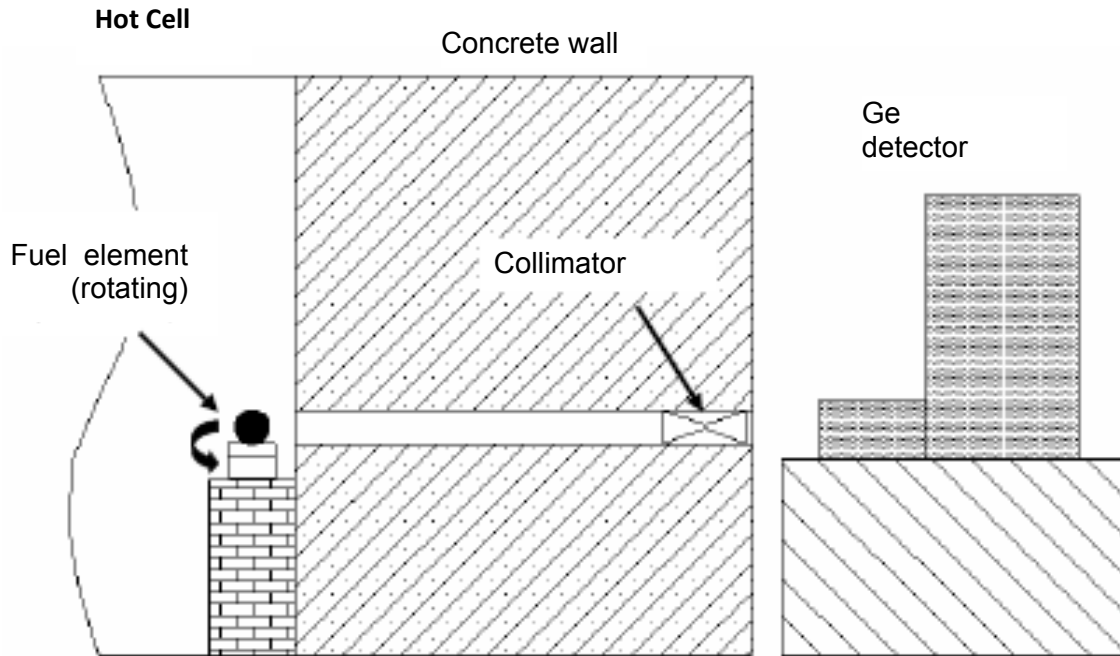


Figure 16: Gamma spectrometry measurement setup

The germanium crystal of the detector employed consists of two differently doped layers. When a high voltage is applied, in this way a barrier layer is formed at the p-n junction. Incident gamma quanta can be absorbed and generate high energy photo electrons. The latter degrade their kinetic energy by lifting additional electrons out of the valence band into the conduction band. As a result, depending on the energy of the incident gamma quanta, a variable number of electron-hole pairs are formed, which can be detected by measurement techniques. The ionization energy (E_i) for generating an electron-hole pair in germanium is about 3 eV. This means that by means of an absorbed gamma quantum with an energy (E_g) of 661.66 keV, approximately 220,500 electron-hole pairs are generated. As opposed to an NaI detector in which the ionization energy is about 120 eV, the relative spread/scatter of the charge carriers generated is therefore very small. This results in a high energy resolution.

$$N = \frac{E_g}{E_i} = \frac{661,66 \text{ keV}}{3 \text{ eV}} = 220553,33$$

Equation 6

The measured pulses are counted by the attached multichannel analyzer and assigned to different channels. This results in the creation of a gamma spectrum with energy-typical peaks that can be evaluated. Depending on the energy resolution of the detector, the peaks have a very narrow or wider half-width. The peaks of the detector used within the scope of this study had a half-width of about 1.8 keV for a gamma energy of 661.66 keV. The InterWinner program identifies the peaks, interpolates the ground and determines the net area between peak and ground. The net area divided by the measurement time, minus the previously determined background, is proportional to the activity of the pertinent nuclide.

At room temperature, strong thermal noise would overlay the measurement signals. Therefore the germanium detectors are usually cooled with liquid nitrogen to -190°C . If too many gamma quanta strike the detector in too short a time it becomes overloaded. As a result of the measurement electronics, at high pulse rates, dead times also are created that must be taken into account in the evaluation.

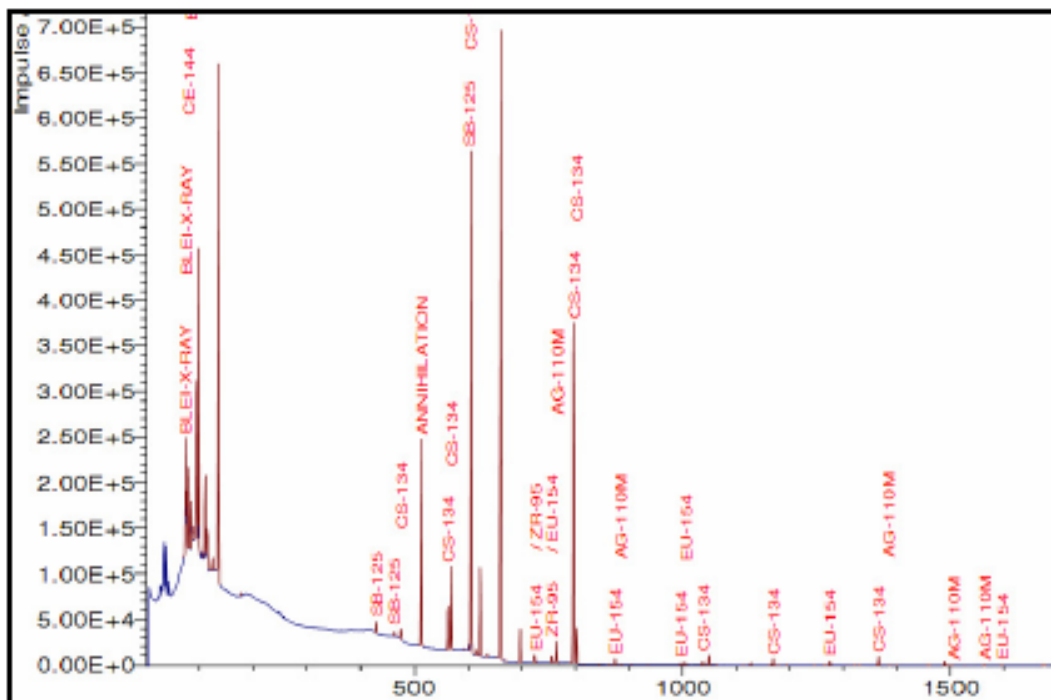


Figure 17: HTR fuel element gamma spectrum (HFR Eu1bis3)

In the first step, an energy calibration is performed. For this purpose, a radiation source with known emission energies is placed in front of the detectors and a spectrum recorded. The peaks are then assigned to the known energies manually. The second step is the determination of the background. For this purpose, the detector is positioned in the later measurement geometry without a sample and typically a spectrum is recorded overnight. The peaks generated by the gamma background are identified and evaluated and the count rates found are saved in a background data file. The constant of proportionality between sample activity and net pulse rate is finally determined by using a reference sample (standard) with known activities of different energies.

Since the detector efficiency is energy-dependent, the nuclides used in the reference sample should cover the entire energy spectrum of interest as fully as possible. Alternatively, a standard may be used with only one gamma energy and an internal calibration performed by utilizing the known emission probabilities. In the evaluation, later correction factors will still have to be considered for the different sample and standard geometries (see Appendix VI). As part of the present study, first a self-fabricated standard was utilized. It consisted of a graphite ball into which a known quantity of a fuel solution with fission products contained in it was introduced [Freis et al. 2006]. Later a fuel element was used that had already been repeatedly measured in Jülich and Karlsruhe and found to be in agreement

An important parameter for nuclear fuel in general and for the particle behavior is the burn-up [BU]. It states how much energy was generated per mass of uranium and how many fissions took place per initially present quantity of heavy metal atoms. In the first case, the burn-up is reported in megawatt days per ton of heavy metal (MWd/tHM), in the second case in % FIMA (Fission per Initial Metal Atoms). If the heavy metal quantity in the fuel element is known, the burn-up can be determined with reference to the Cs-137 inventory by gamma spectrometry.

Cs-137 is formed almost exclusively directly by fission and/or by decomposition of short-lived precursor nuclides. The cumulative fission output upon fissioning by thermal neutrons is relatively high and about equally high for U-235 and Pu-239. It amounts to roughly 6.27% for U-235 and about 6.73% for Pu-239. It must be weighted differentially depending on burn-up and U-235 enrichment. The long half-life of Cs-137 of about 30.07 years as well as the negligibly small cross section of action for (n,g) capture reactions for neutrons of about 0.25 barn are advantageous for the burn-up determination based on the Cs-137 inventory. The brooding of

Cs-137 from Xe-136 by neutron capture also plays no part because of the small cross section of action of about 0.23 barn. The Cs-137 inventory is therefore an approximately linear function of the burn-up. If it is desired to increase the accuracy of the burn-up determination, one can compute a correction factor for the decay during irradiation. Assuming an approximately constant fission power during irradiation, the formation and decay of Cs-137 can be described in simplified form by the following equation:

$$\frac{dN_{Cs-137}}{dt} = -\lambda_{Cs-137} \cdot N_{Cs-137} + \gamma_{Cs-137} \cdot \bar{\sigma}_f \cdot \bar{\phi} \cdot N_{HM} \quad \text{Equation 7}$$

γ_{Cs-137} : weighted fission yield, $\bar{\sigma}_f$: mean action cross section for fission, $\bar{\phi}$: neutron flux,
 λ_{Cs-137} : Decay constant, N_{HM} : Number of heavy metal atoms, N_{Cs-137} : Cs-137 atoms

On the condition that initially no Cs-137 atoms are present, the solution reads

$$N_{Cs-137} = \frac{\gamma_{Cs-137} \cdot \bar{\sigma}_f \cdot \bar{\phi} \cdot N_{HM}}{\lambda_{Cs-137}} \cdot \left(1 - e^{(-\lambda_{Cs-137} \cdot t_{irr.})}\right) \quad \text{Equation 8}$$

With the definition of burn-up (BU) as the total number of fissions divided by the number of initially present heavy metal atoms, equation 8 can be rewritten as:

$$BU = N_{w_{Cs}}(t_{irr.}) \cdot \frac{t_{irr.} \cdot \lambda_{Cs}}{\gamma_{Cs} \cdot N_{HM}} \cdot \left(1 - e^{(-\lambda_{Cs} \cdot t_{irr.})}\right)^{-1} \quad \text{Equation 9}$$

$$\Leftrightarrow BU = \frac{N_{w_{Cs}}(t_{irr.})}{\gamma_{Cs} \cdot N_{HM}} \cdot C_{corr}(t_{irr.}) \quad \text{Equation 10}$$

The correction factor is:

$$C_{corr} = t_{irr} \cdot \lambda_{Cs-137} \cdot \left(1 - e^{(-\lambda_{Cs-137} \cdot t_{irr})}\right)^{-1}$$

Another possibility of determining the burn-up is to use a computer program that computes the burn-up and isotope formation in the reactor on the basis of the power history and based on burn-up-dependent cross sections of action integrated over the reactor-typical neutron spectrum in several time steps. For this purpose the program INVENTAR, developed at FZJ, is available [Duwe & Kühnlein 1975], which has also been used for determining the not-directly-measurable isotopes, and also for comparison purposes the program KORIGEN [Wiese 2002] for which, however, no suitable cross section of capture library was available. The burn-up was determined by adapting the power history so that the calculated and measured inventory of Cs-137 were in agreement.

A total of 22 fuel elements were recorded gamma spectrometrically and their burn-up determined. In Table 11, the measured Cs-137 inventories are listed relative to the irradiation end and the respective burn-up determined on the ITU plus the value reported by the FZJ. On the six fuel elements marked in boldface, CoFA accident simulations were performed within the scope of this study.

Table 11: Measured Cs-137 inventories (related to end of irradiation) and calculated burn-ups

Fuel element	Cs-137 (Bq) ITU	Burn-up %FIMA	Burn-up per FZJ
HFR-K6/1	8,36E+10	7,69 %	7,20 %
HFR-K6/2	1,05E+11	9,71 %	9,30 %
HFR-K6/3	1,06E+11	9,80 %	9,70 %
HFR-K6/4	9,45E+10	8,70 %	9,20 %
HFR-K5/1	7,53E+10	6,93 %	6,70 %
HFR-K5/2	9,57E+10	8,81 %	8,80 %
HFR-K5/3	1,04E+11	9,55 %	9,10 %
HFR-K5/4	1,01E+11	9,26 %	8,70 %

FRJ2-KA2/1	1,24E+10	1,77 %	1,84 %
FRJ2KA2/2	1,27E+10	1,81 %	2,00 %
FRJ2-KA2/3	1,33E+10	1,91 %	2,02 %
AVR-74/16	3,58E+10	3,07 %	3,20 %
AVR-74/18	5,44E+10	4,67 %	4,80 %
AVR-73/22	2,24E+10	3,20 %	3,40 %
AVR-87/07	2,16E+10	3,09 %	3,53 %
AVR-87/08	2,22E+10	3,17 %	3,53 %
AVR-87/09	2,17E+10	3,10 %	3,56 %
AVR-87/10	2,09E+10	3,00 %	3,51 %
HFR Eu1bis	6,48E+10	9,34 %	-
HFR Eu1bis	7,68E+10	11,07 %	-
HFR Eu1bis	7,69E+10	11,07 %	-
HFR Eu1bis	6,73E+10	9.70 %	-

To check on the gamma spectrometric burn-up determination, on two fuel elements a radiochemical method based on the isotope Nd-148 was applied. For this purpose, a sample was taken and pulverized together with the embedded particles. Otherwise, it would be possible to determine an incorrect burn-up since the free uranium concentration of the matrix has a variable enrichment. The powder was then dissolved in nitric acid and several dilutions of the solution prepared. The latter were measured with different mass spectrometric process and the heavy metal vectors and the quantity of Nd-148 contained determined [Freis et al. 2006]. Nd-148 is stable and forms in the reactor chiefly by fission. Capture reactions leading to the decay of Nd-148 play no part because of the small cross section of capture. However, additional Nd-148 is formed by neutron capture (n,g) in short-lived Nd-147. This effect plays a part that is increasingly greater, the higher the neutron flux, and with it, the Nd-147 equilibrium in the reactor is. It is generally accounted for by a tabulated correction factor (K). The entire method is documented in the ASTM E 321-96 standard. The burn-up is ultimately obtained from:

$$BU = \frac{K \cdot \frac{N_{Nd-148}}{\gamma_{Nd-148}}}{\sum N_{Pk} + \sum N_U + K \cdot \frac{N_{Nd-148}}{\gamma_{Nd-148}}}$$

Equation 11

The burn-up was determined once on a pulverized sample from HFR K6/3 after bakeout and on a sample of HFR Eu1bis 2. The entire fuel element HFR Eu1bis 2 was not transferred to Karlsruhe but remained in the Hot Cells of the NRG in Petten and was the subject of post-irradiation studies there [de Groot et al. 2008]. Therefore, the two methods could not be compared in this case, but the result of the chemical analysis fits without conflict into the measured burn-ups of the other HFR Eu1bis fuel elements.

Table 12: Nd-148 and Cs-137 burn-up determination

	HFR K6/3	HFR Eu1bis 2
γ-Spectrometry (Cs-137)	9.80 %	-
Chemical Analysis (Nd-148)	10.01 % ± 0.16 %	10.92 % ± 0.163 %

6. Results of the experimental work

6.1 AVR 73/21

AVR 73/21 was the first fuel element baked out in the Karlsruhe CoFA II. This test was intended to demonstrate on a fuel element the functional capability of the CoFA II and its measuring devices under hot conditions. AVR 73/21 was irradiated in one reactor pass in the AVR reactor in Jülich over about 235 full load days (efpd) to a burn-up of about 2.5% FIMA.

Table 13: Irradiation data of the AVR 73/21 fuel element

Identification number	AVR 73/21	Burn-up: 2.5 %	FIMA
BE Type	GLE-3	Fast neutron fluence s (>0.1 MeV):	$0,4 \cdot 10^{25} \text{ m}^{-2}$
End of irradiation: February	1984	Irradiation temperature	~ 820 °C*
Irradiation time:	235 efpd		

*estimated average temperature for AVR pass

The fuel element was heated in two phases for 5 hours at 1600°C and subsequently at 1800°C. Between the heating phases a controlled cool-down to 300°C was performed (see Fig. 18).

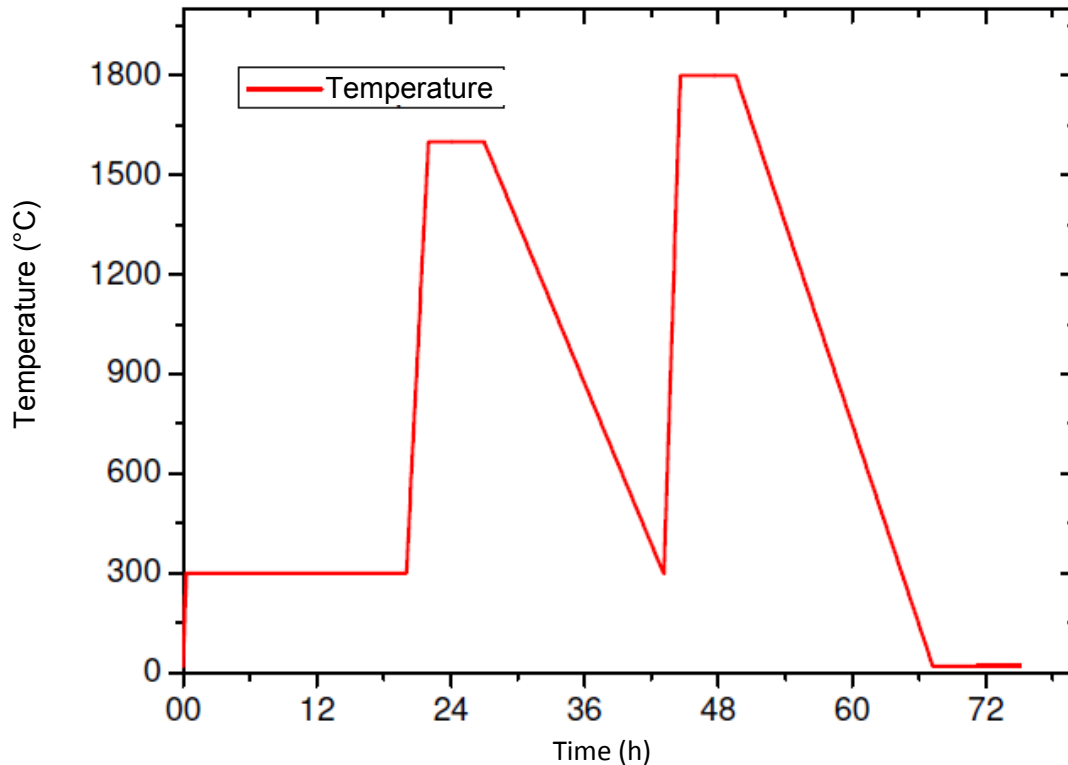


Figure 18: Temperature curve of AVR 73/21 bakeout experiment

Due to the low burn-up and the short heating time, no particle failure and no noteworthy fission product release from particles were anticipated. The fuel elements with BISO particles used in the first years in the AVR retained fission products relatively poorly. Therefore, the reactor core of the AVR displayed a relatively high fission product release. These fission product were deposited on the surfaces of the other spherical fuel elements and then diffusion from the outside into the graphite matrix. Accordingly, a certain release of Cs-137 and Sr-90 from the matrix could be expected for AVR 73/21 [Schenk et al. 1988].

The release of Kr-85 during the experiment was below the detection limit of the measuring device. To be certain, Cs-137 activities could be measured on the condensate plates used, but the evaluation of the isotope ratios of Cs-134 to Cs-137 showed that there must have been additional contamination of the plates and aluminum containers in the cell. Therefore, the results could not be utilized. As a result, following this the procedure was changed and the condensate plates no longer directly touched by the contaminated cell manipulators. In addition, following every experiment, the plates were placed in new, uncontaminated containers.

The results are compared in Table 14.

Table 14: Summary of the results of the AVR 73/21 CoFA experiment

BE	heating temp.	heating time	FR Cs-137	FR Kr-85
AVR 73/21	1600 °C	5 h	-	< NWG
	1800 °C	5 h	-	< NWG

6.2 AVR 74/18

6.2.1 Data of the experiment

The AVR 74/189 fuel element of the GLE-3 type was irradiated in two passages during a total of about 480 days in the AVR reactor in Jülich. The end of the irradiation was in February 1985. Since the AVR was a pebble heap reactor, the times of passage of the individual fuel elements through the core are only approximately known. Therefore, no exact irradiation time can be reported. The burn-up was 4.8% FIMA and the fast neutron fluence was calculated as $0.8 \cdot 10^{25} \text{m}^{-2}$. The average irradiation temperature was estimated as 820°C. It is obtained from the change of the outside temperature of the fuel element during the passage through the reactor and the calculated power history (see Appendix IIIc).

Table 15: Irradiation data of the AVR 74/18 fuel element

Identification number	AVR 74/18	Burn-up:	4.8 % FIMA
BE Type:	GLE-3	Fast neutron fluence (>0.1 MeV):	$0.8 \cdot 10^{25} \text{m}^{-2}$
End of irradiation:	February 1985	Irradiation temperature:	~ 820 °C*
Irradiation time:	480 efpd		

*estimated average temperature for AVR passage

The inventory of the cesium isotopes Cs-137 and Cs-134 were determined gamma spectrometrically. The burn-up was calculated on the basis of the Cs-137 inventory. The activities of Kr-85 and Sr-90 were determined by calculation. Due to the long cool-down time, the activity of Cs-137 and Sr-90 dominated. The fission gas Kr-85 was present in a sufficient

amount to be detected in the case of a particle break during the bakeout. The short-lived isotopes Ag-110m, I-131, Ru-106 and Xe-133 were no longer present in quantities sufficient to permit their measurement.

Table 16: Fission product inventory of AVR 74/18 at beginning of experiment (17 Jan 2006)

Cs-137*:	$3.4 \cdot 10^{10}$ Bq	Sr-90**:	$2.89 \cdot 10^{10}$ Bq
Cs-134*:	$1.56 \cdot 10^7$ Bq	Ru-106**:	
Kr-85**:	$1.45 \cdot 10^9$ Bq	I-131**:	~ 0 Bq
Xe-133**:	~ 0 Bq	Ag-110m**:	~ 0 Bq

* measured, ** calculated

The fuel element was to be heated up in two phases of one hundred hours each, once to 1600°C and then to 1800°C. Between the heating phases it was to be cooled down briefly to 300°C. At the start of the experiment, it was heated for about 10 hours at 1000°C in order to adjust the reactor conditions. Then with a rate of temperature increase of 300°C/h, the first phase of the accident simulation up to 1600°C was started. The experiment was started on 17 January 2006. Since the irradiation data were far below the rated values, no noteworthy releases and no particle damage were anticipated in the first phase. However, releases of Cs-137 due to matrix contamination of the fuel element from the AVR were expected (see AVR 73/21). During the second phase, due to the clearly elevated bakeout temperature of 1800°C, an elevated release due to diffusion and additionally isolated particle failures were expected.

6.2.2 Measured fission product releases

With the start of the experiments, a slight release of fission gases of Kr-85 in the range of a $5 \cdot 10^{-6}$ release portion (FR) could be measured. The latter rose slightly toward the end of the experiment at 1800° to about $6 \cdot 10^{-6}$ FR. The release of Cs-137 followed a typical curve, as is to be expected in the case of release by diffusion, and rose in the first 100 hours at 1600°C to about $6 \cdot 10^{-6}$ FR. There was no intensified release in the second phase at 1800°C. Only a slight increase to about $8 \cdot 10^{-6}$ FR could be measured. A release of Cs-134 could not be measured reliably due to the long subsidence time of the fuel element.

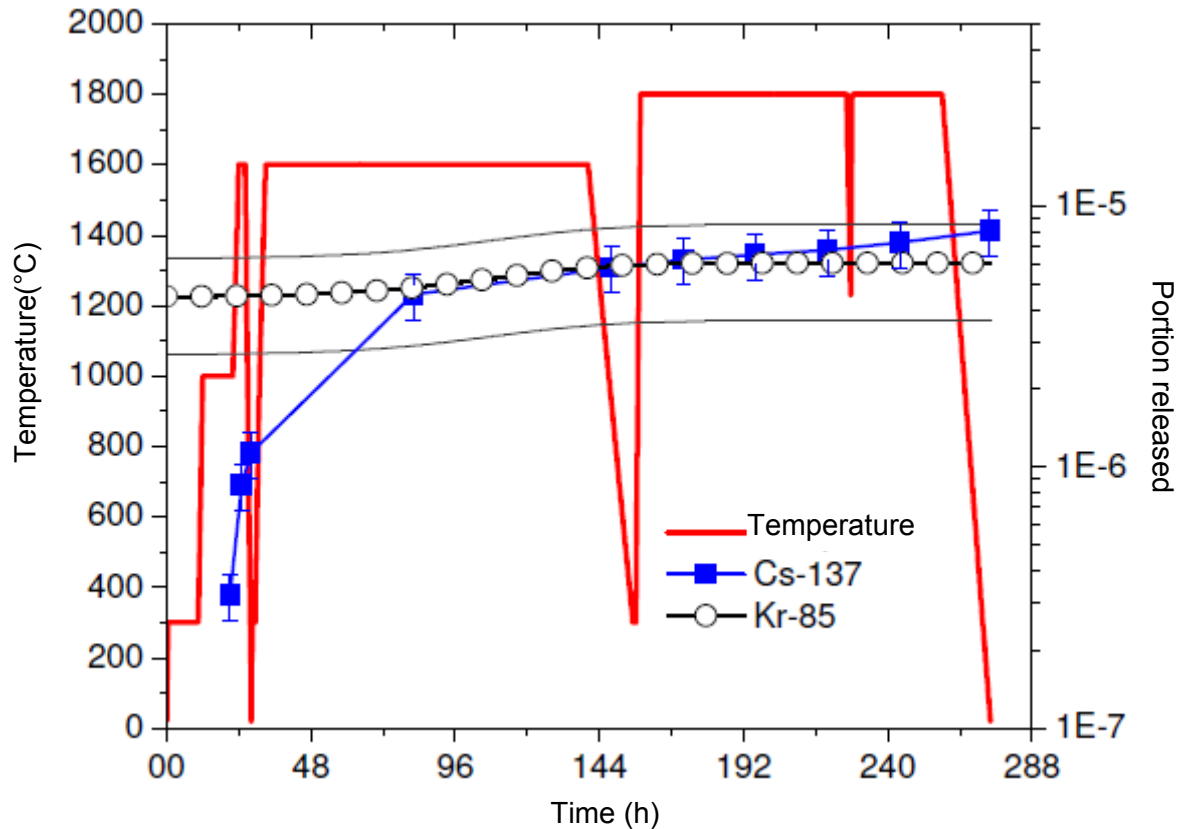


Figure 19: Temperature curve and fission product release of AVR 74/18 bakeout experiment

6.2.3 Summary

During the AVR 74/18 heating test no particle failure could be confirmed. No sudden or intensified gas releases were observed. Only a slight release in the range of $6 \cdot 10^{-6}$ FR could be measured, presumably coming from the graphite matrix. Since the graphite matrix has a low portion of free uranium contamination, fissions take place there during the irradiation. The fission gas produced diffuses when heated out of the graphite grains into the open porosity and can then quickly escape along the grain boundaries. Cesium is probably released through diffusion from the contaminated matrix graphite and through the particle jacket coatings. By and large, the release remains below $1 \cdot 10^{-5}$ FR despite the high temperature of 1800°C . It is surprising that at the elevated temperature in the second phase no qualitatively different release is observed but only a weak continuation of the trend at 1600°C . In the case of the AVR fuel element in question here, one would also expected a stronger initial release from the AVR due to the matrix contamination. The interposed cooling also appears to have had no effect on the integrity of the particles.

Table 17: Summary of the results of the AVR 74/18 CoFA experiment

	Heating temp.	Heating time	FR Cs-137	FR Kr-85
AVR 74/18	1000 °C	10 h	$3,2 \cdot 10^{-7}$	$4,5 \cdot 10^{-6}$
	1600 °C	100 h	$5,8 \cdot 10^{-6}$	$5,9 \cdot 10^{-6}$
	1800 °C	100 h	$8,1 \cdot 10^{-6}$	$6,1 \cdot 10^{-6}$

6.3 HFR K6/2

6.3.1 Data of the experiment

In the irradiation experiment HFR K6, four HTR fuel elements with modern LEU TRISO particles were irradiated under HTR module conditions in the high flow reactor (HFR) in Petten in the Netherlands. This involved the last HTR fuel produced by Nukem, which was produced especially for these tests (proof test fuel). During the irradiation, in 26 HFR cycles, a total of 17 pebble heap reactor passes were simulated up to a burn-up of about 8% to 10% FIMA. To simulate the multiple pass through pebble heap reactor, the central fuel temperature was set at 800°C for one third of the time and at 1000°C for the remaining two thirds. For this purpose, a proven gas mixing technique was employed in which an adjustable helium-neon mixture was passed into an intermediate space around the irradiation capsule containing the fuel elements. Due to the different heat conduction of the two gases, the fuel element temperature could be adjusted via the mixing ratio and the calculated thermal power due to fission and gamma heating in the fuel element.

The goal of the irradiation experiment was to test whether the fuel elements would withstand HTR module conditions without noteworthy fission product releases or particle damage. It was also intended to transport the fuel elements to Jülich after the irradiation and to study their accident behavior in the CoFA I. The irradiation experiment started on 21 June 1990 and ended after 633.6 full load days on 8 April 1993. During the irradiation the release of short-lived fission gases was measured and the release to formation ratio, the so-called release to birth rate (R/B), determined. The HFR K6/2 and K6/3 fuel elements were irradiated jointly in one capsule so that here only a common release value could be registered. The HFR K6/1 and K6/4 fuel element were irradiated in their own capsules respectively. During the test, several temperature

transients with a temperature elevated by 200 °C were simulated, such as were expected for the HTR module reactor during the outage of the main heat sink without pressure loss [Nabielek et al.1990], [Nabielek et al. 1993], [van der Merve & Venter 2008]

Table 18: Irradiation data for the HFR K6/2 fuel element

Identification number	HFR K6/2	Burn-up:	9.3 % FIMA
BE Type:	GLE-4 Proof	Fast neutron fluence (>0.1 MeV):	$4.6 \cdot 10^{25} \text{ m}^{-2}$
End of irradiation:	May 1993	R/B Kr-85m**:	$2,1 \cdot 10^{-7}$
Irradiation time:	634 efpd	R/B Kr-88**:	$2,1 \cdot 10^{-7}$
Irradiation temperature	~ 940 °C (1130 °C*)		

* Maximal temperature during the irradiation, ** at the end of irradiation at 1000°C

The HFR K6/2 fuel element was located in an intermediate irradiation position and achieved a burn-up of 9.3% FIMA. The inventory of the cesium isotopes Cs-137 and Cs-134 were determined gamma spectrometrically and the burn-up confirmed. The activities of Kr-85 and Sr-90 were determined by calculation. Due to the long cool-down time, the activity of Cs-137 and Sr-90 dominated. Kr-85 was sufficiently present to be detected in the case of a particle break. Ag-110m, I-131, Ru-106 and Xe-133 were no longer present in quantities sufficient to permit their measurement.

Table 19: Fission product inventory of HFR K6/2 at beginning of experiment (06 July 2008)

Cs-137*:	$7.81 \cdot 10^{10} \text{ Bq}$	Sr-90**:	$6.29 \cdot 10^{10} \text{ Bq}$
Cs-134*:	$1.47 \cdot 10^9 \text{ Bq}$	Ru-106**:	$5.9 \cdot 10^7 \text{ Bq}$
Kr-85**:	$4.29 \cdot 10^9 \text{ Bq}$	I-131**:	~ 0 Bq
Xe-133**:	~ 0 Bq	Ag-110m**:	~ 2400 Bq

* measured, ** calculated

The CoFA HFR K6/2 experiment was planned in two phases. The experiment started on 6 July 2006. After a roughly nine-hour operation simulation at 1050°C, the fuel element was baked out in a first phase for 100 hours at 1600°C in order to cover the HTR module scenario as it was

originally envisioned in the German research program. The temperature rise amounted to 46°C/h. In the second phase, the temperature was raised to 1800°C for 200 hours.

6.3.2 Measured fission product releases

During the first 240 hours of testing, the cumulative Kr-85 release from HFR K6/2 was below the detection limit of the measuring device. Only after this could a slight rise in activity up to a release portion (FR) of about $2 \cdot 10^{-7}$ be confirmed at 275 hours. By the end of the experiment, the release finally rose to about 10^{-5} FR.

The fission product Cs-137 that was solid at room temperature was released during the 1600°C phase up to about $4 \cdot 10^{-5}$ FR. The portion released then also did not increase substantially during the first 100 hours at 1800°C but rose distinctly during the last 100 hours by the end of the test to $2 \cdot 10^{-3}$ FR. A release of Cs-134 could not be measured reliably due to the age of the fuel element.

6.3.3 Special events - observations

During the first testing phase, the installation shut itself down automatically twice. At the time of the first shut-down, after 45 hours, the maximal temperature of the condensate plate surface had been exceeded. This phenomenon occurs if as a result of the sooting up of the graphite matrix a blackening of the plate surface appears and the emission coefficient increased as a result of this (see above). The plate was replaced and the program restarted. In the second shutdown after 90 hours a logic error in the programming was involved. No significant problems occurred subsequently.

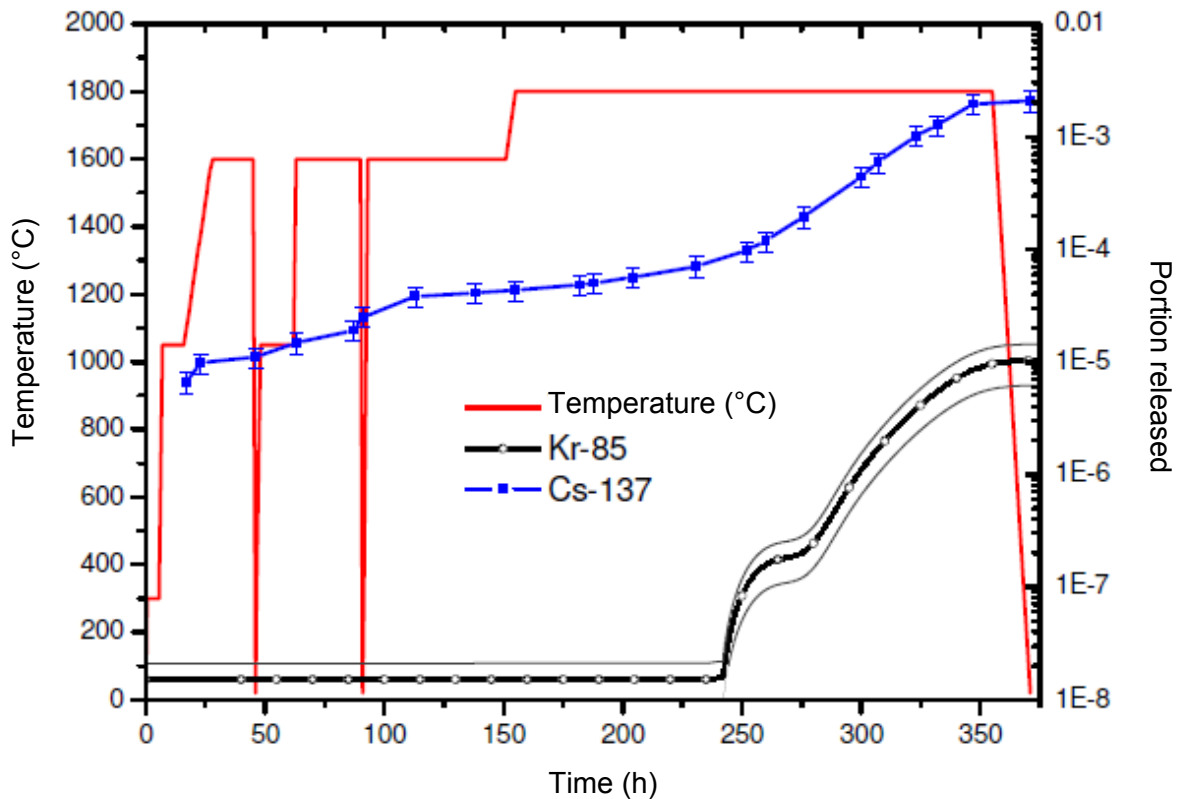


Figure 20: HFR K6/2 bakeout experiment -- Temperature curve and fission product release

6.3.4 Summary

During the HFR K6/2 heating experiment the fuel element was heated for a total of 300 hours at 1600°C and 1800°C. Releases of Cs-137 of up to $2.1 \cdot 10^{-3}$ FR and of Kr-85 up to $1 \cdot 10^{-5}$ FR were measured. Therefore, HFR K6/2 has display an outstanding retention capacity under extreme accident conditions. The low gas release indicates that at 1600°C no particles failed at all and after more than 100 hours at 1800° it lies at one or a few particles. It is possible that this is a partial failure of the SiC coating with subsequently delayed diffusion of the Kr-85 through the outer PyC coating.

After about 250 hours of testing time, a suddenly rising Kr-85 release could be measured, indicating an incipient particle failure. The form and duration of the release over more than one hundred hours points to an ongoing failure of several particles during the entire time frame. However, the release was too small on the whole. At the end of the heating test it corresponded to the inventory of less than one particle.

The cesium release by diffusion during the 1600°C phase moved within the range of the values in the literature, but during the 1800°C phase it was far below the values expected from the past. Cesium was released in noticeable quantities of up to $2.1 \cdot 10^{-3}$ FR only when the SiC coating began to fail at about 250 hours.

Table 20: Summary of the results of the HFR K6/2 CoFA experiment

	Heating temp.	Heating time	FR Cs-137	FR Kr-85
HFR K6/2	1050 °C	10.5 h	$6,6 \cdot 10^{-6}$	< NWG*
	1600 °C	100 h	$4,3 \cdot 10^{-5}$	< NWG*
	1800 °C	200 h	$2,1 \cdot 10^{-3}$	$1,03 \cdot 10^{-5}$

*Detection limit (NWG)

6.3.5 Additional studies on HFR K6/2

The fuel element was measured again by gamma spectrometry after the experiment. No change in the Cs-137 inventory could be confirmed within the scope of measurement accuracy of $\pm 5\%$. This was to be expected since the release measured on the condensate plates of $2.1 \cdot 10^{-3}$ FR was also below the measurement accuracy of the gamma spectrometric inventory measurement of the fuel element.

6.4 HFR K6/3

6.4.1 Data of the experiment

The HFR K6/3 fuel element was irradiated in the HFR K6 irradiation experiment in a test capsule shared with HFR K6/2. At that time it achieved a slightly higher burn-up than HFR K6/2 of 9.7% FIMA. The general data of the irradiation experiment are described in the section HFR K6/2. Since both fuel elements were in the sample capsule, only a common R/B value could be determined.

Table 21: Irradiation data for the HFR K6/3 fuel element

Identification number	HFR K6/3	Burn-up:	9.7 % FIMA
Type:	GLE-4 Proof	Fast neutron Fluence (>0.1 MeV):	4.8 • 10 ²⁵ m ⁻²
End of irradiation:	May 1993	R/B Kr-85m**:	2,1 • 10 ⁻⁷
Irradiation time:	634 efpd	R/B Kr-88**:	2.1 • 10 ⁻⁷
Irradiation temperature:	~ 940 °C (1140°C*)		

* Maximal temperature during the irradiation, ** at the end of irradiation at 1000°C

The inventory of the cesium isotopes Cs-137 and Cs-134 were determined gamma spectrometrically and the burn-up confirmed. The activities of Kr-85 and Sr-90 were determined by calculation. Due to the long cool-down time, the Cs-137 and Sr-90 activity dominated. Kr-85 was present sufficiently to be detected in the case of a particle break. Ag-110m, I-131, Ru-106 and Xe-133 were no longer present in quantities sufficient to be measured.

Table 22: Fission product inventory of HFR K6/3 at start of experiment (15 Feb. 2008)

Cs-137*:	7.92 • 10 ¹⁰ Bq	Sr-90**:	6.57 • 10 ¹⁰ Bq
Cs-134*:	1.54 • 10 ⁹ Bq	Ru-106**:	6.15 • 10 ⁷ Bq
Kr-85**:	4.32 • 10 ⁹ Bq	I-131**:	~ 0 Bq
Xe-133**:	~ 0 Bq	Ag-110m**:	~ 2500 Bq

* measured, ** calculated

The HFR K6/3 CoFA test was conducted in a total of four phases. The experiment started on 15 Feb 2006. After a roughly 14-hour operation simulation at 1050°C, the fuel element was heated in a first phase in the same manner as for the HFR K6/2 for 100 hours at 1600°C. In the second phase, the temperature was raised to 1700°C for another 100 hours and then raised once more to 1800°C for 100 hours. In the fourth phase, further heating was applied at 1800°C for 300 hours. Between the heating phases, the fuel element was cooled down to room temperature each time.

6.4.2 Measured fission product releases

During the first 100-hour experimental phase at 1600°C, a slight release of Kr-85 of 5.2•10⁻⁶ could be detected, which did not increase substantially in the two subsequent 100-hour heating

phases at 1700°C ($6.2 \cdot 10^{-6}$ FR) and 1800°C ($8.1 \cdot 10^{-4}$ FR). Only during the fourth 300-hour heating phase involving a relatively rapid heating to 1800° was there a strong release of up to $5.49 \cdot 10^{-4}$ FR at the end of the experiment. The Cs-137 release was extremely low during the 1600°C phase and 1700°C phase with $5.5 \cdot 10^{-7}$ FR and $2 \cdot 10^{-6}$ FR. It then increased noticeably during the third phase at 1800°C to $9.3 \cdot 10^{-4}$ FR. In the last heating phase, finally there was a massive Cs-137 release of up to $4.3 \cdot 10^{-2}$ FR. The parallel course of the Kr-85 and Cs-137 release curves during the fourth heating phase is striking. While the path of the Cs-137 curve appears to be a continuation of the curve from the third phase and therefore indicates intensified cesium release by diffusion, the path of the Kr-85 curve appears qualitatively to differ from the previous curve and to indicate incipient coating failure.

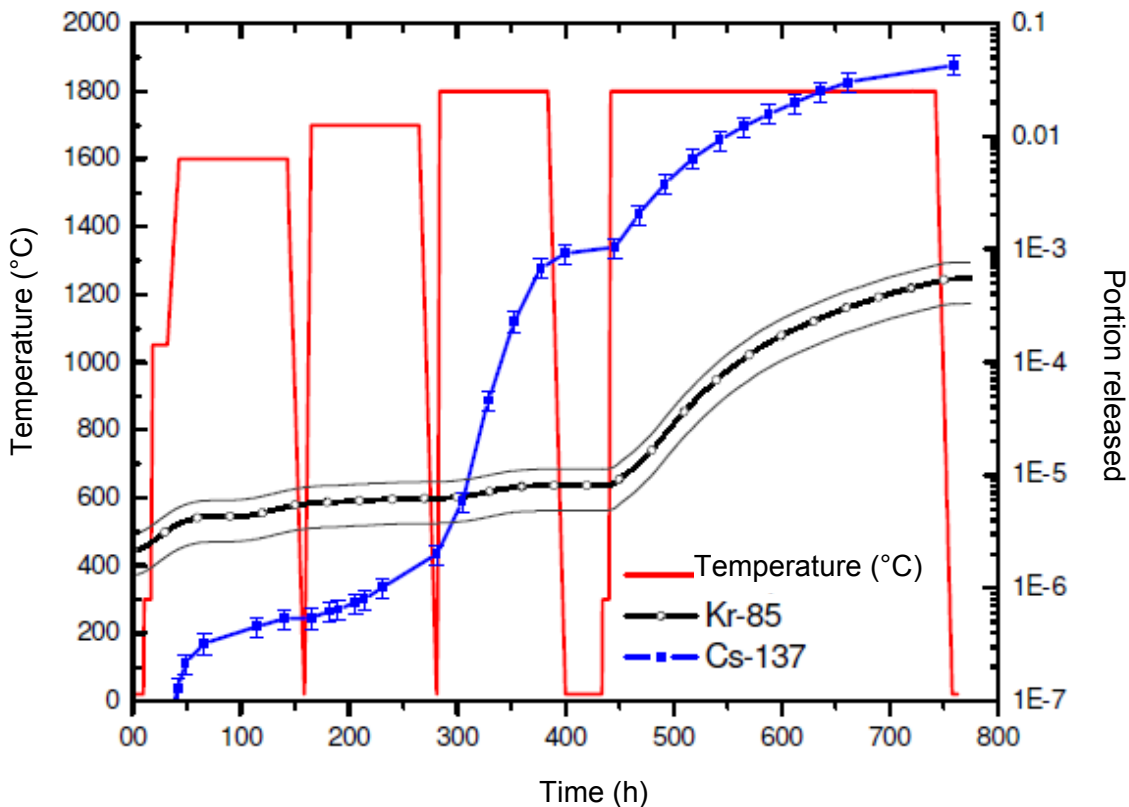


Figure 21: HFR K6/3 bakeout experiment -- Temperature curve and fission product release

6.4.3 Ceramographic studies and micro-hardness measurement

Following the bakeout test, the HFR K6/3 fuel element was studied further. For this purpose a cylinder with a 10 mm diameter was drilled out with a hollow drill and segmented (Fig. 22). Two

of the segments were embedded in a sample holder with epoxy resin and carefully polished. The samples were then studied under a light microscope.

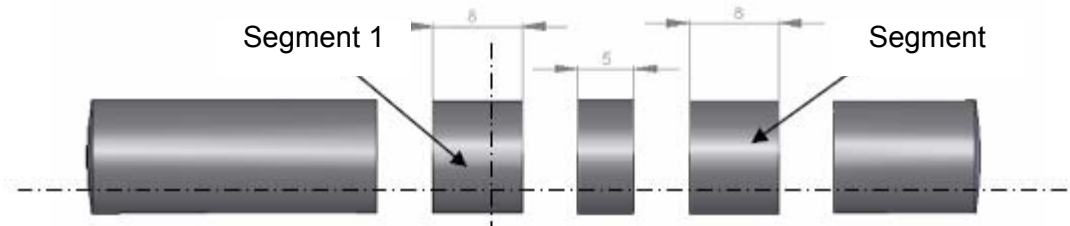


Figure 22: Segmentation plan for the cylinder from HFR K6/3

Figures 23 and 24 show polished sections of two particles from HFR K6/3 after the heating experiment. Particle A from segment 1 (Fig. 23) was cut above the equatorial plane while particle B from segment 2 (Fig. 24) was cut approximately in the center. In both cases the UO_2 core displays a high porosity. The buffer layer appears in both cases to have been detached not only from the core but also from the surrounding IPyC coating. A gap is clearly visible here especially for particle B.

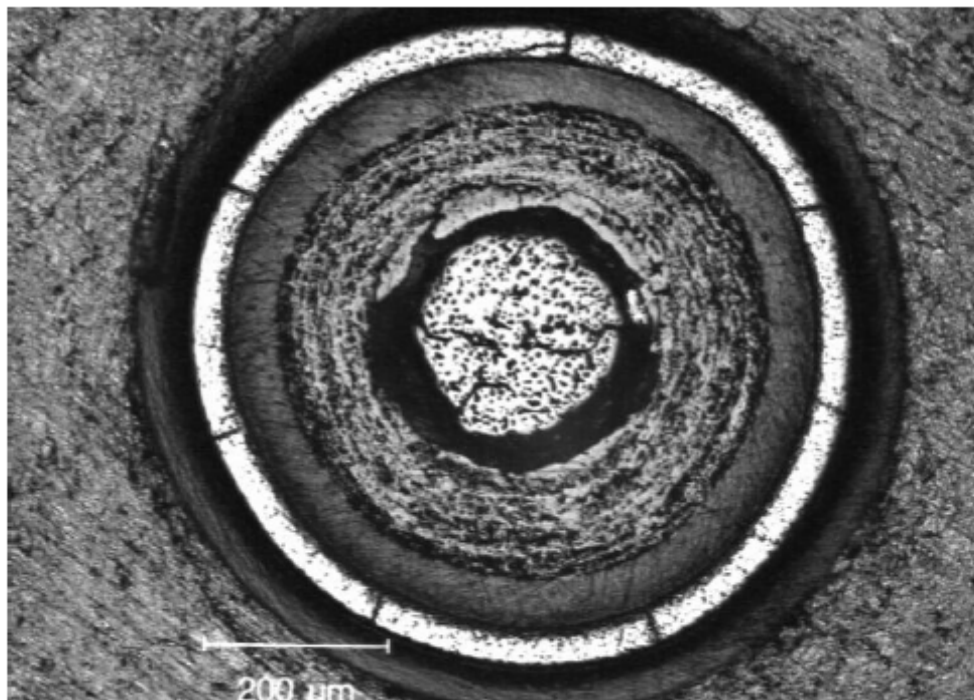


Figure 23: Polished section of HFR K6/3, particle A (after 400 h at 1800°C)

The IPyC coatings appear to be basically intact, but a partial detachment of the SiC coating can be seen (debonding). The SiC coatings display strong signs of incipient fission product corrosion. The cracks running in the radial direction in the SiC coating of particle A indicate mechanical failure due to tangential stresses (pressurized container failure). In particle B apparently there are no cracks in the radial direction. Instead, the SiC coating appears to be cracked in the tangential direction, which indicates high tensile stresses in the radial direction and would be in agreement with the observed partial detachment of the PyC coatings. A total of four particles were studied ceramographically. Two of these particles displayed cracks in the radial direction as in particle A.

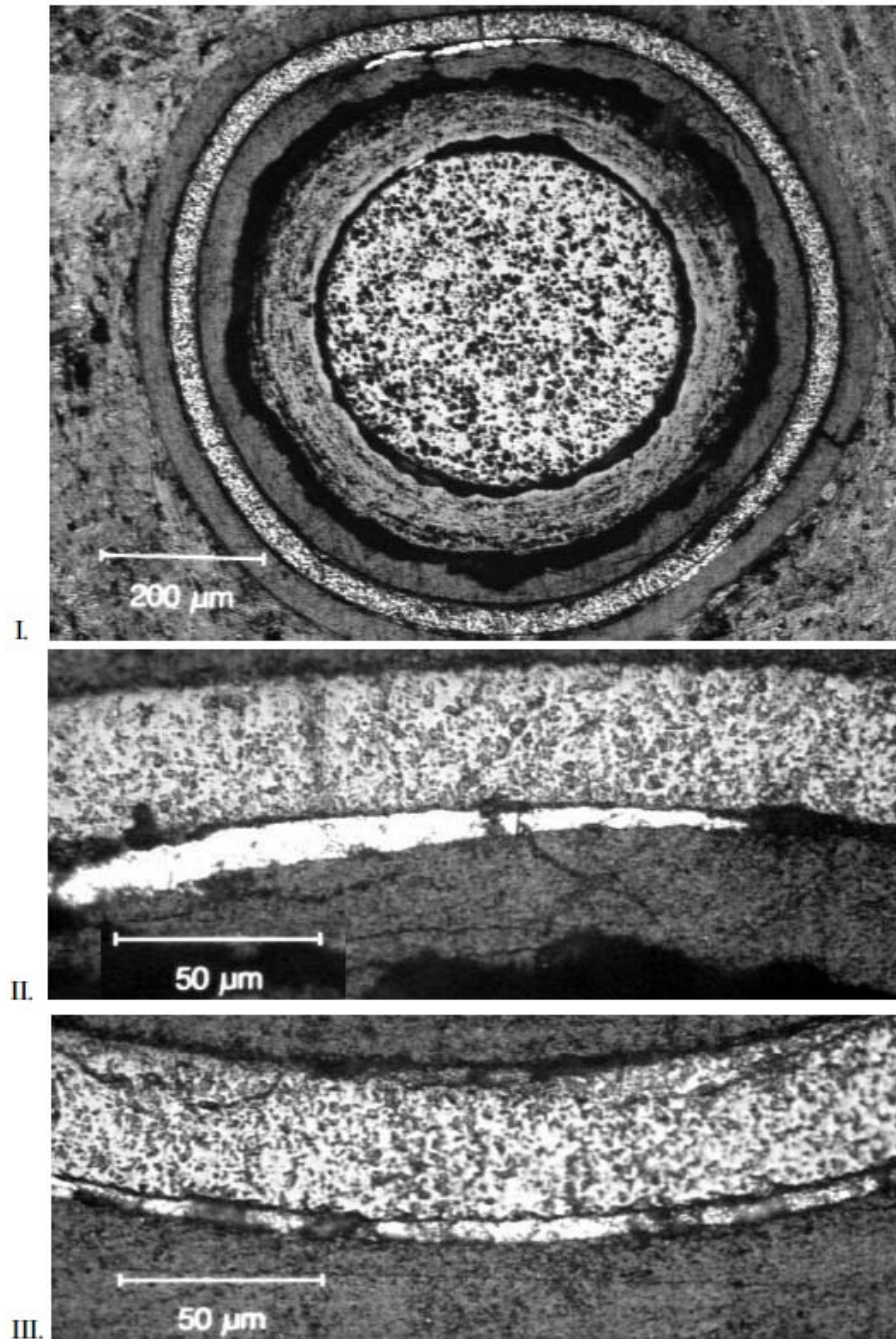


Figure 24: Polished sections of HFR K6/3, particle B (after 400h h at 1800°C)

Besides the ceramographic studies, Vickers micro-hardness tests were also performed on the SiC and PyC coatings (Fig. 25). For this purpose, a polished particle was tested in eight positions with a diamond micro-indenter. The hardness was then determined from the average diameter of the cross-shaped indentations.

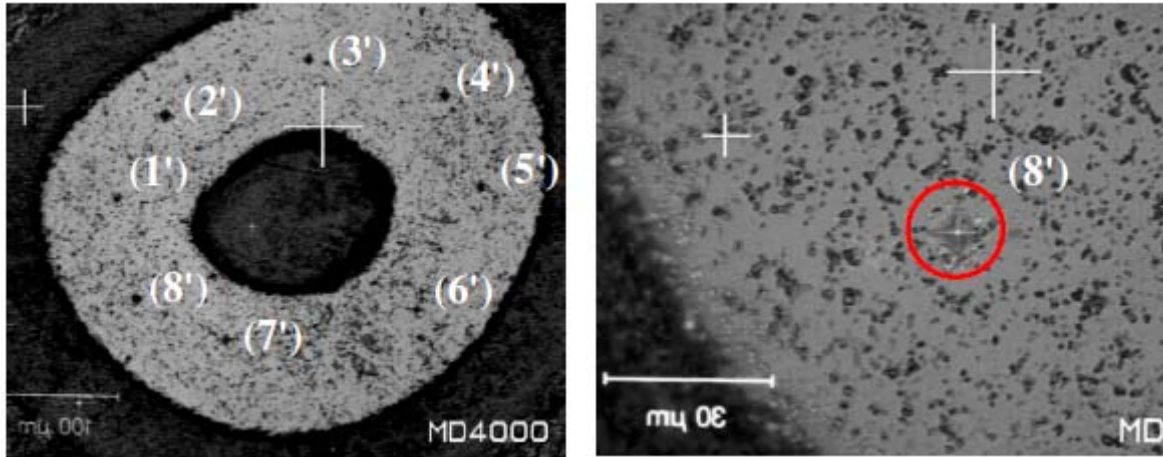


Figure 25: Vickers micro-hardness test, sample with test indentations

The Vickers hardness is calculated from

$$HV = 189031,6 \cdot \frac{F}{d^2}$$

Equation 12

In this case “F” denotes the applied force in newtons and “d” the average diameter of the indentation in micrometers. Table 23 shows the measured indentation diameter and applied loads as well as the corresponding Vickers hardnesses.

Table 23: Micro-hardness test on HFR K6/3

Position	d1 (µm)	d2 (µm)	(d1+d2)/2	d2 (µm)	F (N)	Hardness (HV)
(1')	7,44	7,00	7,22	51,12	0,981	3627
(2')	10,98	11,00	10,99	120,78	1,4715	2303
(3')	9,7	8,7	9,2	84,64	1,4715	3286
(4')	12	11	11,5	132,25	1,4715	2103
(5')	11,16	11,68	11,42	130,41	1,4715	2133
(6')	11	10	10,5	110,25	1,4715	2523
(7')	8,3	8,6	8,45	71,40	1,4715	3896
(8')	11	11,3	11,15	124,32	1,4715	2237
					Average	2764

The measured hardness deviates from the real hardness in an instrument-specific manner. Accordingly, the device must be calibrated with reference samples of known hardness and a correction correlation determined. The real hardness of the SiC coating in this case is found as:

$$HV_{\text{real}} = 0,9943 \cdot HV_{\text{measured}} - 18.603 = \mathbf{2729 \text{ HV}}$$

This value is in good agreement with the values in the literature for β -SiC of ~2600 HV. It may therefore be assumed that the microstructure of the material was still essentially intact/undamaged. The hardness of the OPyC coating was also determined. It was found as 150.82 HV.

6.4.4 Electron microscopy and EDX studies

Following the ceramographic studies, the prepared segments of HFR K6/3 were polished once more and studied in a shielded scanning electron microscope. As a result of the repeated polishing process, this time other particles than those in the ceramographic studies can be analyzed. A total of 6 particles could be studied by electron microscopy. Of these, 4 particles in the SiC coating displayed cracks in the radial direction, indicating pressure vessel failure. On the whole, the electron-microscopic images revealed a significantly better image quality in terms of resolution and accuracy of depth so that many details could be recognized that were previously unclear in the light microscope.

In turn it is clearly apparent that the SiC coating displays cracks in the radial direction, said cracks usually being propagated in the PyC coatings. This may possibly indicate a first failure of a PyC coating with a subsequent stress peak in the SiC coating and a resulting failure of the SiC coating. In Figure 27 II and III it is also clearly evident that the IPyC and the OPyC coatings have separated from the SiC coating. The microstructure of the SiC, conversely, appears to have remained largely intact.

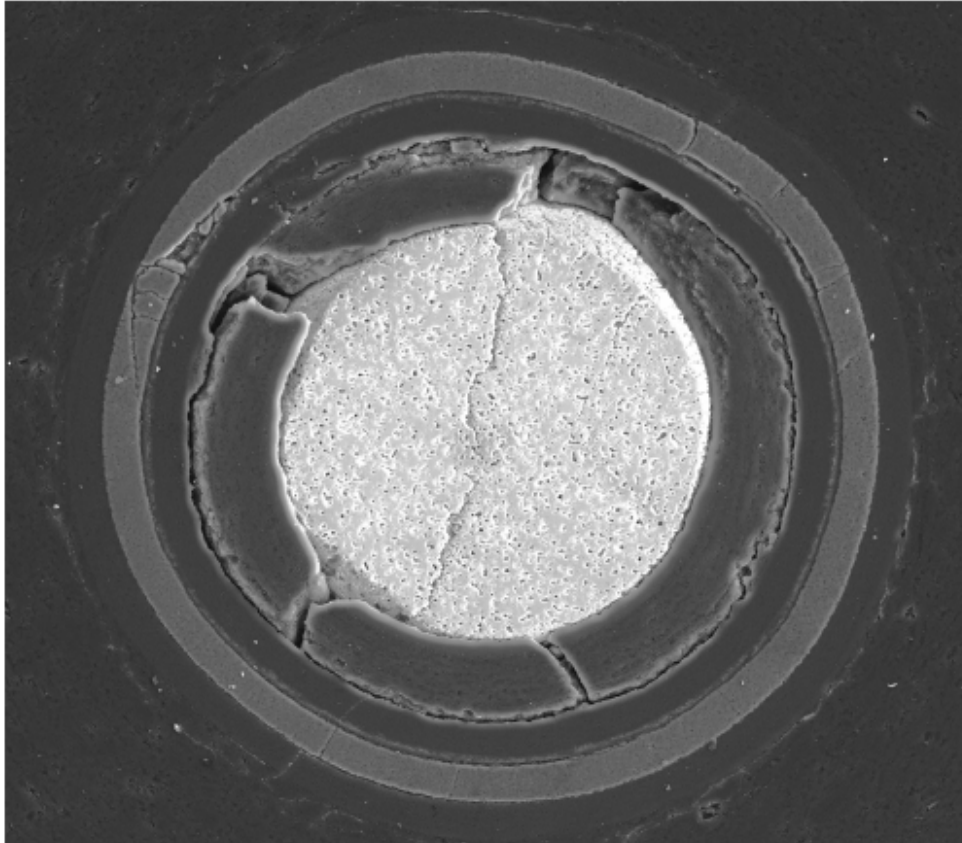


Figure 26: Polished section under the scanning electron microscope of HFR K6/3, particle C

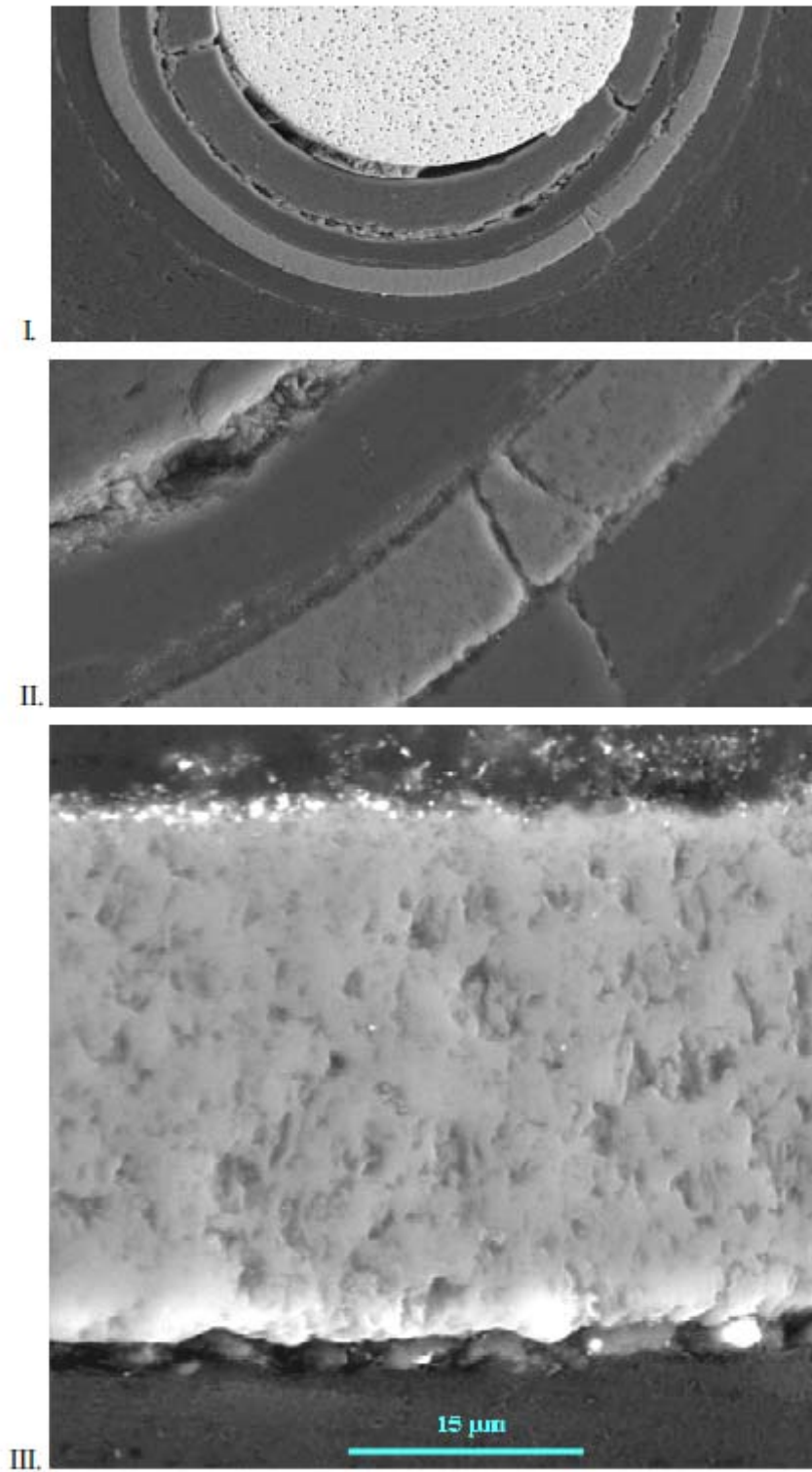


Figure 27: Polished sections under the scanning electron microscope of HFR K6/3, particle D

6.4.5 Determination of the SiC layer thickness

A possible failure mechanism of coated particles is described in the literature [Verfondern and Nabelek 1990] as thinning of the SiC coating due to corrosion or thermal decomposition. In order to make a statement regarding the degree of thinning of the SiC coatings, the polished sections of the particles of HFR K6/3 were systematically evaluated. For this purpose, first the height of the section plane (H) above the equatorial plane of the particle was determined. This is found as the mean value from several radii (R_g) observed on the image and the known nominal radii (R) of the particle or the core (see Table 4) according to equation 13 (see also Fig. 26).

$$H = \frac{\sum_i \sqrt{(R_i^2 - R_{g_i}^2)}}{i}$$

Equation 13

To determine the section height of the particles from HFR K6/3, for each particle four core and four particle radii (R_g) were determined using an image analysis program.

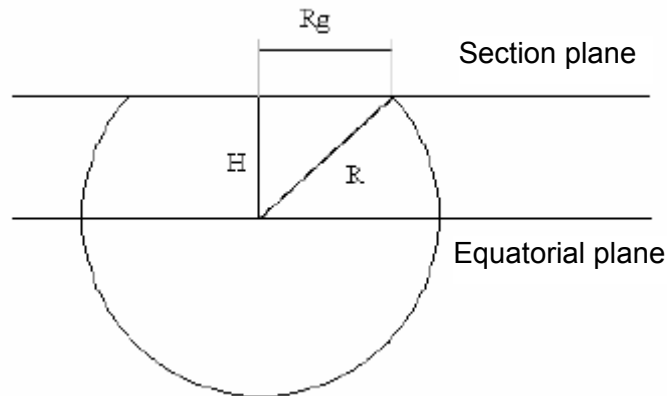


Figure 28: Determination of the section height of a studied particle

Following this, using the same method, the outer ($R_{au\beta en}$) and inner (R_{innen}) of the SiC coating were determined and an average thickness (D_{SiC}) calculated from four measurements in each case.

$$R_{au\beta en} = \sqrt{R_{g, au\beta en}^2 + H^2}$$

Equation 14

$$R_{g,innen} = \sqrt{R_{g,innen}^2 + H^2}$$

Equation 15

$$D_{SiC} = \frac{\sum_i (R_{g,au\beta en,i} - R_{g,innen,i})}{i}$$

Equation 16

$R_{g,au\beta en}$ and $R_{g,innen}$ stand for the outer and inner radii observed in each case. The results of the thickness determinations of the SiC coatings are summarized in Table 24. The nominal thickness of the SiC coatings according to the manufacturer's data was 36 μm ($\pm 2.4 \mu\text{m}$), the observed thickness after the bakeout experiment was 38.1 μm . Apparently there was no noteworthy thinning out of the SiC coating. For the later simulation this failure mechanism was therefore not considered (see below).

Table 24: Average film thickness of the SiC coating

Particle	Section height (μm)	Thickness of the SiC coating (μm)
1A	12.8 \pm 2	36.4 \pm 0.9
1C	48.1 \pm 2	38.5 \pm 0.9
2A	127.1 \pm 2	38.2 \pm 0.9
2B	133.4 \pm 2	41.2 \pm 0.9
2C	143.3 \pm 2	38 \pm 0.9
2D	175.1 \pm 2	36.3 \pm 0.9
Average:		- 38.1 \pm 0.5

Besides the electron microphotographs, on one particle of HFR K6/3 measurements were made with electron-dispersive x-ray spectroscopy (EDX) (see Fig. 29). The process uses the x-radiation characteristic for each element that is emitted upon electron bombardment [de Groot 2008].

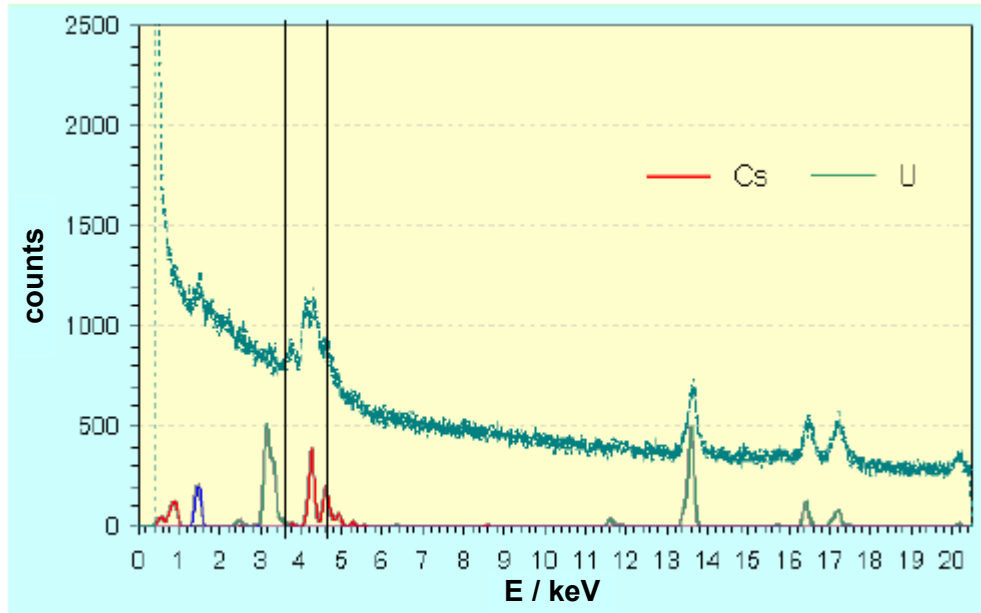


Figure 29: EDX spectrum in the buffer layer of HFR K6/3 particle E (measurement time =1457 s)

A particle with locally intact jacket coatings was selected for the measurement. This was intended to register the fission product distribution caused by the cleanest possible diffusion. Unfortunately, the resolution of the process was not high enough to measure evaluable fission product profiles quantitatively. It was possible only for cesium to plot an at least qualitative profile in the particle jacket coatings (see Table 25). The micro-probe of the Institute, which would have been a better suited instrument, was still under construction at the time of the measurements and therefore not available for this project.

The qualitative cesium profile shows that the SiC coating had apparently retained its barrier function, and the greater part of the cesium inventory had been retained inside the intact particle. Besides cesium, in the IPyC coating at the transition to the SiC coating, a distinct accumulation of palladium could be demonstrated. This observation is in good agreement with earlier investigations [Schen & Nabelek 1989]. Palladium is regarded as one of the elements chiefly responsible for the chemical decomposition of the SiC coating at high temperatures. Since the yield of fission products from palladium for Pu-239 is about ten times higher than for U-235, it plays an especially important part in the case of a little-enriched fuel with high burn-ups, as is present here,

Table 25: Cesium concentration profile

Coating:	Measurement time (s):	Measured impulses (s):	Relative cesium concentration:
Core	-	-	-
Buffer PyC	1457	~ 500	100 %
IPyC	5578	~ 300	16 %
SiC	3485	~ 0	0 %
OPyC	3109	~ 0	0 %

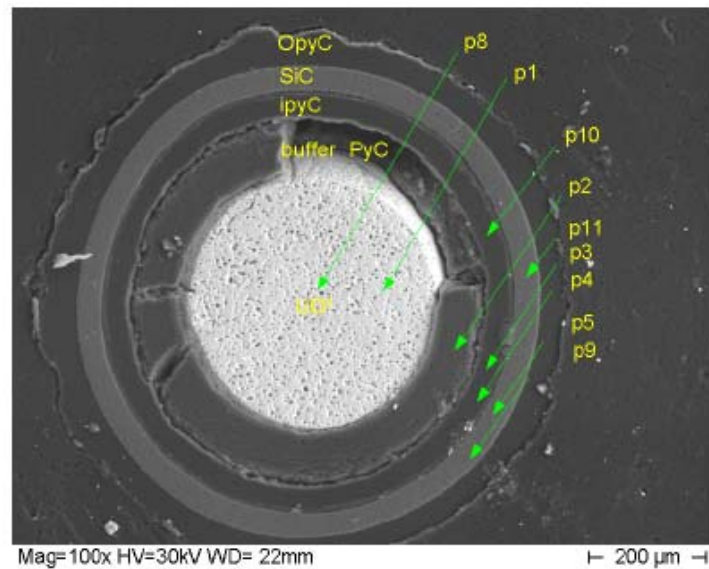


Figure 30: Particle E from HFR K6/3 with EDX measurement positions (100x magnification)

6.4.6 Summary

During the HFR K6/3 CoFA heating experiments the fuel element studied was heated in each case for 100 hours at 1600°C, 1700°C and 1800°C. Between the heating phases, the fuel element was cooled down to room temperature. Following the third phase at 1800°C another heating was conducted for 300 hours at 1800°C. In Table 26, the measured cumulative releases at the end of each heating phase are summarized. The low Kr-85 release indicates that no particle defects occurred in the first three heating phases and that intensified failure of the SiC coating occurred only in the last heating phase at 1800°C. The measured release corresponds to the inventory of about 8 particles. If it is assumed that about 50% of the Kr-85 inventory is released from defective particles, one would have a number of about 20 defective particles. This

is in contrast with the results of the ceramographic and electron-microscopic studies in which of a total of 10 particles, 6 defective particles with signs of pressure vessel failure were found. However, it cannot be excluded that the observed cracks and breaks are traceable to the preparation of the samples.

The amount of Cs-137 released during the first heating phase up to 1700°C was extremely small at $2 \cdot 10^{-6}$. Apparently the barrier layers have fulfilled their retention function. The amount of Cs-137 released only rose to $4.3 \cdot 10^{-2}$ only at 1800°C. The shape of the release curve indicates that the Cs-137 release involved primarily the release by diffusion through intact particle coatings.

The post-irradiation studies SEM, EDX, hardness measurement, and determination of the average SiC coating thickness conducted following the heating tests showed that although about 50% of the particles studied had cracks in the SiC coating, the microstructure and material properties of the SiC coating nevertheless remained largely intact.

The HFR K6/3 fuel element, on the whole, displayed outstanding behavior under extreme conditions. Both at 1600 and at 1700°C and even during the first 100 hours at 1800°C no noteworthy releases occurred. Only Cs release by diffusion from intact particles and release from the matrix graphic could be measured. Under certain conditions, the alternating heating and cooling of the fuel element caused weak points in the jacket coatings that ultimately contributed to the incipient failure finally in the fourth phase. This will have to be clarified by further studies if necessary. If the results should prove to be reproducible in the future, the upper limit for acceptable accident temperatures for inherently safe HTR may have to be set higher than was previously assumed under some conditions.

Table 26: Summary of the results of the AVR K6/3 CoFA experiment

	Heating temp.	Heating time	FR Cs-137	FR Kr-85
HFR K6/3	1050 °C	13.5 h	$1.3 \cdot 10^{-7}$	$3.2 \cdot 10^{-6}$
	1600 °C	100 h	$5.5 \cdot 10^{-7}$	$5.2 \cdot 10^{-6}$
	1700 °C	100 h	$2.0 \cdot 10^{-6}$	$6.2 \cdot 10^{-6}$
	1800 °C	100 h	$9.3 \cdot 10^{-4}$	$8.1 \cdot 10^{-6}$
	1800 °C	300 h	$4.3 \cdot 10^{-2}$	$5.5 \cdot 10^{-4}$

6.5 HFR Eu1bis 1

6.5.1 Data of the experiment

In the HFR Eu1bis irradiation experiment, five HTR fuel elements of the GLE-4.2 type were irradiated in ten cycles for a total of 249 full-load days in the Petten HFR in the Netherlands. The purpose of the experiment was to test the fuel element behavior under VHTR conditions at elevated temperature and also in the case of elevated and accelerated burn-up and elevated fast neutron fluence [Fütterer et al. 2008]. The central fuel element temperature was set during the burn-up cycles at 1250°C (see HFR K6). The target burn-up was estimated at about 15.4% FIMA, but in the most highly burnt-up fuel element only about 11.04% FIMA was reached. The acceleration factor was supposed to be about 7.5 and finally amounted to about 5.4 in the most highly burnt-up element.

During the irradiation, due to an operator error in the gas mixing system for adjusting the temperature, there was a brief temperature rise [Fütterer et al. 2006]. All five fuel elements were located together in a test capsule. During the irradiation experiment, gas samples were collected about once weekly and subsequently measured by gamma spectrometry in order to measure the fission gas release and detect any broken particles. Following the irradiation, four of the five fuel elements were transferred to the Institute for Transuranium Elements (ITU) in order to be studied further there in the Hot Cells and to perform CoFA accident simulations. One fuel element (HFR Eu1bis 2) remained in Petten and was studied there in the Hot Cells of the Nuclear Research and Consultancy Group (NRG) [de Groot et al. 2008].

The HFR Eu1bis 1 fuel element was placed in an upper irradiation position and therefore displayed a lower burn-up of 9.34% FIMA and a lower fast neutron fluence of $3.02 \cdot 10^{25} \text{ m}^{-2}$ than the fuel elements irradiated in the more central positions.

Table 27: Irradiation data for the HFR Eu1bis 1 fuel element

Identification number	HFR Eu1bis 1	Burn-up: 9.34 % FIMA	
Type:	GLE-4.2	Fast neutron fluence (> 0.1 MeV):	$3.02 \cdot 10^{25} \text{ m}^{-2}$
End of irradiation:	October 2005	Irradiation temperature	~ 1250 °C
Irradiation time:	249 efpd		
Fission gas release at end of irradiation			
		R/B Kr-85m:	$3.8 \cdot 10^{-6}$
R/B Xe-135:	$3.6 \cdot 10^{-6}$	R/B Kr-87:	$2.8 \cdot 10^{-6}$
R/B Xe-133:	$8 \cdot 10^{-6}$	R/B Kr-88:	$3.6 \cdot 10^{-6}$

The bakeout experiment of the HFR Eu1bis 1 fuel element started on 28 Mar 2008. Due to the short cool-down time, the possibility existed of measuring, besides the relatively long-lived cesium isotopes, also the release of Ag-110m. Although Ag-110m is not especially accident-relevant, nevertheless because of its high volatility it is of very great interest for reactor operation at elevated operating temperatures. It is considered the main source of the radioactive contamination of the primary cycle and therefore of the radiation burden on the personnel engaged in maintenance and inspection work. This is especially important for future HTR variants with direct circulation and gas turbines. Therefore, an especially long phase of operation simulation at 1250°C of 200 hours was suggested. This was intended to obtain a realistic assessment of the equilibrium release of Ag-110m in operation. In addition, in this way information could be obtained on the cesium contamination of the graphite matrix and therefore of possible particle failure during irradiation. Following the operation simulation, the accident simulation was carried out up to 1600°C with the standard heating rate of 47°C/h. The 1600°C accident simulation was terminated after 200 hours, followed by another heating to 1700°C for 150 hours. Between the phases, the fuel element was cooled down each time to room temperature.

Table 28: Fission product inventory of HFR Eu1bis1 at beginning of experiment (28 Mar. 2008)

Cs-137*:	$6.13 \cdot 10^{10}$ Bq	Sr-90**:	$5.46 \cdot 10^{10}$ Bq
Cs-134*:	$2.81 \cdot 10^{10}$ Bq	Ru-106*:	$4.6 \cdot 10^{10}$ Bq
Kr-85**:	$6.48 \cdot 10^9$ Bq	I-131**:	~ 0 Bq
Xe-133**:	~ 0 Bq	Ag-110m*:	$2.79 \cdot 10^7$ Bq

* measured, ** calculated

6.5.2 Measured fission product releases

During the HFR Eu1bis 1 bakeout experiments, because of the low age of the fuel element, not only Cs-137 and Kr-85 but also releases of Cs-134, Ru-106 and Ag-110m could be measured. The Kr-85 equilibrium release during the 1250°C operation simulation phase amounted to $1.36 \cdot 10^{-6}$ FR, during the second phase at 1600°C a value of $1.01 \cdot 10^{-5}$ FR was measured, and in the third phase at 1700°C, the release rose to $2.36 \cdot 10^{-5}$ FR. This corresponds to 20% of the inventory of a particle.

During the first 200 hours of operation simulation at 1250°C, a distinct release of Cs-137 and Cs-134 of the order of about $7 \cdot 10^{-5}$ FR could already be confirmed. During the second phase, the accident simulation at 1600°C, the release of Cs rose to about $1.2 \cdot 10^{-3}$ FR. In the third phase at 1700°, the release of Cs surprisingly rose more weakly than expected so that at the end a cumulative release of $4.3 \cdot 10^{-3}$ FR was registered. The good agreement of the measured release amounts of Cs-137 and Cs-134 confirmed that activity from the fuel element was actually involved and that no contamination of the plates in the cell or during transportation had occurred. It was conjectured that the strong Cs release is traceably primarily to the high irradiation temperature, which caused an increased diffusion through the intact jacket coatings, especially the SiC coating, of the particles.

Ag-110m was already strongly released in the first phase up to $2.3 \cdot 10^{-3}$ FR. During the 1600°C phase this value rose to $7.2 \cdot 10^{-3}$ FR. The release from the third testing phase at 1700°C could not be measured reliably. Due to the high Cs-137 and Cs-134 releases in this phase, the condensate plates could not be sluiced out and the measurement had to be performed through a window of the glovebox of the Hot Cells. Because of the high background radiation, the

relatively low gamma activities of Ag-110m could no longer be detected. The cumulative detection limits and the corresponding uncertainty are plotted conservatively in the diagram.

Ru-106 releases could only be measured in the first phase up to $6.3 \cdot 10^{-7}$ FR. For phase two and three, in turn, the detection limits and uncertainty bars are plotted in the diagram.

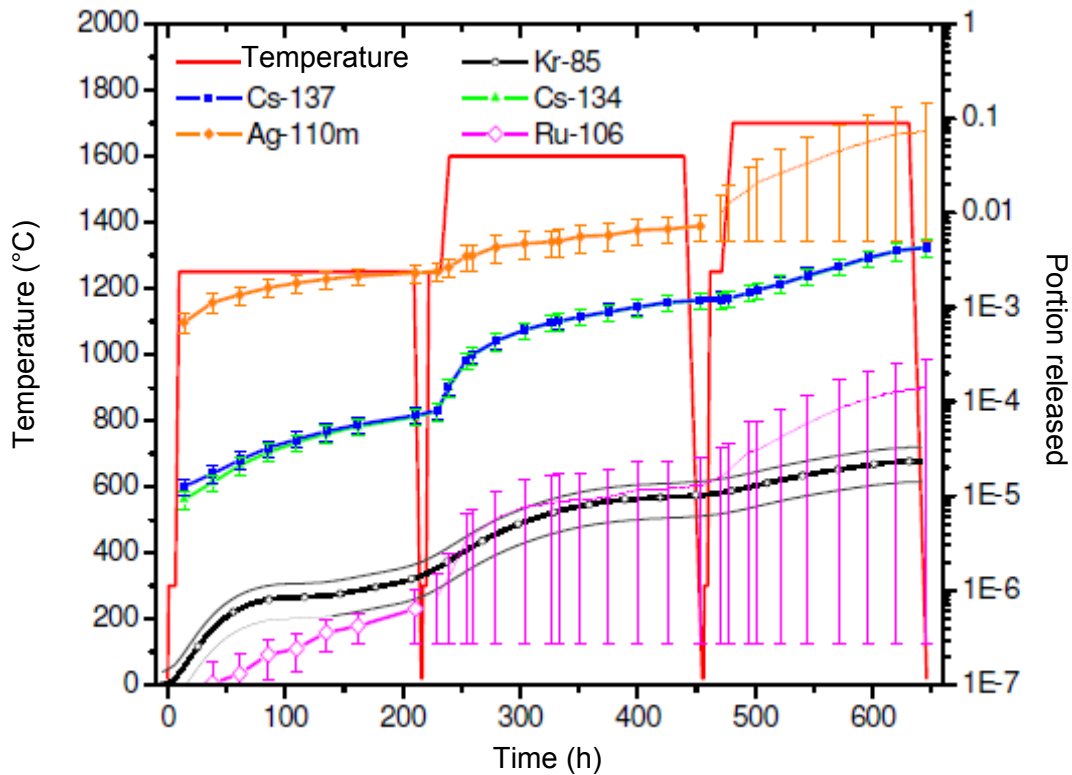


Figure 31: HFR Eu1bis 1 bakeout experiment -- Temperature curve and fission product release

6.5.3 Summary

The HFR Eu1bis 1 fuel element was baked out in three phases up to maximally 1700°C. In the first phase the irradiation temperature of 1250°C was set for 200 hours. This was then followed by a 200-hour accident simulation at 1600°C and finally a 150-hour accident simulation at 1700°C. Between the individual heating phases, the fuel element was cooled down to room temperature.

The generally low Kr-85 release indicates that no particles failed during the experiment. Only the anticipated release from the graphite matrix by free uranium contamination could be confirmed. The relatively high release of solid fission products is striking. This is primarily traceable to the high irradiation temperature, which led to intensified diffusion through intact particle coatings. Under some conditions, however, there was also contamination of the graphite matrix during the irradiation from the outside, possibly from failed particles in one of the other fuel elements irradiated in the HFR Eu1bis experiment.

The flattening release curve for Cs-137 and Cs-134 in the third phase did not correspond to the expectations after the second phase. The elevated temperature in the second phase following the operational simulation may possibly have had the result that the cesium present in the outer particle coating and in the graphite matrix was released more intensively so that the “store” was emptied, and the diffusion from the inner particle coatings through the SiC layer could not compensate for this quickly enough. An initial contamination of the matrix from the outside (see above) would also explain this effect (see Chapter 6).

On the whole, HFR Eu1bis1 in the first phase displayed a high release. The release during the second and third heating phase corresponded in order of magnitude to the expectations for highly stressed fuel elements. Apparently there was no particle failure during the bakeout experiment.

Table 29: Summary of the results of the AVR Eu1bis1 CoFA experiment

	Heating temp.	Heating time	FR Cs-137	FR Cs-134	FR Ag-110m	FR Ru-106	FR Kr-85
Eu1bis 1	1250 °C	210 h	$7,2 \cdot 10^{-5}$	$7 \cdot 10^{-5}$	$2,3 \cdot 10^{-3}$	$6,4 \cdot 10^{-7}$	$1,4 \cdot 10^{-6}$
	1600 °C	200 h	$1,2 \cdot 10^{-3}$	$1,17 \cdot 10^{-3}$	$7,2 \cdot 10^{-3}$	-	$1 \cdot 10^{-5}$
	1700 °C	150 h	$4,3 \cdot 10^{-3}$	$4,3 \cdot 10^{-3}$	-	-	$2,4 \cdot 10^{-5}$

6.6 HFR Eu1bis 3

6.6.1 Data of the experiment

The HFR Eu1bis3 fuel element was irradiated in the HFR Eu1bis irradiation experiment (description, see HFR Eu1bis 1) in a central irradiation position. It reached in 249 full-load days (efpd) a burn-up of 11.07% FIMA and received a fast neutron fluence of $3.98 \cdot 10^{25} \text{m}^{-2}$. The average irradiation temperature was 1250°C. Together with HFR Eu1bis 4 it was the most highly loaded fuel element of the irradiation experiment HFR Eu1bis.

Table 30: Irradiation data for the HFR Eu1bis 3 fuel element

Identification number	HFR Eu1bis 3	Burn-up:	11.07 % FIMA
Type:	GLE-4.2	Fast neutron fluence (>0.1 MeV):	$3.98 \cdot 10^{25} \text{m}^{-2}$
End of irradiation:	October 2005	Irradiation temperature	~ 1250 °C
Irradiation time:	249 efpd		
Fission gas release at end of irradiation			
		R/B Kr-85m:	$3.8 \cdot 10^{-6}$
R/B Xe-135:	$3.6 \cdot 10^{-6}$	R/B Kr-87:	$2.8 \cdot 10^{-6}$
R/B Xe-133:	$8 \cdot 10^{-6}$	R/B Kr-88:	$3.6 \cdot 10^{-6}$

Table 31: Fission product inventory of HFR Eu1bis3 at beginning of experiment (23 July 2008)

Cs-137*:	$7.22 \cdot 10^{10} \text{Bq}$	Sr-90**:	$6.3 \cdot 10^{10} \text{Bq}$
Cs-134*:	$3.5 \cdot 10^{10} \text{Bq}$	Ru-106*:	$4.89 \cdot 10^{10} \text{Bq}$
Kr-85**:	$7.37 \cdot 10^9 \text{Bq}$	I-131**:	~ 0 Bq
Xe-133**:	~ 0 Bq	Ag-110m*:	$3.73 \cdot 10^7 \text{Bq}$

* measured, ** calculated

The HFR Eu1bis 3 heating experiment was conducted in two steps. As in the case of HFR Eu1bis 1, a relatively long phase of 100 hour at irradiation temperature was set in order to gain information on the equilibrium release. This was followed by a classical accident simulation up to 1600°C for 200 hours. Between the two heating steps, the fuel element was cooled down to room temperature. The goal of the experiment was to test the integrity and validity of the

1600°C limit for a fuel element with TRISO particles from one of the last prepared production charges in the case of high burn-up and high irradiation temperature. In order to obtain an unfalsified fuel status after the 1600°C accident simulation for further post-irradiation studies, in this case there was no further heating at higher temperatures.

6.6.2 Measured fission product release

In the first heating phase, the operation simulation, only very small quantities of Kr-85 near the detection limit of the measuring apparatus were released. During the subsequent accident simulation, the release of rose from $3.4 \cdot 10^{-7}$ FR to $2.3 \cdot 10^{-6}$ FR. Apparently, during the entire experiment no particle failure occurred so that exclusively the release from the graphite matrix was involved.

The release of Cs-137 and Cs-134 already during the operation simulation at 1250°C amounted to $4 \cdot 10^{-10}$ FR and increased to about $2.5 \cdot 10^{-3}$ FR during the accident simulation.

The Ag-110m release was clearly distinct and already amounted to $9.6 \cdot 10^{-4}$ FR in the first heating phase. During the accident simulation, it rose to $3.6 \cdot 10^{-3}$ FR. While the cesium release with the start of the 1600°C heating phase clearly visibly rose, the increase in the Ag-110m release was weaker in comparison. There was only a slightly higher release rate than at operating temperature.

A release of Ru-106 could only be confirmed in the phase of operation simulation. It was $2.1 \cdot 10^{-6}$ FR. During the 200-hour 1600°C heating, the release on the condensate plates was below the detection limit. Therefore, in the diagram only the respective detection limits are accumulated and the uncertainties pertaining to them are plotted.

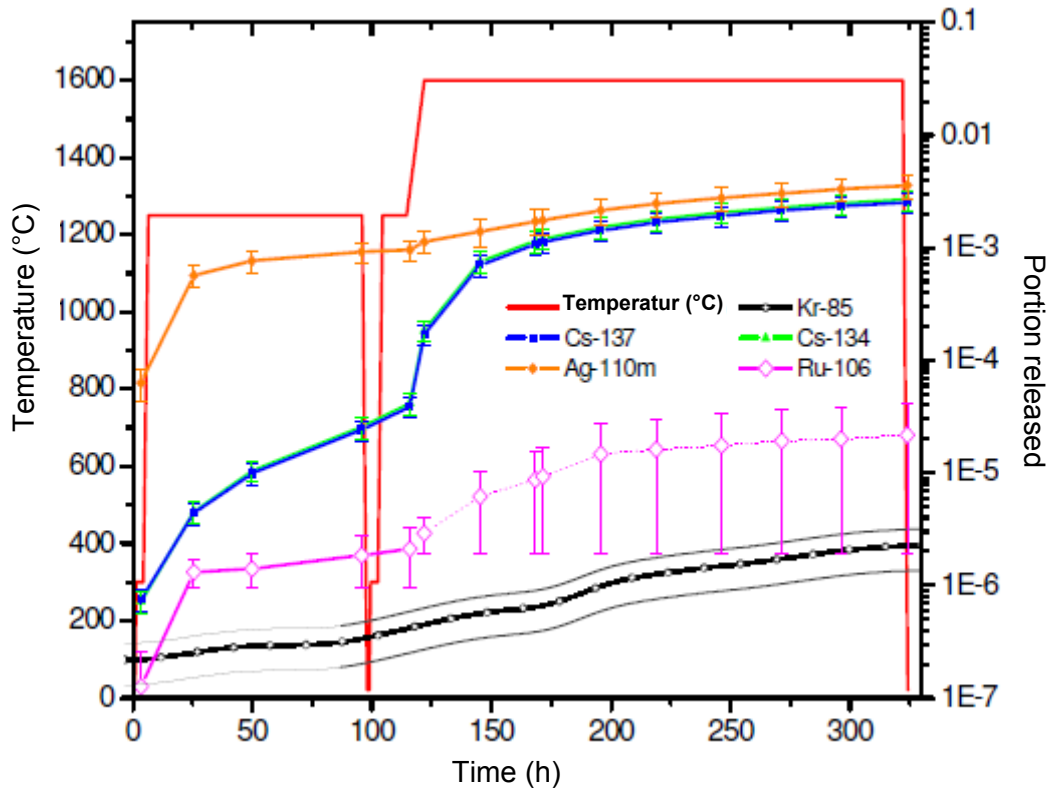


Figure 32: HFR Eu1bis 3 bakeout experiment -- Temperature curve and fission product release

6.6.3 Summary

The HFR Eu1bis 3 fuel element was baked out in two heating phases at 1250°C and 1600°C for 100 and 200 hours, respectively. Between the heatings, the fuel element was cooled down to room temperature.

The release curve of Kr-85 displayed no significant jumps either during the operation simulation phase at 1250°C or during the accident simulation at 1600°C and at the end of the experiment amounted to $2.3 \cdot 10^{-6}$ FR. It is therefore assumed that there were no particle failures.

The release of Ag-110m during the first phase was $9.6 \cdot 10^{-4}$ FR and increased in the second experimental phase to $3.6 \cdot 10^{-3}$ FR. Based on these results, one would have to assume considerable loads on the primary cycle for an HTR with direct circulation and high operating

temperature. The release following this during the accident simulation was smaller than expected.

The cesium release during the operation simulation at about $4 \cdot 10^{-5}$ FR was about one order of magnitude smaller than the Ag-110m release but increased during the accident simulation drastically to $2.5 \cdot 10^{-3}$ FR. The good agreement of the Cs-137 and Cs-134 release amounts shows that the measured plate activities actually involve release from the fuel element and not contamination from the equipment or from the Hot Cells.

On the whole, the retention behavior of HFR Eu1bis 3 was found to be unsatisfactory. To be sure there was no particle failure during the bakeout experiment, but relative releases of cesium of about $2.5 \cdot 10^{-3}$ are not acceptable for inherently safe HTR designs (see HFR Eu1bis 1).

Table 32: Summary of the results of the HFR Eu1bis 3 CoFA experiment

	Heating temp.	Heating time	FR Cs-137	FR Cs-134	FR Ag-110m	FR Ru-106	FR Kr-85
Eu1bis 3	1250 °C	100 h	$3,9 \cdot 10^{-5}$	$4,1 \cdot 10^{-5}$	$9,6 \cdot 10^{-4}$	$2,1 \cdot 10^{-6}$	$3,4 \cdot 10^{-7}$
	1600 °C	200 h	$2,5 \cdot 10^{-3}$	$2,7 \cdot 10^{-3}$	$3,6 \cdot 10^{-3}$	-	$2,3 \cdot 10^{-6}$

6.7 HFR Eu1bis 4

6.7.1 Data of the experiment

The HFR Eu1bis 4 fuel element was irradiated, like the HFR Eu1bis 3, in the HFR Eu1bis irradiation experiment (description, see HFR Eu1bis 1) in a central irradiation position. It reached in 249 full-load days a burn-up of 11.07% FIMA and received a fast neutron fluence of $3.98 \cdot 10^{25} \text{m}^{-2}$. The average irradiation temperature was 1250°C. Together with HFR Eu1bis 3 it was the most highly loaded fuel element of the HFR Eu1bis irradiation experiment.

Table 33: Irradiation data for the HFR Eu1bis 4 fuel element

Identification number	HFR Eu1bis 4	Burn-up:	11.07 % FIMA
Type:	GLE-4.2	Fast neutron fluence (>0.1 MeV):	$3.82 \cdot 10^{25} \text{ m}^{-2}$
End of irradiation:	October 2005	Irradiation temperature:	$\sim 1250 \text{ }^{\circ}\text{C}^*$
Irradiation time:	249 efpd		
Fission gas release at end of irradiation			
R/B Xe-135:	$3.6 \cdot 10^{-6}$	R/B Kr-85m:	$3.8 \cdot 10^{-6}$
R/B Xe-133:	$8 \cdot 10^{-6}$	R/B Kr-87:	$2.8 \cdot 10^{-6}$
		R/B Kr-88:	$3.6 \cdot 10^{-6}$

The HFR Eu1bis 4 bakeout experiment was divided essentially into three phases. In the first phase the fuel element was heated for about 50 hours at 800°C. Since no noteworthy fission product release due to diffusion through the particle jacket coatings was anticipated at this low temperature, this phase was intended to provide information on the fission product contamination of the graphite matrix during the irradiation. Following this, the fuel element was heated for about 10 hours to the irradiation temperature of 1250° in order to establish equilibrium conditions. Finally a 90 hour temperature transient up to 1720°C took place as would be expected for a pressure loss accident with outage of the active secondary heat removal for a V-HTR with a thermal capacity of 600 MWth [Haque et al. 2006]. The peak temperature was then maintained for about 140 hours.

Table 34: Fission product inventory of HFR Eu1bis 4 at beginning of experiment (23 July 2008)

Cs-137*:	$7.18 \cdot 10^{10} \text{ Bq}$	Sr-90**:	$6.26 \cdot 10^{10} \text{ Bq}$
Cs-134*:	$3.16 \cdot 10^{10} \text{ Bq}$	Ru-106*:	$3.9 \cdot 10^{10} \text{ Bq}$
Kr-85**:	$7.23 \cdot 10^9 \text{ Bq}$	I-131**:	$\sim 0 \text{ Bq}$
Xe-133**:	$\sim 0 \text{ Bq}$	Ag-110m*:	$3.15 \cdot 10^7 \text{ Bq}$

* measured, **calculated

6.7.2 Measured fission product release

During the first heating phase at 800°C, the release of Kr-85 was below the detection limit of the measuring apparatus. Only when the 10-hour operation simulation started was Kr-85 released up to $1.6 \cdot 10^{-6}$ FR in the foreground of the accident simulation. During the subsequent 70-hour transient at a temperature of 1720°C the release rose up to $4.1 \cdot 10^{-6}$ FR. At the end of the experiment the total release Kr-85 was $1.7 \cdot 10^{-5}$ FR. Except for two small release jumps of the order of $1 \cdot 10^{-5}$ FR, the release was continuous and did not indicate any particle failures.

The release of Ag-110m during the 800 °C phase amounted to $1.3 \cdot 10^{-5}$ FR. During the 10-hour operation simulation, it clearly rose to $8.2 \cdot 10^{-4}$ FR and during the following transient reached a value of $9.4 \cdot 10^{-4}$ FR. Even afterward the cumulative Ag-110m release rose further to $2.5 \cdot 10^{-2}$ FR at the end of the experiment.

The release curve of cesium ran a power of ten below and parallel to the Ag-110m curve. At 800°C, a portion of about $1.1 \cdot 10^{-5}$ FR was released. At the end of the 10-hour operation simulation, the cumulative release amounted to roughly $2.8 \cdot 10^{-5}$ FR. It rose up to the maximal temperature at the end of the transient after 130 hours of experiment time to $1.7 \cdot 10^{-3}$ FR. At the end of the experiment the release was finally between $9.3 \cdot 10^{-3}$ FR and $9.6 \cdot 10^{-3}$ FR. Both of the isotopes Cs-137 and Cs-134 were released to almost the same extent as in the previous two HFR Eu1 bis experiments.

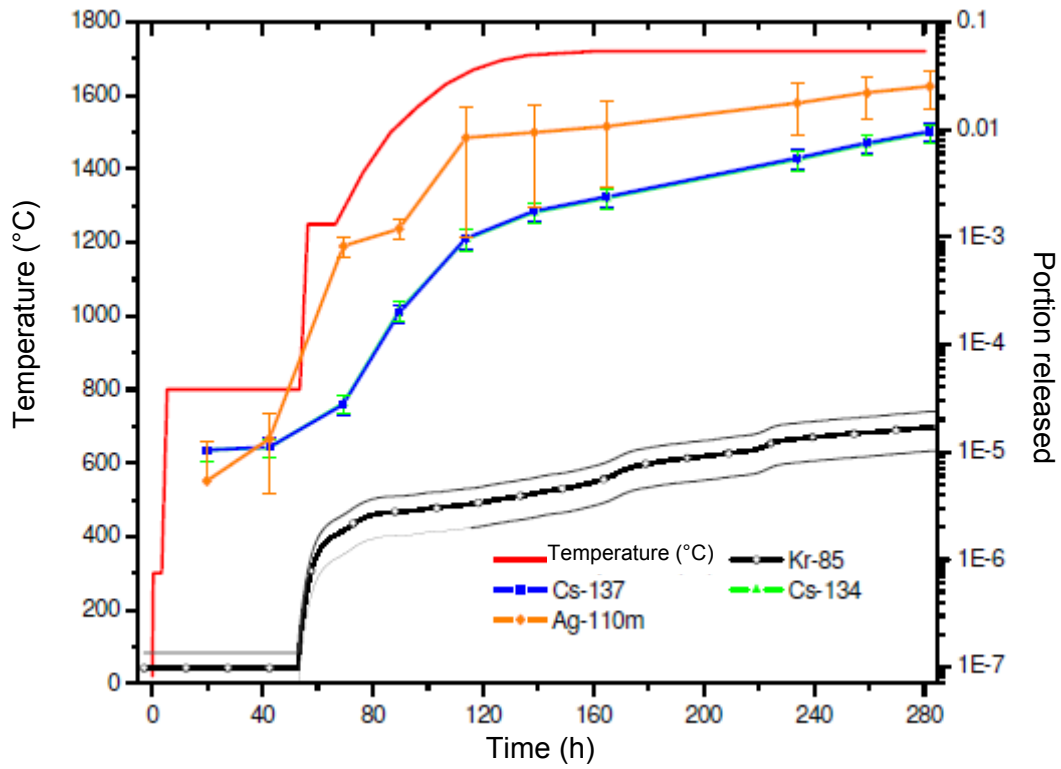


Figure 33: HFR Eu1bis 4 bakeout experiment -- Temperature curve and fission product release

6.7.3 Summary

After a 50 hour heating phase at 800°C, the HFR Eu1bis 4 fuel element was subjected to a 10-hour operation simulation at 1250°C and a subsequent 70-hour accident transient up to 1720°C. The maximal temperature was then maintained for about 140 hours.

The low Kr-85 release indicated that no particle failure had occurred. Two small release jumps can be interpreted under some conditions as the formation of cracks in jacket coatings or as spontaneous release of Kr-85 bubbles in graphite granules (see below). The release of solid fission products was relatively high. Ag-110m was released up to $2,5 \cdot 10^{-2}$ FR, Cs-137 and Cs-134 up to $9,6 \cdot 10^{-3}$ FR and $9,3 \cdot 10^{-3}$ FR. The release curves of Ag-110m and the two cesium isotopes run essentially parallel. Apparently release by diffusion was involved in both cases.

On the whole, the retention behavior of HFR Eu1bis 4 in the accident was found to be unsatisfactory. Apparently there was no particle failure during the bakeout experiment. While the fuel elements HFR K6/2 and HFR K6/3 irradiated at a lower irradiation temperature (~940°C) withstood a temperature of 1700°C effortlessly, the HFR Eu1bis 4 fuel element irradiated at high temperature released solid fission products on a large scale.

Table 35: Summary of the results of the AVR Eu1bis4 CoFA experiment

	Heating temp.	Heating time	FR Cs-137	FR Cs-134	FR Ag-110m	FR Ru-106	FR Kr-85
Eu1bis 4	800 °C	48 h	$1,1 \cdot 10^{-5}$	$1,1 \cdot 10^{-5}$	$1,3 \cdot 10^{-5}$	-	< NWG
	1250 °C	10 h	$2,8 \cdot 10^{-5}$	$2,8 \cdot 10^{-5}$	$8,2 \cdot 10^{-4}$	-	$1,6 \cdot 10^{-6}$
	Transient	70 h	$1,7 \cdot 10^{-3}$	$1,7 \cdot 10^{-3}$	$9,4 \cdot 10^{-3}$	-	$4,1 \cdot 10^{-6}$
	1720 °C	~ 140 h	$9,6 \cdot 10^{-3}$	$9,3 \cdot 10^{-3}$	$2,5 \cdot 10^{-2}$	-	$1,7 \cdot 10^{-5}$

7. Interpretation and modeling

7.1 Damage mechanisms

Coated particles can fail during irradiation or at elevated accident temperatures and release their inventory into the graphite matrix. As a criterion of failure, ordinarily the breaking of the SiC coating is assumed since this acts, on the one hand, as the main diffusion barrier, and on the other, is the mechanically most stable coating that absorbs most of the arising forces. A failure of the SiC coating therefore generally also leads to the failure of the PyC coatings. A complete breakage of the SiC coating with subsequent complete bursting of the particle as well as a partial failure when only local cracks appear in the SiC coating are possible (in the case of still intact PyC coatings), through which the fission products can escape. Since the starting conditions of the system being analyzed must be known, an analysis of the accident behavior can only be conducted jointly with an analysis of the previous irradiation.

7.1.1 Pressure vessel failure

During the irradiation, in the particle due to the release of fission gases an internal gas pressure builds up due to release of fission gases and the oxygen liberated from the uranium dioxide core. At the same time the fission products generated lead to a swelling of the core. If the voltages in the jacket coating induced by this are too high, a failure may occur. Breakage of the SiC coating is the criterion for particle failure. Since the jacket coatings are ceramic materials, it is only possible to state a probability of failure. In the case of a large number of particles this then corresponds roughly to the portion of broken particles. Ordinarily, the failure probability (P) in the case of ceramic materials is expressed by a Weibull statistic [Verfondern & Nabelek 1990].

$$P(\sigma_{SiC}) = 1 - \exp\left(-\ln(2) \cdot \left(\frac{\sigma_{SiC}}{\sigma_0}\right)^m\right)$$

Equation 17

P = Probability of failure

σ_{SiC} = Reference stress

σ_0 = Average tensile strength $[P(\sigma_{SiC} = \sigma_0) = 0.5]$

m = Weibull parameter

The Weibull parameter and the average tensile strength are empirical values. The average tensile strength is defined as the reference tension at which half of all jacket coatings fails. The

reference tension is computed formally from the integration of the maximal primary tension over the entire volume of the jacket coating.

$$\sigma_{SiC}^m = \frac{\int_V \sigma(\bar{V})^m \cdot d\bar{V}}{V} = \frac{\int_{r_i}^{r_a} \int_0^{2\pi} \int_0^\pi \sigma(\vartheta, \varphi, r)^m \cdot r^2 \cdot \sin(\vartheta) d\vartheta d\varphi dr}{\frac{4}{3}\pi(r_a^3 - r_i^3)}$$

Equation 18

The mechanical system to be analyzed consists of the IPyC coating, the SiC coating and the OPyC coating. Due to the higher porosity of the buffer layer, it is assumed that no forces from the core are transmitted through the buffer layer/coating. Core and buffer coating are therefore not analyzed in the model. In a first approach, one can simplify further and analyze only the SiC coating as a linear-elastic pressure vessel. The simplest approach to the determination of the reference stress is then the determination of the tangential stress with the so-called pressure vessel formula. It is derived from the integration of the internal pressure over the inner surface of the pressure-loaded hollow body and the force equilibrium in the equatorial section plane.

$$\sigma_{SiC} = \frac{\int_0^{2\pi} \int_0^{\pi/2} (p \cdot r^2 \cdot \cos(\vartheta) \cdot \sin(\vartheta)) d\vartheta d\varphi}{\pi \cdot d \cdot s} = \frac{p \cdot d}{4 \cdot s}$$

Equation 19

The pressure vessel formula can be applied for thin-walled hollow balls or hollow cylinders if the ratio of the outer to the inner diameter is less than 1.2.

Jacket coating	Thickness	Ratio (d _a /d _i)
Kernel	Ø 500 µm ±2 µm	1 (not relevant)
Buffer PyC	93 µm ± 14%	1.372 (not relevant)
IPyC	38 µm ± 10%	1.111 (not relevant)
SiC	35 µm ± 6%	1.092
OPyC	40 µm ± 9%	1.096 (not relevant)

A more accurate solution for the entire linear-elastic three-layer system (IPyC, SiC and OPyC), which also yields a local stress distribution in the tangential and radial direction over the radius, is obtained if by analogy with the solution for a thick-walled, cylindrical container [Klapp1980],

an analytic solution is derived for a thick-walled spherical container and the boundary conditions between the coatings is used (see Appendix I).

$$\sigma_r = \frac{1}{(r_a^3 - r_i^3)} \left((p_i - p_a) \frac{r_a^3 r_i^3}{r^3} + (p_a r_a^3 - p_i r_i^3) \right)$$

Equation 20

$$\sigma_t = \frac{1}{(r_a^3 - r_i^3)} \left(\frac{1}{2} (p_i - p_a) \frac{r_a^3 r_i^3}{r^3} + (p_i r_i^3 - p_a r_a^3) \right)$$

Equation 21

The three-layer pressure vessel system of a coated particle behaves in a much more complex way during the irradiation. A silicon carbide coating is generally considered to be linear-elastic. As opposed to this, the pyrolytic carbon coatings change their dimensions under fast neutron irradiation and display creep behavior. The dimensional variation is different in the radial and tangential direction and dependent on the Bacon anisotropy factor (BAF), which is a measure of the alignment of the carbon in a preferred direction. Other parameters are the temperature, the density and the fast neutron flux. In [Prados & Scott 1967], [Walther 1971] and [Miller & Bennet 1993] analytic solutions are proposed for the stress distributions in the jacket coatings. These solutions have the advantage that they can be implemented simply in a program. By random variation of the input parameters corresponding to the production deviations, failure statistics can be obtained by the Monte Carlo method. In this work, another approach was selected and the stress distribution during irradiation and heating experiments calculated with the aid of the abacus of the finite element method (FEM) program. The stress history obtained was finally the basis for the failure statistics according to Weibull.

7.1.2 Fabrication defects

A small portion of the particles can display defects or weak sites during production or during the pressing of the fuel element.

7.1.3 Ameba effect

The so-called ameba effect is a phenomenon in which the particle core migrates out of its central position into the jacket coatings. It occurs only in the presence of high temperature differences over the diameter and also in oxidic fuel. The oxygen released during the fission from the

uranium dioxide reacts with the carbon of the jacket coatings to form carbon monoxide and carbon dioxide. Since the thermodynamic equilibrium of the O-CO-CO₂ system depends on the temperature, different equilibria are established on both sides. The Boudouard reaction causes mass transport of carbon from the hotter to the colder side. The particle core moves upward accordingly along the temperature gradient.

(side with higher temperature) $2 \text{CO} \leftrightarrow \text{CO}_2 + \text{C}$ (side with lower temperature)

The ameba effect normally occurs only during irradiation since the necessary temperature gradients are generated by the heating power of the core. During an accident, the temperature gradient in the fuel element is much smaller since the chain reaction is interrupted and only post-decay heat is released. In spherical fuel elements, the ameba effect does not appear due to the low packing density and the related low temperature gradients. Therefore, it will not be simulated in the following as a damage mechanism. For prismatic fuel, the ameba effect is of significance since here one is working with considerably higher packing densities (see Table 2). In the US design, the prismatic fuel elements, as a rule, contain carbidic fuel (UCO or UC) in order to avoid a high O₂ or CO partial pressure.

7.1.4 Decay of the SiC coating by fission product corrosion

Corrosive fission products can be released from the particle core, diffuse through the buffer and IPyC coating and attack the SiC coating. Palladium, in particular, is known for its corrosive effect. Since the fission output for palladium upon the fission of Pu-239 is about two powers of ten higher than in the case of U-235 fission, palladium has a great significance for LEU fuel since here the brooded and in-situ burned [sic] Pu-239 at high burn-ups constitutes a noteworthy part of the fissions.

7.1.5 Oxidic and thermal decomposition of the SiC coating

At temperatures below 1600°C and oxygen contact, a protective coating of SiO₂ is formed which prevents further corrosion. About 1600°C and at low oxygen partial pressures, however, gaseous SiO is formed so that here progressing corrosion is to be expected. This mechanism can lead to the thinning out and later on to the failure of the stressed SiC coating. Although temperatures clearly above 1600°C were quite obviously reached within the scope of this project, all of the experiments were conducted in a pure helium atmosphere so that oxidic decay

and thinning out of the SiC coating were not given further consideration during the simulation of the damage mechanism. In an inert atmosphere, SiC thermally decomposes above 2200°C. Since this high value is not considered in this project, the thermal decomposition was also not given further consideration as a possible damage mechanism.

7.2 Gas release

The release of gaseous fission products can take place through four different mechanisms.

1. Sudden release from particles in the case of complete pressure vessel failure.
2. Release from partially defective particles
3. Equilibrium release from the graphite matrix
4. Diffusion through particle coatings

Since the graphite matrix has a low portion of effective free uranium contamination, fissions take place there during the irradiation. The generated fission gas diffuses upon heating out of the graphite grains into the open porosity and can then escape rapidly along the grain boundaries. This process leads to a constant temperature-dependent balancing release during the experiment. In the release diagram, this can be plotted as a straight line with variable slope at with varying temperature. The release rate (R) is obtained from the slope of the line with linear scaling (see Fig. 34).

$$R = \frac{\Delta FR}{\Delta t} = \tan(\alpha)$$

Equation 22

Regular release jumps (ΔFR) can be seen in the diagram in some instances. These can occur as a result of total particle failure or as a result of crack formation in the jacket coatings. However, it is also conceivable that closed gas pores inside the graphite grains of the matrix graphite migrate to the grain surface and then release their inventory into the open porosity all at once.

The release of long-lived, gaseous fission products from matrix graphite grains during the irradiation can be described by the Booth model (equivalent sphere model). In this case, an average grain radius is defined and assumed that the gas atoms first diffuse slowly inside the

grain to the open porosity and are rapidly released from there (Nabielek & Myers 1982), [Booth 1957]. In this case 6 μm can be assumed as the average grain radius [Verfondern et al. 1997].

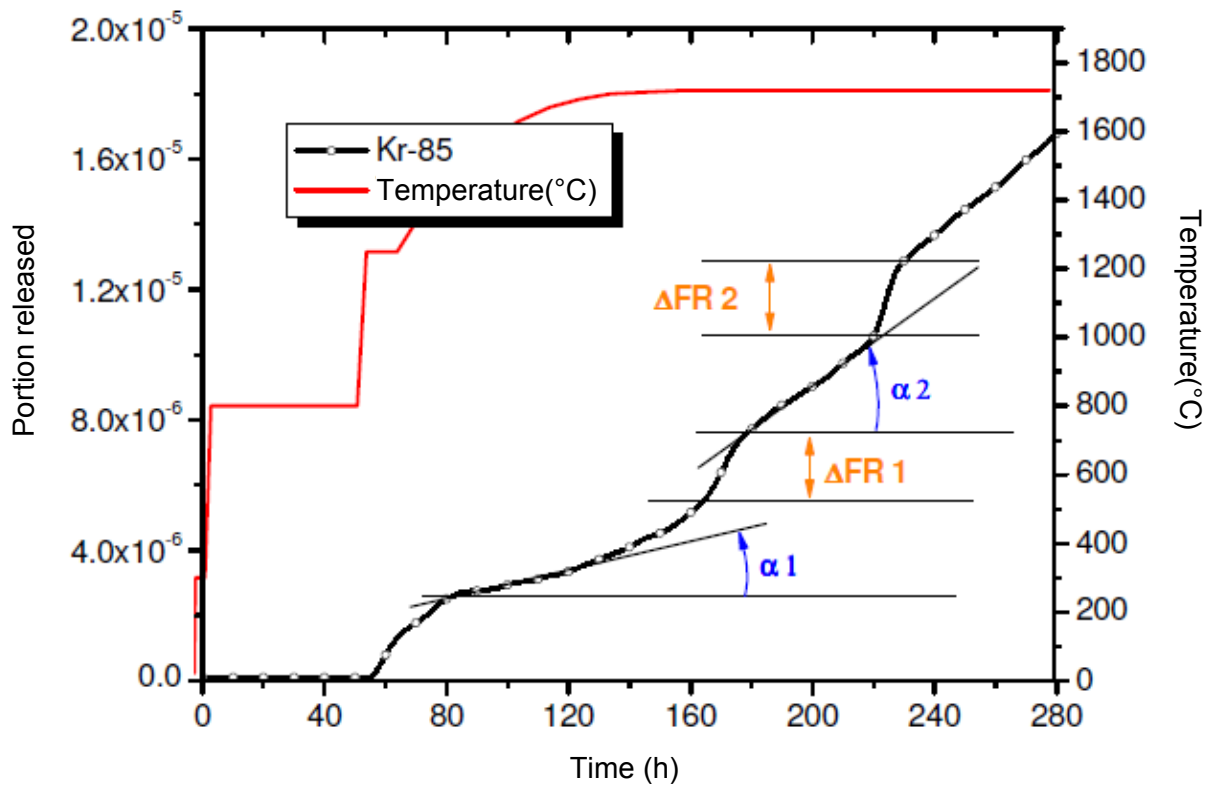


Figure 34: Equilibrium release and release jumps for the HFR Eu1bis 4

During the irradiation, the portion released can be calculated approximately with the following formula.

$$FR = K_U \cdot \left(1 - \frac{6}{D't} \sum_{n=1}^{\infty} \frac{1 - \exp(-n^2 \pi^2 D't)}{n^4 \pi^4} \right)$$

Equation 23

- D' = Reduced diffusion coefficient ($D' = D / r^2$)
- D = Diffusion coefficient (m^2 / s)
- K_U = Free Uranium contamination in the graphite matrix
- r = Equivalent grain radius (m)
- t = Irradiation time (s)

With the temperature-dependent diffusion coefficient according to Arrhenius:

$$D = D_0 \cdot \exp\left(-\frac{Q}{RT}\right)$$

Equation 24

- D_0 = Frequency factor (m^2 / s)
- Q = Activation energy (J)
- R = general gas constant (8.3144 J / mol K)
- T = Temperature (K)

A similar procedure may be used for gas release from a defective particle. In this case, the diffusion coefficient must be used for the fission gas in question in UO_2 . In addition, instead of the effective grain radius, the average core [sic] radius (about 250 μm) and instead of the free contamination in the matrix, the proportional inventory of the particle must be stated.

The release of long-lived, gaseous fission products from matrix graphite grains during the irradiation can be described by the following approximation [Nabielek et al. 1974].

$$FR_A = K_U \cdot \left(1 - \frac{1}{6} \sum_{n=1}^{\infty} \frac{\exp(-n^2 \pi^2 D' t)}{n^2 \pi^2}\right)$$

Equation 25

Again, a similar procedure may be used for the release from defective particles. Gaseous fission products are not released from intact particles.

7.3 Release of solid fission products

As opposed to the gaseous fission products krypton and xenon, the solid fission products such as cesium, strontium and silver are not only released from the graphite matrix and from defective particles but also diffuse through intact jacket coatings. At the comparatively low temperatures during the operation, the process is usually slow enough to be able to speak of almost complete retention (with the exception of silver). At elevated operating temperatures and at accident temperatures, however, the release clearly increases.

The same correlations apply for the release due to uranium contamination of the matrix and from defective particles as apply for gaseous fission products (see above). In the case of release through intact jacket coatings, the SiC coating is the primary diffusion barrier. In order to get some idea of the time required until the release from a single intact particle, one can state the so-called breakthrough time (t_D).

$$t_D \approx \frac{s^2}{6D}$$

Equation 26

s = Coating thickness
 D = Diffusion coefficient (m^2 / s)

The solution to the coupled diffusion equations for the release of metallic fission products from coated particles with several coatings and a surrounding graphite matrix is usually obtained numerically.

However, if one assumes for the sake of simplicity that only the SiC coating represents a noteworthy diffusion barrier, a more accurate description of the mass transfer can also be obtained by setting up the equation of diffusion in the intact SiC jacket coating.

$$\frac{\partial C}{\partial t} = D \frac{1}{r^2} \cdot \frac{\partial}{\partial r} \left(r^2 \frac{\partial C}{\partial r} \right)$$

Equation 27

In this case, the radioactive decay of long-lived fission products is neglected. The concentration of material (C_i) inside the interior zone consisting of the UO_2 core and the PyC coatings enclosed in the SiC coating is assumed to be constant over the radius and is found as:

$$C_i = \frac{3N}{4\pi r_i^3}$$

Equation 28

N = Quantity of material
 r_i = internal radius of SiC coating

The mass transfer from the interior zone into the SiC coating can be described by the following equation.

$$\frac{4\pi r_i}{3} \cdot \frac{dC_i}{dt} = 4\pi r_i^2 D \frac{dC}{dr} \Big|_{r=r_i}$$

Equation 29

The solution to the partial differential equation ultimately leads to the cumulative portion of release (FR) according to [Minato et al. 1995].

$$FR = 1 - \sum_{m=0}^{\infty} T_m \exp\left(-y_m^2 \frac{Dt}{(r_a - r_i)^2}\right)$$

Equation 30

r_a = external radius of the SiC coating

$$\tan y_m = \frac{3\gamma \cdot y_m}{y_m^2 - 3\gamma^2}, \quad y_m > 0$$

$$\gamma = \frac{r_a - r_i}{r_i}$$

$$T_m = \frac{1 + \gamma}{\cos y_m} \cdot \frac{1}{\frac{y_m^2}{6\gamma} + \frac{1}{2} + \gamma + \frac{6\gamma^2 + 9\gamma^3}{2y_m^2 - 6\gamma^2}}$$

The transporting of solid fission products in matrix graphite can generally be described by a trapping theorem [Verfondern et al. [1997]. In this case, the matrix is subdivided into two locally equal zones, the transport zone and the trapping zone. A constant exchange of material between the trapping and transporting zones is superimposed on the simple diffusion in the transport zone. The concentration in the transport zone is denoted by C, the concentration in the trapping zone by m. The processes can be described by equation 31 and equation 32. For transporting processes over long periods of time, the model can be simplified and an effective diffusion coefficient calculated by equation 33.

$$\frac{\partial C}{\partial t} = D \frac{\partial^2 C}{\partial x^2} - \mu C + bm$$

Equation 31

$$\frac{\partial m}{\partial t} = +\mu C - bm$$

Equation 32

$$D_{\text{eff}} = \frac{D}{1 + \mu/b}$$

Equation 33

7.4 Diffusion model

The release of solid, long-lived fission products from intact particles and from the graphite matrix due to uranium contamination was simulated by using a one-dimensional diffusion model in Excel. The heterogeneous structure of coated particles and graphite matrix was imaged by two parallel tables that interacted with each other. As a starting value, the assumed fission product profiles in the coated particles and the graphite matrix are entered at the beginning of the simulation. The entire simulation from start of irradiation until the end of the bakeout experiment was computed in several time steps. The calculated fission product profiles at the end of a time step served as input values for the next step. The calculation table consisted of a total of more than 3,500,000 cells.

In the first table, the spherical fuel element was simulated by 60 spherical shell lying one inside the other with a thickness of 0.5 mm each. They served as control volumes and were imaged by 60 cell lying horizontally side by side. The values in the cells represented the fission product concentration in the control volume. The series of cells that formed was repeated 48,000 times in the vertical direction. Each row represented a time step (t). Calculation formulae were introduced into the cells that calculated the time-dependent and place-dependent fission product concentration from the values of the previous time step. For this purpose it was assumed that the respective concentration $C_{i,t}$ in a shell (j) at a time (t_i) is composed of:

- the concentration in the control volume at the time t_{i-1} ($C_{j,i-1}$),
- Quantity of material divided by the control volume (V_j),

- the quantity of material transported from the neighboring outer shell into the control volume (V_j) divided by the control volume,
- the quantity of material transported from the control volume (V_j) into the neighboring zones divided by the control volume,
- a swelling term in the fuel zone that describes the release from the particles into the matrix divided by the control volume, and
- a swelling term that allows for the build-up of fission products in the matrix by the free uranium contamination.

The streams of material (I'') between the control volumes $j-1$ and j were calculated according to Ficke's first law.

$$I''_{j-1 \rightarrow j} = D \cdot \frac{dC}{dr}_{j-1 \rightarrow j} = D \cdot \frac{(C_{j-1} - C_j)}{(r_j - r_{j-1})}$$

Equation 34

On the whole, for the concentration change in the control volume (i) in the time step ($j-1 \rightarrow j$) one obtains the following first order equation.

$$C_{j,i} = C_{j,i-1} + \ddot{\phi}_{i-1} \cdot (t_i - t_{i-1}) + D \cdot \frac{(t_i - t_{i-1})}{V_j} \cdot \left(\left(\frac{(C_{j-1,i-1} - C_{j,i-1})}{(r_j - r_{j-1})} \cdot A_{j-1} - \frac{(C_{j,i-1} - C_{j+1,i-1})}{(r_{j+1} - r_j)} \cdot A_j \right) \right)$$

Equation 35

The time steps were chosen sufficiently small to minimize the local discretization error. An excerpt from the calculation table used is shown in Figure 35. The arrows mark the calculated streams of material. In the left column, the swelling term calculated for the time step in question is given. For simplification, it was assumed that the release from the particles into the matrix is independent of location and the diffusion into the matrix is spherically symmetrical. The swelling term is obtained from the material concentration in the outer particle coating and the average material concentration in the matrix and is the same for all control volumes. This, of course, neglects the concentration gradient in the matrix, but the latter, due to the relatively high diffusion coefficient, is relatively small anyhow compared with the jacket coatings and especially

with the SiC coating. In the case of an external contamination of the graphite matrix, the material flow can assume negative values, therefore, diffuse into the outer particle coatings.

r (mm)	0	0.5	1	1.5	2	
A (mm ²)	0	3.141592654	12.56637062	28.27433389	50.26548246	
V (mm ³)	0	0.523598776	3.66519143	9.948376738	19.3731547	
Swelling term	time (s)	time	coatings →	j-1	j	j+1
0.00247183	835200	↓	2200.164276	2201.531196	2204.261155	2208.346157
0.00247183	835201		2200.198432	2201.5653	2204.295157	2208.380004
0.00246519	835202	i-1	2200.232587	2201.599403	2204.329157	2208.413851
0.00245889	835203	i	2200.266733	2201.633498	2204.36315	2208.44769
0.00245292	835204	i+1	2200.300872	2201.667586	2204.397135	2208.481521
0.00244726	835205		2200.335004	2201.701667	2204.431113	2208.515345
0.00244189	835206		2200.36913	2201.735741	2204.465084	2208.549162
0.0024368	835207		2200.403248	2201.769808	2204.499048	2208.582973

Figure 35: Excerpt from the Excel calculation page

The diffusion processes in the particle were calculated by analogy with the calculation of the diffusion in the graphite matrix. For simplification, a Table with 13 control volumes was used for the calculation. An important distinction was the buildup of the spherically symmetrical particle from coatings of different materials. For the latter, in each case the specific temperature-dependent diffusion coefficients were computed. In addition, for the irradiation phase, a swelling term was defined that allowed for the buildup of fission products during the irradiation.

The following data had to be entered for the calculation:

- Temperature
- Duration of the time step
- Fission product studied
- Quantity of the fission product in question produced during one time step (during irradiation)
- Geometric data of the coated particles
- Fast neutron fluence
- Fission product profiles in particles and matrix at the beginning of the time step

To determine the diffusion coefficients of different fission products in the particle jacket coatings and in the graphite matrix, calculation functions were used according to material data from the literature [Verfordern et al. 1997]. The diffusion parameters are given in Appendix V.

Since the diffusion coefficients are temperature-dependent, it had to be checked whether it was permissible to assume a uniform temperature over the fuel element and particle radius. Since a small gradient is created during the heating experiments, maximally during the heating-up phase, this aspect could be neglected here. During the irradiation, however, significant temperature differences can occur between fuel element center and its edge. These were calculated for each fuel element studied in Appendix III.

For calculating the release into the helium atmosphere, a method was selected that was analogous with the FZJ FRESCO program for calculating the fission product release in HTR [Krohn 1982]. In this case, it was assumed that above the graphite surface an equilibrium is always established between the fission product concentration in the outer graphite coating (c_{gr}) and in the gas atmosphere (c_{gas}). This equilibrium is established practically without a time lag and is described by the following equation:

$$c_{gr} = \alpha \cdot c_{gas}$$

Equation 36

The factor α is a dimensionless temperature-dependent mass transfer coefficient. In the region of low fission product concentrations α can be described by the Henry law.

$$\alpha_H = \frac{1}{T} \cdot \exp\left(A_H + \frac{B_H}{T}\right)$$

Equation 37

At higher concentrations, for calculating the release into the gaseous phase a formula according to Freundlich was chosen. Both the coefficients for α_H and for α_F are tabulated in the literature [Verfordern et al. 1997]:

$$\alpha_F = \frac{1}{T} \cdot \exp\left(A_F + \frac{B_F}{T} + (D_F + E_F) \cdot \ln(c_{gr})\right)$$

Equation 38

The material quantity flow (I) in the Excel model is now obtained from the equilibrium concentration in the gas atmosphere multiplied by the gas volume flow (V).

$$I = \frac{c_{gr}}{\alpha} \cdot \dot{V}$$

Equation 39

To review and check the model, the release from a pure graphite sphere with a material quantity initially concentrated in the center was calculated over one hundred hours at 1300°C and the result compared with the analytic solution. The analytic solution is obtained from the diffusion equation with the initial conditions.

$$\frac{\partial C}{\partial t} = D \frac{1}{r^2} \cdot \frac{\partial}{\partial r} \left(r^2 \frac{\partial C}{\partial r} \right)$$

Equation 40

Initial conditions:

$$C(r, 0) = 0 \quad (\text{für } r \neq 0)$$

$$C(0, 0) = N \quad (N = \text{atoms in the center})$$

$$\int_0^{\infty} 4\pi r^2 C(r, t) dr = N$$

$$C(r, \infty) = 0$$

Solution:

$$C(r, t) = N \frac{e^{\left(\frac{-r^2}{4Dt}\right)}}{(4\pi Dt)^{3/2}}$$

Equation 41

$$FR = \int_R^{\infty} 4\pi r^2 \frac{e^{\left(\frac{-r^2}{4Dt}\right)}}{(4\pi Dt)^{3/2}} dr$$

Equation 42

Figure 36 shows the result of the analytic solution and the result of the calculation with the Excel table described here.

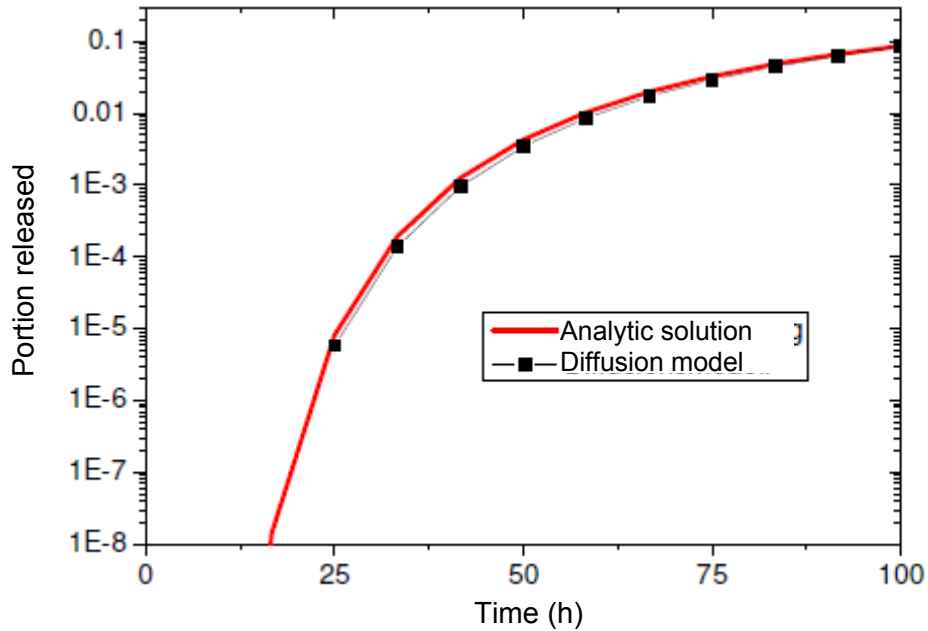


Figure 36: Cs-137 diffusion through an A3 graphite sphere at 1300°C

The entire calculation table was finally checked for plausibility based on the release values of the HFR Kr3/3 bakeout experiment [Schenk et al. 1988], [Verfondern et al. 1997]. The HFR K3/3 involved a fuel element with LEU TRISO particles that was irradiated in the HFR material testing reactor in Petten, Netherlands and subsequently transported to Jülich. There it was baked out in the CoFA I at 1800°C for 100 hours (the total heating time with bakeout phase was 187 h).

Table 36: Data for the HFR K3/3 fuel element

Identification number	HFR K3/3	Burn-up:	10.2 % FIMA
Type:	GLE-3	Fast neutron fluence (>0.1 MeV):	$6 \cdot 10^{25} \text{ m}^{-2}$
End of irradiation:	September 1983	Irradiation temperature	800 °C - 1000 °C
Irradiation time:	359 efpd		
Bakeout temperature:	1800 °C	Bakeout time:	100 h (+ 87 h)

In the first step, the fission product distribution in the particles and the graphite matrix during the irradiation was computed. This served as the starting value for the simulation of the bakeout experiment. Figure 37 shows the result of the calculation of the release during the bakeout phase and the measured release of Cs-137 as well as the results of a reference calculation with the FRESCO program [Verfondern & Nabielek 2008].

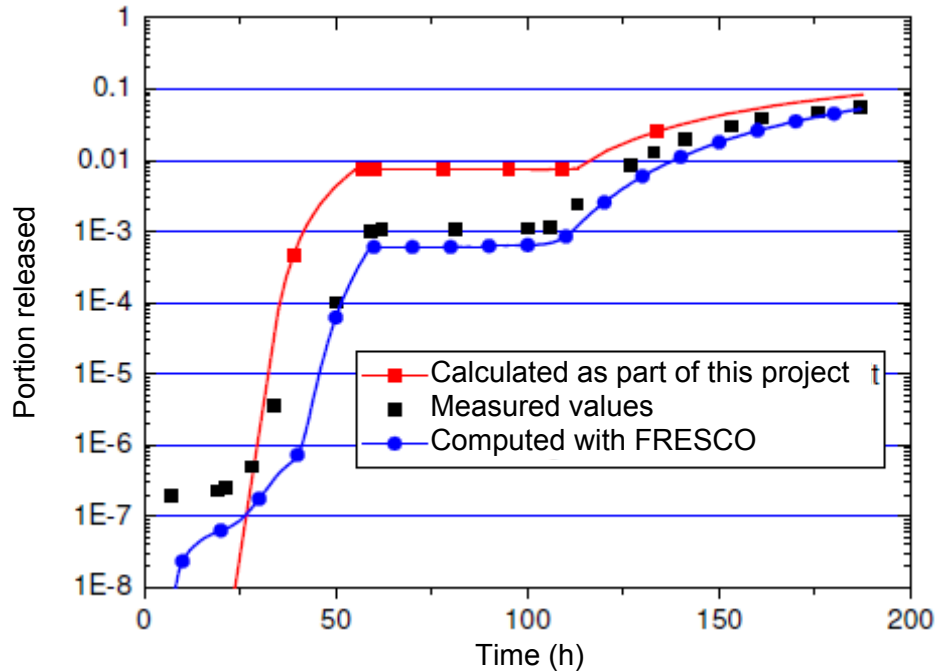


Figure 37: Benchmark of the diffusion model employed at 1600°C test temperature (HFR K3/3)

7.5 Mechanical particle failure

The mechanical behavior of the coated particles was computed in this work with the FEM Abaqus program. In this case the procedure was essentially the same as that of [Miller & Bennet 1991]. First, a two-dimensional axially symmetrical FEM model of the three jacket coatings IPyC, SiC and OPyC was prepared. A spherical coordinate system was defined for the implementation of the direction-dependent material properties. As opposed to the real particles, all of which are different and display deficient roundness and bulges, the jacket coatings were simulated as perfect spherical shells. As a boundary condition, in addition, for simplification, it was assumed that all coatings are firmly connected to each other and that no detachment occurs.

In each case specific analysis steps were defined for irradiation, storage and heating test. The irradiation was simulated viscoelastically. All other steps were simulated linear-elastically. The variable thermal expansion and the linear-elastic behavior were simulated for all coatings. For the PyC coatings, in addition, neutron-induced creep and neutron-induced dimensional changes were simulated. The external and internal pressure as well as the temperature were defined as boundary conditions.

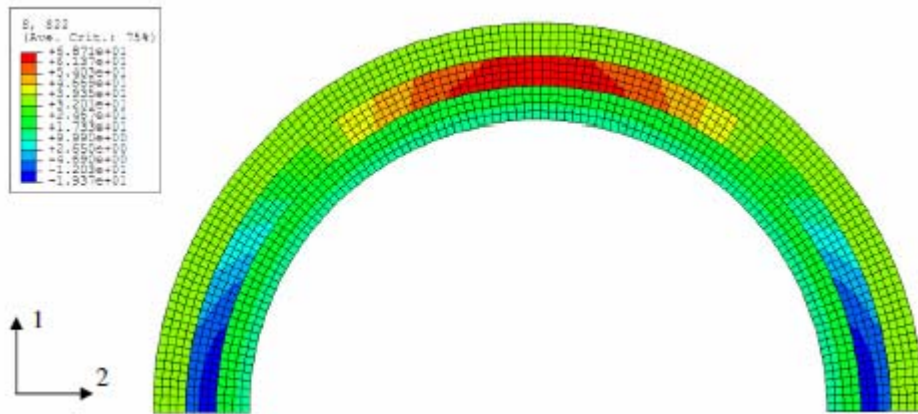


Figure 38: FEM model of the three-layer system IPyC, SiC and OPyC coating

7.5.1 Internal gas pressure

The empirical model from [Verfondern & Nabelek 1990] was adopted for simulating the internal gas pressure. The internal gas pressure (p_i) is obtained according to the ideal gas law from the fission gas (n_{SG}) released from the core and the oxygen (n_O) released from the UO_2 matrix. In this case the porosity of the buffer coating of about 50% was assumed as the free volume (V_f) in which the gas collects and the pressure builds up.

$$p_i = \frac{(n_{SG} + n_O) RT}{V_f}$$

Equation 43

The quantity of released fission gas is obtained from the initially present quantity of heavy metal (n_{SM}), the burn-up (BU), the effective fission yield for stable and long-lived fission gases ($F_f \approx 0.31$) and the released portion (F_d).

$$n_{SG} = n_{SM} \cdot BU \cdot F_d \cdot F_f$$

Equation 44

The released portion is calculated by:

$$F_d = \frac{(\tau_i + \tau_a) \cdot f(\tau_i + \tau_a) - \tau_a \cdot f(\tau_a)}{\tau_i}$$

Equation 45

The parameters τ_i and τ_a are obtained by multiplication of the irradiation time (t_i), and the experiment time (t_a), with the reduced diffusion coefficient. The function $f(\tau)$ again follows from the Booth model (see above).

$$f(\tau) = 1 - \frac{6}{\tau} \sum_{n=1}^{\infty} \frac{1 - \exp(-n^2 \pi^2 \tau)}{n^4 \pi^4}$$

Equation 46

$$\tau_i = t_i \cdot D'$$

$$\tau_a = t_a \cdot D'$$

D' = Reduced diffusion coefficient ($D' = D / r^2$)

The reduced diffusion coefficient for UO_2 particle cores can be approximated according to an empirical relation [Verfondern & Nabielek 1990] as:

$$D' = 10^{\left(-2,3 - \frac{8116}{T}\right)}$$

Equation 47

The quantity of released oxygen is obtained from the burn-up (BU), the initially present quantity of UO_2 and an empirical relations for the average number of oxygen atoms released per fission (OPF) (see equation 48 and equation 49k). At irradiation and accident temperatures the released oxygen in the buffer coating is present almost exclusively as CO .

Irradiation:

$$\log(OPF) = -10,08 - \frac{8500}{T_i} + 2 \cdot \log(t_i)$$

Equation 48

Accident:

$$\log(OPF) = -10,08 - \frac{8500}{T_i} + 2 \cdot \log(t_i) - 0,404 \cdot \left(\frac{10000}{T} - \frac{10000}{T_i + 75} \right)$$

Equation 49

The upper limit for the number of oxygen atoms released per fission is reported at 0.625 [Verfondern & Nabielek 1990].

7.5.2 Material data for the FEM simulation

The following material data are used for the FEM simulation of the pressure vessel composite from IPyC, SiC and OPyC coating. The parameters on which the property in question depends are given in parentheses.

- Elasticity modulus (temperature, density, fast neutron fluence, average grain size)
- Cross contraction number
- Coefficient of thermal expansion
- Neutron-induced dimensional variation of the PyC (temperature, density, fast neutron fluence)
- Neutron-induced creep (temperature, density, fast neutron fluence, tension/stress)

The elasticity modulus of the PyC coatings is a function of the temperature, the density, the average grain size and the fast neutron fluence. In [Pelletier 2003] one finds a comprehensive compilation of material data for pyrolytic carbon and silicon carbide in coated particle jacket coatings according to literature from FZJ, BNFL and CEGA. Here for simplification, the Jülich value (FZJ) of constantly 29,000 MPa is selected as the elasticity modulus of the PyC.

	FZJ ^[1]	BNFL ^[2]
"buffer" layer E(MPa) $\Phi(10^{25}\text{n/m}^2 > 0.1\text{MeV})$	For $0 < \Phi < 0.5$ $E = 7000 + 6000$ For $\Phi > 0.5$ $E = 10000$	$E = 12500(1 + 0.18\Phi)$
"dense" PyC layers E(MPa) $\Phi(10^{25}\text{n/m}^2 > 0.1\text{MeV})$	$E = 29000$	$E = 25000(1 + 0.18\Phi)$

Figure 39: Elasticity modulus of PyC according to FZJ and BNFL [Pelletier 2003]

	CEGA
"buffer" layer E(MPa) P(/)	For $0.2 < P < 0.6$ $E = 34500 \exp(-2.03 P)$
"dense" PyC layers E(MPa) $\Theta(^{\circ}\text{C})$ P (g/cm ³) Lc (nm) ** $\Phi(10^{25}\text{n/m}^2 > 0.1\text{MeV})$	$E_1 = k_p k_{\text{BAF01}} k_{\text{Lc}} k_{\Phi} k_T E_{01}$ and $E_3 = k_p k_{\text{BAF03}} k_{\text{Lc}} k_{\Phi} k_T E_{03}$ <i>With:</i> $E_{01} = E_{03} = 25500$ $K_p = 0.384 + 0.324p$ (1.8 < p < 2)* $k_{\text{Lc}} = 2.985 - 0.662 Lc$ (2.5 < Lc < 3.5)* $k_{\Phi} = 1 + 0.23\Phi$ (< 4 · 10 ²⁵)* $k_T = 1 + 0.00015 (\Theta - 20)$ (20 < Θ < 2000)* $k_{\text{BAF01}} = 0.481 + 0.519 \text{BAF}_0$ $k_{\text{BAF03}} = 1.463 - 0.463 \text{BAF}_0$ (1 < BAF_0 < 2)*

* Recommended ranges of variation of the parameters

** Lc: crystallite size

Figure 40: Elasticity modulus of PyC according to CEGA [Pelletier 2003]

The elasticity modulus of SiC, according to the data of FZJ, is a function of the temperature in the range of 200 to 1600°C (see equation 50).

$$E = E_{298K} \cdot (-2.12 \cdot 10^{-7} \cdot T^2 + 2.52 \cdot 10^{-4} \cdot T + 0.9252) \quad \text{Equation 50}$$

$$E_{298K} = 386,000 \text{ MPa}$$

The cross contraction number was assumed as 0.33 for the pyrolytic carbon. A cross contraction number of 0.13 was used for calculating the SiC coating [Pelletier 2003].

The coefficients of thermal expansion of PyC and SiC are different and lead to thermal stresses in the case of temperature variations. The following values were assumed within the scope of this project.

$$\alpha_{\text{PyC}} = 3,5 \cdot 10^{-6} \text{ K}^{-1} \quad (\text{FZJ})$$

$$\alpha_{\text{SiC}} = 5 \cdot 10^{-6} \text{ K}^{-1} \quad (\text{FZJ})$$

During irradiation, the PyC coatings are subject to a neutron-induced dimensional alteration. At the beginning, they pull together and thereby generate a pre-stressing in the SiC. Above a fast neutron fluence of roughly $2 \cdot 10^{25} \text{ m}^{-2}$ the PyC then begins to expand in the radial direction while it continues to shrink in the tangential direction. The dimensional variation is different in the radial and tangential direction and dependent on the Bacon anisotropy factor (BAF), which is a measure of the alignment of the carbon in a preferred direction. Other parameters are the temperature (T), the density (ρ) and the fast neutron flux (Φ_s).

$$\dot{\epsilon} = f(\rho, T, BAC, \phi_s) \quad \text{Equation 51}$$

According to CEGA data [Pelletier 2003] the dimensional change in the radial and tangential direction can be expressed as a function of the fast neutron fluence ($E > 0.18 \text{ MeV}$) by:

$$\dot{\epsilon}_r = CR_1 + 2 \cdot CR_2 \cdot \phi_s \quad \text{Equation 52}$$

$$\dot{\epsilon}_t = CT_1 + 2 \cdot CT_2 \cdot \phi_s \quad \text{Equation 53}$$

where the coefficients CR_1 , CR_2 , CT_1 and CT_2 are in turn functions of the anisotropy factor and temperature. The implementation in the FEM model was accomplished by tabulation of the rates

of expansion that were previously computed manually based on irradiation and material data. As parameters, in the FEM model, the fast neutron fluence is defined as field. The expansion rate can be entered in Abaqus as a function of time. Since the rate of expansion in the CEGA model is a function of the fluence, a conversion must be performed first (see equation 54)

$$\frac{d\varepsilon}{dt} = \frac{d\varepsilon}{d\phi_s} \cdot \frac{\phi_{s,irr}}{t_{irr}} \quad \text{Equation 54}$$

Due to the pulling together/contraction, a tensile stress is induced in the PyC coatings, which is degraded again in part by the neutron-induced creep. The creep behavior of the PyC coatings is dependent on the density, the temperature and the fast neutron fluence.

$$\dot{\varepsilon}_1 = K \cdot (\sigma_1 - \nu_1 \cdot (\sigma_2 + \sigma_3)) \cdot \frac{d\phi}{dt} \quad \text{Equation 55}$$

K = Creep constant ($\text{MPa } 10^{25} \text{ m}^{-2}$)⁻¹

σ_i = Stress in the i direction (MPa)

ν_i = cross contraction number

Φ = Fast neutron fluence (10^{25} m^{-2})

The creep rate cannot be reported directly in Abaqus as a function of the neutron fluence. Therefore, the creep constant also had to be converted (see equation 57). Both the conversion of the expansion rates and the conversion of the creep constant were done on the simplifying assumption that the fast neutron flux during the irradiation was almost constant.

$$\dot{\varepsilon}_{1,A} = K_A \cdot (\sigma_1 - \nu_1 \cdot (\sigma_2 + \sigma_3)) \quad \text{Equation 56}$$

K_A = Creep constant for entering into Abaqus (MPa^{-1})

$$K_A = K \cdot \frac{\phi_{s,irr}}{t_{irr}} \quad \text{Equation 57}$$

7.5.3 Simulation of the voltage curve and failure statistics

Figure 41, for example, shows the calculated curve of the tangential stresses in the jacket coatings of HFR K6/3 during the irradiation. One can see that the pyrolytic carbon coatings initially draw together and therefore stand under tensile stress while the SiC is compressed. Only above an irradiation time of about 10^7 seconds (115 days) can a reversal of the trend be observed. The IPyC and OPyC coating expand again and are unloaded. At the same time, the internal gas pressure rises and contributes to degrading the compressive stress in the SiC.

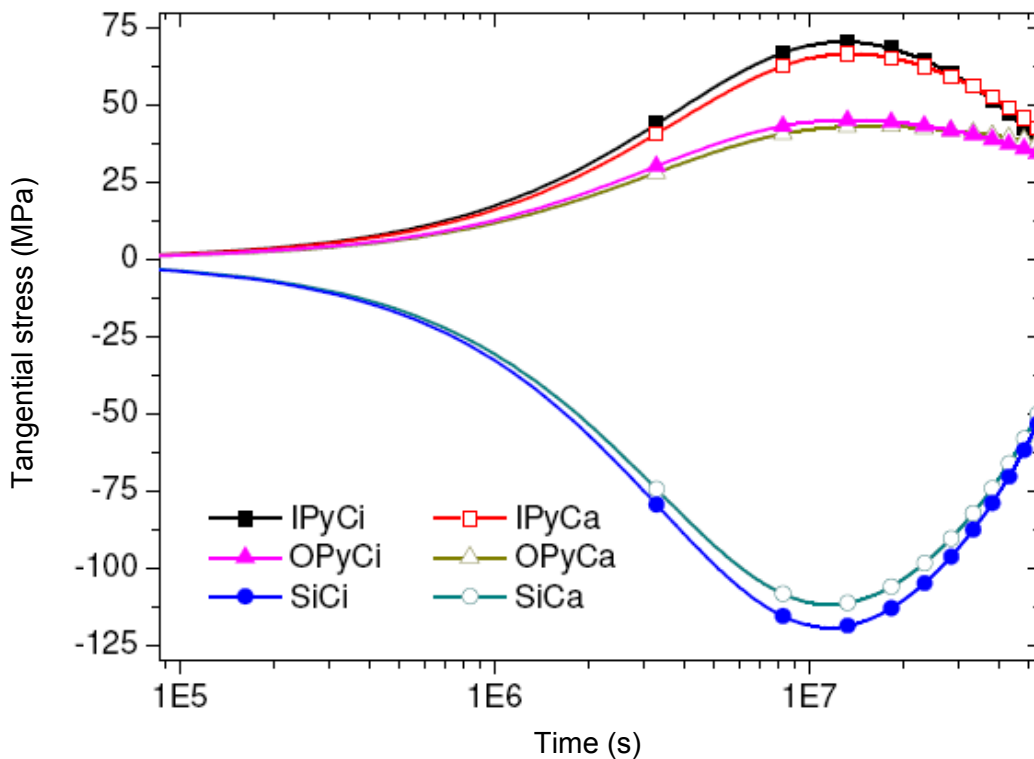


Figure 41: HFR K6/3 – Tangential stress curve during the irradiation

From the figure above it becomes apparent that a failure during the irradiation is to be expected first in the pyrolytic carbon and not in the SiC coating. Since a breakage of the PyC coatings has effects on the stress curve in the SiC coating, two scenarios are simulated for each case. First, the stress history in the jacket coatings is calculated for the case that all coatings remain intact. This history was subsequently the basis for the computation of the failure probability of the SiC coating and the PyC coatings. Following this, the stress history in the SiC coating was simulated for the case when the IPyC coating (conservative case) had failed earlier. The probability for SiC failure calculated from this multiplied by the probability of PyC failure from the first step then

yielded, together with the probability of SiC failure from the first step, the total probability of a failure of the SiC coating (see equation 61).

$$P_{SiC,1}(t) = 1 - \exp\left(-\ln(2) \cdot \left(\frac{\sigma_{SiC,1}(t)}{\sigma_0}\right)^m\right)$$

Equation 58

$$P_{PyC,1}(t) = 1 - \exp\left(-\ln(2) \cdot \left(\frac{\sigma_{PyC,1}(t)}{\sigma_{0,PyC}}\right)^{m_{PyC}}\right)$$

Equation 59

$$P_{SiC,2}(t) = 1 - \exp\left(-\ln(2) \cdot \left(\frac{\sigma_{SiC,2}(t)}{\sigma_0}\right)^m\right)$$

Equation 60

$$P_{SiC}(t) = P_{SiC,1}(t) + P_{PyC,1}(t) \cdot P_{SiC,2}(t)$$

Equation 61

Weibull parameter and average tensile strength of SiC and PyC were taken from [Pelletier 2003]. The following values were found for the pyrolytic carbon according to the data of BNFL.

$$\sigma_{0,PyC} = 190 \text{ MPa}$$

$$m_{PyC} = 7$$

For SiC both the average tensile strength and also the Weibull parameter (m) are a function of the temperature (T) and the fast fluence (Φ_s) [Allelein 1983]. For the tensile strength a minimal values applies of 196 MPa, for the Weibull parameter (m) a minimal value of 2 applies [Verfondern & Nabielek 1990].

$$\sigma_0 = \sigma_{00} \cdot \left(1 - \frac{\phi_s}{1,67 \cdot \phi_{s,0}}\right)$$

Equation 62

$$\phi_{s,0} = 10^{0,556 + \frac{650}{T}}$$

Equation 63

$$\sigma_{00} = 834 \text{ MPa}$$

$$m = m_0 \cdot \left(1 - \frac{\phi_s}{1,67 \cdot \phi_{s,m}} \right)$$

Equation 64

$$\phi_{s,m} = 10^{0,394 + \frac{650}{T}}$$

Equation 65

$$m_0 = 8,02$$

The temperature (T) must be entered in Kelvin. The factor 1.67 in the denominator of equation 62 and equation 64 was used for converting the fast neutron fluence of/from EDN to >0.1 MeV. The assumed average tensile strength of 834 MPa and the Weibull parameter at the start of irradiation were taken from the literature [Verfondern & Nabelek 1990].

7.6 AVR 74/18

7.6.1 Mechanical particle failure

Table 37: Input data for the AVR 74/18

Burn-up:	4.8 % FIMA	σ_{00} unirradiated:	834 MPa
Fast neutron fluence (>0.1 MeV):	$0.8 \cdot 10^{25} \text{ m}^{-2}$	σ_{00} irradiated:	806 MPa
Irradiation temperature:	~ 820 °C	m_0 unirradiated:	8,02
Irradiation time:	480 efpd	m_0 irradiated:	7,63

The simulation of the mechanical failure behavior of the coated particles in AVR 74/18 was conducted according to the assumed irradiation history in two steps with a declining temperature in each case (see Fig. 42). The calculation revealed a low probability for the failure of a PyC coating of about $4 \cdot 10^{-3}$ but a probability of zero for a failure of the SiC coating since in the latter only compressive stresses occurred in the tangential direction. Although low tensile

stresses occurred in the radial direction (~15 MPa), these were neglected within the scope of the model employed. Therefore, the probability of a total failure of the particle was also zero.

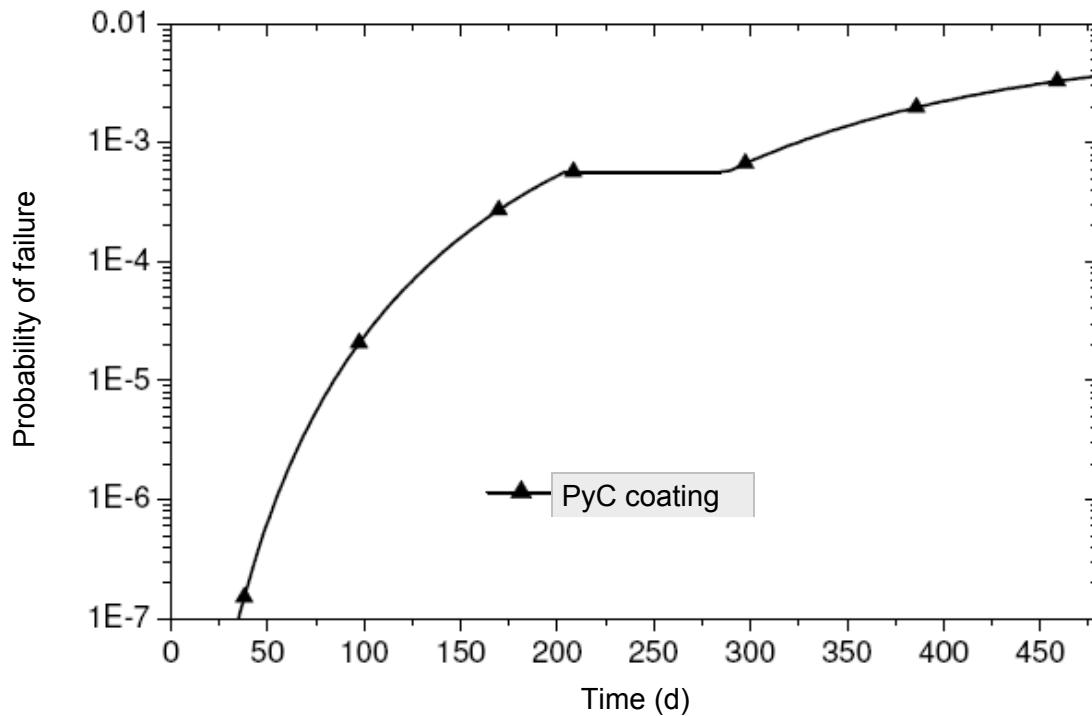


Figure 42: AVR 74/18 – calculated probability for failure of a PyC coating during irradiation

During the bakeout experiment there was also no noteworthy failure probability for the SiC coating. This agrees with the measurement of the Kr-85 release during the experiment, which gave no indication of particle failure. In Figure 43, the temperature curve, the Kr-85 release and the calculated failure probabilities of the PyC coatings, the SiC coating in the case of an already failed PyC coating and of the SiC coating in general are represented. The failure criterion is the failure of the SiC coating.

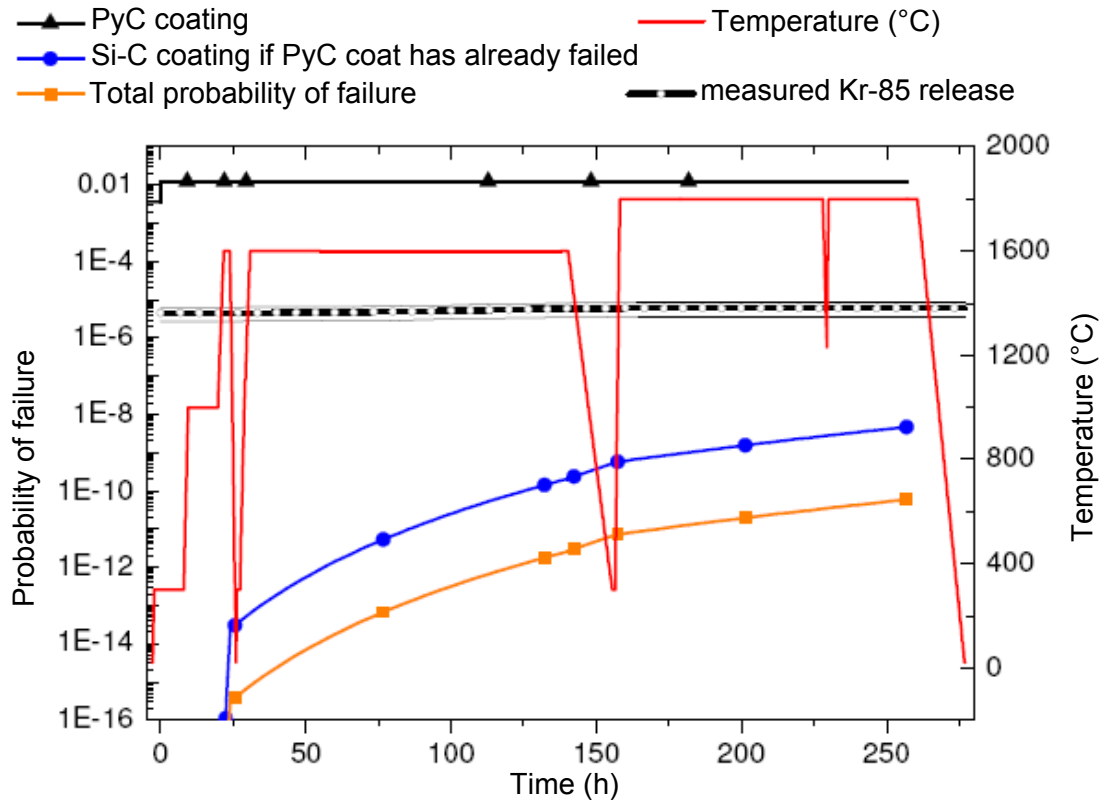


Figure 43: AVR 74/18 – particle failure probability and measured Kr-85 release

7.6.2 Fission product release (Cs-137) by diffusion

The simulation of the Cs-137 release showed a deviation from the measured values by a power of ten in the first heating step and even four powers of ten for the second heating phase at 1700°C. Besides these small releases due to diffusion through the jacket coatings, in the experiment also no release could be detected due to intensified matrix contamination from the AVR.

An approach of the simulation result to the measured release portions could be achieved by reducing the diffusion coefficient for cesium in the SiC coating by a factor of 20, therefore a substantially stronger retention capacity of SiC for cesium was assumed than previously. Another possibility for explaining the low Cs-137 release that was not verified here would be an elevated storage capacity of the graphite matrix. However, even this could not fully explain the effect.

A satisfactory agreement of the simulation with the experiment results could not be achieved with the model employed. Apparently, the material data used (diffusion coefficients) are biased by great uncertainties.

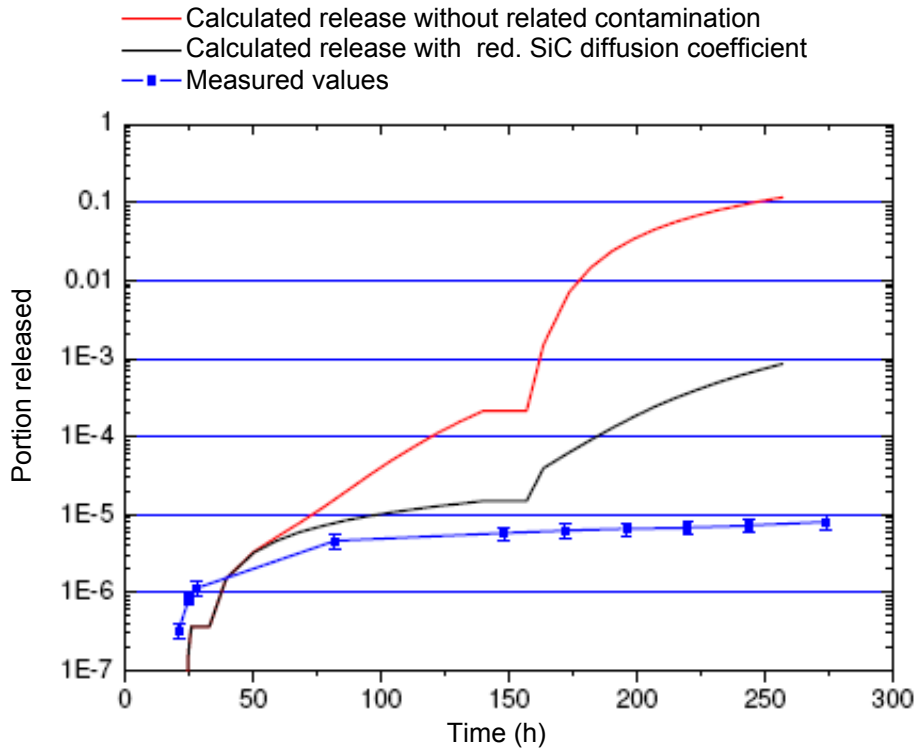


Figure 44: AVR 74/19 Bakeout experiment – calculated and measured Cs-137 release

7.7 HFR K6/2

7.7.1 Mechanical particle failure

Table 38: Input data for the HFR K6/2

Burn-up:	9.3 % FIMA	σ_{00} unirradiated:	834 MPa
Fast neutron fluence (>0.1 MeV):	$4.6 \cdot 10^{25} \text{ m}^{-2}$	σ_{00} irradiated:	650 MPa
Irradiation temperature:	~ 940 °C	m_0 unirradiated:	8,02
Irradiation time:	249 efpd	m_0 irradiated:	5,42

The results of the simulation of the mechanical particle failure during the irradiation of HFR K6/2 are shown in Fig. 45. One can see that the failure probability of the PyC first increases rapidly and after about 50 days irradiation time remains constant at roughly $6 \cdot 10^{-4}$. This corresponds to the calculated stress curve. Figure 41 shows the stress curve of HFR K6/3, which is similar to the curve of HFR K6/2.

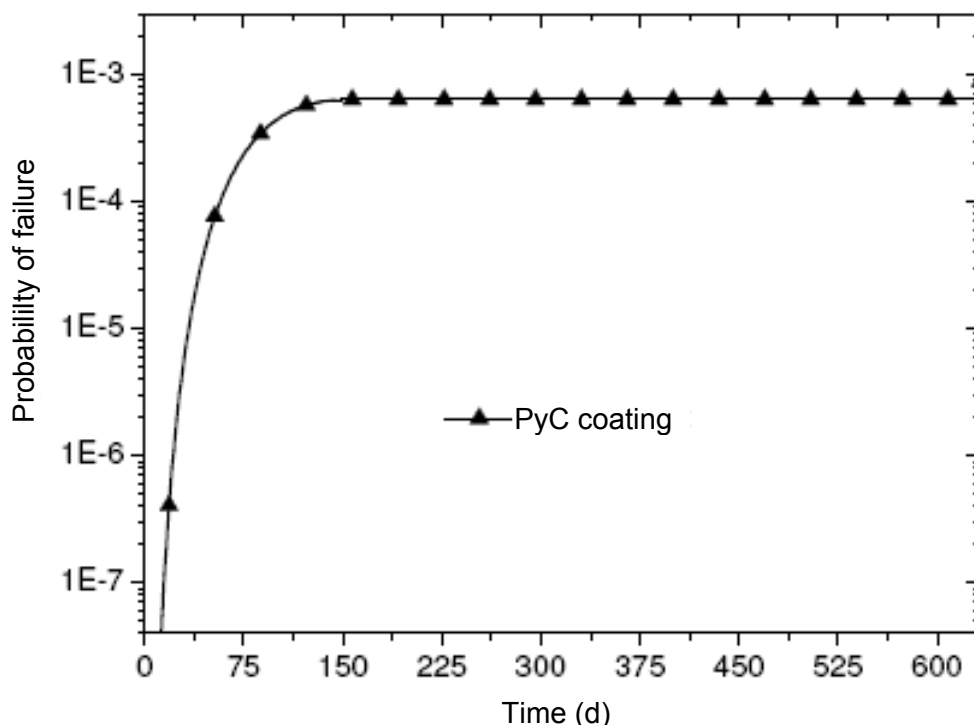


Figure 45: HFR K6/2 – calculated probability for failure of a PyC coating during irradiation

The calculated total probability of SiC failure and with it, of particle failure, is negligibly small. This also becomes understandable from the stress curve since the contracting PyC coatings induce a tangential compressive stress in the SiC coating that counteracts the building-up gas pressure in the particle interior. It is therefore to be assumed that at the end of the irradiation, no irradiation-related defective particles were present. This agrees with the reports on the HFR K6 irradiation experiment [Nabielek et al. 1993].

During the bakeout experiment, the calculated failure probability of the PyC coatings remained essentially unchanged. Due the rising gas pressure in the particle, however, the stress increased (see Fig. 46) and with it the probability of failure of the SiC coating. In the first heating step at 1600°C, one can observe a steady rise, which is traceably primarily to the release of

fission gas and oxygen from the particle core and the expansion of the gas due to the rise in temperature. In the second heating phase, this trend continues until the tangential stresses in the SiC coating have reached roughly 150 MPa. From the stress diagram it becomes clear that the SiC coating absorbs approximately the entire mechanical load and the stresses in the PyC coatings remain comparatively small.

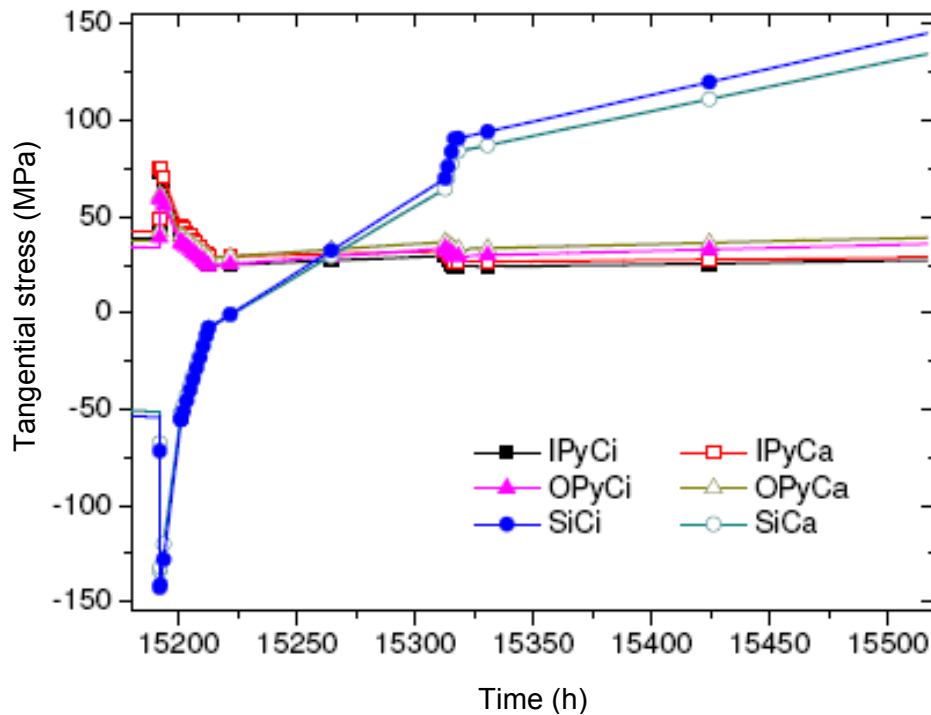


Figure 46: HFR K6/3 –calculated tangential stress curve during the bakeout test

Finally, Fig. 47 shows the calculated failure probability of HFR K6/2 during the bakeout experiment. It reaches a value of about $2 \cdot 10^{-4}$ and is therefore about one power of ten higher than the measured Kr-85 release. The latter reached a value of only $1 \cdot 10^{-5}$ FR. The total probability of particle failure here is apparently dominated by the failure probability of the SiC coating without defective PyC coating. Although the probability of failure in the case of already failed PyC coating is clearly higher, it plays practically no part here due to the low probability of PyC failure under the present conditions.

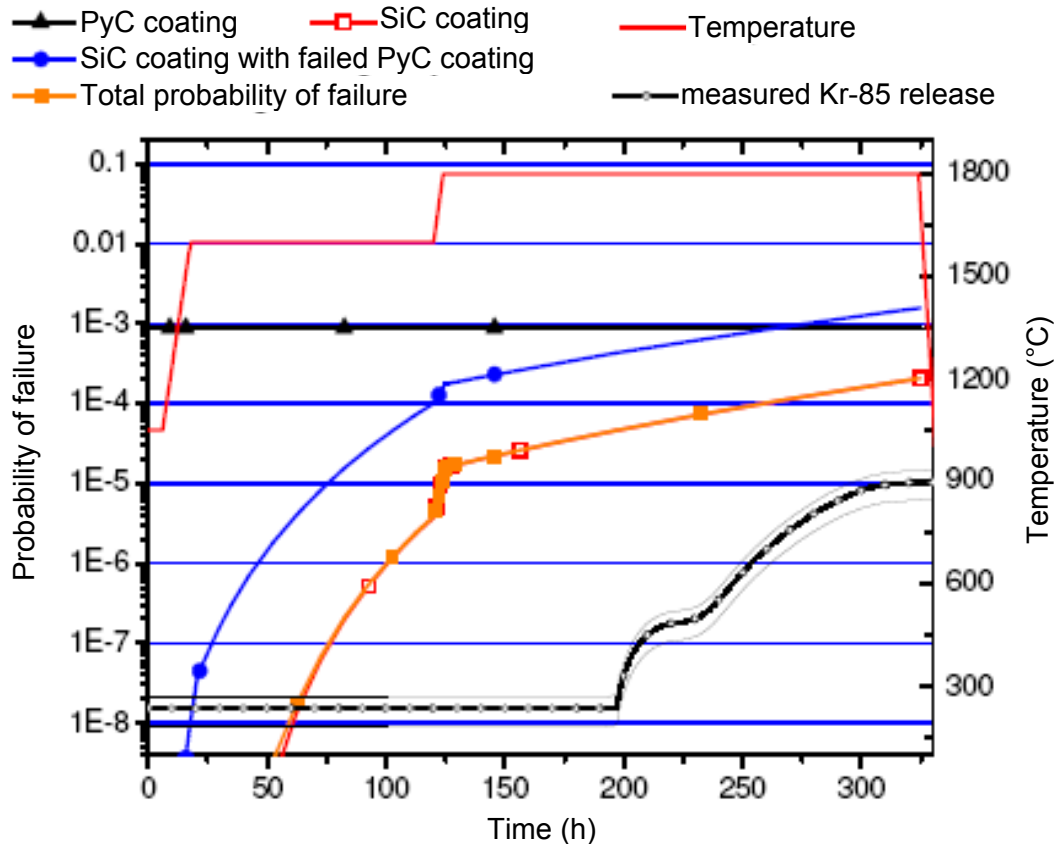


Figure 47: HFR K6/2 – particle failure probability and measured Kr-85 release

The initially practically not present and then suddenly rising Kr-85 release from individual particles at about 200 hours of experiment time can be predicted only with difficulty with the model employed here.

7.7.2 Fission product release by diffusion

The formation and diffusion of cesium during the irradiation of HFR K6/2 led in the calculation to typical cesium profiles in the graphite matrix and the coated particles, which are shown in Figures 48 and 49 respectively.

One can clearly perceive that the SiC coating represents the real barrier for cesium release and that the fission product concentration in the matrix is negligibly small compared to the concentration in the particle. Furthermore, it can be affirmed that in the simulation large parts of the cesium inventory were released in the buffer layer. These results agree substantially with the micro-probe measurements from the past [Schenk et al. 1988].

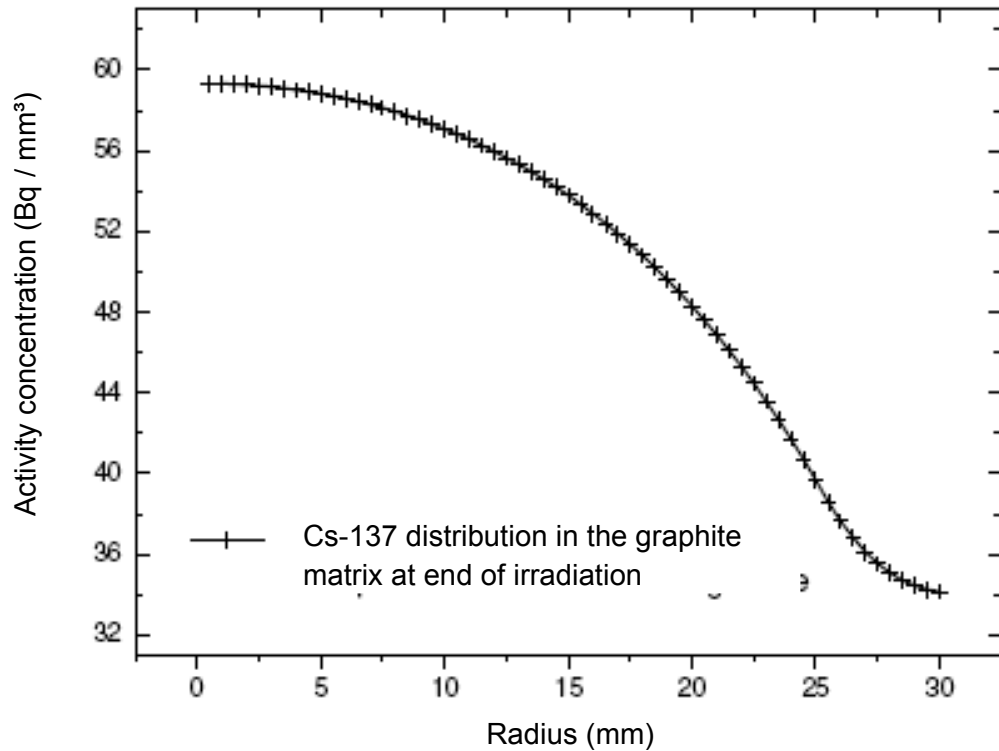


Figure 48: HFR K6/2 – calculated Cs-137 distribution in the graphite matrix at the end of the irradiation.

The calculation of the release during the bakeout experiment overestimated the measured release by several orders of magnitude as already occurred in the case of AVR 74/18 (see Fig. 30). Here also, the result could be approximated by reducing the diffusion coefficient.

Apparently, the particles and jacket coatings that were produced for the proof fuel elements displayed further improved retention capacity at accident temperatures compared to the previous charges of German production.

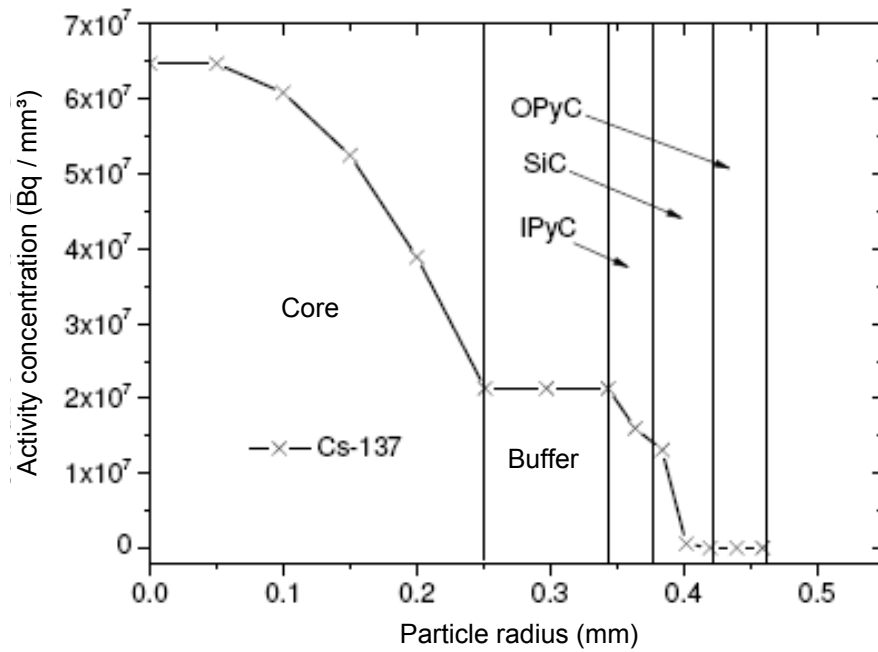


Figure 49: HFR K6/2 – calculated Cs-137 distribution in a coated particle at the end of the irradiation

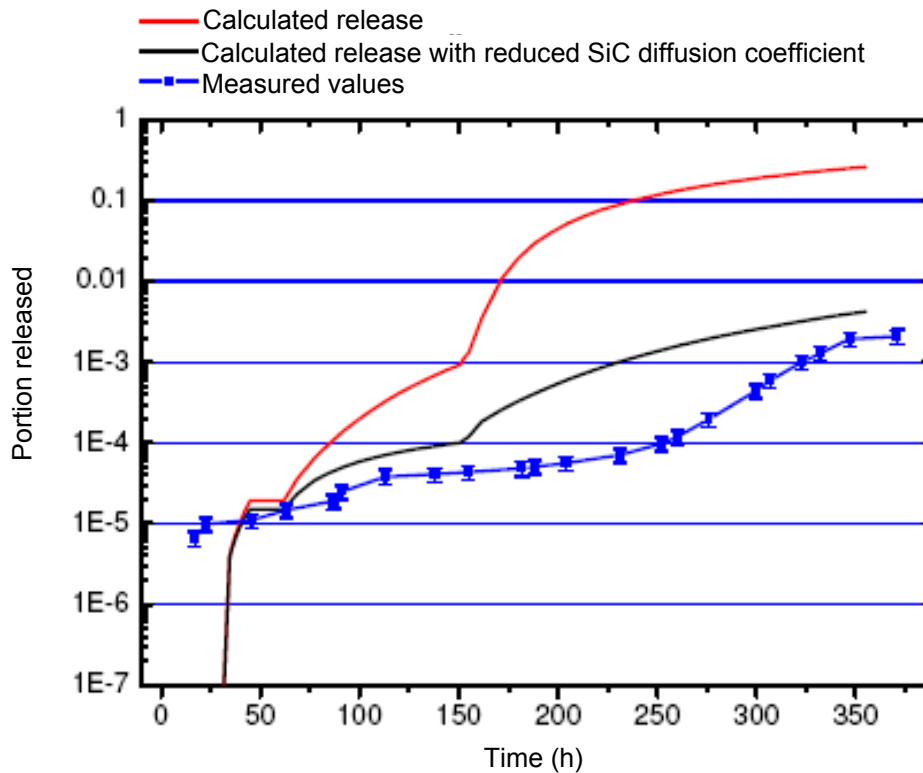


Figure 50: HFR K6/2 bakeout experiment – calculated and measured Cs-137 release

7.8 HFR K6/3

7.8.1 Mechanical particle failure

Table 39: Input data for the HFR K6/3

Burn-up:	9.7 % FIMA	σ_{00} unirradiated:	834 MPa
Fast neutron fluence (>01 MeV)	$4.8 \cdot 10^{25} \text{ m}^{-2}$	σ_{00} irradiated:	642 MPa
Irradiation temperature:	~ 940 °C	m_0 unirradiated:	8.02
Irradiation time:	634 efpd	m_0 irradiated:	5.31

The results of the mechanical particle failure simulation during irradiation are naturally close to each other since the HFR K6/3 and HFR K6/2 were irradiated in a common test capsule. The failure probability of the PyC first increases rapidly and after about 50 days of irradiation time remains constant at roughly $6 \cdot 10^{-4}$.

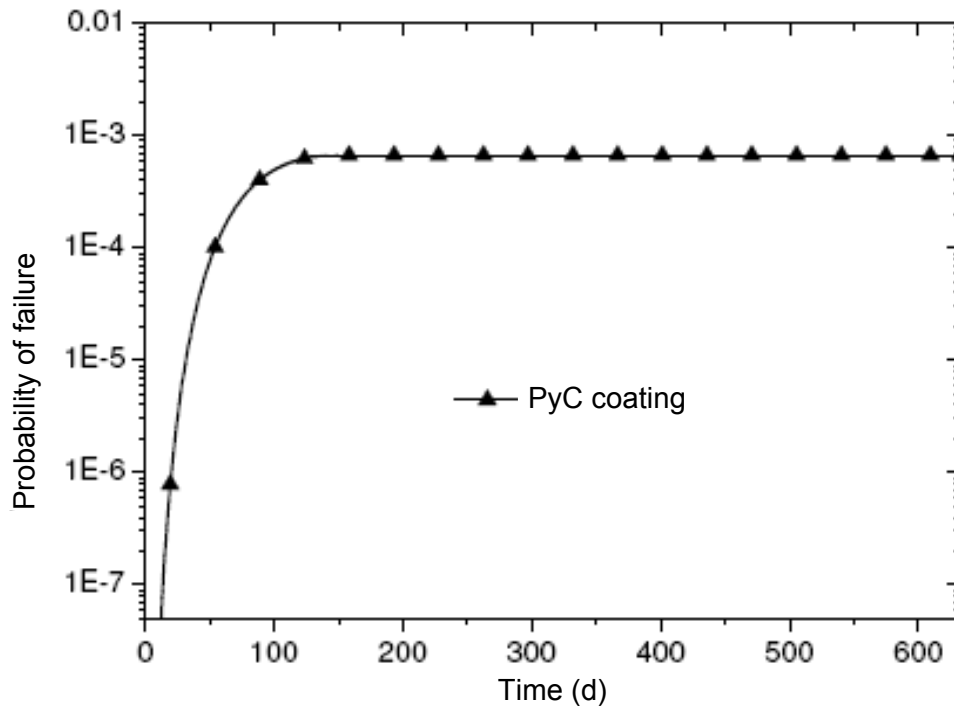


Figure 51: HFR K6/3 – calculated probability for failure of a PyC coating during irradiation

The calculated total probability of SiC failure and with it, of particle failure, during the irradiation is negligibly small. This also becomes easily understandable from the stress curve which clearly

shows that the contracting PyC coatings induce a tangential compressive stresses in the SiC coating that compensate for the gas pressure in the particle. It is therefore to be assumed that with high probability no defective particles were present at the end of the irradiation.

Fig. 52 shows the failure probability of HFR K6/3 during the bakeout experiment. As in the case of HFR K6/2, the failure rate increases linearly during the 1600°C heating phase with increasing gas release from the UO₂ core and then increases in steps during the following heating phases at higher temperatures. The calculated portion of failed particles at the end of the heating experiment runs to about $4 \cdot 10^{-4}$ and is therefore approximately in the range of the measured Kr-85 release.

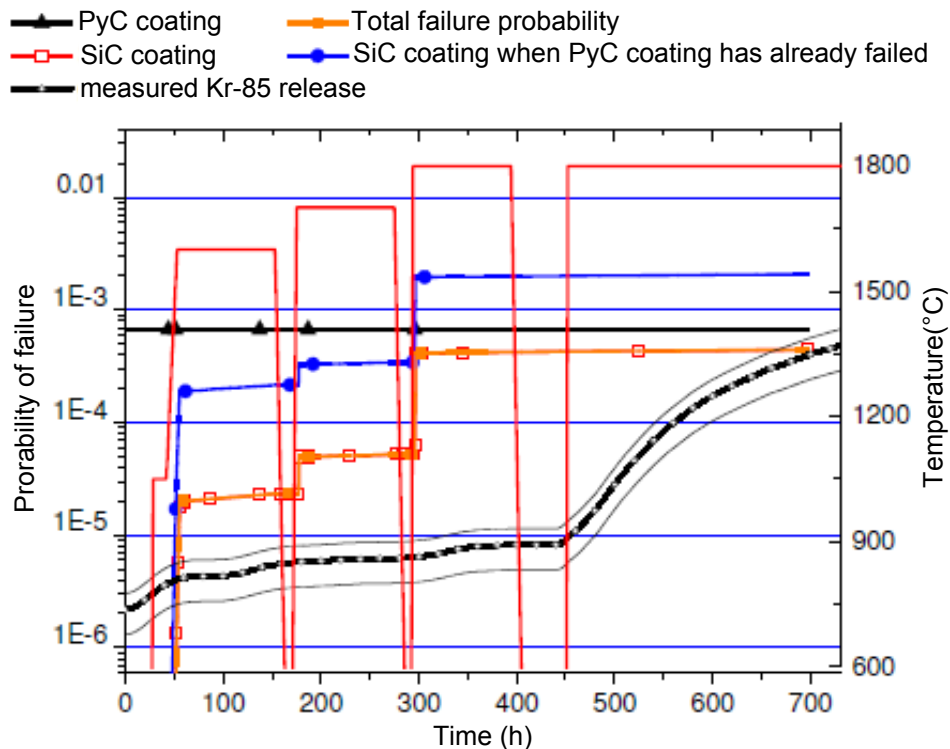


Figure 52: K6/3 – particle failure probability and measured Kr-85 release

Strong tangential alternating tensile and compressive loads occurred in the SiC coating caused by the cooling phase and the extreme temperature changes between the experimental phases related to it. In the failure model applied here, which only analyzes the maximal primary stresses, this did not lead to an increased failure rate. In a more detailed analysis, certainly, it would be necessary to consider additionally processes that are triggered by the thermal cycling.

The discrepancy between model and experiment at the start of the last heating phase at 1800°C is striking. Here, in the experiment, a rapidly increasing Kr-85 release could be observed, which the model does not predict. A parallel to HFR K6/2 is the fact that an increased failure occurs upon reaching a threshold load.

7.8.2 Fission product release by diffusion

The release of solid fission products could only be demonstrated for Cs-137 and was therefore also only considered in the calculations for cesium. As was already confirmed in the previous experiments, the simulation produced substantially higher release values than were actually measured. In particular, during the first one-hundred hours at 1600°C and the following hundred hours at 1700°C the calculation exceeded the measurement by three to four powers of ten. During the last two heating phases at 1800°C the simulation produces a release of almost 50. A reduction in the pre-factor of the diffusion coefficient of cesium by a factor of 20 as practiced in the previous calculations again led to a distinct drawing together of measurement and simulation in the last heating phases. The release at 1600°C and 1700°C was so low that it can only be explained with the model employed here with difficulty. In Fig. 53, the results of the calculations and the measured values and the results of a calculation performed with the FRESCO program [Verfondern & Nabielek, 2008] and shown.

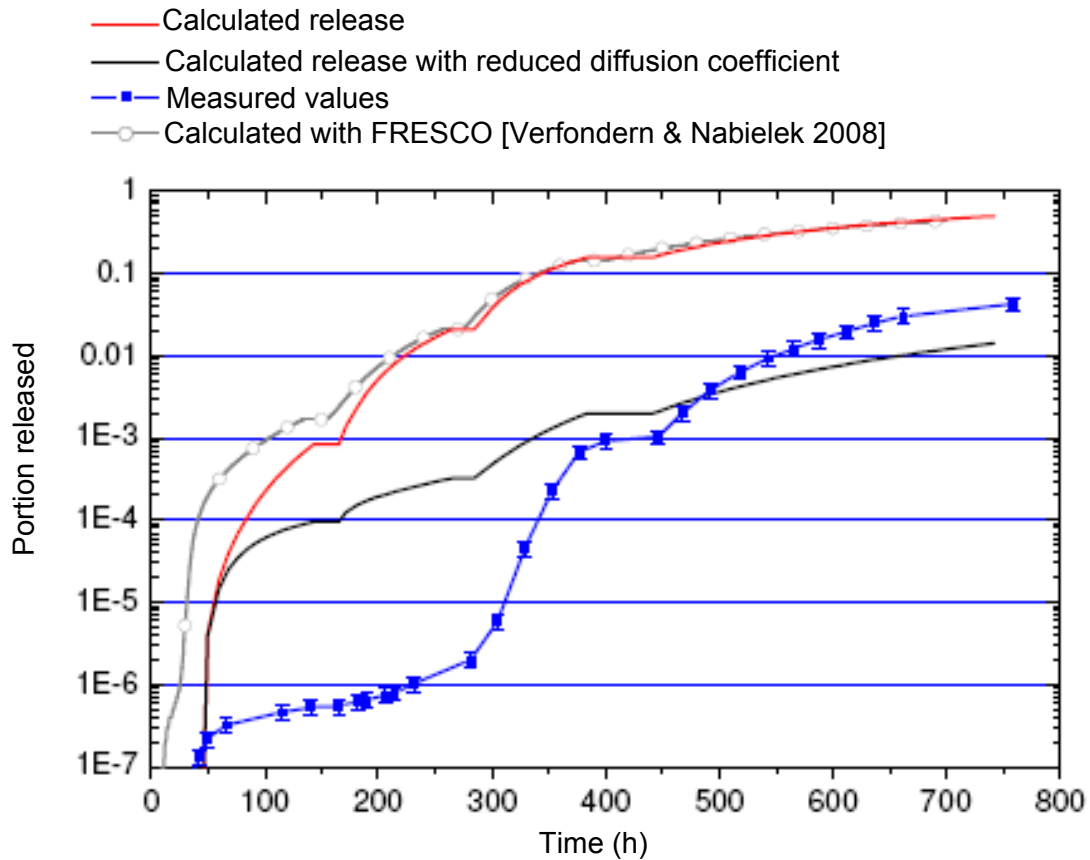


Figure 53: HFR K6/3 bakeout experiment – calculated and measured Cs-137 release

The quantitative cesium profiles in a coated particle of HFR K6/3 calculated with standard parameters and reduced diffusion coefficients are plotted in Fig. 54. For comparison, the qualitative concentration curve measured by using EDX (see Chapter 6.4.4) is shown.

In all three cases, one recognizes that the SiC coating represents the actual barrier layer and that the inventory remaining in the particle was retained behind it. Conversely, this means that the greatest part of the cesium atoms that were able to overcome the SiC coating was also released. The 50% release of the calculation with standard coefficients is reflected in the inventory remaining in the SiC coating calculated with standard coefficients, which amounts to approximately the remaining 50%.

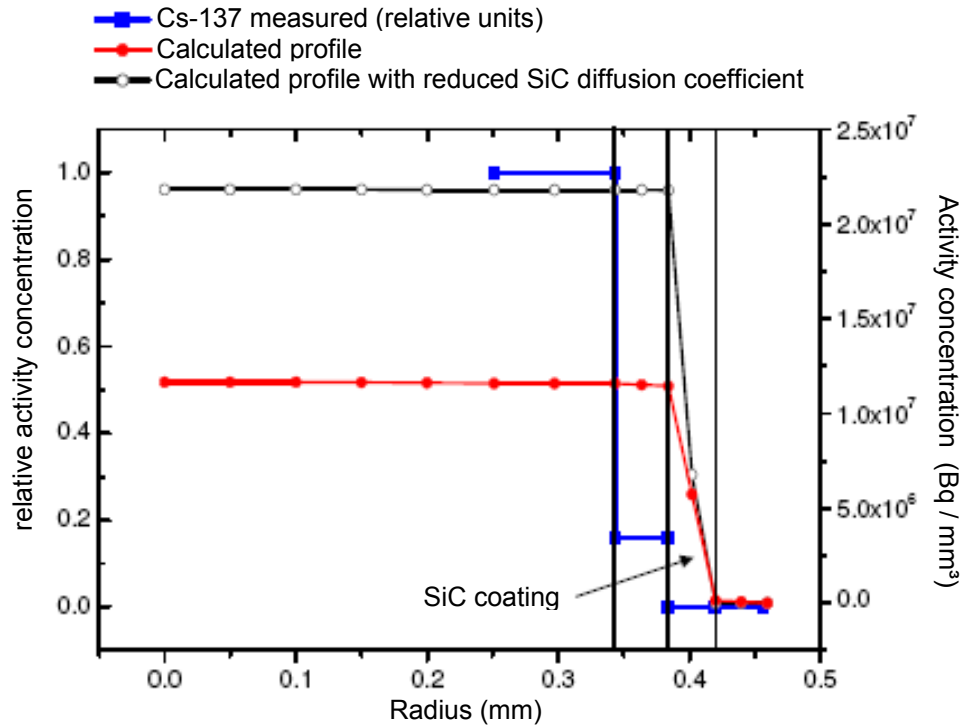


Figure 54: K6/3 – calculated and measured Cs-137 distribution in the coated particle at end of the experiment

7.9 HFR Eu1bis irradiation

The diffusive release of solid fission products during the irradiation was calculated as a basis for computing the heating experiment for all HFR Eu1bis fuel elements.

Since in the case of HFR Eu1bis, besides the Cs-137 release, also Cs-134 and, above all, releases of the short-lived isotope Ag-110m could be measured, a calculation was also performed for this. This caused, as Fig. 55 shows, a significant release already during the irradiation phase in the range of $2 \cdot 10^{-3}$. The decisive factors here were apparently the high irradiation temperature of 1250°C and the known high volatility of silver.

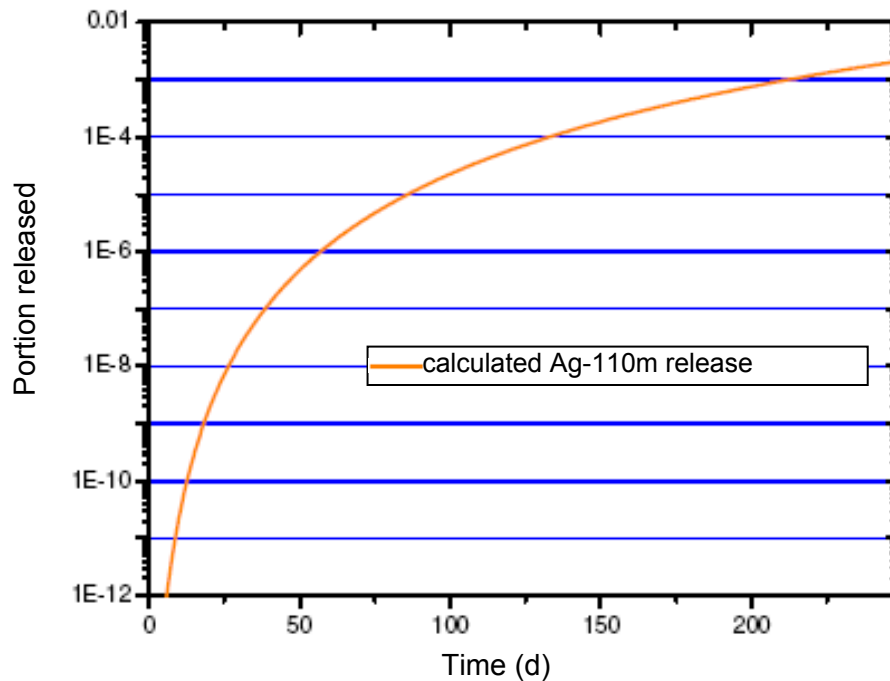


Figure 55: HFR Eu1bis – calculated Ag-110m release during irradiation

Fig. 56 and Fig. 57 show the release of cesium and the calculated Cs-137 profile in the graphite matrix at the end of the irradiation. The calculated release of Cs-137 and Cs-134 by diffusion from intact particles moved in the range of $3 \cdot 10^{-6}$ FR and therefore in the range of the matrix contamination. Any higher releases during the irradiation for which indications were found during the bakeout experiments would accordingly have to stem from individual defective particles or be caused by a clearly higher irradiation temperature.

Apparently the higher irradiation temperature, compared with the HFR K6, resulted in a clearly higher release of cesium in the graphite matrix. The calculated concentration in the matrix of HFR Eu1bis 1 at the end of irradiation amounted to about ten times the value calculated for HFR K5/2 (see Fig. 48 and Fig. 57).

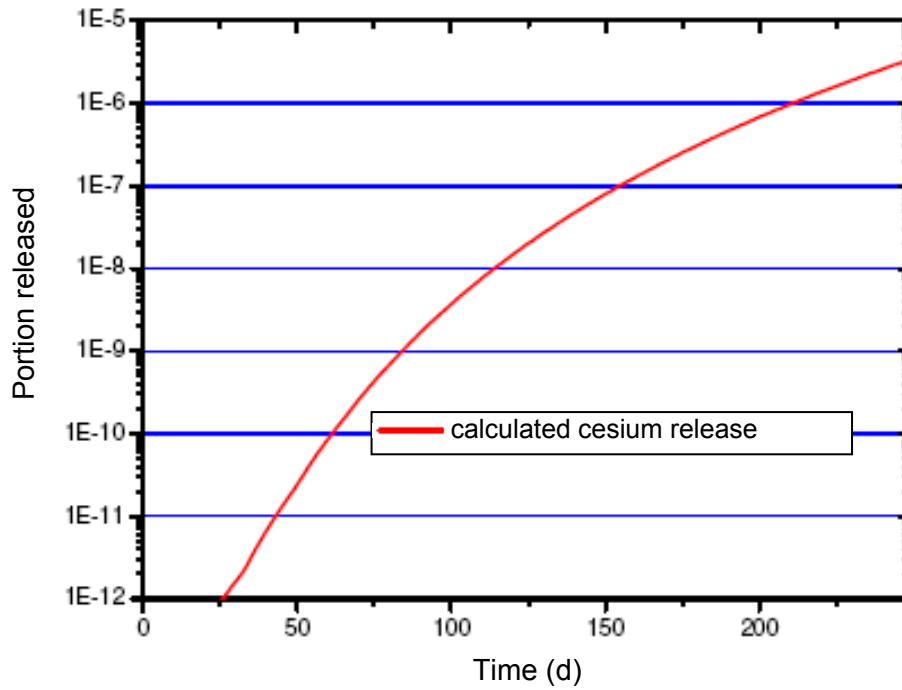


Figure 56: HFR Eu1bis – calculated cesium release during irradiation

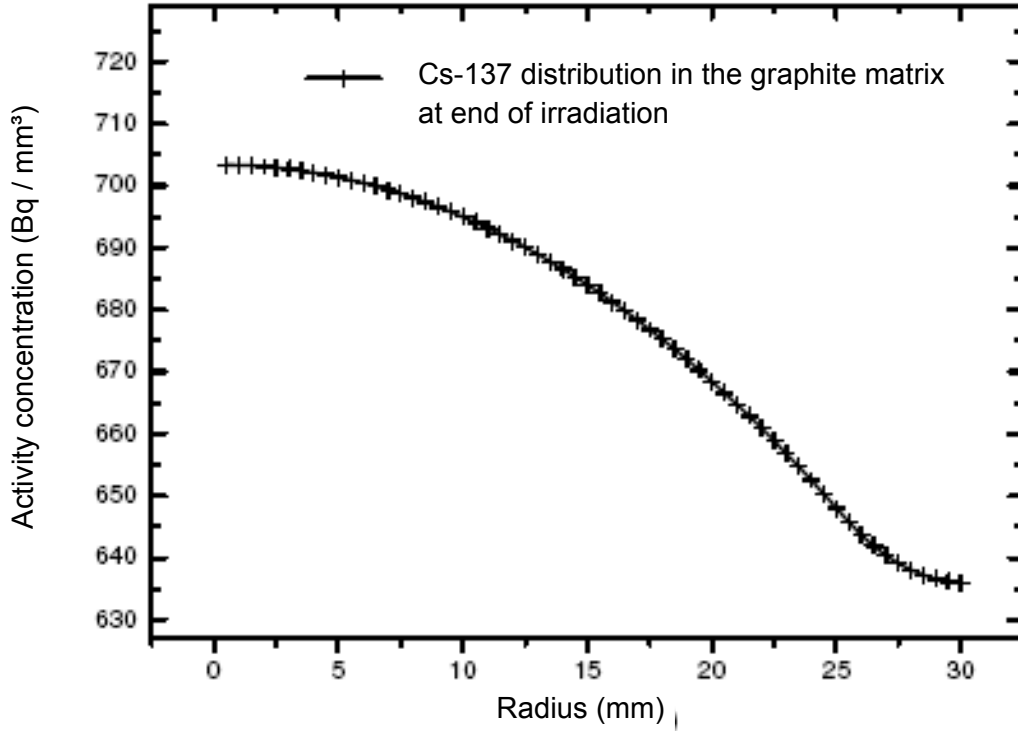


Figure 57: HFR Eu1bis – calculated Cs-137 distribution in the graphite matrix at the end of the irradiation.

7.10 HFR Eu1bis1

7.10.1 Mechanical particle failure

Table 40: Input data for the HFR Eu1bis 1

Burn-up:	9.34 % FIMA	σ_{00} unirradiated:	834 MPa
Fast neutron fluence (>0.1 MeV):	$3.02 \cdot 10^{25} \text{ m}^{-2}$	σ_{00} irradiated:	679 MPa
Irradiation temperature:	~ 1250 °C	m_0 unirradiated:	8.02
Irradiation time:	249 efpd	m_0 irradiated:	5.83

The simulation of the mechanical particle failure of HFR Eu1bis 1 during the irradiation resulted in an extremely low failure probability of about $1 \cdot 10^{-9}$. This followed chiefly from the probability of failure of the SiC coating when the PyC coating had already failed. The probability of a failure of the PyC coating in the diagram first increases rapidly and then remains at $4 \cdot 10^{-4}$.

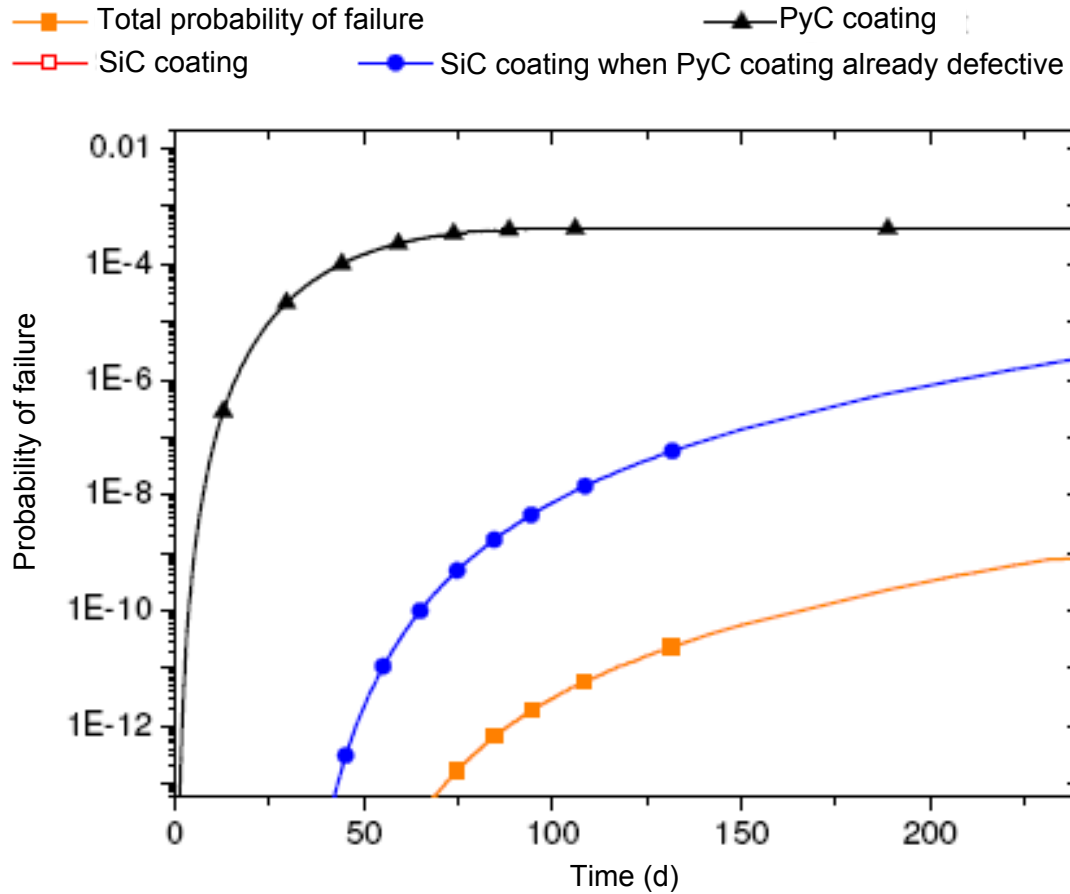


Figure 58: HFR Eu1bis1 – calculated probability of a particle break during irradiation

Figure 67 shows the tangential stress curve of HFR Eu1bis 4 during the irradiation, which is comparable with the stress curves of the remaining fuel element irradiated within the scope of HFR Eu1bis. Due to the elevated temperature and the accelerated irradiation, the stress values reach the reversing point relatively quickly, after which the PyC coatings no longer contract but begin to expand. The maximal tensile stress in the PyC coatings therefore occurs at about $7 \cdot 10^6$ seconds or 81 days. The subsequent expansion ultimately leads, together with the building-up gas pressure in the interior, to a tangential tensile stress of about 25 MPa in the SiC coating. However, this is too low to cause any noteworthy failure rate.

In the case of an IPyC coating that has already failed, conversely, a tensile stress appears very early in the SiC coating (see Fig. 59), which ultimately reaches about 80 MPa. The failure probability resulting from this is about $2 \cdot 10^{-6}$.

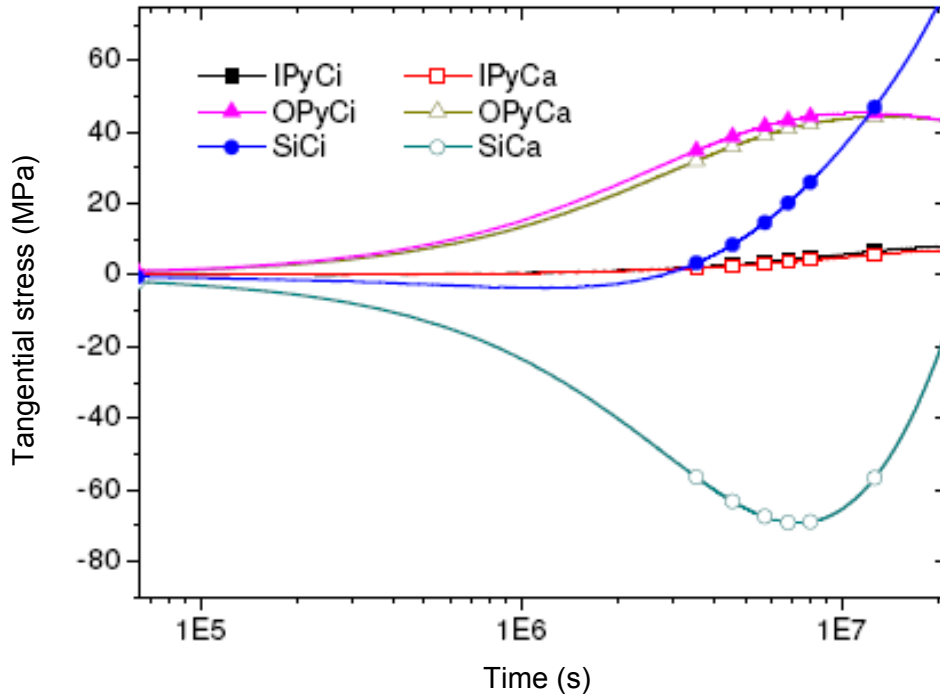


Figure 59: HFR Eu1bis 1– calculated tangential stress curve during the irradiation when the IPyC coating has already failed.

The calculated failure probability during the bakeout of HFR Eu1bis 1 showed in the first heating phase at 1250°C (irradiation temperature) as expected displayed no change relative to the irradiation. In the simulation of the subsequent heating phases at 1600 and 1700°C, the total probability of particle failure rose to about $2 \cdot 10^{-6}$. It was therefore about one power of ten below the measured Kr-85 release. Both calculation and also the measured Kr-85 release therefore show no particle failure in the case of HFR Eu1bis 1 since both values were clearly below 10^{-4} .

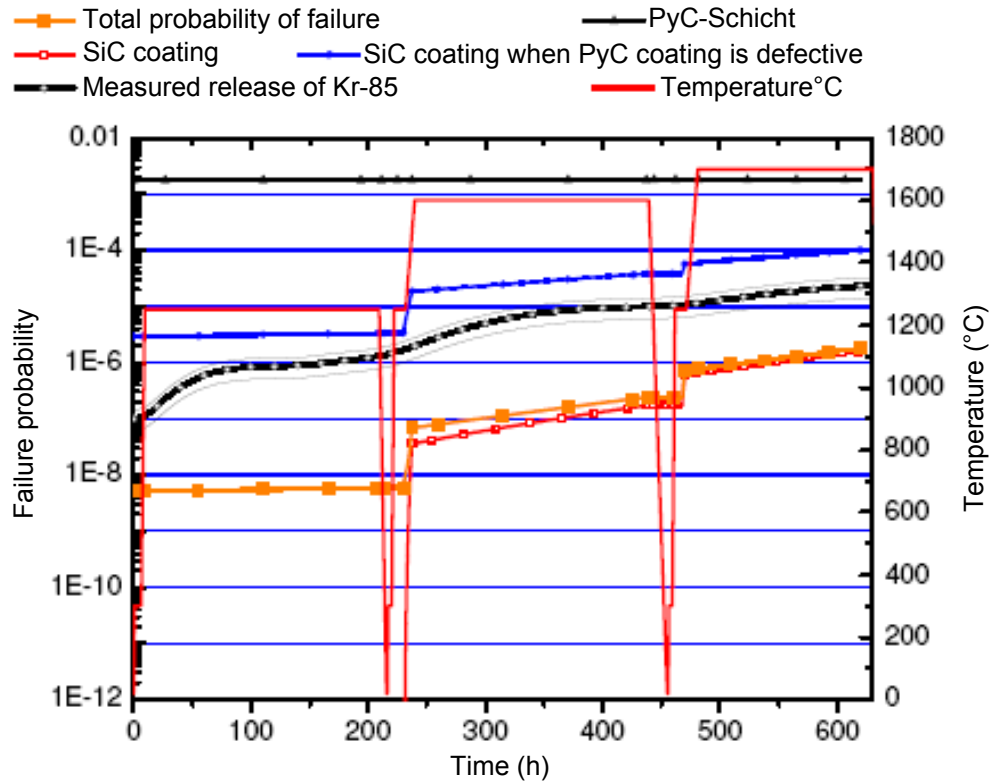


Figure 60: HFR Eu1bis1 – particle failure probability and measured Kr-85 release

7.10.2 Fission product release by diffusion

The calculation of the cesium release during the bakeout experiment HFR Eu1bis 1 showed that during the first heating phase in the experiment an unexpectedly large amount of cesium was released. While the first calculation gave the anticipated value of about $1 \cdot 10^{-6}$ FR, in the experiment a portion of $7.2 \cdot 10^{-5}$ FR (Cs-137) was measured. The high irradiation temperature and the related higher concentration of cesium in the graphite matrix was already allowed for in the simulation.

A possible explanation for the high release at 1250°C is that under some conditions a clearly higher initial contamination of the graphite matrix from the irradiation experiment was present. This was checked by a second calculation in which the equivalent of about 20 defective coated particles was input as additional contamination of the graphite matrix. As Fig 61 shows, this led to a good agreement between experiment and simulation. In addition, the calculation was compared with a FRESCO calculation [Verfondern & Nabielek 2008], which is also shown in Fig. 61.

The calculation of the Cs-137 release for the accident simulation at 1600°C gave a value of about 1% at the end of the 1600°C phase and approximately 5% at the end of the 1700°C phase. The deviation from the experiment amounted to about one power of ten. By reducing the diffusion coefficient (see HFR K6), this result could have been approximated further but this was decided against within the scope of this project.

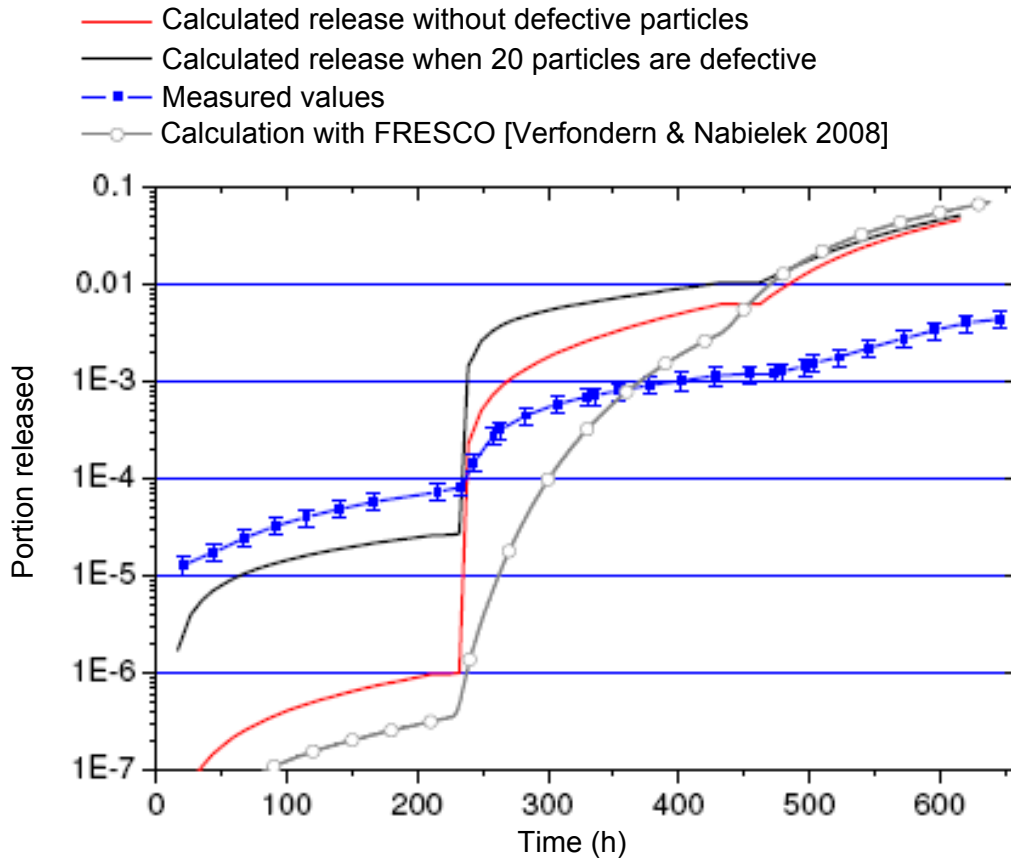


Figure 61: HFR Eu1bis1 bakeout experiment – measured and calculated cesium release

The calculation of the silver release by diffusion and the comparison with the measurement results gave a picture similar to that for cesium. Figure 62 clearly shows that the anticipated release of Ag-110m during the phase of operation simulation is approximately one power of ten below the measured values. In turn, the explanation for this could be found in an additional contamination of the graphite matrix. This can either be introduced from the outside or stem from a number of defective particles from the irradiation.

The release during the accident simulation at 1600°C is overestimated with the diffusion parameters used here by about two powers of ten. While the calculation gives a 60 percent release of the total inventory, the measured values displayed only a release in the range of about $7 \cdot 10^{-3}$.

Due to the missing measured values in the third heating phase, here only an upper limit for the release of Ag-110m can be reported. This is about 20% of the inventory, while the calculation predicts an almost total release.

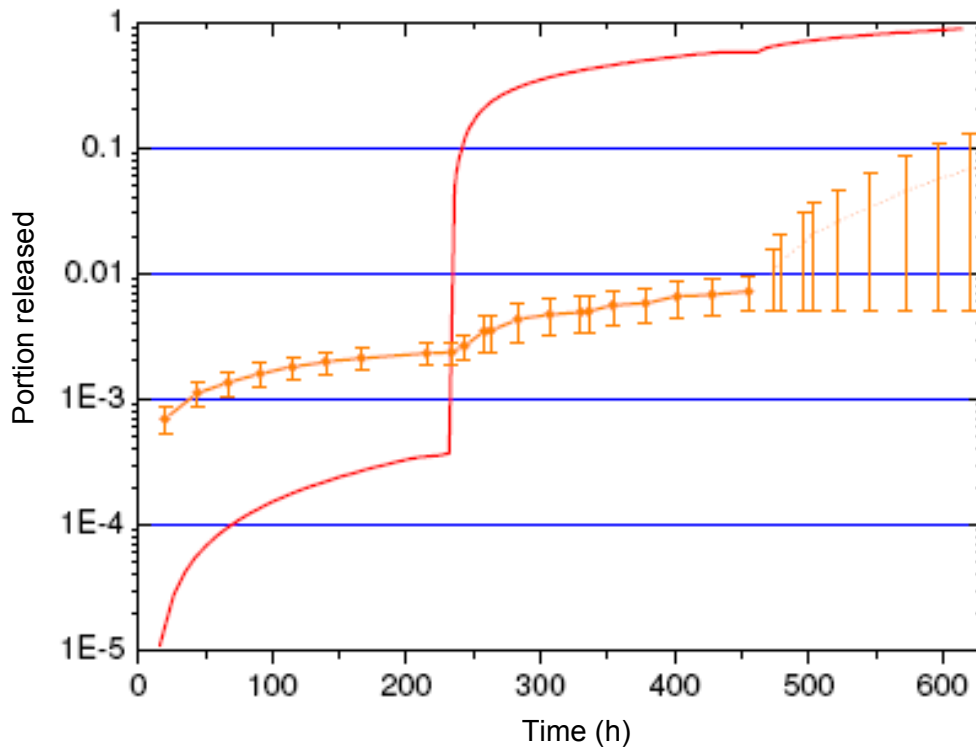


Figure 62: HFR Eu1bis1 bakeout experiment – measured and calculated silver release

7.11 HFR Eu1bis3

7.11.1 Mechanical particle failure

Table 41: Input data for the HFR Eu1bis 3

Burn-up:	11.07 % FIMA	σ_{00} unirradiated:	834 MPa
Fast neutron fluence (>0.1 MeV):	$3.98 \cdot 10^{25} \text{ m}^{-2}$	σ_{00} irradiated:	629 MPa
Irradiation temperature:	~ 1250 °C	m_0 unirradiated:	8,02
Irradiation time:	249 efpd	m_0 irradiated:	5,13

The calculation of the failure probability for the particles of HFR Eu1bis 3 during the irradiation experiments differs only insignificantly from the calculation for HFR Eu1bis 1. Due to the higher burn-up and the higher fast neutron flux (see Table 41), slightly higher stress values occur, which at the end of the irradiation result in a total failure probability of about $7 \cdot 10^{-8}$ (see Fig. 63).

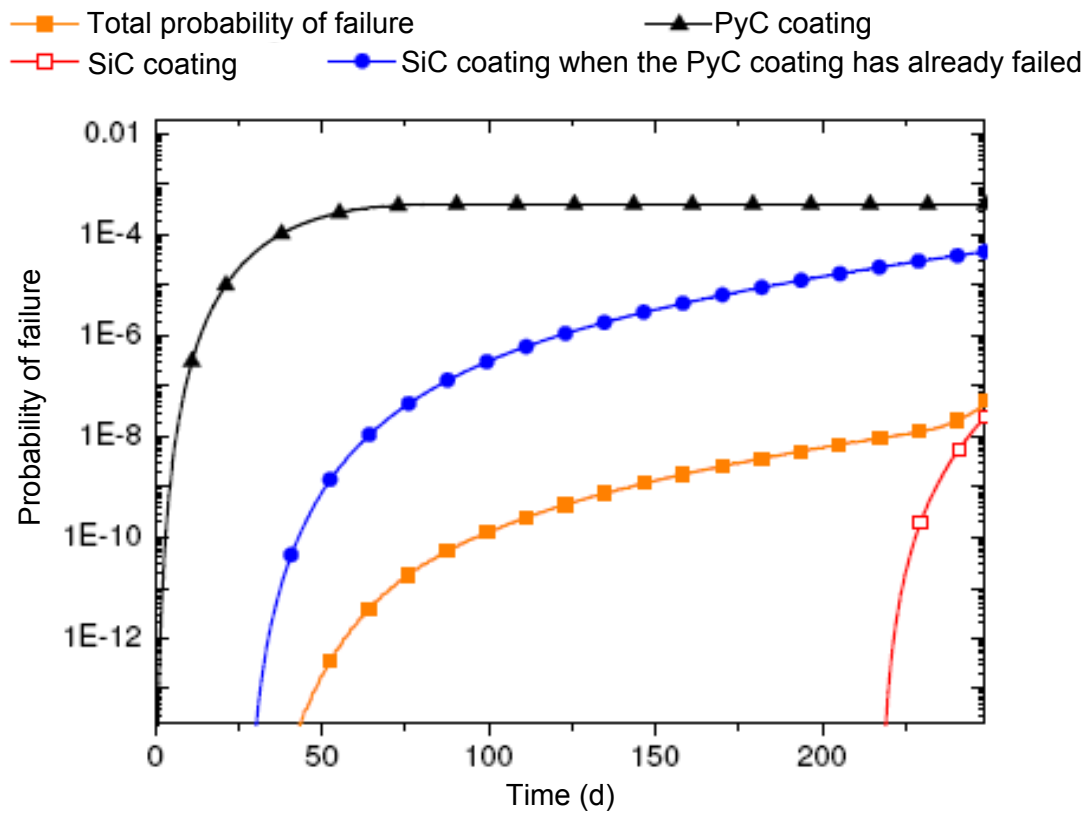


Figure 63: HFR Eu1bis3 – calculated probability of a particle break during irradiation

In the calculation of the failure probability for the accident simulation (see Fig. 64) the difference between the moderately burned-up fuel element HFR Eu1bis 1 and the highly burned-up fuel element HFR Eu1bis 3 becomes clearer. While the calculated failure probability of HFR Eu1bis 1 after 200 hours at 1600°C amounts to about $2 \cdot 10^{-7}$, for HFR Eu1bis 3 it is about one hundred times higher, about $3 \cdot 10^{-5}$. The measured Kr-85 release was about one power of ten lower. Broadly speaking, in agreement with the calculation and the measurement of the gas release, for HFR Eu1bis 3 also, it can be assumed that no particles will fail during the bakeout experiment.

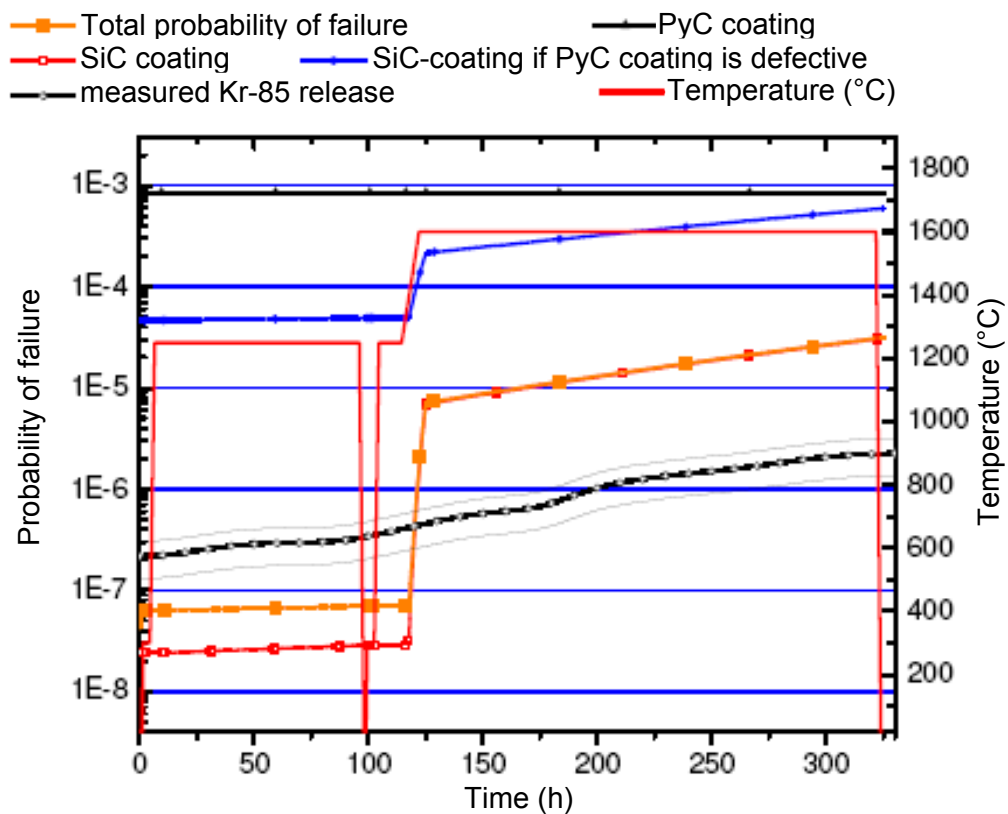


Figure 64: HFR Eu1bis3 – particle failure probability and measured Kr-85 release

7.11.2 Fission product release by diffusion

The calculation of the diffusive release of solid fission products for the first heating phase (i.e. at operating temperature) led to a comparable result to that of the calculation of HFR Eu1bis 1. Both for cesium and also for silver, the calculation underestimated the actual release considerably without additional contamination of the graphite matrix in the order of magnitude of

the inventory of 10 particles. Only by adding this starting condition was good agreement obtained between measurement and calculation.

For the second heating phase, the accident simulation at 1600°C, a good agreement could be achieved between the simulation of the Cs-137 release and the release measurement. To be certain, the trend from the previous calculations was confirmed according to which the calculation overestimated the release.

In turn, the release of Ag-110m was overestimated by more than two powers of ten.

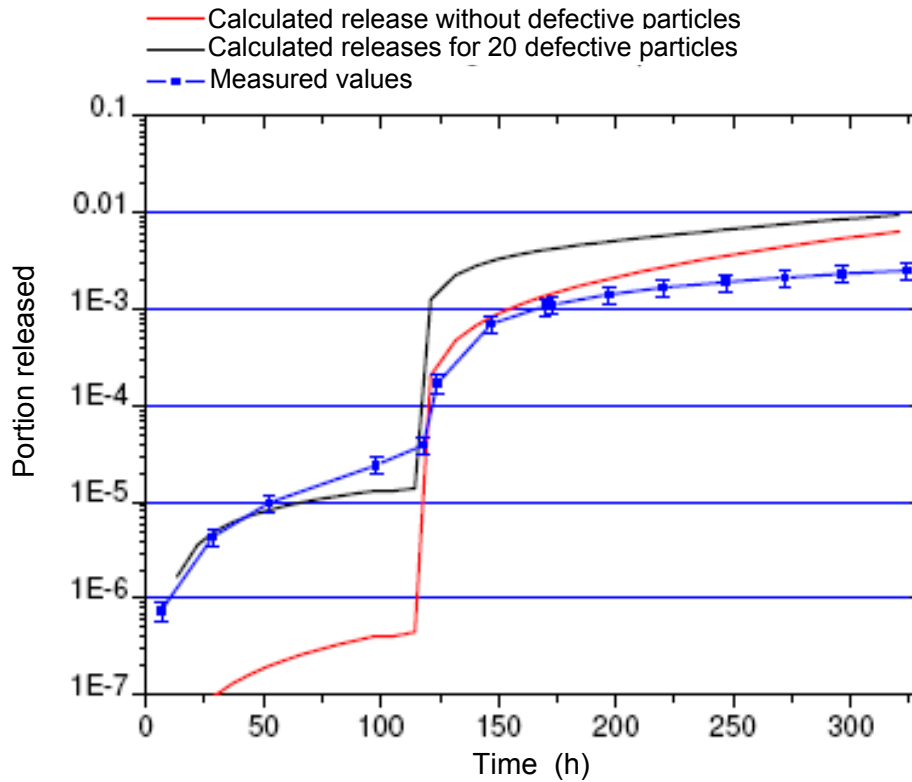


Figure 65: HFR Eu1bis3 bakeout experiment – measured and calculated cesium release

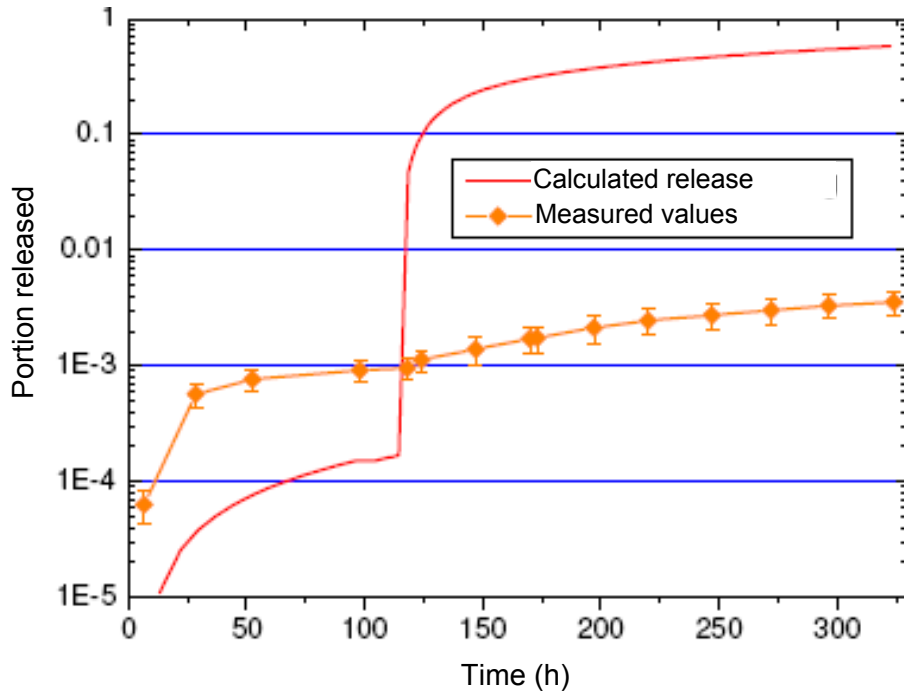


Figure 66: HFR Eu1bis3 bakeout experiment – measured and calculated silver release

7.12 HFR Eu1bis 4

7.12.1 Mechanical particle failure

Table 42: Input data for the HFR Eu1bis 4

Burn-up:	11.07 % FIMA	σ_{00} unirradiated:	834 MPa
Fast neutron fluence (>0.1 MeV):	$3.82 \cdot 10^{25} \text{ m}^{-2}$	σ_{00} irradiated:	637 MPa
Irradiation temperature:	~ 1250 °C	m_0 unirradiated:	8.02
Irradiation time:	249 efpd	m_0 irradiated:	5.25

The irradiation of HFR Eu1bis 4 did not differ essentially from HFR Eu1bis 3. Due to the position below HFR Eu1bis 3, there was only a somewhat lower fast neutron fluence (see Table 42). Accordingly, the results of the calculation of the failure probabilities are nearly identical (see Fig. 68).

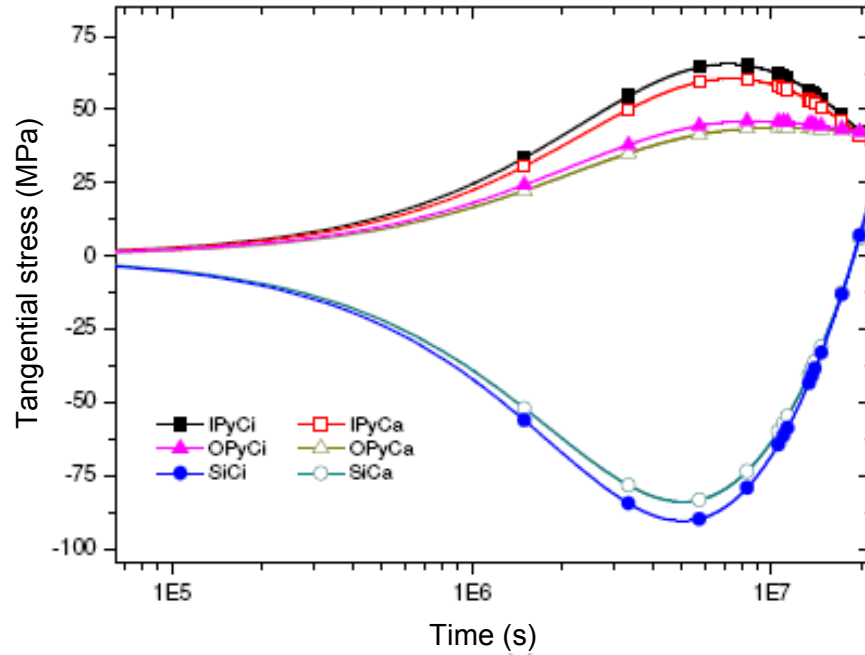


Figure 67: HFR Eu1bis 4 – calculated tangential stress curve during the irradiation

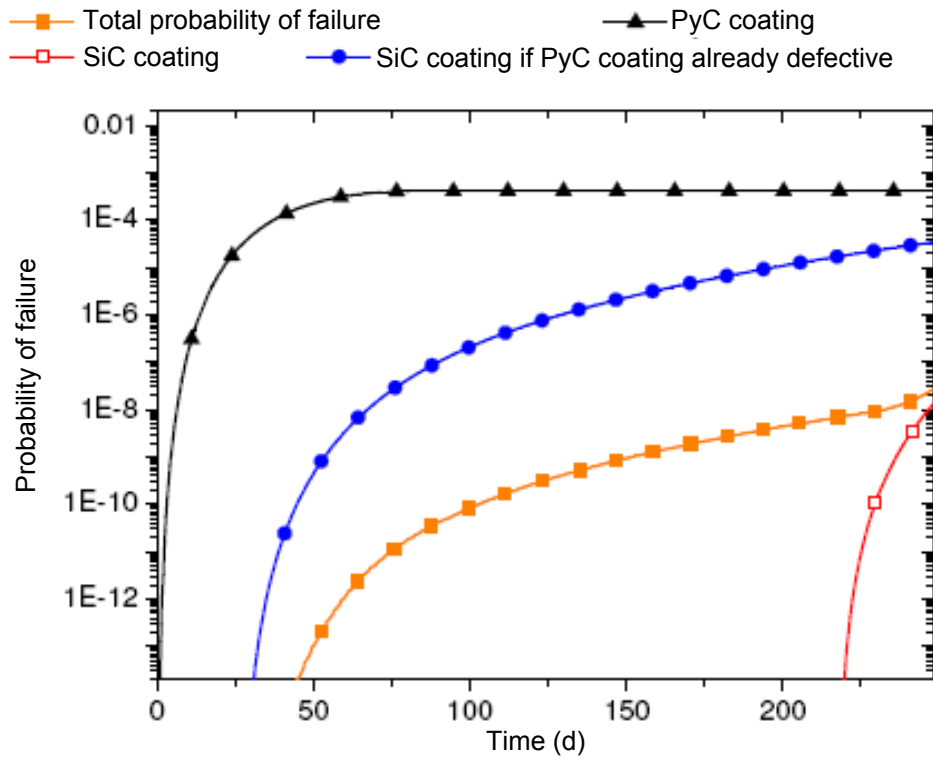


Figure 68: HFR Eu1bis – calculated probability of a particle break during irradiation

The results of the simulation of the bakeout experiment HFR Eu1bis 4 are presented in Fig. 69. In the first phase of the accident simulation, the failure probability rises in parallel with the heating curve. After the maximal temperature is reached, the failure probability continues to rise due to the tensile stress in the SiC coating, which is building up due to the rising gas pressure. At the end of the experiment, the probability of failure of a particle amounts to about $1 \cdot 10^{-4}$. This value is about five times higher than the measured Kr-85 release and would correspond to a failed particle in the fuel element ($\sim 10,000$ particles per BE). The form and quantity of the Kr-85 release, to be sure, indicate that no particle has failed during the bakeout experiment.

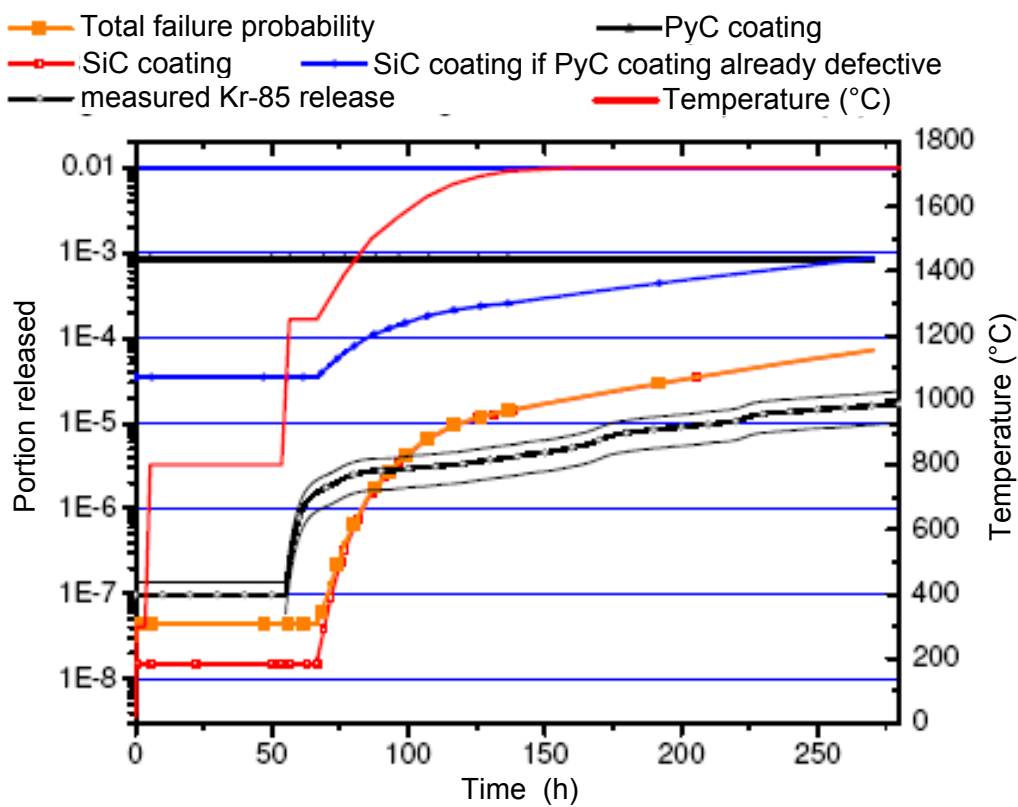


Figure 69: HFR Eu1bis4 – particle failure probability and measured Kr-85 release

7.12.2 Fission product release by diffusion

The Cs-137 release during the bakeout experiment HFR Eu1bis 4 could be illustrated very well by the diffusion model employed and is shown in Fig. 70. Only the measured release during the first phase of the experiment, which was conducted at 800°C, clearly below the operating temperature, is not in agreement with the calculation. As in the case of the previous fuel elements, the release was overestimated in the calculation during the accident simulation.

The simulation of the release of Ag-110m showed a distinct deviation from the measured release values (see Fig. 71). The initial release of $1 \cdot 10^{-5}$ at 800°C could not be reproduced by the calculation. In addition, the calculation indicated an almost total release of the Ag-110m inventory at the end of the experiment. In fact, a release of about two to three percent was measured. The curves of the calculation and the measurement run essentially parallel in the accident simulation.

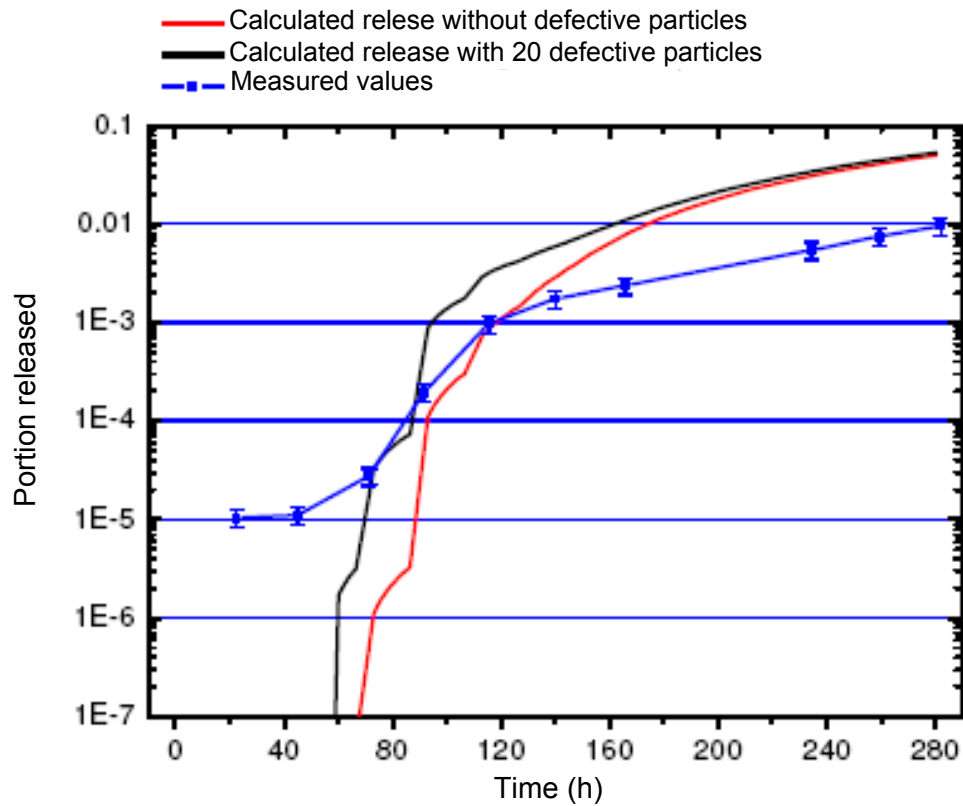


Figure 70: HFR Eu1bis4 bakeout experiment – measured and calculated cesium release

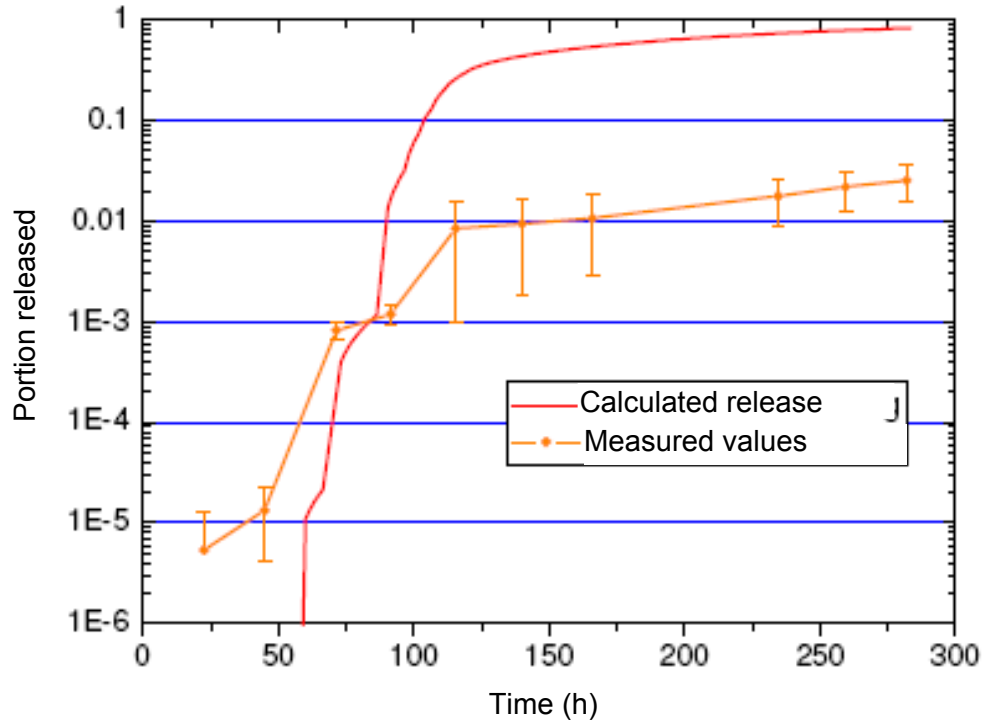


Figure 71: HFR Eu1bis bakeout experiment – measured and calculated silver release

8. Significance of the results

As part of this project, experimental accident simulations were carried out on a total of six spherical fuel elements for high temperatures with modern LEU TRISO coated particles. The key data of the experiments and the results are summarized in Table 43 and Table 44. The Cs releases at 1600°C and 1800°C are shown in summary form in Fig. 72 and Fig. 73, respectively. The Kr releases measured within the scope of this project are summarized in Fig. 75 as functions of the heating temperature.

In the experiments conducted here, the known 1600°C limit, below which no particle failure can be expected, could be confirmed. No sudden gas releases were measured in the temperature range of 1600°C.

The AVR 74/18 fuel element with a relatively low burn-up, a low irradiation temperature and low fast neutron fluence, as expected, released at 1600°C and also at 1800°C a portion of less than $1 \cdot 10^{-5}$ FR of its inventory. In addition, no particle failures apparently occurred either at 1600 or at 1800°C.

The HFR K6/2 and HFR K6/3 fuel elements that were irradiated under HTR module conditions displayed an outstanding accident behavior. No particle failure could be confirmed either at 1600°C or at 1700°C. Even an accident temperature of 1800°C was withstood by both fuel elements for at least one hundred hours before measurable particle failure occurred. In addition, the release of solid fission products was far below the anticipated value due to diffusion by the jacket coatings. Compared to the releases described in the literature, the release of cesium was about one power of ten lower [Schenk et al. 1988]. Other post-irradiation studies on HFR K6/3 showed that the microstructure of the SiC coating remained largely intact even after 400 hours at 1800°C. If these values should be confirmed and the results can be repeated, wherever possible larger and therefore more competitive high temperature reactors would be conceivable which, despite this, would display the criterion of inherent safety in the case of an outage of the active secondary heat removal system.

As opposed to HFR K6, the retention behavior of the fuel elements of HFR Eu1bis, which were irradiated at an elevated temperature of 1250°C and increased power up to a burn-up of 11% FIMA, were found not to be especially good. Although there was apparently no particle failure

during the bakeout experiments, the relative releases of cesium in the range of 10^{-3} show the limits of the fuel.

The relatively high initial release of cesium and silver at 1250°C was first attributed mainly to the high irradiation temperature. A more detailed analysis using a mechanical failure model and a diffusion model, however, revealed a suspected contamination of the graphite matrix from the irradiation experiment. During an irradiation cycle the latter experienced an unexpectedly high temperature excursion due to an operator error. This may possibly have led to damage to several particles, whose inventory was then released into the graphite matrix.

The contamination of the graphite matrix was apparently of subordinate importance for the cesium releases from the HFR Eu1bis fuel elements under accident conditions. The latter could be calculated relatively well with the diffusion model applied here. However, for 1500°C it was about two to three powers of ten above the releases of HFR K6 (see Figure 72). In this case, no qualitative difference could be perceived between the fuel element HFR Eu1bis 1 with the lowest burn-up and the highly burned-up fuel elements HFR Eu1bis 3 and HFR Eu1bis 4. Apparently the irradiation temperature of HTR fuel elements should therefore clearly lie below 1250°C.

The fuel elements HFR Eu1bis 1 and HFR Eu1bis 4 were baked out at 1700°C. At this clearly elevated accident temperature, both fuel elements released cesium on the order of 0.5 to 1%, i.e. about three to four powers of ten more than was released from HFR K6/3 at 1700°C. This is traceable with high probability to the higher temperature during the irradiation (see Figure 74).

From the fuel elements of the irradiation experiment HFR Eu1bis, besides the long-lived isotopes, releases of Ru-106 and Ag-110m could also be measured. The releases of Ru-106 were too inconsistent to permit further statements to be made. The measured releases of Ag-110m were relatively high in all three cases during the phase of operation simulation ($\sim 10^{-3}$ FR) and continued to rise during the accident simulation. However, the release at high temperatures in all three cases remained below the values expected according to the calculations.

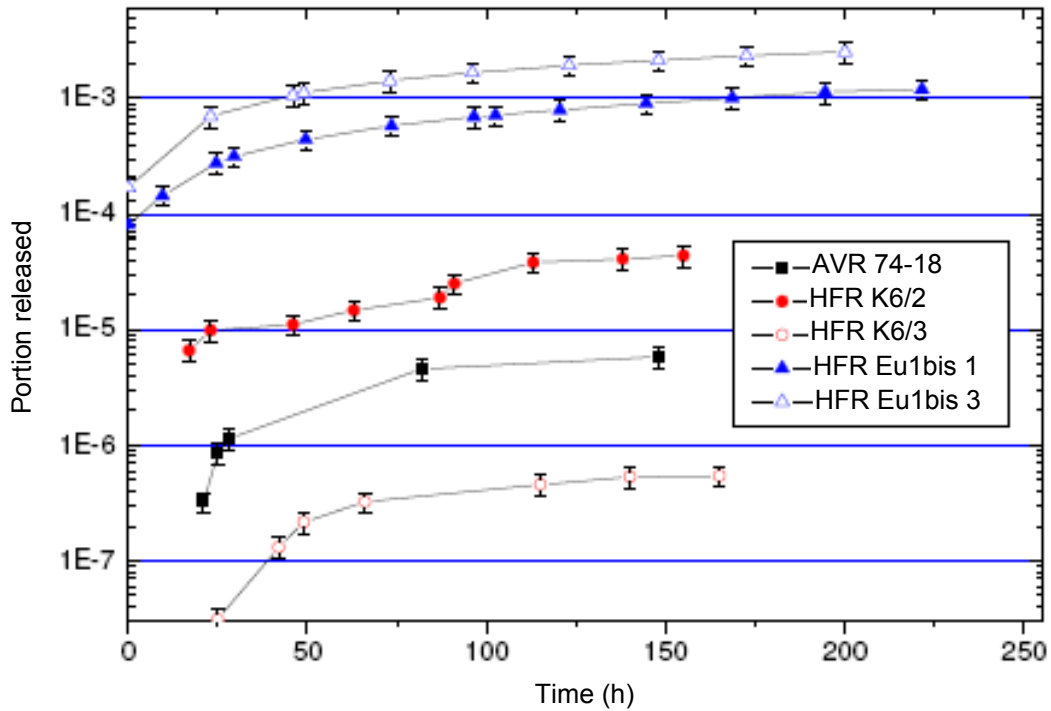


Figure 72: Summary of the Cs-137 releases at 1600°C

Table 43: Summary of the experimental data

	Burn-up:	Irradiation temperature:	Fast neutron fluence	Heating		FR	
				temp.	time	Cs-137	Kr-85
AVR 73/21	2.5 %	820 °C	0,4 10^{25} m^{-2}	1600 °C	5 h	-	< NWG
	FIMA			1800 °C	5 h	-	< NWG
AVR 74/18	4.8 % FIMA	820 °C	0,8 · 10^{25} m^{-2}	1000 °C	10 h	$3,24 \cdot 10^{-7}$	$4,51 \cdot 10^{-6}$
				1600 °C	100 h	$5,8 \cdot 10^{-6}$	$5,92 \cdot 10^{-6}$
				1800 °C	100 h	$8,05 \cdot 10^{-6}$	$6,05 \cdot 10^{-6}$
HFR K6/2	9.3 % FIMA	940 °C	4.6 · 10^{25} m^{-2}	1050 °C	10,5 h	$6,6 \cdot 10^{-6}$	< NWG
				1600 °C	100 h	$4,34 \cdot 10^{-5}$	< NWG
				1800 °C	200 h	$2,09 \cdot 10^{-3}$	$1.03 \cdot 10^{-5}$

HFR K6/3	9.7 % FIMA	940 °C	$4.8 \cdot 10^{25} \text{ m}^{-2}$	1050 °C	13,5 h	$1,31 \cdot 10^{-7}$	$3,21 \cdot 10^{-6}$
				1600 °C	100 h	$5,45 \cdot 10^{-7}$	$5,23 \cdot 10^{-6}$
				1700 °C	100 h	$1,99 \cdot 10^{-6}$	$6,2 \cdot 10^{-6}$
				1800 °C	100 h	$9,25 \cdot 10^{-4}$	$8,1 \cdot 10^{-6}$
				1800 °C	300 h	$4,3 \cdot 10^{-2}$	$5,49 \cdot 10^{-4}$
Eu1bis 1	9.34 % FIMA	1250 °C	$3.02 \cdot 10^{25} \text{ m}^{-2}$	1250 °C	210 h	$7,2 \cdot 10^{-5}$	$1,36 \cdot 10^{-6}$
				1600 °C	200 h	$1,19 \cdot 10^{-3}$	$1,01 \cdot 10^{-5}$
				1700 °C	150 h	$4,33 \cdot 10^{-3}$	$2,36 \cdot 10^{-5}$
Eu1bis 3	11.07 % FIMA	1250 °C	$3,98 \cdot 10^{25} \text{ m}^{-2}$	1250 °C	100 h	$3,88 \cdot 10^{-5}$	$3,42 \cdot 10^{-7}$
				1600 °C	200 h	$2,53 \cdot 10^{-3}$	$2,27 \cdot 10^{-6}$
Eu1bis 4	11.07 % FIMA	1250 °C	$3.98 \cdot 10^{25} \text{ m}^{-2}$	800 °C	48 h	$1,11 \cdot 10^{-5}$	< NWG
				1250 °C	10 h	$2,76 \cdot 10^{-5}$	$1,55 \cdot 10^{-6}$
				Transients	70 h	$1,74 \cdot 10^{-3}$	$4,1 \cdot 10^{-6}$
				1720 °C	~140h	$9,59 \cdot 10^{-3}$	$1,69 \cdot 10^{-5}$

Table 44: Summary of the experimental results

	Heating temp.	Heating time	Particle damage	FR	FR	FR	FR
				Cs-137	Cs-134	Ag-110m	Kr-85
AVR 73/21	1600 °C	5 h	0	-	-	-	< NWG
	1800 °C	5 h	0	-	-	-	< NWG
AVR 74/18	1000 °C	10 h	0	$3,24 \cdot 10^{-7}$	$3,24 \cdot 10^{-7}$	-	$4,51 \cdot 10^{-6}$
	1600 °C	100 h	0	$5,8 \cdot 10^{-6}$	$5,8 \cdot 10^{-6}$	-	$5,92 \cdot 10^{-6}$
	1800 °C	100 h	0	$8,05 \cdot 10^{-6}$	$8,05 \cdot 10^{-6}$	-	$6,05 \cdot 10^{-6}$
HFR K6/2	1050 °C	10,5 h	0	$6,6 \cdot 10^{-6}$	$6,6 \cdot 10^{-6}$	-	< NWG
	1600 °C	100 h	0	$4,34 \cdot 10^{-5}$	$4,34 \cdot 10^{-5}$	-	< NWG
	1800 °C	200 h	kA*	$2,09 \cdot 10^{-3}$	$2,09 \cdot 10^{-3}$	-	$1,03 \cdot 10^{-5}$
HFR K6/3	1050 °C	13,5 h	0	$1,31 \cdot 10^{-7}$	$1,31 \cdot 10^{-7}$	-	$3,21 \cdot 10^{-6}$
	1600 °C	100 h	0	$5,45 \cdot 10^{-7}$	$5,45 \cdot 10^{-7}$	-	$5,23 \cdot 10^{-6}$
	1700 °C	100 h	0	$1,99 \cdot 10^{-6}$	$1,99 \cdot 10^{-6}$	-	$6,2 \cdot 10^{-6}$
	1800 °C	100 h	0	$9,25 \cdot 10^{-4}$	$9,25 \cdot 10^{-4}$	-	$8,1 \cdot 10^{-6}$
	1800 °C	300 h	~ 20**	$4,3 \cdot 10^{-2}$	$4,3 \cdot 10^{-2}$	-	$5,49 \cdot 10^{-4}$
Eu1bis 1	1250 °C	210 h	0	$7,2 \cdot 10^{-5}$	$7,2 \cdot 10^{-5}$	$2,32 \cdot 10^{-3}$	$1,36 \cdot 10^{-6}$
	1600 °C	200 h	0	$1,19 \cdot 10^{-3}$	$1,19 \cdot 10^{-3}$	$7,24 \cdot 10^{-3}$	$1,01 \cdot 10^{-5}$
	1700 °C	150 h	0	$4,33 \cdot 10^{-3}$	$4,33 \cdot 10^{-3}$	-	$2,36 \cdot 10^{-5}$
Eu1bis 3	1250 °C	100 h	0	$3,88 \cdot 10^{-5}$	$3,88 \cdot 10^{-5}$	$9,57 \cdot 10^{-4}$	$3,42 \cdot 10^{-7}$
	1600 °C	200 h	0	$2,53 \cdot 10^{-3}$	$2,53 \cdot 10^{-3}$	$3,56 \cdot 10^{-3}$	$2,27 \cdot 10^{-6}$

Eu1bis 4	800 °C	48 h	0	$1,11 \cdot 10^{-5}$	$1,11 \cdot 10^{-5}$	$1,33 \cdot 10^{-5}$	< NWG
	1250 °C	10 h	0	$2,76 \cdot 10^{-5}$	$2,76 \cdot 10^{-5}$	$8,2 \cdot 10^{-4}$	$1,55 \cdot 10^{-6}$
	Transients	70 h	0	$1,74 \cdot 10^{-3}$	$1,74 \cdot 10^{-3}$	$9,38 \cdot 10^{-3}$	$4,1 \cdot 10^{-6}$
	1720 °C	~140h	0	$9,59 \cdot 10^{-3}$	$9,59 \cdot 10^{-3}$	$2,52 \cdot 10^{-2}$	$1,69 \cdot 10^{-5}$

*an unequivocal quantification was not possible, ** the ceramography performed showed a clearly higher failure rate (6 out of 10 particles).

The essential conclusions from this project can be summarized as follows:

- Modern HTR fuel with LEU TRISO coated particles has the potential to withstand clearly higher accident temperatures than previously assumed without releasing noteworthy amounts of radioactive fission products.
- High burn-ups up to 10% FIMA, probably also up to 11% FIMA only insignificantly impair the particle integrity in an accident.
- High neutron fluences of up to $4.8 \cdot 10^{25} \text{ m}^{-2}$ ($E > 0.1 \text{ MeV}$) only negligibly impair the particle integrity in an accident.
- The temperature of TRISO fuel elements in operation should clearly remain below the 1250°C limit.

Because of the suspected additional contamination of the graphite matrix by particles already damaged during the irradiation of the HFR Eu1bis fuel elements, no verifiable statements can be made regarding the retention capacity of Ag-110m at irradiation temperatures of 1250°C.

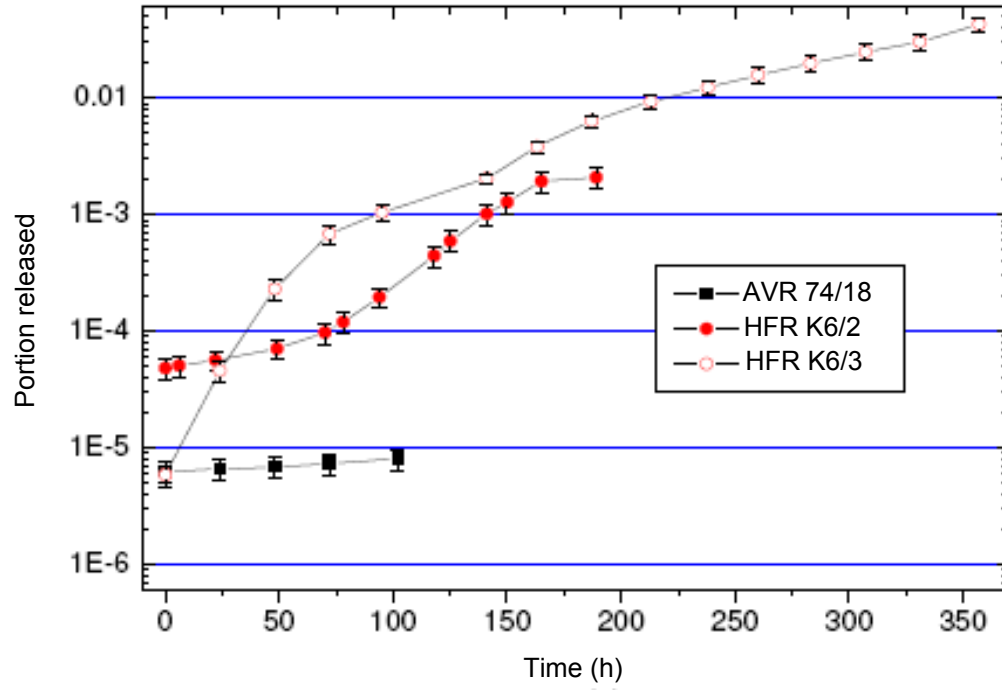


Figure 73: Summary of the Cs-137 releases at 1800°C

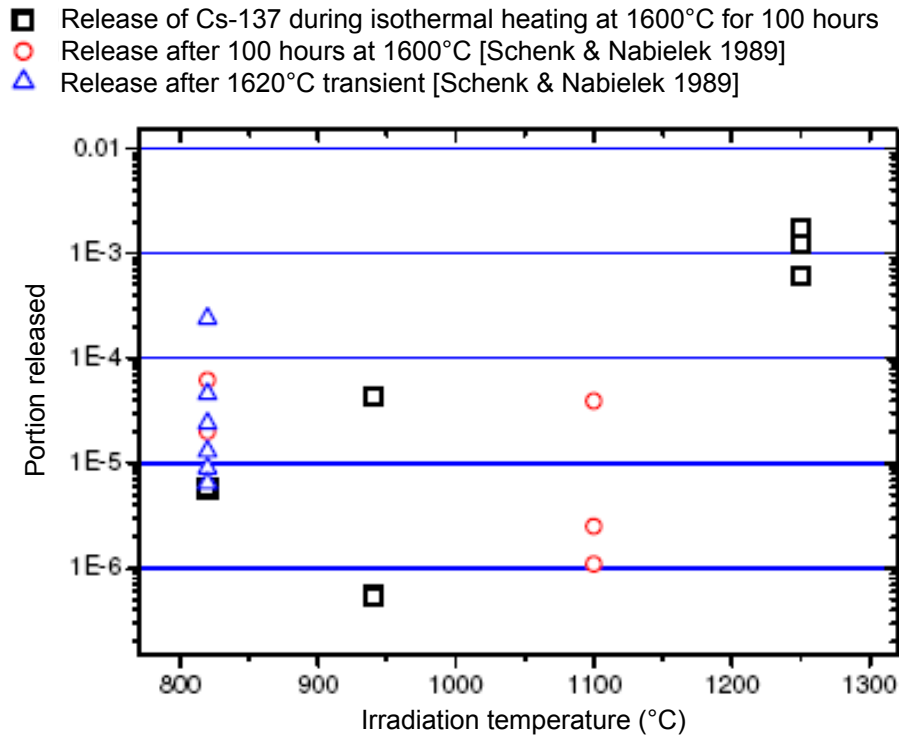


Figure 74: Release of Cs-137 at 1600°C as a function of the irradiation temperature

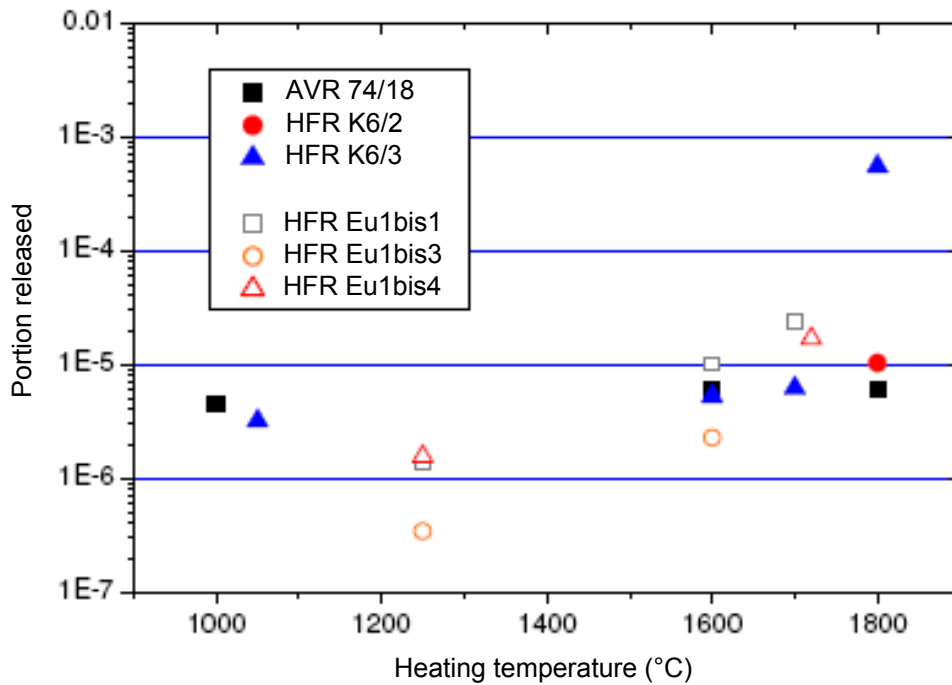


Figure 75: Summary of the Kr-85 releases as a function of the heating temperature

9. Prospects

In recent years, there has been increased activity worldwide in the field of high temperature reactor engineering. In the past designs with modular reactor of the small structure type, despite their inherent safety, often failed ultimately due to being uneconomical. Based on the experiments performed as part of this project on highly burned-up HTR fuel elements, the conclusion can be drawn that future high temperature reactors were able under some conditions to accept higher maximally possible accident temperatures than the previously assumed 1600°C with losing their inherently safe properties. Therefore, reactor designs with higher power outputs might be possible again, which would be advantageous from the economic aspect.

The primary precondition for this would be to avoid elevated irradiation temperatures. Since both the design of the direct cycle with helium turbine as well as the co-generation of current and hydrogen, as is envisioned in the V-HTR design, are based on high process temperatures above 1000°C, these applications appear to be less capable of implementation than a conventional secondary water and steam cycle with helical steam generators, which would be suitable both for current generation and also for supplying process steam. With such a design, the helium exit temperature could remain limited to about 750°C and supercritical steam states achieved despite this. As opposed to high fuel temperatures during operation, high burn-ups up to 11% and fast neutron fluences up to $4.8 \cdot 10^{25} \text{ m}^2$ ($E > 0.1 \text{ MeV}$) appear conceivable.

Because of the small database, it appears advisable to conduct further experiments at elevated accident temperatures up to 1800°C. In particular, four fuel elements that were irradiated within the scope of experiment HFR K5 and are presently in the ITU and which have not, until now, been baked out in accident experiments appear to be predestined for this. Beside the mere expansion of the database, it would be of interest, e.g., to study the influence of the thermal cycling on the particle behavior. Since indications were found in this project of a possible effect on the failure behavior by thermal fatigue, this aspect could have relevance for acceptable load cycles of future HTR. In the core it is necessary to investigate the question of whether a reactor core that was exposed to a pressure loss accident with outage of the active secondary heat removal system can subsequently continue to be operated or whether all fuel elements have to be replaced.

Besides the release of gases, another method for determining the proportion of defective particles in a baked out fuel element would be desirable. For this purpose, the graphite matrix of the fuel element has to be dissolved (disintegration) and the particles sorted out. Then the particles would have to be measured out and the results evaluated in an automated process. Besides giving the number of defective particles, this process can also provide information on the release behavior of various fission products in the particle and in the matrix also provide information on the statistical distribution. In the past, such a process was already developed under the name IMGGA (irradiated microsphere gamma analyzer) and used [Kania & Baldwin 1989]. The dissolving and sorting out process has already been conducted as part of the present HTR activities at the ITU and can therefore be used in the future.

One aspect that could not be considered within the scope of this project is the penetration of air or water during an accident. Earlier studies [Schenk et al. 1997] have shown that the fuel elements can withstand such an accident only conditionally. Therefore, further experimental work is required here. The so-called corrosion apparatus (KorA), that was installed earlier together with the CoFA-1 in the Hot Cells of the FJB is presently being assembled in the ITU.

References

[Allelein 1980], H.-J. Allelein, "Spaltproduktverhalten – Speziell Cs-137 in HTR-TRISO Brennstoffteilchen" [Fission product behavior, especially Cs-137 in the HTR TRISO fuel particle], Jül 1695, Dissertation RWTH Aachen, 1980

[Allelein et al. 1983], Allelein H.-J., Bornschein R., Nabielek H., Christ A., Hanson D.L., Mehner A.-W., Bongartz K., "The Behavior of HTR Fuel under Irradiation", Trans. 7 SmiRT Conference, Paper C5/9, pp. 203-213, 1983

[Arnold et al. 2004], Dirk Arnold, Menno Blaauw, Stjepko Fazinic, Vladimir P. Kolotov, "The 2002 IAEA intercomparison of software for low-level g-ray spectrometry"

[Ball 2006], Syd Ball, "Sensitivity studies of modular high-temperature gas-cooled reactor postulated accidents", Nuclear Engineering and Design, 236, p. 454-462, 2006

[Birely 1973], William C. Birely, „Operating Experience of the Peach Bottom Atomic Power Station“, Nuclear Engineering and Design, 26, p. 9-15, 1973

[Booth 1957], A.H. Booth, "A Method of Calculating Fission Gas Diffusion from UO₂ Fuel and its Application to the X-2-F Loop Test", Report CRDC-721, Atomic Energy of Canada Ltd., 1957

[Brandes & Kohl 1988], S. Brandes and W. Kohl, „Design and application of the HTR-100 industrial nuclear power plant“, Nuclear Engineering and Design, 109, p. 107-113, Amsterdam, The Netherlands, 1988

[de Groot 2008], S. de Groot, R. Dubourg, K. Bakker, M. Kissane, M. Barrachin, "Fission-Product Behaviour during Irradiation of TRISO-Coated Particles in the HFREU1bis Experiment", Proceedings of HTR 2008, Washington DC, USA, 28 Sept. – 1 Oct. 2008

[Dragon Project Report 1000 1978], O.E.C.D. High Temperature Reactor Project (Dragon) 1959 – 1976, "Dragon Project Report 1000", A.E.E. Winfrith, Dorchester, Dorset, England, United Kingdom, 1978

[Duwe & Kühnlein 1975] R. Duwe, W. Kühnlein, "Berechnung des Spaltproduktinventars in Brenn-elementen mit U 235, Th 232 und U 238 als Schwermetalleinsatz" [Calculation of the fission product inventory in fuel elements with U 235, Th 232 and U 238 as heavy metal inventory], KfA-Internal-Report No FZJ-IRW-IB_11/75, Jülich, Germany, 1975

[Duwe et al.1977], Duwe, R., Kühnlein, W., Schröder, R., „Gamma-spektrometrische Abbrandmessung an kugelförmigen Brennelementen“[Gamma spectrometric burn-up measurement on spherical fuel elements] Printed as manuscript : Institut für Reaktorwerkstoffe Kernforschungsanlage Jülich GmbH, 1977

[Freis et al. 2006], Freis, D., Nasyrow, R., Toscano, E.H., 2006. "Burn-up determination of High Temperature Reactor spherical fuel elements by gamma spectrometry", Proceedings of HTR 2006, Johannesburg, South Africa, 1–4 October 2006

[Freis et al. 2008], D. Freis, D.P. Bottomley, J. Ejton, W. de Weerd, H. Kostecka und E.H. Toscano, "Post Irradiation Testing of High Temperature Reactor Spherical Fuel Elements Under Accident Conditions", Proceedings of HTR 2008, Washington DC, USA, 28 Sept. – 1 Oct. 2008

[Fütterer et al. 2006], M.A. Fütterer, A. Marmier, E.H. Toscano, K. Bakker, "Irradiation Results of AVR Fuel Pebbles at Increased Temperature and Burn-up in the HFR Petten", Proc. HTR 2006, Johannesburg, South Africa, 1-4 October 2006

[Fütterer et al. 2008], M.A. Fütterer, G. Berg, A. Marmier, E.H. Toscano, D. Freis, K. Bakker, S. de Groot, „Results of AVR fuel pebble irradiation at increased temperature and burn-up in the HFR Petten“, Nuclear Engineering and Design, 238, p. 2877 - 2885, 2008

[Gauthier et al. 2006], Jean-Claude Gauthier, Gerd Brinkmann, Bernie Copsey, Michel Lecomte, "ANTARES: The HTR / VHTR project at Framatome ANP", Nuclear Engineering and Design, 236, p. 526–533, 2006

[Habush & Harris 1968], A.L. Habush, A.M. Harris, "330-MW(e) Fort St. Vrain High-Temperature Gas-Cooled Reactor", Nuclear Engineering and Design, 7, p. 312-321, Amsterdam, The Netherlands, 1968

[Haque et al. 2006], H. Haque, W. Feltes, G. Brinkmann, "Thermal response of a modular high temperature reactor during passive cooldown under pressurized and depressurized conditions", Nuclear Engineering and Design, 236, p. 475-484, 2006

[Heit et al. 1985], W. Heit, H. Huschka, W. Rind and G.G. Kaiser, "Status of qualification of high temperature reactor fuel element spheres", Nuclear Technology, 69, p. 44-69, 1985

[Hrovat et al. 1988], M. Hrovat, H. Huschka, A.W. Mehner, W. Warzawa, „Spherical Fuel Elements for Small and Medium Sized HTR“, Nuclear Engineering and Design, 109, p. 253-256, Amsterdam, The Netherlands, 1988

[IAEA 2008], "Power Reactor Information System (PRIS)", International Atomic Energy Agency, Wien, Österreich, 2008

[Kania & Baldwin 1989], M.J. Kania, C.A. Baldwin, "IMGA Examination and Postheating Characterization of Individual Particles from Heatup Simulation Tests Performed on HFRK3 and R2-K13 Irradiated Fuels", Experts Meeting on MHTGR/HTR Fuel Performance under Accident Conditions, Oak Ridge National Laboratory, 1989

[Kiryushin et al. 1997], A.I. Kiryushin, N.G. Kodochigov, N.G. Kouzavkov, N.N. Ponomarev-Stepnoi, E.S. Gloushkov, V.N. Grebennik, "Project of the GT-MHR hightemperature helium reactor with gas turbine", Nuclear Engineering and Design, 173, p. 119-129, 1997

[Klapp 1980], E. Klapp, „Apparate- und Anlagentechnik“, Heidelberg, Springer Verlag 1980

[Krohn 1982], H. Krohn, „Freisetzung von Spaltprodukten aus dem Core eines Kugelhaufenreaktors bei Störfällen mit Coreaufheizung“ [Release of fission products from the core of a pebble heap reactor during accidents with core heating] Jül-1791, Dissertation RWTH Aachen, 1982

[Kugeler & Schulten 1989], K. Kugeler, R. Schulten, "Hochtemperaturreaktortechnik HTR", Berlin; Heidelberg; New York; London; Paris; Tokyo; Hong Kong: Springer, 1989

[Kunitomi et al. 2004], Kazuhiko Kunitomi, Shoji Katanishi, Shoji Takada, Takakazu Takizuka, Xing Yan, "Japan's future HTR - the GTHTR300 ", Nuclear Engineering and Design, 233, p. 309–327, 2004

[Lee et al. 2008], Kyung-Hoon Lee, Kang-Seog Kim, Jin-Young Cho, Jae-Seung Song, Jae-Man Noh, Chung-Chan Lee, "IAEA GT-MHR benchmark calculations by using the HELIOS / MASTER physics analysis procedure and the MCNP Monte Carlo code", Nuclear Engineering and Design, 238, p. 2654–2667, 2008

[Lohnert et al. 1988], G.H. Lohnert, H. Nabielek, W. Schenk, „The Fuel Element of the HTR-Module, a Prerequisite of an Inherently Safe Reactor“, Nuclear Engineering and Design, 109, p. 257-263, Amsterdam, The Netherlands, 1988

[MacLean 2004], H.J. MacLean, "Silver Transport in CVD Silicon Carbide", PhD-Thesis, Massachusetts Institute of Technology, USA, 2004

[Maki et al. 2007], J.T. Maki, D.A. Petti, D.L. Knudson, G.K. Miller, "The challenges associated with high burn-up, high temperature and accelerated irradiation for TRISOcoated particle fuel", INEL, Idaho, USA, 2007

[Maki & Miller 2005], J.T. Maki, G.K. Miller, "TRISO-Coated Particle Fuel Performance Benchmark Cases", March 14, 2005

[Miller & Bennet 1991], G. K. Miller, R. G. Bennet, "Finite Element Stress Analysis of NP-MHTGR Target Particles with the Abaqus Code", INEL, Idaho, USA, 1991

[Miller & Bennet 1993], G. K. Miller, R. G. Bennet, Analytical Solution for Stresses in TRISO-Coated Particles, INEL, Idaho, USA, 1993

[Miller et al. 2001], G.K. Miller, D.A. Petti, D.J. Varacalle and J.T. Maki, "Consideration of the Effects on Fuel Particle Behaviour from Shrinkage Cracks in the Inner Pyrocarbon Layer", INEL, Idaho, USA, 2001

[Minato et al. 1995], K. Minato, T. Ogawa, K. Fukuda, H. Nabielek, H. Sekino, Y. Nozawa, I. Takahashi, "Fission product release from ZrC-coated fuel particles during post irradiation heating at 1600°C", Journal of Nuclear Materials 224, p. 85-92, 1995

[Moore et al. 1982], R.A. Moore, M.E. Kantor, H.L. Brey, H.G. Olson, „HTGR Experience, Programs and Future Applications“, Nuclear Engineering and Design, 72, p. 153-174, 1982

[Nabielek et al. 1974], Nabielek H., Hick H., Wagner-Löffler M., Voice E. H., "Performance limits of coated particle fuel. Part III: Fission product migration in HTR fuel", Dragon Project Report 828/ part III. Winfrith, June 1974

[Nabielek & Myers 1982], H. Nabielek, B. F. Myers, „Fission Product Retention in HTR Fuel“, Gas-cooled Reactors Today, British Nuclear Society, London, 1982

[Nabielek et al. 1990], H. Nabielek, W. Kühnlein, W. Schenk, W. Heit, A. Christ, H. Ragos, „Development of Advanced HTR Fuel Elements“, Nuclear Engineering and Design, 121, p. 199-210, 1990

[Nabielek et al. 1992], H. Nabielek, K. Fukuda, K. Minato and T. Ogawa, Calculation of Particle Temperatures in NSRB Tests, March 13, 1992

[Nabielek et al. 1993], H. Nabielek, R. Conrad, K. Roellig, B.F. Meyers, Conference Article: "Fuel Irradiation Experiments on HFR-K6 and HFR-B1 with Intermittent Water Vapour Injections", Technical Committee Meeting on Response of Fuel, Fuel Elements and Gas Cooled Reactor Cores under Accidental Air or Water Ingress Conditions, Beijing, China, 25-27 Oct 1993

[Nabielek et al. 2005], H. Nabielek, K. Verfondern, H. Werner, „Selection of Benchmark Cases for Mechanical Failure Prediction“, HTR-F Report, Forschungszentrum Jülich, 2005 [Nabielek 2008], H. Nabielek, Jülich, private Mitteilung

[Pelletier et al. 2003], Pelletier, M., Nabielek, H., Abram, T., and Martin, D., "HTR-F Project: Selection of properties and models for the coated particle –PyC and SiC," Report CEA SESC/LSC/03-028 ind. 0, August 2003

[Petti et al. 2002], D. A. Petti, J. T. Maki, J. Buongiorno, R. R. Hobbins, G. K. Miller, "Key Differences in the Fabrication and Safety Testing of U.S. and German TRISO-coated Particle Fuel and Their Implications on Fuel Performance", INEEL/EXT-02-00300, Idaho Falls, Idaho, USA, 2002

[Prados & Scott 1967], J.W. Prados, J.L. Scott, The Influence of Pyrolytic-Carbon Creep in Coated-Particle Fuel Performance, ORNL, Tennessee, USA, 1967

[Reutler & Lohnert 1984], H. Reutler und G.H. Lohnert, „Advantages of Going Modular in HTR“, Nuclear Engineering and Design, 78, p. 129-136, Amsterdam, The Netherlands, 1984

[Schenk 1978], W. Schenk, „Untersuchungen zum Verhalten von beschichteten Brennstoffteilchen und Kugelbrennelementen bei Störfalltemperaturen“ [Studies of the behavior of coated fuel particles and spherical fuel elements at accident temperatures], Dissertation RWTH Aachen, 1978

[Schenk et al. 1984], W. Schenk, A. Naoumidis, H. Nickel, "The Behaviour of Spherical HTR fuel Elements under Accident Conditions", Journal of Nuclear Materials, 124, p. 25, 1984

[Schenk et al. 1988], W. Schenk, D. Pitzer und H. Nabielek, "Fission Product Release Profiles from Spherical HTR Fuel Elements at Accident Temperatures", Jülich Report 2234, Jülich, Germany, September 1988

[Schenk & Nabielek 1989], W. Schenk, H. Nabielek, „Kugelbrennelemente mit TRISO-Partikeln bei Störfalltemperaturen“ [Spherical fuel elements with TRISO particles at accident temperatures], Spezieller FZJ Bericht Nr. 487, Jülich, 1989

[Schenk et al. 1997], W. Schenk, R. Gontard, H. Nabielek, „Performance of HTR Fuel Samples under High-Irradiation and Accident Simulation Conditions, with Emphasis on Test Capsules HFR-P4 and SL-P1“, Jülich Report 3373, Jülich, Germany, April 1997

[Schöning & Elter 1988], J. Schöning, K. Elter, „Design Characteristics of the HTR 500 Reactor Components“ Nuclear Engineering and Design, 109, p. 189-197, Amsterdam, The Netherlands, 1988

[Shiozawa. et al. 2004], S. Shiozawa, S. Fujikawa, T. Iyoku, K. Kunitomi, Y. Tachibana, “Overview of HTTR design features”, Nuclear Engineering and Design, 233, p. 11–21, 2004

[Sterbentz 2007], Sterbentz, J. W., “Low-Enriched Very High Temperature Reactor Core Design”, 2007, International Congress on Advances in Nuclear Power Plants, ICAPP 2007

[Stradal 1970], K.A. Stradal, „Apparatur zur Messung der Freisetzung von Spaltgasen und anderer Spaltprodukte durch Ausheizen [Apparatus for measuring the release of fission gases and other fission products by baking out]“, Jülich Report 707 - RW, Jülich, Germany, October 1970

[Takada et al. 2004], Eiji Takada, Shigeaki Nakagawa, Nozomu Fujimoto, Daisuke Tochio, “Core thermal–hydraulic design of HTTR”, Nuclear Engineering and Design, 233, p. 37-43, 2004

[Tang et al. 2002], Chunhe Tang, Yaping Tang, Junguo Zhu, Yanwen Zou, Jihong Li and Xiaojun Ni, "Design and manufacture of the fuel element for the 10 MW high temperature gas-cooled reactor", Nuclear Engineering and Design, 218, 91–102, 2002

[Toscano et al. 2004], E.H. Toscano, H. Kosticka, J. Eجتon, W. de Weerd, “Post-Irradiation Testing of HTR-Fuel Elements under Accident Conditions, Part 1 and 2”, Conference Contribution, 2nd International Topical Meeting on High Temperature Reactor Technology Beijing, China, 2004

[Touloukain & DeWitt 1970], TOULOKAIN, Y.S.; DEWITT, D.P.: Thermal Radiative Properties – Metallic Elements and Alloys. New York: IFI/Plenum, 1970

[van der Merve & Hanson 2008], H. van der Merve, D. Hanson, The HTR Factbook, 2008 [van der Merve & Venter 2008], H. van der Merve, J. Venter, „A method to evaluate fission gas release during irradiation testing of spherical fuel”, Proceedings of HTR 2008, Washington DC, USA, 28 Sept. – 1 Oct. 2008

[Venter & Mitchell 2007], P.J. Venter, M.N. Mitchell, „Integrated Design Approach of the Pebble Bed Modular Reactor using Models“, Nuclear Engineering and Design, 237, p. 1341-1353, 2007

[Verfondern und Nabielek 1990], K. Verfondern and H. Nabielek, The Mathematical Basis of the Panama-I Code for Modeling Pressure Vessel Failure of TRISO Coated Particles under Accident Conditions, FZJ-Report, Jülich, Germany, 1990

[Verfondern & Müller 1991], K. Verfondern, D. Müller, „FRESCO-I, Programm zur Berechnung der Spaltproduktfreisetzung aus dem Core eines Kugelhaufenreaktors bei Kernaufheizung – Benutzerhandbuch“ [Program for calculating the fission product release from the core of a ball heap reactor during core heating], Internal Report FZJ-ISR-IB-2/91, Research Center Jülich, 1991

[Verfondern et al. 1997], K. Verfondern (Editor), "Fuel Performance and Fission Product Behaviour in Gas Cooled Reactors", IAEA-TECDOC-978, Vienna, Austria, 1997

[Verfondern & Nabielek 2008], K. Verfondern und H. Nabielek, „Fission Product Release from HTGR Fuel under Core Heatup Accident Conditions“, Proceedings of HTR 2008, Washington DC, USA, 28 Sept. – 1 Oct. 2008

[Walther 1971], H. Walther, "On Mathematical Models for Calculating the Mechanical Behaviour of Coated Fuel Particles", SORIN, Centro Ricerche National, Saluggia, Italy, 1971

[Wiese 2002], H.W. Wiese, „Status und Weiterentwicklung des Inventarcodes KORIGEN, der Szenariocodes KORREC und SOLEQ sowie des Nachwärmecodes CALOR. Programm Nukleare Sicherheitsforschung“, Jahresbericht 2001, Teil 1, [Status and continued development of the KORIGEN inventory code, the KORREC and SOLEQ scenario codes and the CALOR post-heating code. Nuclear Safety Research Program, Annual Report 2001, Part 1]. Wissenschaftliche Berichte, FZKA-6741, June 2002, p.314-17

[Wu et al. 2002], Zongxin Wu, Dengcai Lin and Daxin Zhong, "The design features of the HTR-10", Nuclear Engineering and Design, 218, p. 25–32, 2002

[Xu et al. 2005], Yuanhui Xu, Shouying Hu, Fu Li and Suyuan Yu, "High Temperature Reactor Development in China", Progress in Nuclear Energy; Vol. 47, No. 1-4, pp. 260-270, 2005

[Zhang et al. 2006], Zuoyi Zhang, Zongxin Wu, Yuliang Sun, Fu Li, "Design aspects of the Chinese modular high-temperature gas-cooled reactor HTR-PM", Nuclear Engineering and Design, 236, p. 485–490, 2006

[Zhang et al. 2009], Zuoyi Zhang, Zongxin Wu, Dazhong Wang, Yuanhui Xu, Yuliang Sun, Fu Li, Yujie Dong, "Current status and technical description of Chinese 2 × 250 MWth HTR-PM demonstration plant", Nuclear Engineering and Design, Volume 239, Issue 7, July 2009, Pages 1212-1219, 2009

I. Appendix – Results in Tabular Form

In the following tables, the heating programs of the experiments conducted as part of this project are listed stating the times and temperatures of the steps. In addition, the usage times of the condensation plates used and their activities measured in connection with the experiments can be viewed. In all cases the inaccuracy of the measured values of the gamma spectrometric measurement is reported. In order to determine the total inaccuracy, in addition, the inaccuracy of the cold finger efficiency must be taken into account. The cumulative release portion is obtained by division with the previously determined total inventory at the beginning of the experiment and the cold finger efficiency.

la. AVR 74/18

Table 45: Heating program and plate change of the AVR 74/18

Time (hh:mm)	Coating:	Temperature (°C)	Temperature rise (°C/h)	Plate
00:00	30	20	560	3
00:30	600	300	0	3
10:30	89	300	797.75	3
11:59	564	1000	0	3
21:25	34	1000	0	3 - 4
21:59	120	1000	300	4
23:59	71	1600	0	4
25:10	60	1600	0	4 - 7
26:10	120	1600	-790*	7
28:10	17	20	988.24	7 - 10
28:27	60	300	0	10
29:27	89	300	471.91	10
30:56	120	1000	300	10
32:56	2924	1600	0	10
81:40	3516	1600	0	10 – 9
140:16	444	1600	-86.96	9
147:40	453	935	-86.96	9 - 11
155:13	60	300	0	11
156:13	90	300	1000	11

157:43	837	1800	0	11
171:40	1440	1800	0	11 – 12
195:40	1440	1800	0	12 – 13
219:40	395	1800	0	13 – 14
226:15	85	1800	-401.65*	14
227:40	30	1231	1138	14
228:10	930	1800	0	14
243:40	870	1800	0	14 - 15
258:10	960	1800	-111.25	15
274:10		20		

* uncontrolled cooling

Table 46: Cs-137 activities of the condensate plates of AVR 74/18

Plate	Cs-137 activity (Bq)	Inaccuracy (Bq)	Date	Cumulative release portion
3	7,698E+03	2,531E+02	04.08.06	3,24E-07
4	1,267E+04	1,661E+02	03.08.06	8,56E-07
7	6,679E+03	2,237E+02	04.08.06	1,14E-06
10	8,235E+04	1,555E+03	02.08.06	4,6E-06
9	2,871E+04	2,500E+02	03.08.06	5,80E-06
11	1,036E+04	2,233E+02	04.08.06	6,24E-06
12	7,162E+03	2,424E+02	03.08.06	6,54E-06
13	5,803E+03	2,113E+02	03.08.06	6,78E-06
14	1,140E+04	2,172E+02	02.08.06	7,26E-06
15	1,874E+04	3,018E+02	04.08.06	8,05E-06

lb. HFR K6/2

Table 47: Cs-137 activities of the condensate plates of AVR K6/2

Plate	Cs-137 activity (Bq)	Inaccuracy (Bq)	Date	Cumulative release portion
50	3,608E+05	6,816E+03	17.08.06	6,6E-6
51	1,765E+05	3,916E+03	17.08.06	9,83E-6
52	6,585E+04	1,584E+03	17.08.06	1,10E-5
53	1,995E+05	4,708E+03	17.08.06	1,47E-5
54	2,329E+05	5,291E+03	17.08.06	1,9E-5
55	3,261E+05	6,146E+03	17.08.06	2,49E-5
56	7,210E+05	9,977E+03	17.08.06	3,81E-5
57	1,490E+05	3,198E+03	17.08.06	4,08E-5
58	1,424E+05	3,244E+03	17.08.06	4,34E-5
59	2,608E+05	5,869E+03	17.08.06	4,82E-5
60	1,181E+05	2,397E+03	17.08.06	5,04E-5
61	3,082E+05	5,408E+03	17.08.06	5,6E-5
62	7,925E+05	1,193E+04	17.08.06	7,05E-5
63	1,456E+06	2,049E+04	17.08.06	9,71E-5
64	1,196E+06	1,723E+04	17.08.06	1,19E-4
66	4,143E+06	1,589E+05	08.09.06	1,95E-4
67	1,353E+07	4,192E+05	08.09.06	4,42E-4
68	8,239E+06	2,791E+05	08.09.06	5,93E-4
69	2,278E+07	7,388E+05	08.09.06	0,00101
70	1,454E+07	4,754E+05	08.09.06	0,00128
71	3,586E+07	1,105E+06	08.09.06	0,00193
72	8,408E+06	2,895E+05	08.09.06	0,00209

Table 48: Heating program and plate change of the AVR K6/2

Time (hh:mm)	Step duration (min)	Temperature (°C)	Temperature rise (°C/h)	Plate
00:00	30	20	560	50
00:30	600	300	0	50
05:30	90	300	500	50
07:00	560	1050	0	50
16:00	60	1050	46	50
17:00	360	1096	46	50 - 51
23:00	300	1372	46	51 - 52
28:00	1020	1600	0	52
45:00	60	1600	-1580*	52
46:00	30	20	560	52 - 53
46:30	90	300	500	53
48:00	840	1050	0	53
62:00	60	1050	550	53
63:00	1440	1600	0	53 – 54
87:00	180	1600	0	54 – 55
90:00	60	1600	-1580*	55
91:00	30	20	560	55 - 56
91:30	90	300	866.67	56
93:00	1200	1600	0	56
113:00	1500	1600	0	56 - 57
138:00	780	1600	0	57 - 58
151:00	240	1600	50	58
155:00	1620	1800	0	58 – 59
182:00	360	1800	0	59 – 60
188:00	960	1800	0	60 – 61
204:00	1620	1800	0	61 – 62
231:00	1260	1800	0	62 – 63
252:00	480	1800	0	63 – 64
260:00	960	1800	0	64 – 66
276:00	1440	1800	0	66 – 67
300:00	420	1800	0	67 – 68

307:00	960	1800	0	68 – 69
323:00	540	1800	0	69 – 70
332:00	900	1800	0	70 – 71
347:00	480	1800	0	71 – 72
355:00	960	1800	-11.25	72
371:00		20		72

lc. HFR K6/3

Table 49: Heating program and plate change of the AVR K6/3

Time (hh:mm)	Step duration (min)	Temperature (°C)	Temperature rise (°C/h)	Plate
00:00	600	20	0	19
10:00	30	20	560	19
10:30	390	300	0	19
17:00	90	300	500	19
18:30	390	1050	0	19
25:00	420	1050	0	19 - 20
32:00	600	1050	50	20
42:00	60	1550	50	20 - 21
43:00	360	1600	0	21
49:00	1020	1600	0	21 - 22
66:00	2940	1600	0	22 - 23
115:00	1500	1600	0	23 - 24
140:00	180	1600	0	24 - 25
143:00	960	1600	-98.75	25
159:00	360	20	280	25
165:00	1020	1700	0	25 - 26
182:00	480	1700	0	26 - 27
190:00	960	1700	0	27 – 28
206:00	480	1700	0	28 – 29
214:00	1020	1700	0	29 - 30
231:00	2040	1700	0	30 - 31

265:00	960	1700	-105	31
281:00	60	20	280	31 – 32
282:00	120	300	750	32
284:00	1260	1800	0	32
305:00	1440	1800	0	32 - 33
329:00	1440	1800	0	33 - 34
353:00	1440	1800	0	34 - 35
377:00	420	1800	0	35 - 36
384:00	960	1800	-11.25	36
400:00		20		36 – 37

Time (hh:mm)	Step duration (min)	Temperature (°C)	Temperature rise (°C/h)	Plate
400:00	2040	20	0	36 - 37
434:00	30	20	60	37
434:30	360	300	0	37
440:30	90	300	1000	37
442:00	60	1800	0	37
443:00	180	1800	0	37
446:00	1320	1800	0	37 - 38
468:00	1440	1800	0	38 - 39
492:00	1560	1800	0	39 - 40
518:00	1500	1800	0	40 - 41
543:00	1320	1800	0	41 - 42
565:00	1380	1800	0	42 - 43
588:00	1440	1800	0	43 - 44
612:00	1440	1800	0	44 - 45
636:00	1560	1800	0	45 - 46
662:00	4800	1800	0	46 - 47
742:00	990	1800	-111.25	47
758:30	30	20	0	47
759:00		20		47 – 48

Table 50: Cs-137 activities of the condensate plates of HFR K6/3

Plate	Cs-137 activity (Bq)	Inaccuracy (Bq)	Date	Cumulative release portion
19	1,622E+03	6,913E+01	10.08.06	3,12E-08
20	5,189E+03	3,136E+02	09.08.06	1,31E-07
21	4,440E+03	1,747E+02	08.08.06	2,16E-07
22	5,559E+03	1,919E+02	09.08.06	3,23E-07
23	6,968E+03	4,803E+02	08.08.06	4,57E-07
24	3,881E+03	1,705E+02	08.08.06	5,32E-07
25	6,765E+02	9,150E+01	09.08.06	5,45E-07
26	4,076E+03	1,793E+02	09.08.06	6,23E-07
27	1,155E+03	9,726E+01	08.08.06	6,45E-07
28	5,218E+03	1,499E+02	09.08.06	7,46E-07
29	2,295E+03	4,235E+01	10.08.06	7,9E-07
30	1,158E+04	5,068E+02	09.08.06	1,01E-06
31	5,099E+04	8,265E+02	08.08.06	1,99E-06
32	1,991E+05	2,789E+03	08.08.06	5,82E-06
33	2,068E+06	2,683E+04	02.08.06	4,56E-05
34	9,583E+06	1,192E+05	03.08.06	2,3E-04
35	2,345E+07	2,988E+05	02.08.06	6,81E-04
36	1,273E+07	1,606E+05	02.08.06	9,25E-04
37	5,849E+06	6,701E+04	16.08.06	1,04E-03
38	5,232E+07	1,641E+06	08.09.06	2,04E-03
39	9,146E+07	2,871E+06	08.09.06	3,80E-03
40	1,328E+08	4,113E+06	08.09.06	6,36E-03
41	1,530E+08	4,733E+06	08.09.06	9,3E-03
42	1,531E+08	4,752E+06	08.09.06	1,22E-02
43	1,841E+08	5,692E+06	08.09.06	1,58E-02
44	2,060E+08	6,380E+06	08.09.06	1,97E-02
45	2,705E+08	8,360E+06	08.09.06	2,49E-02
46	2,788E+08	8,626E+06	08.09.06	3,03E-02
47	6,584E+08	2,042E+07	08.09.06	4,3E-02

Id. HFR Eu1bis 1

Table 51: Heating program and plate change of the HFR Eu1bis1

Time (hh:mm)	Step duration (min)	Temperature (°C)	Temperature rise (°C/h)	Plate
00:00	30	20	600	86
00:30	300	300	0	86
06:30	180	300	316.6	86
09:30	630	1250	0	86
20:00	1440	1250	0	86 - 87
44:00	1380	1250	0	87 - 88
67:00	1440	1250	0	88 - 89
91:00	1440	1250	0	89 - 90
115:00	1500	1250	0	90 - 91
140:00	1580	1250	0	91 - 92
166:30	2580	1250	0	92 - 94
209:30	300	1250	0	94
215:30		20		94 - 95
215:30	60	20	0	95
216:30	30	20	560	95
217:00	180	300	0	95
220:00	120	300	475	95
222:00	600	1250	0	95
232:00	90	1250	46.66	95
233:30	360	1320	46.66	95 - 96
239:30	210	1600	0	96
243:00	900	1600	0	96 - 97
258:00	300	1600	0	97 - 98
263:00	1200	1600	0	98 - 99
283:00	1440	1600	0	99 - 100
307:00	1380	1600	0	100 - 101
330:00	360	1600	0	101 - 102
336:00	1080	1600	0	102 - 103
354:00	1440	1600	0	103 - 104

378:00	1440	1600	0	104 - 105
402:00	1560	1600	0	105 - 106
428:00	690	1600	0	106 - 107
439:30	930	1600	-101.94	107
455:00		20		107 - 108

Time (hh:mm)	Step duration (min)	Temperature (°C)	Temperature rise (°C/h)	Plate
455:00	60	20	0	108
456:00	30	20	560	108
456:30	180	300	0	108
459:30	120	300	475	108
461:30	600	1250	0	108
471:30	90	1250	47.37	108
473:00	360	1321	47.37	108 - 109
479:00	120	1605	47.37	109 - 110
481:00	930	1700	0	110
496:30	420	1700	0	110 - 111
503:30	1140	1700	0	111 - 112
522:30	1380	1700	0	112 - 113
545:30	1620	1700	0	113 - 114
572:30	1440	1700	0	114 - 115
596:30	1440	1700	0	115 - 116
620:30	630	1700	0	116 - 117
631:00	900	1700	-112	117
646:00	0	20	0	117
646:00		20		117 - 118

Table 52: Cs-137 and Cs-134 activities of the condensate plates of HFR Eu1bis 1

Platte	Cs-137 (Bq)	+ - (Bq)	Cs-134 (Bq)	+ - (Bq)	Date
86	5.446E+05	1.710E+04	1.807E+05	5.667E+03	10.04.08
87	1.971E+05	6.180E+03	9.289E+04	2.889E+03	10.04.08
88	2.995E+05	9.385E+03	1.406E+05	4.369E+03	09.04.08
89	3.446E+05	1.090E+04	1.613E+05	5.057E+03	10.04.08
90	3.286E+05	1.035E+04	1.542E+05	4.848E+03	10.04.08
91	3.653E+05	1.152E+04	1.690E+05	5.321E+03	10.04.08
92	3.728E+05	1.176E+04	1.734E+05	5.462E+03	09.04.08
94	6.359E+05	2.030E+04	2.996E+05	9.569E+03	10.04.08
95	3.954E+05	1.624E+04	1.792E+05	8.020E+03	05.05.08
96	2.704E+06	1.003E+05	1.230E+06	5.021E+04	05.05.08
97	5.613E+06	2.163E+05	2.564E+06	1.085E+05	05.05.08
98	1.659E+06	6.169E+04	7.572E+05	3.083E+04	06.05.08
99	5.416E+06	2.087E+05	2.468E+06	1.043E+05	05.05.08
100	5.952E+06	2.242E+05	2.680E+06	1.113E+05	05.05.08
101	4.811E+06	1.775E+05	2.165E+06	8.751E+04	06.05.08
102	1.065E+06	4.336E+04	4.792E+05	2.128E+04	05.05.08
103	3.370E+06	1.303E+05	1.573E+06	6.800E+04	05.05.08
104	4.737E+06	1.753E+05	2.123E+06	8.596E+04	06.05.08
105	4.349E+06	1.698E+05	1.962E+06	8.408E+04	05.05.08
106	5.297E+06	1.943E+05	2.366E+06	9.317E+04	06.05.08
107	2.569E+06	1.007E+05	1.150E+06	4.931E+04	05.05.08
108	1.083E+06	1.904E+05	4.607E+05	8.428E+04	20.05.08
109	1.113E+06	1.710E+05	5.922E+05	9.403E+04	20.05.08
110	8.148E+06	8.784E+05	4.093E+06	6.021E+05	20.05.08
111	4.065E+06	4.517E+05	1.978E+06	2.910E+05	20.05.08
112	9.771E+06	1.044E+06	4.764E+06	7.113E+05	20.05.08
113	1.817E+07	1.914E+06	6.767E+06	7.396E+05	20.05.08
114	2.355E+07	2.496E+06	1.081E+07	1.597E+06	20.05.08
115	2.609E+07	2.751E+06	1.232E+07	9.701E+05	20.05.08
116	2.670E+07	2.813E+06	1.297E+07	1.958E+06	20.05.08
117	1.587E+07	1.666E+06	7.590E+06	1.164E+06	20.05.08

Table 53: Ag-110m and Ru-106 activities of the condensate plates of HFR Eu1bis 1

Plate	Ag-110m (Bq)	+ - (Bq)	Ru-106 (Bq)	+ - (Bq)	Date
86	86 1.312E+04	1.839E+03	<2.240E+03*	2.240E+03	10.04.08
87	8.092E+03	1.050E+03	1.122E+03	5,615E+02	10.04.08
88	4.322E+03	6.469E+02	8.475E+02	6,258E+02	09.04.08
89	4.804E+03	7.316E+02	2.556E+03	1,476E+03	10.04.08
90	3.880E+03	6.048E+02	1.050E+03	9,765E+02	10.04.08
91	3.356E+03	5.492E+02	3.771E+03	1,955E+03	10.04.08
92	2.601E+03	4.495E+02	1.949E+03	1,961E+03	09.04.08
94	3.726E+03	7.256E+02	<2.000E+03*	2,000E+03*	10.04.08
95	8.429E+02	6.866E+02	<7,698E+03*	7,698E+03	05.05.08
96	4.891E+03	2.899E+03	<1,610E+04*	1,610E+04	05.05.08
97	<1.457E+04*	1.457E+04	<6,696E+04*	6,696E+04	05.05.08
98	6.908E+02	8.340E+02	<1,094E+04*	1,094E+04	06.05.08
99	<1.444E+04*	1.444E+04	<6,547E+04*	6,547E+04	05.05.08
100	6.942E+03	4.885E+03	<5,946E+04*	5,946E+04	05.05.08
101	3.612E+03	3.042E+03	<2,241E+04*	2,241E+04	06.05.08
102	1.460E+03	1.491E+03	<1,947E+04*	1,947E+04	05.05.08
103	1.038E+04	1.210E+04	<7,050E+02*	7,050E+02	05.05.08
104	3.522E+03	3.114E+03	<2,539E+04*	2,539E+04	06.05.08
105	<1.321E+04*	1.321E+04	<5,880E+04*	5,880E+04	05.05.08
106	3.949E+03	2.960E+03	<1,112E+04*	1,112E+04	06.05.08
107	< 7.863E+03*	7.863E+03	<3,537E+04*	3,537E+04	05.05.08

Table 54: Cumulative release portions for HFR Eu1bis1

Plate	Time (h)	Cumulative portion released Cs-137	Cumulative portion released Cs-134	Cumulative portion released Ag-110m	Cumulative portion released Ru-106
86	20	1,26917E-05	9,18658E-06	6,94E-04	6,95652E-08
87	44	1,7285E-05	1,39095E-05	0,00112	1,0441E-07
88	67	2,42601E-05	2,10574E-05	0,00135	1,30745E-07
89	91	3,23002E-05	2,92578E-05	0,00161	2,10124E-07

90	115	3,99441E-05	3,70971E-05	0,00181	2,42733E-07
91	140	4,84735E-05	4,56889E-05	0,00199	3,59938E-07
92	166,5	5,71662E-05	5,44992E-05	0,00213	4,20497E-07
94	215	7,19646E-05	6,97509E-05	0,00232	6,36957E-07
95	233,5	8,11932E-05	7,8851E-05	0,00237	8,76E-07*
96	243	1,44209E-04	1,41383E-04	0,00265	1,38E-06*
9	258	2,74994E-04	2,71734E-04	0,00348	3,46E-06*
98	263	3,1368E-04	3,10219E-04	0,00352	3,8E-06*
99	283	4,39991E-04	4,35689E-04	0,00434	5,83E-06*
100	307	5,78653E-04	5,71937E-4	0,00474	7,67E-06*
101	330	6,90748E-04	6,82257E-04	0,00494	8,37E-06*
102	336	7,15451E-04	7,06151E-04	0,00502	8,98E-06*
103	354	7,93987E-04	7,86477E-04	0,00561	9,0E-06*
104	378	9,04451E-04	8,94255E-04	0,00582	9,79E-06*
105	402	0,00101	9,93899E-04	0,00656	1,16E-05*
106	428	0,00113	0,00111	0,00679	1,2E-05*
107	455	0,00119	0,00117	0,00724	1,31E-05*
108	473	0,00121	0,0012	0,01018*	1,62E-05*
109	479	0,00124	0,00123	0,01255*	1,85E-05*
110	496,5	0,00143	0,00143	0,0178*	3,02E-05*
111	503,5	0,00152	0,00153	0,02105*	3,08E-05*
112	522,5	0,00175	0,00178	0,02616*	4,17E-05*
113	545,5	0,00218	0,00212	0,0336*	5,94E-05*
114	572,3	0,00272	0,00267	0,04556*	8,43E-05*
115	596,5	0,00333	0,0033	0,05643*	1,07E-04*
116	620,5	0,00395	0,00396	0,06841*	1,29E-04*
117	646	0,00433	0,00434	0,07353*	1,41E-04*

* detection limit

le. HFR Eu1bis 3

Table 55: Heating program and plate exchange of HFR Eu1bis3

Time (hh:mm)	Step duration (min)	Temperature (°C)	Temperature rise (°C/h)	Plate
00:00	60	20	0	120
01:00	30	20	560	120
01:30	180	300	0	120
04:30	120	300	475	120
06:30	10	1250	0	120
06:40	1310	1250	0	120 - 121
28:30	1440	1250	0	121 - 122
52:30	2610	1250	0	122 - 123
96:00	120	1250	-615	123
98:00	60	20	0	123 - 124
99:00	30	20	560	124
99:30	180	300	0	124
102:30	120	300	475	124
104:30	600	1250	0	124
114:30	207	1250	46.98	124
118:00	240	1412	46.98	124 - 125
122:00	120	1600	0	125
124:00	1380	1600	0	125 - 126
147:00	1380	1600	0	126 - 127
170:00	180	1600	0	127 - 128
173:00	1440	1600	0	128 - 129
197:00	1380	1600	0	129 - 130
220:00	1620	1600	0	130 - 131
247:00	1500	1600	0	131 - 132
272:00	1470	1600	0	132 - 133
296:30	1530	1600	0	133 - 134
322:00	120	1600	-790	134
324:00		20		134 - 135

Table 56: Cs-137 and Cs-134 activities of the condensate plates of HFR Eu1bis 3

Plate	Cs-137 (Bq)	+ - (Bq)	Cs-134 (Bq)	+ - (Bq)	Date
120	3,832E+04	3,998E+03	1,769E+04	1,854E+03	20.08.08
121	1,827E+05	1,684E+04	9,261E+04	8,548E+03	25.08.08
122	2,754E+05	2,504E+04	1,428E+05	1,299E+04	20.08.08
123	7,192E+05	6,571E+04	3,704E+05	3,386E+04	20.08.08
124	7,436E+05	6,760E+04	3,890E+05	3,544E+04	28.08.08
125	6,600E+06	5,989E+05	3,466E+06	3,148E+05	28.08.08
126	2,696E+07	2,447E+06	1,402E+07	1,273E+06	20.08.08
127	1,851E+07	1,680E+06	9,519E+06	8,645E+05	25.08.08
128	2,459E+06	2,234E+05	1,272E+06	1,156E+05	20.08.08
129	1,514E+07	1,377E+06	7,848E+06	7,148E+05	20.08.08
130	1,265E+07	1,148E+06	6,477E+06	5,879E+05	28.08.08
131	1,296E+07	1,176E+06	6,568E+06	5,964E+05	25.08.08
132	1,077E+07	9,773E+05	5,474E+06	4,973E+05	28.08.08
133	9,736E+06	8,833E+05	4,913E+06	4,457E+05	25.08.08
134	9,915E+06	8,999E+05	5,015E+06	4,557E+05	28.08.08

Table 57: Ag-110m and Cs-134 activities of the condensate plates of HFR Eu1bis 3

Plate	Ag-110m (Bq)	+ - (Bq)	Ru-106 (Bq)	+ - (Bq)	Date
120	1,524E+03	3,951E+02	<4,096E+03*	<4,096E+03*	20.08.08
121	1,204E+04	1,274E+03	3,814E+04	7,591E+03	25.08.08
122	4,738E+03	4,793E+02	<3,044E+03*	<3,044E+03*	20.08.08
123	3,659E+03	6,636E+02	<1,457E+04*	<1,457E+04*	20.08.08
124	9,657E+02	2,809E+02	<8,150E+03*	<8,150E+03*	28.08.08
125	4,088E+03	9,118E+02	2,554E+04	2,641E+04	28.08.08
126	6,245E+03	5,923E+03	<1,064E+05*	<1,064E+05*	20.08.08
127	7,657E+03	2,663E+03	<8,024E+04*	<8,024E+04*	25.08.08
128	9,451E+02	5,667E+02	<2,026E+04*	<2,026E+04*	20.08.08
129	9,571E+03	6,372E+03	<1,759E+05*	<1,759E+05*	20.08.08
130	7,432E+03	1,521E+03	<4,453E+04*	<4,453E+04*	28.08.08
131	7,007E+03	1,613E+03	<4,669E+04*	<4,669E+04*	25.08.08

132	6,601E+03	1,747E+03	<5,338E+04*	<5,338E+04*	28.08.08
133	6,877E+03	9,940E+02	<2,530E+04*	<2,530E+04*	25.08.08
134	5,645E+03	1,490E+03	<5,241E+04*	<5,241E+04*	28.08.08

* detection limit

Table 58: Cumulative release portions for HFR Eu1bis3

Plate	Time (h)	Cumulative portion released Cs-137	Cumulative portion released Cs-134	Cumulative portion released Ag-110m	Cumulative portion released Ru-106
120	6,66	7,58526E-07	7,23074E-07	6,30962E-05	1,25956E-07
121	28,5	4,37459E-06	4,50848E-06	5,68517E-04	1,30977E-06
122	52,5	9,82601E-06	1,03454E-05	7,64663E-04	1,40347E-06
123	98	2,40702E-05	2,54854E-05	9,1637E-04	1,85125E-06
124	118	3,87775E-05	4,14061E-05	9,56978E-04	2,10579E-06
125	124	1,69421E-04	1,83078E-04	0,00113	2,90268E-06*
126	147	7,03102E-04	7,56182E-04	0,00139	6,17374E-06*
127	170	0,00107	0,00115	0,00171	8,66367E-06*
128	173	0,00112	0,0012	0,00175	9,28834E-06*
129	197	0,00142	0,00152	0,00215	1,46973E-05*
130	220	0,00167	0,00178	0,00246	1,60868E-05*
131	247	0,00192	0,00205	0,00275	1,75346E-05*
132	272	0,00214	0,00228	0,00303	1,92014E-05*
133	296,5	0,00233	0,00248	0,00332	1,99866E-05*
134	324	0,00253	0,00268	0,00356	2,16212E-05*

* detection limit

lf. HFR Eu1bis 4

Table 59: Heating program and plate exchange of HFR Eu1bis4

Time (hh:mm)	Step duration (min)	Temperature (°C)	Temperature rise (°C/h)	Plate
00:00	30	20	560	136
00:30	180	300	0	136
03:30	120	300	250	136
05:30	1020	800	0	136
22:30	420	800	0	136 - 137
29:30	930	800	0	137
45:00	510	800	0	137 -138
53:30	180	800	150	138
56:30	600	1250	0	138
66:30	300	1250	14	138
71:30	300	1320	14	138 - 139
76:30	600	1390	11	139
86:30	300	1500	7	139
91:30	300	1535	7	139 - 140
96:30	600	1570	6	140
106:30	540	1630	4	140
115:30	60	1666	4	140 - 141
116:30	600	1670	2.5	141
126:30	600	1695	1.5	141
136:30	210	1710	0.42	141
140:00	1230	1711.5	0.42	141 - 142
160:30	330	1720	0	142
166:00	1110	1720	0	142 - 143
184:30	1440	1720	0	143
208:30	1440	1720	0	143
232:30	120	1720	0	143
234:30	1320	1720	0	143 - 144
256:30	180	1720	0	144
259:30	1260	1720	0	144 - 145

280:30	120	1720	- 850	145
282		20		145
				169

Table 60: Cs-137 and Cs-134 activities of the condensate plates of HFR Eu1bis 4

Plate	Cs-137 (Bq)	+ - (Bq)	Cs-134 (Bq)	+ - (Bq)	Date
136	5.206E+05	1.814E+04	2.297E+05	8.501E+03	27.11.08
137	3.644E+04	1.541E+03	1.446E+04	6.573E+02	27.11.09
138	8.313E+05	2.881E+04	3.811E+05	1.398E+04	27.11.10
139	8.459E+06	2.945E+05	3.918E+06	1.448E+05	27.11.11
140	3.909E+07	1.895E+06	1.654E+07	1.477E+06	19.12.08
141	3.861E+07	1.732E+06	1.629E+07	1.432E+06	19.12.08
142	3.192E+07	1.529E+06	1.374E+07	1.217E+06	19.12.08
143	1.536E+08	6.882E+06	6.481E+07	5.715E+06	19.12.08
144	1.034E+08	4.671E+06	4.444E+07	3.950E+06	19.12.08
145	1.051E+08	4.730E+06	4.547E+07	4.022E+06	19.12.08

Table 61: Ag-110m and Ru-106 activities of the condensate plates of HFR Eu1bis 4

Plate	Ag-110m (Bq)	+ - (Bq)	Ru-106 (Bq)	+ - (Bq)	Date
136	1.124E+02	1.483E+02	-	-	27.11.08
137	1.652E+02	1.086E+02	-	-	27.11.09
138	1.684E+04	6.525E+02	-	-	27.11.10
139	7.696E+03	2.100E+03	-	-	27.11.11
140	1.422E+05	1.422E+05	-	-	19.12.08
141	1.867E+04	1.310E+04	-	-	19.12.08
142	2.517E+04	3.267E+04	-	-	19.12.08
143	1.366E+05	5.744E+04	-	-	19.12.08
144	8.363E+04	4.737E+04	-	-	19.12.08
145	6.588E+04	4.680E+04	-	-	19.12.08

Table 62: Cumulative release portions for HFR Eu1bis4

Plate	Time (h)	Cumulative portion released Cs-137	Cumulative portion released Cs-134	Cumulative portion released Ag-110m	Cumulative portion released Ru-106
136	22,5	1,03625E-05	1,03744E-05	5,38434E-06	-
137	45	1,1087E-05	1,10293E-05	1,32977E-05	-
138	71,5	2,76279E-05	2,82417E-05	8,19888E-04	-
139	91,5	1,96003E-04	2,05185E-04	0,00119	-
140	115,5	9,74144E-04	9,5208E-04	0,00843	-
141	140	0,00174	0,00169	0,00938	-
142	166	0,00238	0,00231	0,01066	-
143	234,5	0,00544	0,00523	0,01762	-
144	259,5	0,00749	0,00724	0,02188	-
145	282	0,00959	0,00929	0,02523	-

Appendix II. Stress analysis

The stress distribution in a thick-walled spherical shell is derived by analogy with the procedure used for a thick-walled cylinder. A derivation for the thick-walled cylindrical container is found in [Klapp 1980]. By analogy with the procedure used there, the positive [plus] sign is used for compressive stress in the radial direction and positive [sic] for tensile stress in the tangential direction. This unusual convention is valid only for this subordinate point in order to assure comparability. Everywhere else in this report, compressive stress is indicated by a negative [minus] sign. The following infinitesimal equilibrium exists for the spherical geometry.

$$0 = \frac{d}{dr}(r^2\sigma_r) + r\sigma_\theta + r\sigma_\varphi$$

Equation 66

Due to the symmetry, the tangential stress is the same in all directions.

$$\sigma_\theta = \sigma_\varphi = \sigma_t$$

Equation 67

Now if one considers the displacement conditions in the radial and tangential direction, one obtains three differential equations.

$$\Leftrightarrow 0 = \sigma_r + \frac{r}{2} \cdot \frac{d\sigma_r}{dr} + \sigma_t$$

Equation 68

$$\varepsilon_r = \frac{dw}{dr} = -\frac{\sigma_r}{E} - \frac{2\nu\sigma_t}{E}$$

Equation 69

$$\varepsilon_t = \frac{w}{r} = \frac{\sigma_t}{E} + \frac{\nu\sigma_r}{E}$$

Equation 70

Rearranging equation 69 and equation 70 to $\sigma_r(w)$ and $\sigma_t(w)$ we get

$$\sigma_r = \frac{E}{1-\nu-2\nu^2} \left(-\frac{2\nu w}{r} - (1-\nu) \frac{dw}{dr} \right) \quad \text{Equation 71}$$

$$\sigma_t = \frac{E}{1-\nu-2\nu^2} \left(\frac{w}{r} + \nu \frac{dw}{dr} \right) \quad \text{Equation 72}$$

By substituting into equation 68 one finally obtains:

$$0 = \frac{r^2}{2} \frac{d^2 w}{dr^2} + r \frac{dw}{dr} - w \quad \text{Equation 73}$$

The general solution for this differential equation is:

$$w(r) = C_1 r + \frac{C_2}{r^2} \quad \text{Equation 74}$$

The solution can now be substituted together with the boundary conditions $\sigma_r(r_i) = p_i$ and $\sigma_r(r_a) = p_a$ into equation 71 and solved for C_1 and C_2 .

$$C_1 = \frac{(p_i r_i^3 - p_a r_a^3) (1-2\nu)}{E (r_a^3 - r_i^3)} \quad \text{Equation 75}$$

$$C_2 = \frac{1}{2} (p_i - p_a) \frac{(\nu+1) (r_i^3 r_a^3)}{E (r_a^3 - r_i^3)} \quad \text{Equation 76}$$

With the terms for C_1 and C_2 , equation 74 can now be substituted into equation 71 and equation 72 in order to obtain the radial and tangential stress distribution.

$$\sigma_r = \frac{1}{(r_a^3 - r_i^3)} \left((p_i - p_a) \frac{r_a^3 r_i^3}{r^3} + (p_a r_a^3 - p_i r_i^3) \right) \quad \text{Equation 77}$$

$$\sigma_r = \frac{1}{(r_a^3 - r_i^3)} \left(\frac{1}{2} (p_i - p_a) \frac{r_a^3 r_i^3}{r^3} + (p_i r_i^3 - p_a r_a^3) \right)$$

Equation 78

The stress distribution in the three-layer system IPyC, SiC and OPyC is obtained now by substituting the boundary conditions between the coatings/layers.

$$\sigma_{r,IP}(r_{i,IP}) = p_i$$

Equation 79

$$\sigma_{r,IP}(r_{a,IP}) = \sigma_{r,SI}(r_{i,SI}) = p_1$$

Equation 80

$$\sigma_{r,SI}(r_{a,SI}) = \sigma_{r,OP}(r_{i,OP}) = p_2$$

Equation 81

$$\sigma_{r,OP}(r_{a,OP}) = p_a$$

Equation 82

$$w_{IP}(r_{a,IP}) = w_{SI}(r_{i,SI})$$

Equation 83

$$w_{SI}(r_{a,SI}) = w_{OP}(r_{i,OP})$$

Equation 84

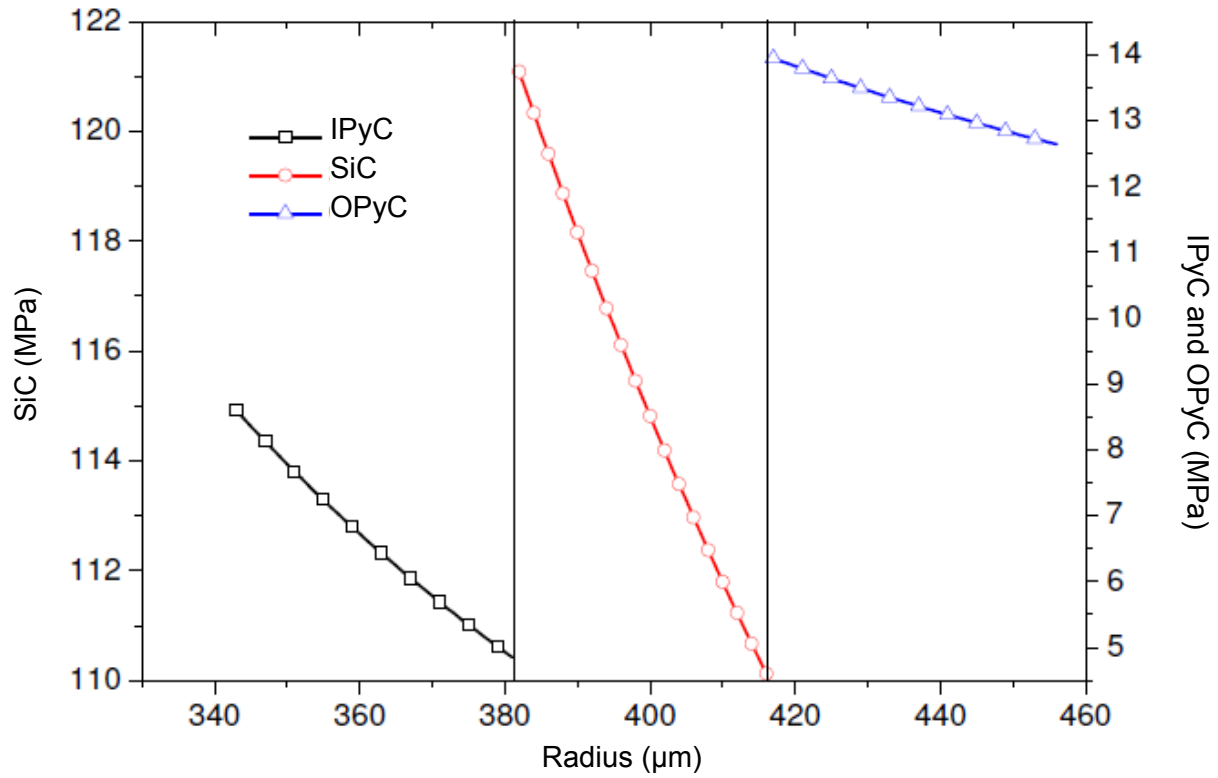


Figure 76: Tangential stress distribution for a linear elastic, spherically symmetrical three layer system at an internal pressure of 33 MPa.

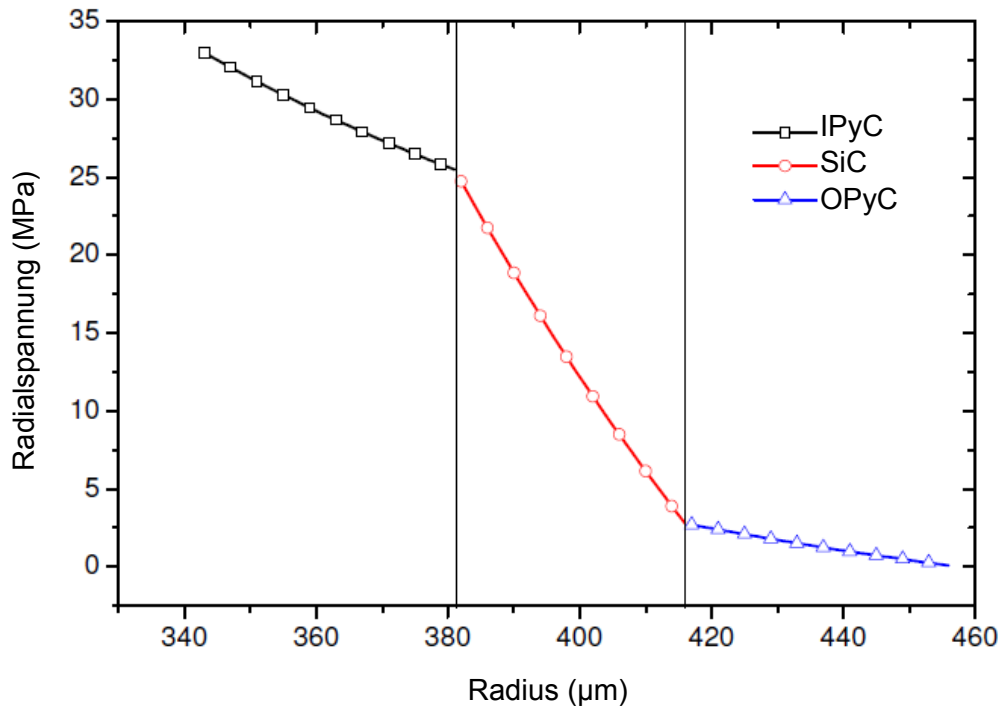


Figure 77: Radial stress distribution for a linear elastic, spherically symmetrical three layer system at an internal pressure of 33 MPa.

In Figure 76 and Figure 77, the tangential and radial stress distribution for a linear elastic, spherically symmetrical three layer system with a pronounced internal pressure of 33 MPa is represented. The behavior of the real IPyC coating, SiC coating and OPyC coating system during irradiation is more complicated. Thus, for example, the various thermal expansion coefficients and the effect of the fast neutron fluence on the dimensional variation of the PyC must be allowed for (see Fig. 78). To be sure, the literature contains some formulas for analytic solutions that allow for these factors in part [Prados & Scott 1967], [Walther 1971], [Miller & Bennet 1993], but even these models do not succeed without simplifications. Within the scope of this project, the method of finite element calculation was applied for simulation of the buildup of stresses in the jacket coatings of the particles.

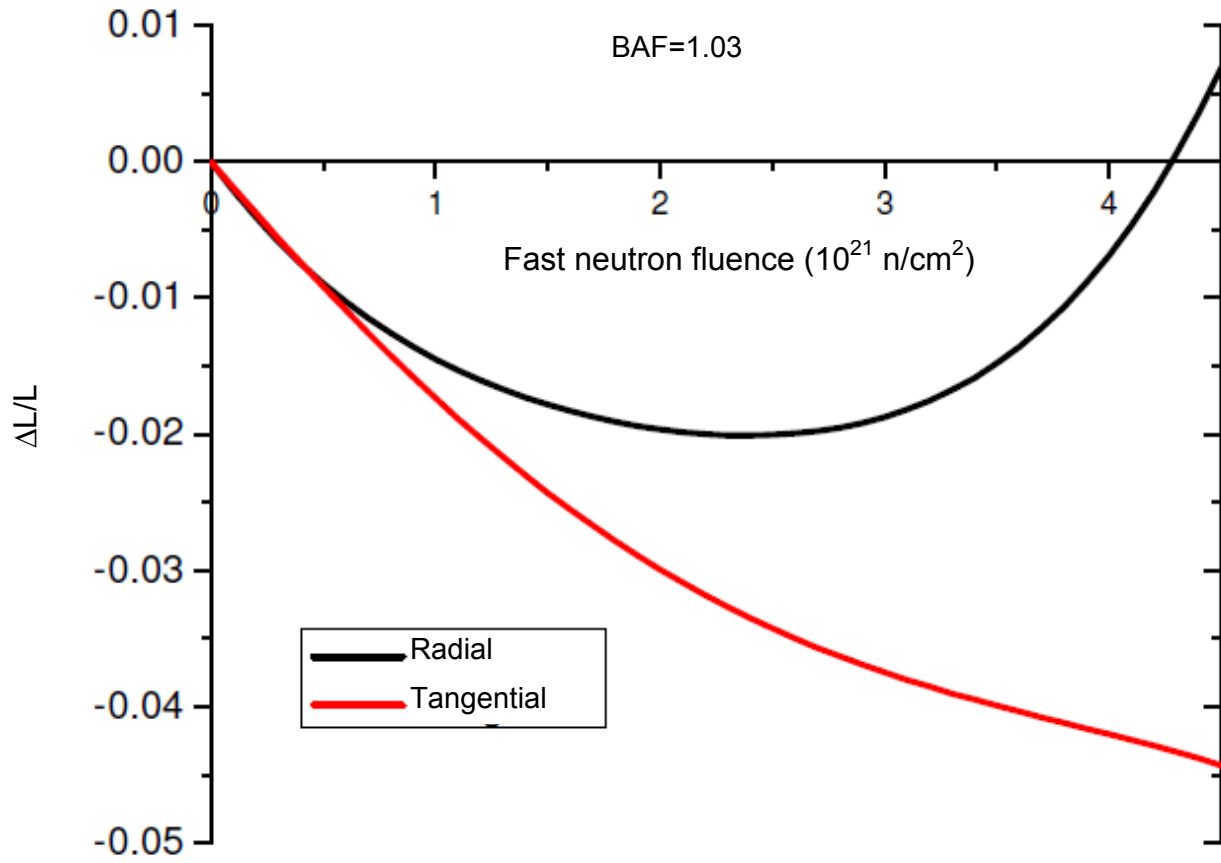


Figure 78: Irradiation-induced dimensional variation of PyC in the radial and tangential directions as a function of the fast neutron fluence ($E > 0.1 \text{ MeV}$)

Appendix III. Temperature calculations

IIIa. Temperature distribution in the fuel elements

An estimation of the temperature distribution in the fuel element during the irradiation is obtained from the simplified heat balance. As a simplification, it is assumed here that the volumetric heat production in the fuel zone and the thermal conductivity in the entire fuel element are constant.

$$\frac{1}{r^2} \cdot \frac{d}{dr} \left(\lambda r^2 \frac{dT_b}{dr} \right) + \ddot{\phi} = 0$$

Fuel zone Equation 85

$$\frac{1}{r^2} \cdot \frac{d}{dr} \left(\lambda r^2 \frac{dT_s}{dr} \right) = 0$$

Spherical shell Equation 86

$$\ddot{\phi} = \frac{3P_{BE}}{4\pi r_i^3}$$

Solution:

$$T_b = -\frac{P_{BE} r^2}{8\pi \lambda r_i^3} + C_0$$

Equation 87

Q

$$T_s = \frac{C_1}{r} + C_2$$

Equation 88

Boundary conditions:

$$\left. \frac{dT_b}{dr} \right|_{r=0} = 0$$

$$T_b(r = r_i) = T_s(r = r_i)$$

$$T_s(r = r_a) = T_a$$

$$-\lambda \left. \frac{dT_s}{dr} \right|_{r=r_a} = \frac{P_{BE}}{4\pi r_a^2}$$

Solution:

$$C_1 = \frac{P_{BE}}{4\pi\lambda}$$

$$C_2 = T_a - \frac{P_{BE}}{4\pi\lambda r_a}$$

$$C_0 = \frac{P_{BE}}{4\pi\lambda} \left(\frac{1}{r_i} - \frac{1}{r_a} + \frac{1}{2r_i} \right) + T_a$$

$\ddot{\phi}$ = volumetric power output = fuel element power output

λ = thermal conductivity, = temperature of the fuel zone,

T_s = Temperature of the shell, = external temperature of the fuel element,

r = radius, r_i = radius of the fuel zone, r_a = outer radius

A similar procedure is used for the temperature distribution in the particle. The heat conductance of the graphite matrix is a function of the temperature and the fast neutron fluence (see Fig. 79).

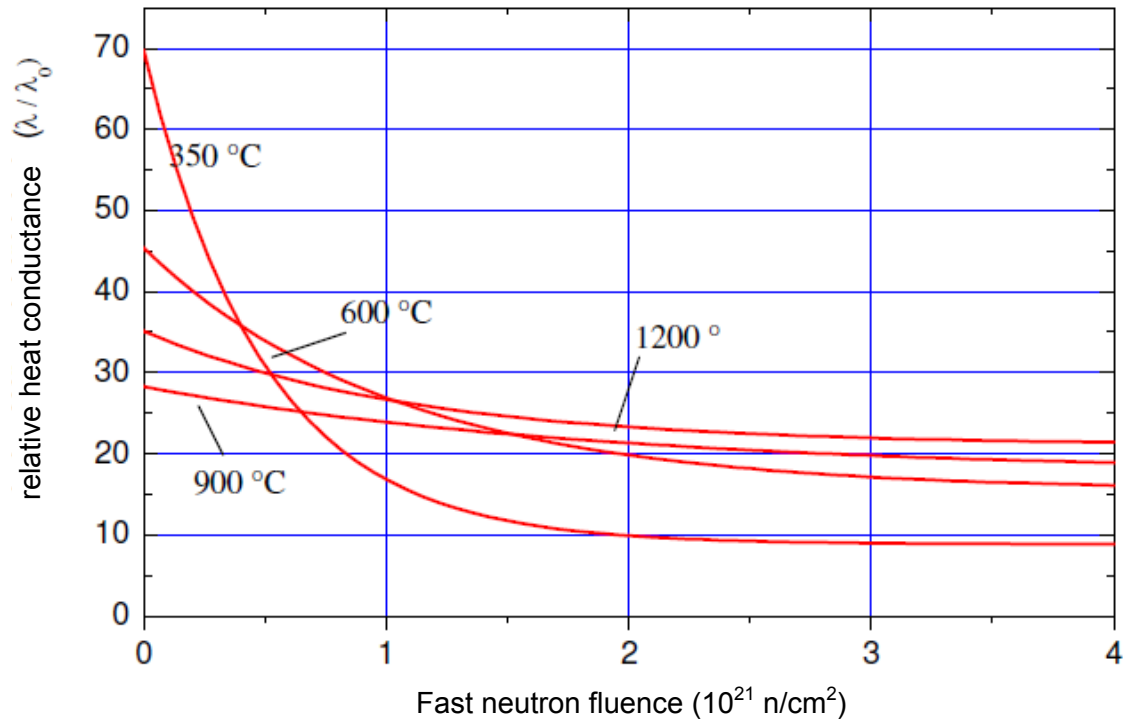


Figure 79: Relative heat conductance of matrix graphite as a function of the fast neutron fluence and temperature [Kugeler & Schulten 1989]

Figure 80 gives the thermal conductivity in the particle jacket coatings as a function of the temperature

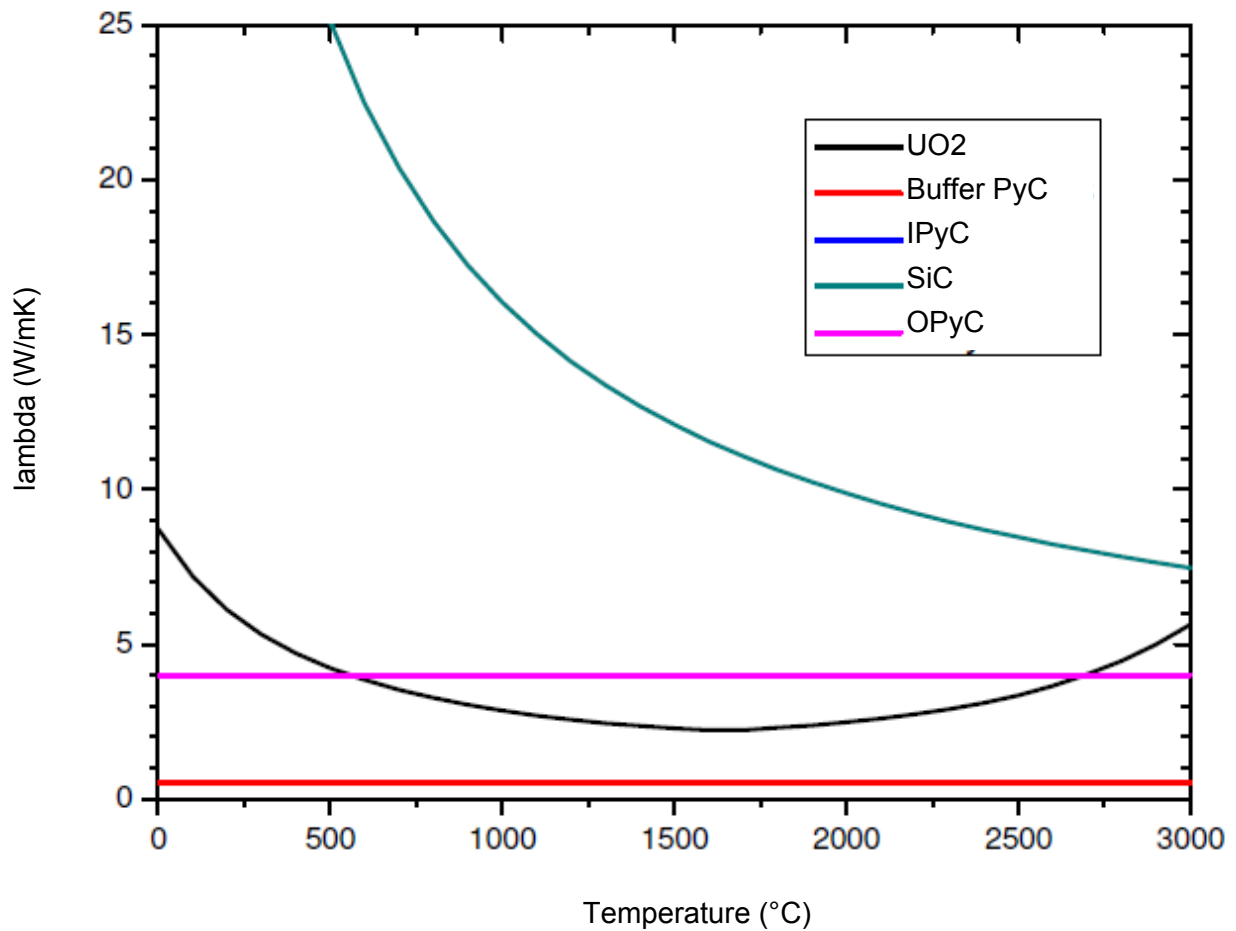


Figure 80: Thermal conductivity of particle coating materials as a function of the temperature [Nabielek et al. 1992]

The calculated average irradiation temperature of the fuel elements studied in this project are listed in Table 63.

Table 63: Irradiation temperatures of the fuel elements studied

Fuel element	External temperature of sphere	Temperature in center of the sphere	Fuel temperature	Temperature gradient in the particle
AVR 74/18	~ 720 °C	~ 820 °C	~ 834°C	~ 13°C
HFR K6/2	~ 800 °C	~ 940 °C	~ 962°C	~ 21°C

HFR K6/3	~ 800 °C	~ 940 °C	~ 963°C	~ 22°C
HFR Eu1bis 1	~ 1000 °C	~ 1250 °C	~ 1305°C	~ 55°C
HFR Eu1bis 3	~ 1000 °C	~ 1250 °C	~ 1316°C	~ 65°C
HFR Eu1bis 4	~ 1000 °C	~ 1250 °C	~ 1316°C	~ 65°C

IIIb. Temperature distribution in the CoFA II

The heating of the CoFA II is accomplished by Joulean heat that is released in the heating element at high current intensities. The fuel element is surrounded by the cylindrical heating element. The configuration and therefore the temperature distribution in the fuel element are axially symmetrical. The surrounding heat shields limit the heat loss to the outside and assure a homogenization of the temperature over the height (see Fig. 9). Despite this, the temperature distribution over the height during a bakeout experiment in the furnace/kiln parts and the fuel element is not homogeneous. Rather a diminishing gradient is created from the center to the water-cooled components cold finger and current connection. With the aid of the finite element (FEM) program Abaqus, the temperature distribution in the CoFA II is calculated at different heating powers. For this purpose, the tantalum parts heating element, gas guiding cylinder and heating shield as well as the copper block, the cold finger, the thermocouple and the fuel element are simulated as a two-dimensional axially symmetrical FEM model. In addition, the temperature-dependent material properties density, thermal conductivity, heat capacity and degree of emission are simulated [Touloukain & DeWitt 1970].

Table 64: Required CoFA heating powers for different temperatures

Power (W)	Measured temperature (°C)	Calculated temperature (°C)
1356	600	742
2905	1000	1036
4772	1300	1262
8160	1600	1535
9696	1700	1630
10960	1800	1700

The surrounding, water-cooled hood was modeled as the surrounding space with 20°C wall temperature, which is in a state of radiation exchange with the internal components of the furnace/kiln. The heating power was simulated by a constant-volume swelling term in the simulated heating element. As heat transporting mechanisms between the component, heat

conduction and heat radiation were simulated. Since the two above-noted mechanisms strongly predominate at high temperatures, the heat transport by convection could be neglected. In Table 64 and Figure 81, the measured and Abaqus-calculated temperatures on the thermocouple at a preassigned heating power are compared. The agreement is largely satisfactory; at higher temperatures, however, the calculation underestimates the actual values.

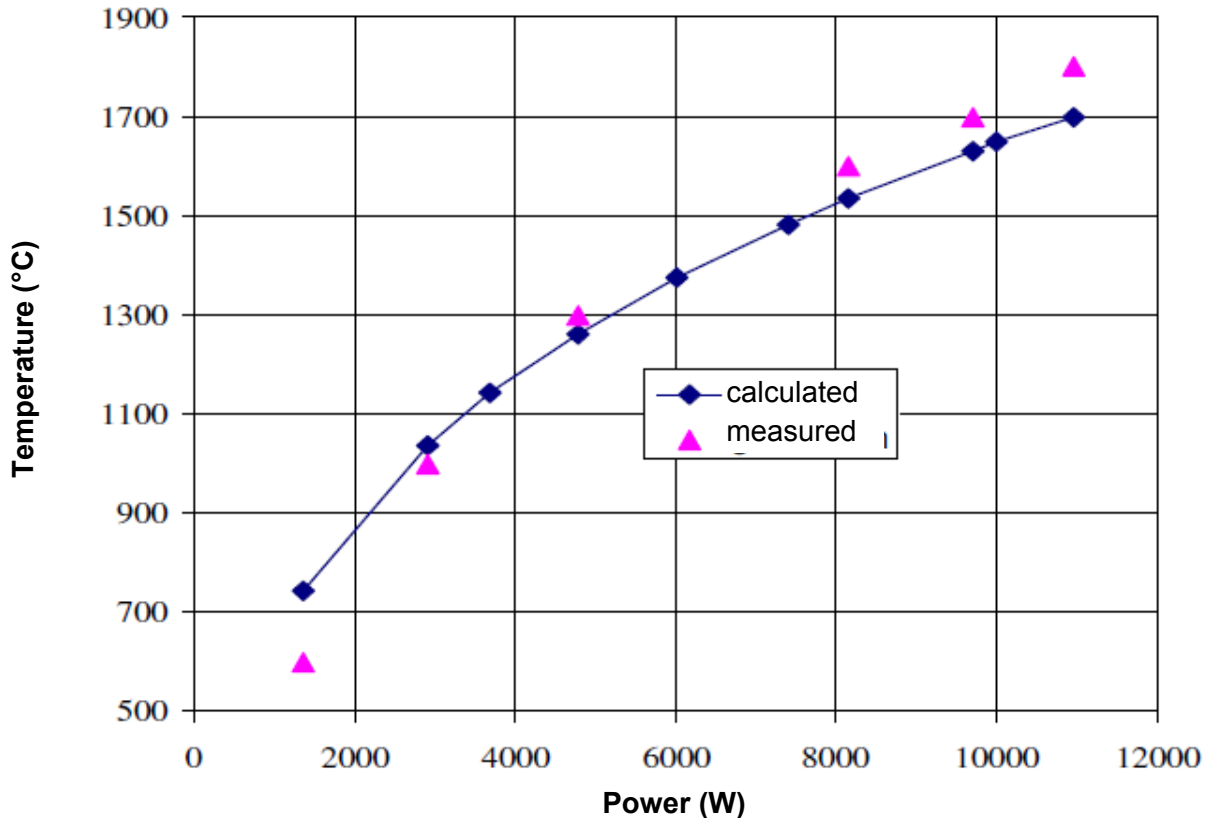


Figure 81: Calculated and measured CoFA temperature as a function of the heating power

In the colored illustration of the temperature distribution (Figure 82 and Figure 83) one sees that the fuel element is located in the center of the zone of highest temperature. The temperature difference between hottest and coldest point in the fuel element amounts to roughly 100°C, the average temperature agreeing well with the value on the thermocouple.

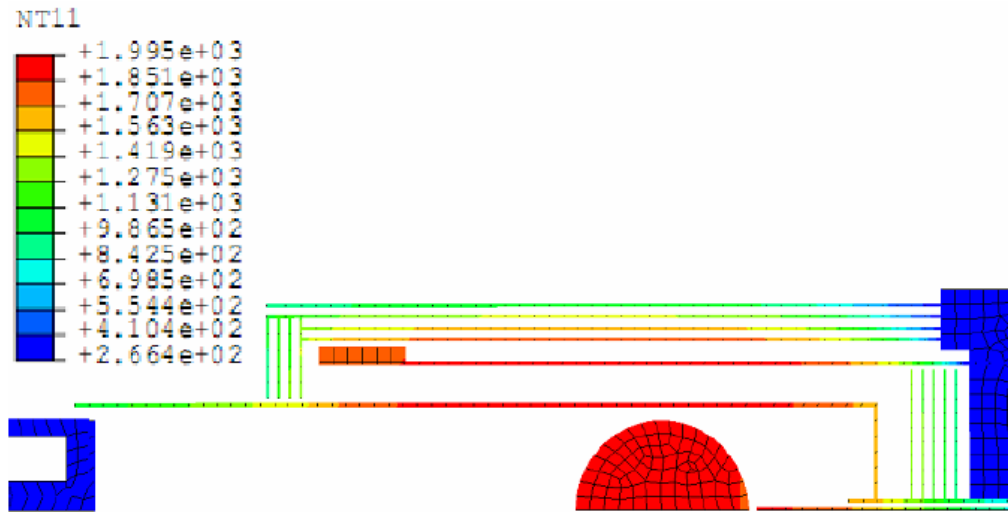


Figure 82: Temperature distribution (in K) in the CoFA II at 1650°C temperature on the thermocouple

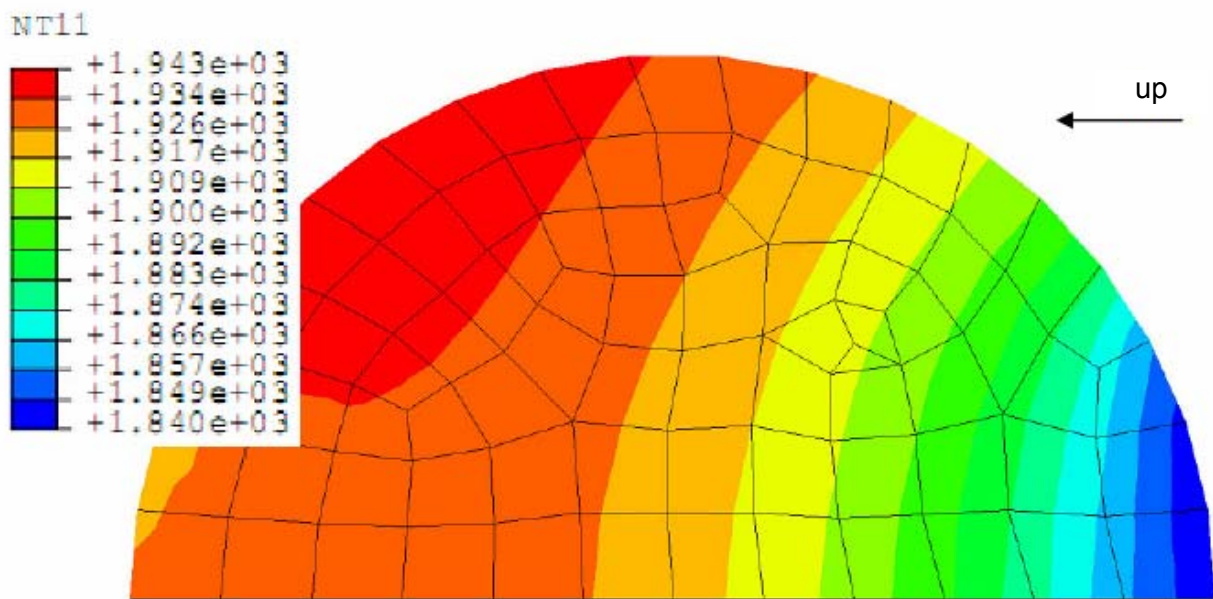


Figure 83: Temperature distribution (in K) in the fuel element at 1650°C temperature on the thermocouple

IIIc. AVR 74/18

As opposed to the other fuel elements studied, AVR 74/18 was not irradiated in a material testing reactor under controlled conditions but rather passed through the pebble heap core of the AVR. Coolant gas and fuel elements were passed in countercurrent in the AVR, i.e. the helium passed through the reactor from bottom to top and was heated up from 250 to 950°C in the process. The fuel element power during the pass through the reactor was also highest at the start and diminished toward the end with increasing burn-up. This resulted in general in a decreasing temperature curve from the start until the end of a cycle. The exact temperature history of a fuel element is not known because of the nature of the pebble heap reactor. During the AVR operation, however, as part of the experiment, a total of 106 monitor balls [pebbles] with fusible wires of different melting temperatures were inserted and passed through the pebble heap. The latter were subsequently studied, and it was determined which wires had fused and which had reached the maximal temperature [Schenk & Nabielek 1989]. Figure 84 shows the assumed temperature curve for AVR 74/18. The temperature difference between fuel element surface and fuel is already allowed for in this case (see Table 63).

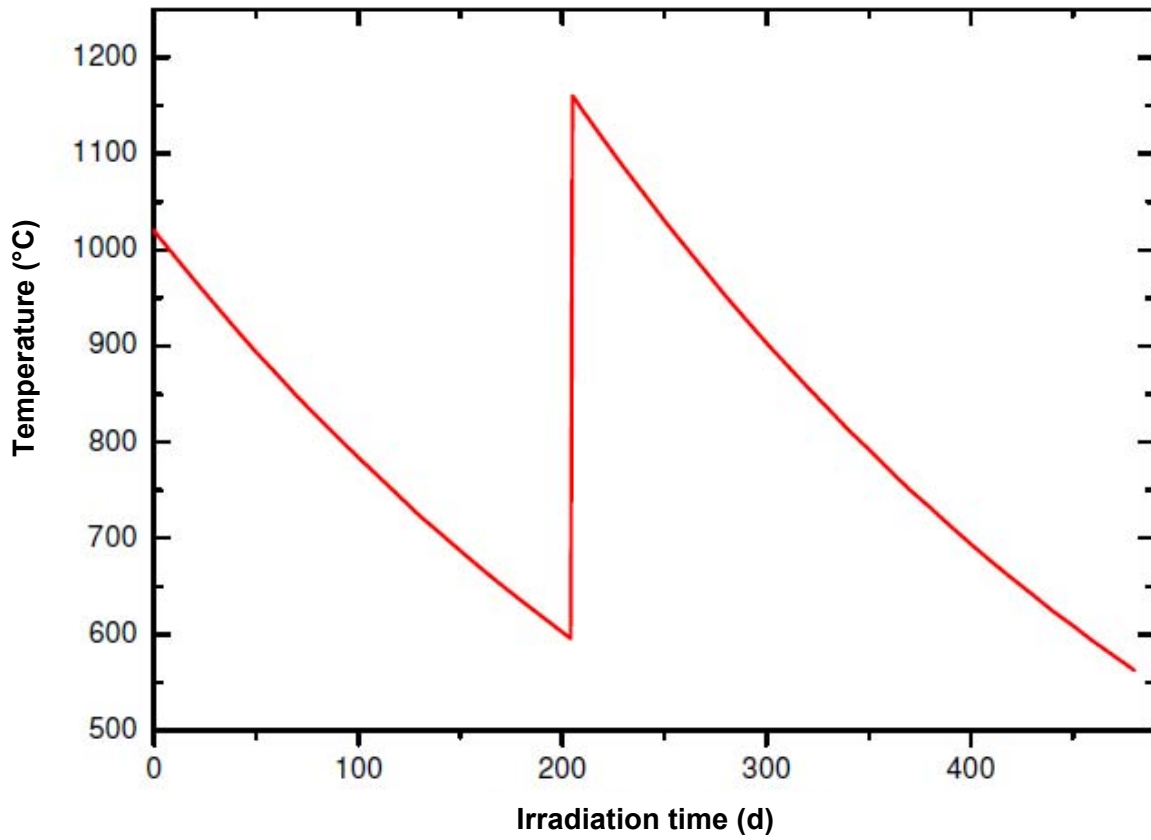


Figure 84: Assumed temperature curve during the irradiation of AVR 74/18 [Nabielek 2008].

Appendix IV. Determining the uncertainty

As part of this project, a series of measurements was performed for which the uncertainty values had to be determined. This involved primarily the determination of the fission product activity by gamma spectrometry. The following measurements were performed using this procedure.

- Determination of the activity on the condensate plates for measuring the release of solid fission products.
- Determination of the activity in the cold traps for measuring the fission gas release.
- Measuring the activity of the fuel elements for determining the inventory and burn-up.

In addition, the uncertainty of the cold finger efficiency, the uncertainty of the temperature measurements in the CoFA II and the uncertainty of the dimension measurement of the particle jacket coatings and of the fuel elements had to be determined.

1. Statistical error

The distribution of measured values is described mathematically by the Poisson distribution. If the number of measured values or impulses is large enough, the Poisson distribution can be approximated by a standard distribution. The point spread of the distribution around the anticipated mean value is expressed by the standard measurement uncertainty. For a number (n) of measurements, the mean value (x_m) of the measured values (x_i) is found as:

$$x_m = \frac{1}{n} \sum_{i=1}^n x_i$$

Equation 89

The standard uncertainty of measurement is found as:

$$\sigma = \sqrt{\frac{\sum_{i=1}^n (x_i - x_m)^2}{n-1}}$$

Equation 90

For a large number of registered impulses (X) in a gamma detector, the standard measurement uncertainty can be estimated:

$$\sigma \approx \sqrt{X}$$

Equation 91

It may be expected that the actual value lies within the interval $\pm\sigma$ with a probability of 68.3%. The twofold standard measurement uncertainty is usually reported. This means that the actual value lies with a probability of 95.7% within the stated uncertainty interval.

$$X = B - U$$

Equation 92

If the measured value (X) is composed of an underground measurement and a sample measurement (see equation 92), the entire statistical error can be determined from the error of the measured underground and the sample measurement.

$$\sigma_{stat} \approx \sqrt{U + B}$$

Equation 93

The statistical error of the gamma spectrometric measurements was determined automatically by the InterWinner program used after the entry of the data of the reference emitter, after the recording of the background spectrum and after the calibration.

2. Systematic errors

Besides the statistical measurement uncertainty, the systematic errors, i.e. the errors that are always the same in a series of measurements, must be determined. An example of a systematic error is, e.g., the inaccuracy of the radionuclide standards used for the gamma spectrometry and the nuclear data (decay constants, emission probabilities etc.). As a rule, these uncertainties could also be allowed for in the InterWinner evaluation. In some cases, however, they had to be calculated additionally. In these case, the GUM Workbench program was used.

To determine the uncertainty with GUM Workbench, first the mathematical relationships of the input and target values were entered. The known or estimated uncertainties (σ_i) were

coordinated with the input values (xi). The total uncertainty of the target value (F) was finally computed by the program by the Gaussian Error Propagation method.

$$\sigma_g \approx \sqrt{\sum_{i=1}^n \left(\sigma_i \frac{dF}{dx_i} \right)^2}$$

Equation 94

In the following, the process is illustrated by the example of the activity measurements of the condensate plates. For the measurement, the plate was placed at a specified distance in front of a germanium detector. The background had previously been determined in the laboratory by an overnight measurement. A point source of Cs-137 was used as the standard for determining the constant of proportionality. Besides the statistical error and the uncertainty of the standard activity, it also had to be kept in mind that the measurement distance between the measurement standard and the sample measurement varied slightly. Ordinarily, for calibration a reference sample is used that displays the most similar possible geometry and activity distribution as the sample to be measured. However, since the distribution of the fission products on the condensate plates was unknown, conservatively a rectangular distribution was assumed for the possible distribution of the fission products. This ranged from a concentration in the center to a concentration of all fission products at the edge of the plate. The greatest possible error would appear in the case of complete concentration on the edge.

The relationship between the Cs-137 activity of the reference sample (A_s) and measured impulse rate (I_s) is found as:

$$A_s = \frac{I_s}{F_{s,137}} = \frac{4\pi \cdot l_s^2}{P_{\gamma,661} \cdot E_{661}} \cdot I_s$$

Equation 95

With the emission probability ($p_{\gamma,661}$) and the intrinsic detector efficiency (E_{661}) at 661.66 keV and the distance (l_s) between reference sample and detector. Ordinarily, these factors are combined to form a calibration factor F_{137} , which is determined by calibration. The attenuation of the radiation by self absorption and absorption in the atmosphere was neglected in this analysis.

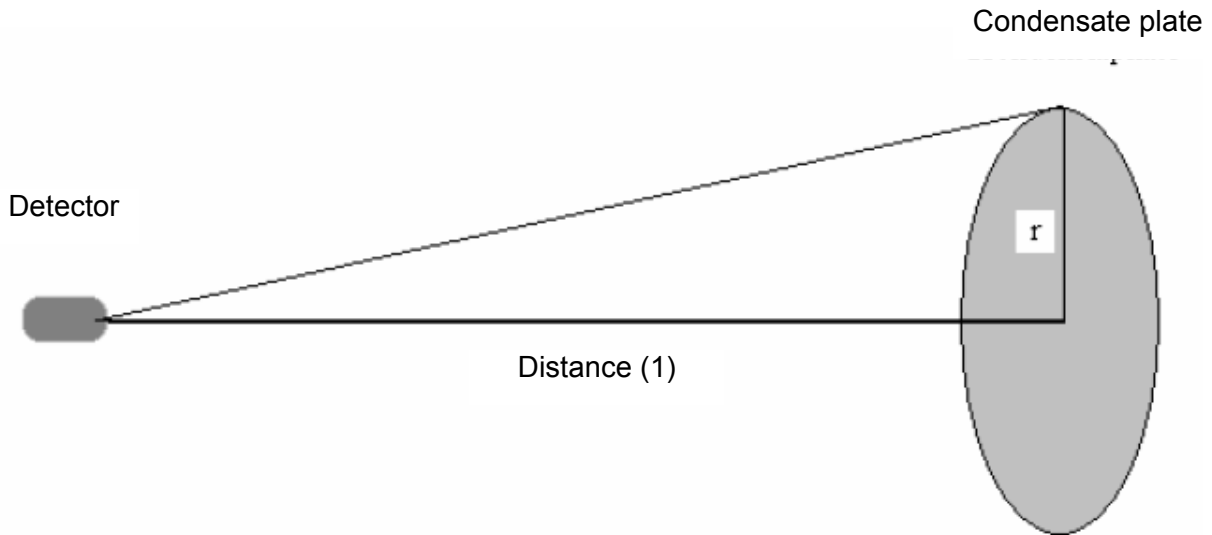


Figure 85: Representation of the measurement geometry for measuring the activity of the condensate plates

When the condensate plates are measured, the impulse rate is obtained from the integration of the distribution of the plate activity (A_p) over the plate radius (r):

$$I_p = P_{\gamma,661} \cdot E_{661} \cdot \int_0^R \frac{A_p(r)}{4\pi \cdot (l_p^2 + r^2)} dr$$

Equation 96

With the distance (l_p) between condensate plate and detector and the outer radius R of the condensate plate (see Fig. 85). If the total activity were concentrated in the edge zone, the impulse rate would be obtained by the following equation:

$$I_p = P_{\gamma,661} \cdot E_{661} \cdot \frac{A_p}{4\pi \cdot (l_p^2 + R^2)}$$

Equation 97

However, since the activity is calculated on the basis of the experimentally determined calibration factor from the measured impulse rate, one obtains a fundamental error (ΔA).

$$A_B = \frac{1}{F_{s,137}} \cdot I_p$$

Equation 98

The maximal fundamental or systematic error can now be determined by insertion/substitution.

..

$$\Delta A \leq \left(\frac{(l_p^2 + R^2)}{l_s^2} - 1 \right) \cdot \frac{1}{F_{s,137}} \cdot I_p$$

Equation 99

At a measuring distance of 50 cm, total concentration of the activity on the edge of the plate and a deviation of the measurement distances of 0.5 cm (sample and standard were fixed in holders for the measurement) one would obtain a maximal, relative, systematic uncertainty of 2.4%.

Appendix V. Diffusion parameters

The temperature-dependent diffusion coefficient is found according to Arrhenius as:

$$D = D_0 \cdot e^{\left(\frac{-Q}{RT}\right)}$$

(Arrhenius equation)

Equation 100

D_0 = Pre-exponential constant

R = General gas constant, Q = activation energy

In the following tables (Table 85 through Table 68) the parameters used within this project for the diffusion model employed are summarized [Verfondern et al. 1997].

Table 65: Diffusion parameters for cesium in jacket coatings and A3 graphite [Verfondern et al. 1997]

	D_0 (m ² /s)	Q (kJ/mol)
A3 graphite	3,6E-04	189
Core (UO ₂)	5,6E-08	209
	5,2E-04	362
Buffer coating	1E-08	0
PyC coating	6,3E-08	222
SiC coating	5.5E-14 • exp($\phi/5$) *	125
	1,6E-02	514

*Fast neutron fluence (> 0.1 MeV) (10²⁵ / m²)

Table 66: Diffusion parameters for strontium in jacket coatings and A3 graphite [Verfondern et al. 1997]

	D_0 (m ² /s)	Q (kJ/mol)
A3 graphite	1,0E-02	303
Core (UO ₂)	2,2E-03	488
Buffer coating	1E-08	0
PyC coating	2,3E-06	197
SiC coating	1,2E-09	205
	1,8E+06	791

Table 67: Diffusion parameters for silver in jacket coatings and A3 graphite [Verfondern et al. 1997]

	D_0 (m ² /s)	Q (kJ/mol)
A3 graphite	68	262
A3-27 graphite	1,3	246
A3-3 graphite irradiated	1,6	258
Core (UO ₂)	6,7E-09	165
Buffer coating	1E-08	0
PyC coating	5,3E-09	154
SiC coating	3,6E-09	215

Table 68: Diffusion parameters for krypton, xenon and iodine in jacket coatings and A3 graphite [Verfondern et al. 1997]

	D_0 (m ² /s)	Q (kJ/mol)
A3 graphite (along grain boundaries)	6,0E-06	0
A3 graphite (in the grain)	1E-18	71
Core (UO ₂)	8,8E-15	54
	6,0E-01	480
Buffer coating	1E-08	0
PyC coating	2,9E-08	291
	2,0E+05	923
SiC coating	~ 0	~ 0

The diffusion coefficient of cesium is composed of one part for high temperatures and a part for low temperatures. The low temperature part also contains a term describing the pre-exponential constant as a function of the fast [neutron] fluence [Allelein 1980], [Verfondern et al. 1997]. The composition from both of the parts is illustrated in Figure 86.

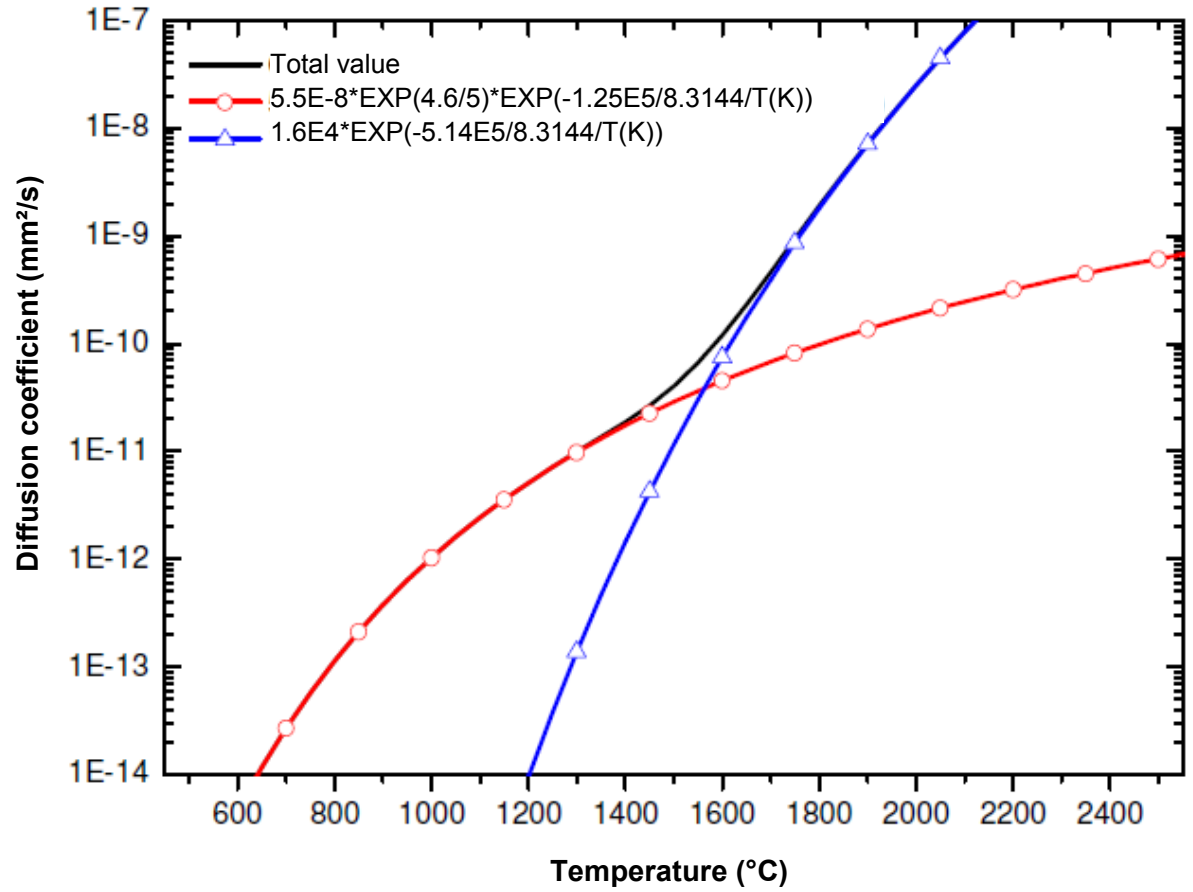


Figure 86: Composition of the temperature-dependent diffusion coefficient of cesium in silicon carbide ($\Phi = 4.6 \cdot 10^{25} \text{m}^{-2}$)

Appendix VI. Correction factors for gamma spectrometry

The intrinsic absorption in fuel and graphite matrix is dependent on the type of sphere. An improvement of the measurement accuracy can be achieved by determining correction factors for the various types of spheres [Freis et al.2006]. In this case, the fuel zone may be considered a homogeneous medium for simplicity. The specific gamma activity per unit volume amounts in the fuel zone to:

$$a = \frac{3A_\gamma}{4\pi r_i^3}$$

r_i is the radius of the fuel zone and A_γ is the total gamma activity of a certain emission energy in the fuel element. Since the complete volume integral cannot be solved directly, the fuel zone of the spherical element is broken up into infinitely many differential hollow cylinders and for these in each case, the attenuation of the radiation calculated by integration over the length.

$$f_{kugel} = \frac{3}{4\pi r_i^3 a} \int_0^{r_i} \int_{-\frac{1}{2}L(y)}^{\frac{1}{2}L(y)} 2\pi a y f_{eigen}(x, y) f_{enf}(x, y) f_{schale}(x, y) dx dy$$

The variable y is the radius of a given hollow cylinder. In the following illustration (Figure 87), the layered structure of a ball/sphere of hollow cylinders is illustrated.

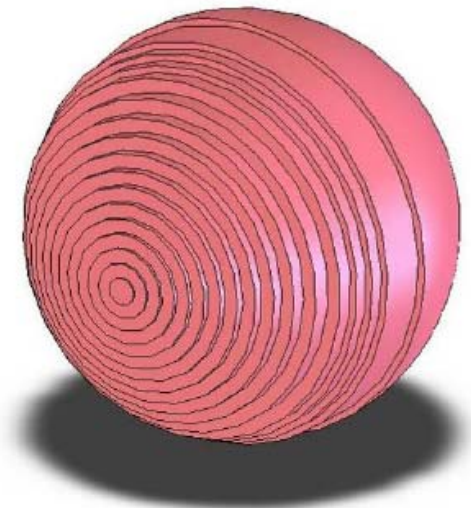


Figure 87: Layered structure of a ball of cylinder elements

The error (ε) taken in the bargain by this simplification consists essentially of the falsification of the path distance from the radiation source point being considered to the collimator by the neglect of the variable incident angles. For the least favorable point it amounts to maximally 0.093%, upon integration over the ball volume to less than 0.0306% and is therefore negligibly small.

$$\varepsilon_{\max} \leq \left| \frac{f_{BE,K}^2}{r_a^2 + f_{BE,K}^2} - 1 \right| = 0,000929 \quad (\text{VI-1})$$

$$\int_V \varepsilon(\bar{V}) d\bar{V} \leq 0,000306$$

$$r_a = 30\text{mm}, \quad f_{BE,K} = 984\text{mm}$$

Instead of integration over the height (y), one can also use the angle φ as a control variable. The geometric relations are then found in accordance with the following diagram (see Figure 88).

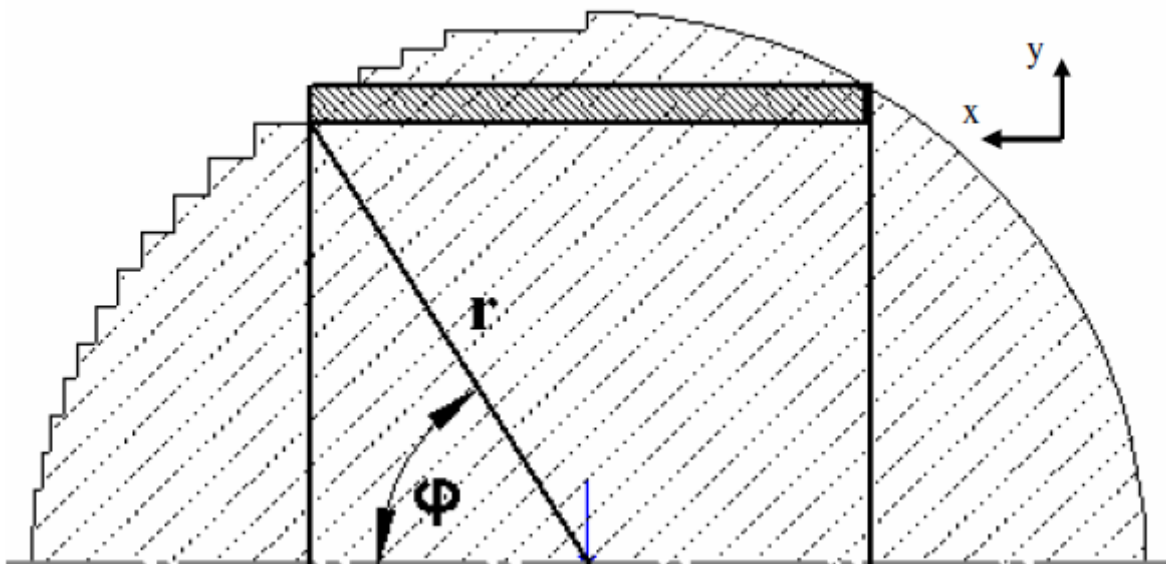


Figure 88: Composition of a ball of cylinder elements

The following relationships apply between the individual magnitudes:

$$y = r \sin(\varphi)$$

$$\frac{dy}{d\varphi} = r \cos(\varphi)$$

$$L(\varphi, r) = 2r \cos(\varphi)$$

The attenuation in the fuel zone is computed for a cylinder with the energy-dependent mass attenuation coefficient of:

$$f_{\text{eigen}} = \int_{\frac{L(\varphi)}{2}}^{\frac{L(\varphi)}{2}} e^{-\mu_B \left(\frac{L(\varphi)}{2} - x \right)} dx$$

$L(\varphi)$ is the length of the differential cylinder elements as a function of the angle (φ). It amounts to:

$$L(\varphi) = 2r_i \cos(\varphi)$$

The effect of the graphite shell can also be detected by an attenuation factor:

$$f_{\text{schale}} = e^{(-\mu_G s(\varphi))}$$

$s(\varphi)$ is the path distance through the outer shell that the radiation has to pass through from the fuel zone edge to the fuel element edge. It is obtained from a simple geometric analysis and depends on the angle φ .

$$s(\varphi) = \sqrt{r_a^2 - r_i^2 \sin^2(\varphi)} - r_i \cos(\varphi)$$

From these analyses, finally, the complete integral is obtained for determining the attenuation factor (f_{kugel})

$$f_{\text{kugel}} = \int_0^{\pi/2} \int_{-r_i \cos(\varphi)}^{r_i \cos(\varphi)} \left(\frac{2a\pi r_i^2 \sin(\varphi) \cos(\varphi)}{\frac{4}{3} a\pi r_i^3} \cdot e^{\left(-\mu_G \left(\sqrt{r_a^2 - r_i^2 \sin^2(\varphi)} - r_i \cos(\varphi) \right) \right)} \cdot \left(\frac{e^{\left(-\mu_B (r_i \cos(\varphi) - x) \right)}}{4\pi (f_{\text{BE},K} - x)^2} \right) \right) dx d\varphi$$

To obtain the correction factor (f_{kor}), the attenuation factor must first be computed for the standard used. This involves a graphite ball of A3 graphite in the center of which a defined quantity of fuel solution was introduced containing a known quantity of fission products. For 661.61 keV, the attenuation factor for the standard ball (f_{st}) is calculated as:

$$f_{\text{st}} = \frac{e^{-\mu_G s}}{4\pi (f_{\text{BE},K})^2} = 5,748 \cdot 10^{-8}$$

$$\mu_G = 0,013 \text{ mm}^{-1}, f_{\text{BE},K} = 984 \text{ mm}, s = 27,5 \text{ mm}$$

The mass attenuation coefficient of the fuel zone (μ_B) can be determined in a simplified manner according to the following equation from the coefficients of the graphite and of the fuel as well as the mass portions. For 661.66 keV one obtains:

$$\begin{aligned} \mu_B &= \mu_G V_G + \mu_{\text{UO}_2} V_{\text{UO}_2} \\ &= \mu_G \frac{\rho_B}{\rho_G} W_G + \mu_{\text{UO}_2} \frac{\rho_B}{\rho_{\text{UO}_2}} W_{\text{UO}_2} \end{aligned}$$

$$\mu_G = 0,013 \text{ mm}^{-1}, \mu_{\text{UO}_2} = 0,1276 \text{ mm}^{-1}$$

$$\rho_{\text{UO}_2} = 0,01081 \frac{\text{g}}{\text{mm}^3}, \rho_G = 0,00176 \frac{\text{g}}{\text{mm}^3}$$

V_G, V_{UO_2} : Volume parts

W_G, W_{UO_2} : mass parts

The correction factor (f_{korr}) now follows from:

$$A_{\gamma} = \frac{\dot{I}}{f_{\text{korr}} K} \Rightarrow f_{\text{korr}} = \frac{f_{\text{kugel}}}{f_{\text{st}}}$$

with K as the calibration factor. In Table 69 below, correction factors for different fuel element types are reported with a statement of the fuel element geometry and the mass attenuation coefficient of the fuel zone at 661.61 keV. The subscript 1 stands for the correction factor when the self-fabricated standard is applied, the subscript 2 may be referred to when the standard fuel element is use.

Table 69: Correction factors for different fuel element types at 661.61 keV

BE Type	μ_{B} (mm^{-1})	r_{i} (mm)	r_{a} (mm)	f_{kugel}	$f_{\text{korr},1}$	$f_{\text{korr},2}$
Proof	0,0147	25	30	$5,8387 \cdot 10^{-8}$	1,0158	0,9885
AVR-GLE 3	0,0148	25	30	$5.8291 \cdot 10^{-8}$	1,0141	0,9869
AVR-GLE 4	0,0141	25	30	$5.9067 \cdot 10^{-8}$	1,0276	1

Appendix VII. Determination of the ball diameter

During the irradiation, the matrix graphite is subject to dimensional variations. To determine the degree of dimensional change, the diameters of three fuel elements were measured with a test gauge. For this purpose, first a steel cylinder with a known length and then the fuel element in question were measured at five positions (see Figures 89 and 90). All of the measured fuel elements displayed a reduction of the diameter relative to the manufacturing specifications of 60 mm.

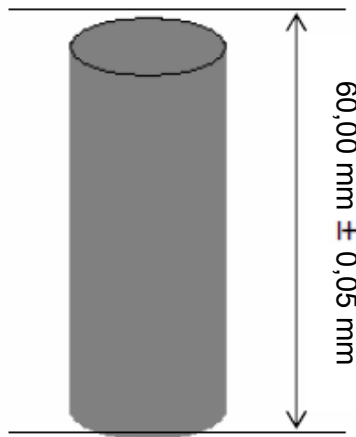


Figure 89: Standard cylinder for dimension measurement.

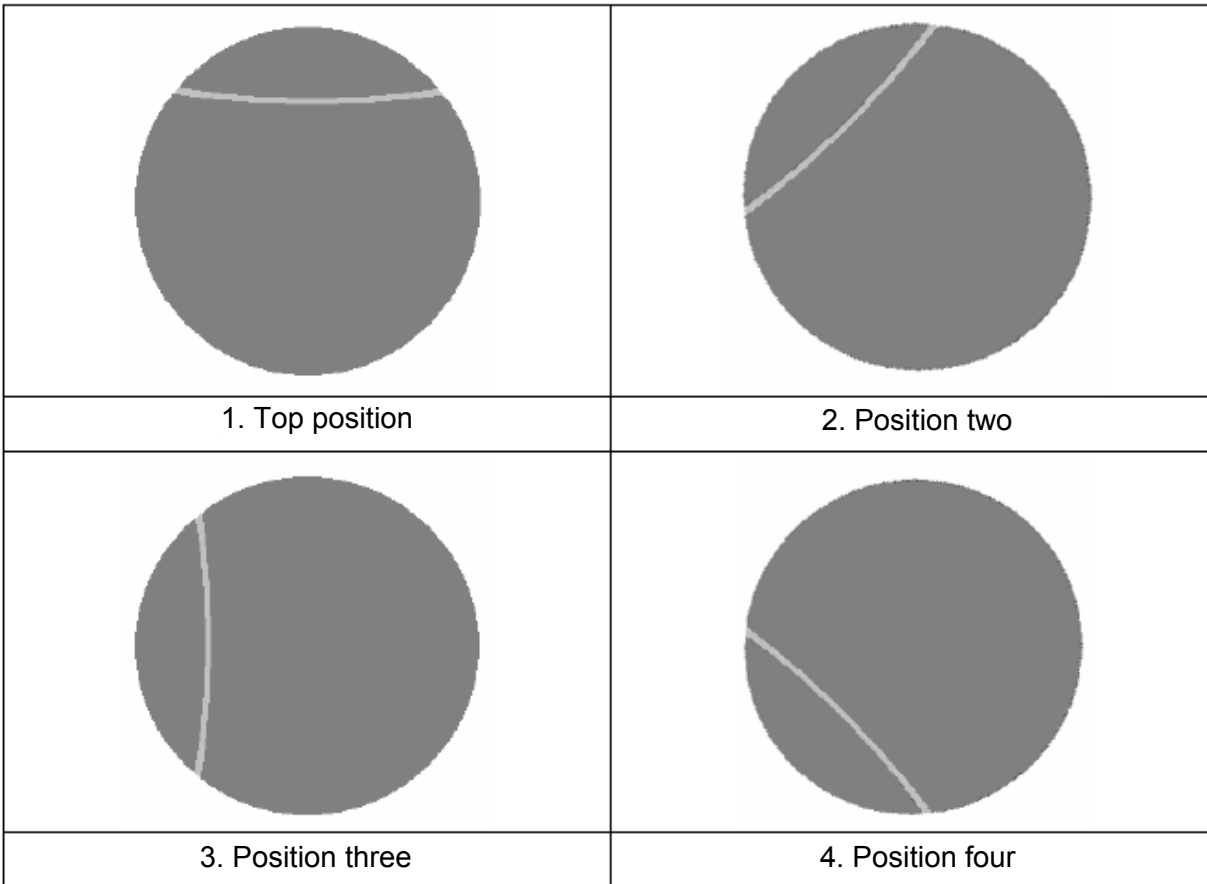


Figure 90: Measurement position for measuring the dimension change of the fuel elements.

Ball/sphere HFR K6 2 (after bakeout experiment)

Position	x (mm)	Δx (mm)	\varnothing (mm)
Standard cylinder	10,03	0	$60 \pm 0,05$
1. top	9,44	0,59	$59,41 \pm 0,1$
2. two	9,45	0,58	$59,42 \pm 0,1$
3. three	9,46	0,57	$59,43 \pm 0,1$
4. four	9,45	0,58	$59,42 \pm 0,1$
5. bottom	9,43	0,6	$59,40 \pm 0,1$
Average	9,446	0,584	$59,416 \pm 0,045$

Ball/sphere HFR Eu1bis 1 (after bakeout experiment)

Position	x (mm)	Δx (mm)	\varnothing (mm)
Standard cylinder	10,03	0	$60 \pm 0,05$
1. top	9,00	1,03	$58,97 \pm 0,1$
2. two	8,89	1,14	$58,86 \pm 0,1$
3. three	8,79	1,24	$58,76 \pm 0,1$
4. four	8,86	1,17	$58,83 \pm 0,1$
5. bottom	8,99	1,04	$58,59 \pm 0,1$
Average	8,906	1,124	$58,876 \pm 0,045$

Ball/sphere HFR Eu1 bis 3 (before bakeout experiment)

Position	x (mm)	Δx (mm)	\varnothing (mm)
Standard cylinder	10,03	0	$60 \pm 0,05$
1. top	8,76	1,27	$58,37 \pm 0,1$
2. two	8,68	1,35	$58,65 \pm 0,1$
3. three	8,49	1,54	$58,46 \pm 0,1$
4. four	8,66	1,37	$58,63 \pm 0,1$
5. bottom	8,78	1,25	$58,75 \pm 0,1$
Average	8,674	1,356	$58,644 \pm 0,045$

Ball: HFR Eu1 bis 3 (after bakeout experiment)

Position	x (mm)	Δx (mm)	\varnothing (mm)
Standard cylinder	10,04	0	$60 \pm 0,05$
1. top	8,78	1,26	$58,74 \pm 0,1$
2. two	8,71	1,33	$58,67 \pm 0,1$
3. three	8,56	1,48	$58,52 \pm 0,1$
4. four	8,71	1,33	$58,67 \pm 0,1$
5. bottom	8,82	1,22	$58,78 \pm 0,1$
Average	8,674	1,324	$58,676 \pm 0,045$

BIBLIOGRAPHIC DATA SHEET

(See instructions on the reverse)

3806

2. TITLE AND SUBTITLE

Accident Simulations and Post-irradiation Investigations on Spherical Fuel Elements for High Temperature Reactors

3. DATE REPORT PUBLISHED

MONTH

YEAR

3

2010

4. FIN OR GRANT NUMBER

5. AUTHOR(S)

Grad. Eng. Daniel Freis

6. TYPE OF REPORT

Dissertation

7. PERIOD COVERED (Inclusive Dates)

2010

8. PERFORMING ORGANIZATION - NAME AND ADDRESS (If NRC, provide Division, Office or Region, U.S. Nuclear Regulatory Commission, and mailing address; if contractor, provide name and mailing address.)

U.S. Translation Company
1893 E. Skyline Dr. #203
South Ogden, UT 84403

9. SPONSORING ORGANIZATION - NAME AND ADDRESS (If NRC, type "Same as above"; if contractor, provide NRC Division, Office or Region, U.S. Nuclear Regulatory Commission, and mailing address.)

U.S. Nuclear Regulatory Commission
Washington D.C. 20555

10. SUPPLEMENTARY NOTES

11. ABSTRACT (200 words or less)

The safety of high-temperature reactors depends on fuel quality and high temperature stability to guard against fission product releases. In this project accidents were simulated on burnt-up high temperature reactor fuel elements with TRISO-coated particles and the fission product releases were measured using the cold finger apparatus previously used at Jülich Nuclear Research Center and used in the hot cells of the European Institute for Transuranium elements since 2005 permitting accident simulations on irradiated high temperature reactor fuel elements in a helium atmosphere at temperatures up to 1800 degrees Celsius or several hundred hours, registering the release of fission gases and of solid fission products. The mechanical behavior of the particles and the transporting mechanisms of the most important fission products were analyzed and the releases recalculated. In addition, post-irradiation studies were conducted on the fuel elements. Finally, the test results were analyzed and compared with the results in the literature. The goal was to expand the database for modern HTR fuel to include higher burn-ups, higher fast neutrons fluences, higher operating temperatures, and higher accident temperatures.

12. KEY WORDS/DESCRIPTORS (List words or phrases that will assist researchers in locating the report.)

13. AVAILABILITY STATEMENT

unlimited

14. SECURITY CLASSIFICATION

(This Page)

unclassified

(This Report)

unclassified

15. NUMBER OF PAGES

16. PRICE